Physical and Numerical Modeling of Fracture in Rock:

With Special Emphasis on the
Potash Mines of Saskatchewan

by

Bruce J. Carter

A Thesis
Submitted to the Faculty of Graduate Studies
in Partial Fulfillment of the Requirements
for the Degree of

Doctor of Philosophy

Civil Engineering Department
University of Manitoba
Winnipeg, Manitoba

April 1, 1992

ISBN 0-315-77741-9

PHYSICAL AND NUMERICAL MODELING OF FRACTURE IN ROCK: WITH SPECIAL EMPHASIS ON THE POTASH MINES OF SASKATCHEWAN

BY

BRUCE J. CARTER

A Thesis submitted to the Faculty of Graduate Studies of the University of Manitoba in partial fulfillment of the requirements for the degree of

DOCTOR OF PHILOSOPHY

ABSTRACT

Physical and numerical modeling of fractures in rock is performed using three different rock types: potash, limestone and granite, with particular emphasis placed on the potash rock. Fractures in both tensile and compressive stress fields are described, based on simple laboratory tests (such as uniaxial compression, Brazilian tension, cycled triaxial compression) and models simulating circular underground excavations.

A number of theories exist for predicting crack evolution and rock failure but most of these are inadequate to describe fracture under both tension and compression. A simple fracture/failure criterion (***USR***) is proposed which is capable of modeling fracture under any stress state. This fracture criterion is also suitable for analyzing the stress gradient dependence of strength and fracture initiation around cavities.

There are numerous factors which control the initiation of fractures around underground cavities. These include cavity size and shape, time, stress state, chemical environment, stratigraphy, etc. Cavity size is analyzed by testing models with various-sized circular openings. In general, the fracture initiation stress decreases with increasing hole size for relatively small cavities. The stress and time dependence are examined through several creep tests which show that cracks increase in length and number with increasing time and/or stress. The effects of stratigraphy, opening shape and the presence of multiple openings are examined through physical models as well.

A finite element code (SIMEX), that uses the ***USR*** criterion for state of fracture, the Rocker function for triaxial strength and the concept of stress averaging for size effect, accurately predicts the fracture pattern for the simplest physical models in potash.

ACKNOWLEDGMENTS

I would like to thank my advisor, Dr. Emery Lajtai, for his advice and guidance throughout this study and for his assistance in the preparation of this thesis. He helped to keep the research focussed, suggested numerous ideas and often lent his hand during the physical testing.

I would also like to thank Dr. B. Stimpson, Dr. A. Shah and Dr. B. Pinkney for their time and effort in reviewing this work. All of their advice, suggestions and criticisms were much appreciated. I am also indebted to Dr. A. Ingraffea for acting as the external examiner.

I would like to express my gratitude to W. Grajewski for his technical assistance and advice during the physical modeling and testing. He helped set up many of the physical experiments, often operated the equipment and always made sure everything was working properly.

I would like to thank Dr. M.L. Ayari and Y. Yuan for their unending assistance during the numerical modeling stages of this study. They were always there to lend a hand or provide a thoughtful insight. I would also like to thank Scott Duncan and Rui Chen for their help in understanding the material behavior of potash. Derek Martin initiated many interesting discussions on size effect and fracture in LDB granite. All the other graduate students who offered their assistance and advice along the way are appreciated as well. Ingrid Trestrail, our administrative assistant, always made work more enjoyable.

In addition, I would like to thank the members of the Potash Working Group who have not already been mentioned. In particular, Mr. D. Mackintosh of Cominco Fertilizers Limited provided many insights into the process of fracturing around the potash mine openings. He also helped obtain the necessary samples as well as giving direction to the modeling program.

The author was supported by a Natural Science and Engineering Research Council of Canada (NSERC) Scholarship, a University of Manitoba Fellowship and a Manitoba Hydro, Stephens Memorial Fellowship. The research was supported by NSERC and two potash mining companies, Cominco Fertilizers Limited and the Potash Corporation of Saskatchewan.

The author was supported throughout his years of University by his family and friends and especially by his wife, Judy, whom he lovingly thanks.

TABLE OF CONTENTS

LIST OF FIGURES

LIST OF TABLES

NOTATION AND SYMBOLS

CI	- crack intiation
CD	- crack damage, corresponds to VR
VR	- volumetric reversal
USR	- unconfined strength ratio
CP	- crack potential
K_{IC}	- critical stress-intensity factor
Rocker	- an empirical strength function
FIWEC	- finite width elliptical cavity
C_o or σ_c	- uniaxial compressive strength
T_o or σ_t	- tensile strength
SIF	- stress intensity factor
COD	- crack opening displacement
LEFM	- linear elastic fracture mechanics
NLFM	- non-linear fracture mechanics

1 INTRODUCTION

1.0 General Introduction

Although fractures in rock have been studied for many years, it was not until the end of the nineteenth century that structural geologists realized that some cracks form in tensile stress fields while others form in compressive stress fields (Van Hise, 1896). Structural geologists often refer to such things as joints (tension fractures), which are fractures upon which little or no shear movement has occurred, and faults (shear fractures), which are generally recognized and classified according to the relative displacement that has occurred along the fracture plane.

In the early 1900's, there was a lot of debate concerning the origin and location of these different fracture types. Many geologists felt that tensile fractures were only a surface feature associated with cooling of magma or anticlines of folds where obvious tensile stresses exist. Consequently, all other fractures had to be shear fractures which formed in a compressive stress field (Engelder, 1987). It was not until the 1960's that theories began to emerge explaining the formation of tensile fractures or joints at depth within the earth's crust (Secor, 1965; Price, 1968; Scholz, 1968; Lajtai, 1977). Shear fractures could then be explained as forming within a system of small tensile fractures, producing a shear—fracture zone or fault (Brace, 1964). Both types of fracture, tensile and shear (zone), are a common feature in rocks and can often be seen in rock outcrops, quarries, rock foundations, rock slopes and underground excavations.

Fracture around underground excavations is of considerable interest at the present time for a number of reasons. There are underground research sites in Canada, the United States and Europe where large amounts of time and money are being invested in attempts to design permanent storage sites for nuclear waste (Martin and Christiansson, 1991; Blejwas, 1987; Cramer *et al.*, 1987). For these sites, it is desirable to have very few fractures through which radioactive waste could travel. At the very least, fractures would have to be carefully controlled.

Mining companies are continuously attempting to increase extraction ratios and are developing ever deeper mines. Along with increasing depth or increasing extraction ratios come increasing stress concentrations. High stresses can lead to dangerous rock-burst conditions, failure of pillars, and collapse, or in ductile rock, complete closure of the opening (Hoek and Brown, 1980; Baeza *et al.*, 1987; Steed *et al.*, 1985; Kaiser *et al.*, 1985). Civil engineering installations are also becoming more numerous and often much larger as well (Honisch, 1988). Fractures can be useful and are often induced during the excavation of underground caverns, but in many cases they are undesired and costly.

In particular, the Saskatchewan potash mines have encountered numerous problems associated with fracturing, including micro-seismic events or small earthquakes, which result from the rapid release of elastic strain energy during fracturing (Horner, 1983; Gendzwill, 1983; Ahmed, 1990), and water inflow or flooding, where the water may follow existing fracture paths or hydraulically create new ones (Morgenstern and Sepehr,

1991). Subsidence, resulting from closure of the openings (Steed *et al.*, 1985), can also be related to fracturing.

Fractures due to the stress concentrations around underground openings manifest themselves in varying degrees of intensity, ranging from harmless spalling to violent rockbursts (Hoek and Brown, 1980). They occur in various locations with respect to the opening, forming in the roof and floor, the side walls, and even remote to the opening. Assuming the maximum principal compressive stress is vertical, the fractures that form in the roof and floor are often harmless and sometimes helpful in relieving stress concentrations. The sidewall fractures may consist of harmless spalling but may also include violent rockbursts, causing damage and production loss. A third type of fracture, the remote fractures, are rarely seen as they usually only intersect the cavity at the side walls just prior to the collapse of the tunnel and may be mistaken for sidewall fractures.

The motivation for this research comes from visiting the Cominco potash mine near Vanscoy, Saskatchewan where the stress conditions are high enough to cause extensive fracturing in the yield pillars and in the sidewalls of tunnels. Recent re-excavation of older abandoned parts of the mine exposed several sections of collapsed workings. Many of the openings were almost completely closed. Fractures could be seen within the pillars as well as above and below the collapsed rooms. These fractures may have formed immediately upon excavation but it is probable that the original cracks grew and that new fractures formed over time. Although subcritical crack growth in rocks is a well-studied phenomenon (Atkinson and Meredith, 1987), time-dependent fracture growth in potash, and especially in the potash mines has not yet, to the author's knowledge, been studied.

1.1 Problem Statement and Objectives

This study is part of a collaborative research project between the University of Manitoba and two Saskatchewan potash mining companies, Cominco Fertilizers Limited and the Potash Corporation of Saskatchewan. The ultimate goal of this research is to predict fracture initiation and growth around the potash-mine openings. For generality, two other rock types were also studied.

Potash mines and most other underground excavations exist in an all-compressive-stress environment. The presence of the opening alters the compressive stress field, producing compressive- and perhaps tensile-stress concentrations around the cavity. Fractures will form within both types of stress concentration. Accordingly, a fracture theory should be capable of modeling fractures in both types of stress fields. At present, no single fracture criterion appears suitable. Therefore, the first step towards the final goal is the development of a general fracture criterion and experimental tests on three rock types, in both tension and compression, have been used to verify this fracture criterion.

The second step is the application of this criterion to the fractures which form around underground cavities. Three classes of fractures commonly exist around circular cavities in rock: primary, remote or secondary, and sidewall fractures (Hoek and Brown, 1980; Gay, 1976; Carter *et al.*, 1991*a*). Even though the three fractures form in very different stress fields, they are all genetically similar. Fractures form parallel to the maximum compressive stress and grow perpendicular to the minimum principal stress (compression is positive). Primary fractures form in the roof and floor where biaxial tension often

exists. Sidewall fractures grow out of a region subjected to high compressive stresses. Remote fractures develop in an area of high compressive stress parallel to the crack and either low tensile or low compressive stress perpendicular to the crack.

As part of this second step, physical model tests were used to aid in understanding the fracture process around underground cavities. The information obtained from these small models needs to be related, however, to the large underground excavations. Previous researchers recognized that fracture initiation depends on the cavity size of the physical models (Lajtai, 1972; Haimson and Herrick, 1989). Therefore, before the physical models can be compared to actual mine openings, a size-effect law must be established which accounts for size- and/or stress-gradient effects on the fracture process. Several theories exist already, including fracture mechanics (Ingraffea, 1987; Ewy and Cook, 1990) or the related critical strain energy model (Gonano, 1974), Weibull's theory (Weibull, 1939), Bazant's size effect law (Bazant, 1984), the pressure dependence of the elastic modulus (Santarelli and Brown, 1987), or stress averaging (Lajtai, 1972 and Nesetova and Lajtai, 1973). However, none of these theories correctly predicts all the data trends observed during this study. Thus, a variation of the stress-averaging procedure was developed which can interpret the size dependence of fracture.

In addition to cavity size, fracture growth in rock also depends on time and stress level (Atkinson and Meredith, 1987). Underground excavations are developed in a pre-stressed environment. Depending on the stress level and the rate of excavation, fractures may form immediately upon excavation but may also develop over time. Many of the time-dependent properties of potash have already been studied (Duncan, 1990). However,

time-dependent discrete fracture growth in potash has not yet been analyzed in detail. The third step, therefore is to model time- and stress-dependent fracture growth around the mine openings.

Because of the many parameters controlling fracture, the only feasible method of predicting discrete fracture growth around underground openings in potash is through numerical modeling using finite elements. The fourth step involves the incorporation of the rock strength and fracture parameters into the numerical model along with the appropriate fracture criterion. Finite elements can then be used to model more complex cases involving different stress fields with various opening shapes and sizes. Numerical modeling can be used to accomplish the final objectives, predicting 1) the location of fracture initiation, 2) the direction of propagation and 3) the final length of the fractures, for different mine opening shapes and sizes under arbitrary stress fields. Other aspects, such as layered stratigraphy and the presence of multiple openings may also be included in the finite element model.

1.2 Scope of Study

Three different rock types were used in this study, as fractures seem to occur in all rocks. A granite, a limestone and a potash-salt rock were tested, representing a range from most brittle to least brittle. Chapter 2 contains a description of the geology, appearance and physical behavior for each rock type. Each of these three rock types has been well studied at the University of Manitoba and large amounts of experimental data

have been accumulated. Chapter 2 contains some of this data plus the results from a number of tests which were completed during the course of this study.

Chapter 3 describes the basics of rock fracture and failure. The science of fracture mechanics and the use of empirical failure criteria are discussed in terms of the physical evidence obtained from experiments on rock. The size-effect phenomenon is also reviewed. A new fracture criterion is developed which can predict fracture initiation and growth in both tensile- and compressive-stress fields. The new fracture criterion also addresses the aspect of stress gradient or size dependence.

The experimental data from Chapter 2 and the fracture criteria from Chapter 3 can be used to analyze the results of the physical model tests of underground openings. The modeling procedure and results of the experiments are described in Chapter 4. The fracture pattern around a circular opening is shown and the three fracture types (primary, remote and sidewall) are discussed in detail. Different hole sizes have been used to relate the model test data to real underground openings. The effect of the hole size and the associated stress gradients are discussed in terms of the strength anomalies seen in the physical tests. The various theories used to model size dependence are examined and a variation of the stress averaging method is employed, utilizing the new fracture criterion.

Chapter 5 begins by describing time- and stress-dependent fracture growth around tunnels in potash. The next section describes a simple uniaxial compressive test on a layered potash model which was an attempt to simulate the actual stratigraphic layering within the Cominco—Vanscoy potash mine. The final section describes a physical test on a large block of potash with three horizontally aligned, circular holes.

Chapter 6 delves into the field of finite elements and numerical modeling which allows more complicated configurations to be studied. A finite element code, SIMEX (SIMulated Mining EXcavation) was written by Dr. M.L. Ayari (Ayari, 1991) with some later additions by Y. Yuan. This program was designed specifically for the task of modeling discrete fracture propagation around underground openings in a compressive-stress field. The physical modeling in this study involved simple configurations of circular holes under uniaxial compression. These physical tests were used to calibrate the numerical model so that more complex cases of biaxial loading and multiple openings could be analyzed using SIMEX.

Chapter 7 is a discussion and a summary of the main points in the thesis. The first sections indicates that all rocks behave in a similar manner when they fracture, regardless of scale. This includes a description of the physical processes involved, processes which have been seen in the physical model tests, in the potash mines and in laboratory compression tests. The next portion discusses the procedure of numerically modeling the observed fractures. The problems and advantages of both fracture mechanics and the stress-averaging fracture criterion developed during this study are examined. The final section indicates several possible directions for future research.

Chapter 8 is a brief, point-by-point summary of the main conclusions of the thesis.

2 GEOLOGY AND MATERIAL PROPERTIES OF THE THREE ROCK TYPES

2.0 Introduction

Three different rock types were used during the course of this study, a brittle granite, a semi-brittle limestone, and a more ductile potash rock. The physical properties for these three rock types are quite different although, in general, most rocks seem to behave in a similar manner. This chapter describes some of the observed physical properties of these three rocks.

All three rocks have been widely studied at the University of Manitoba over the last few years. Some of the experimental data will be summarized here as the values are required for development of a fracture criterion and for analysis of the physical and numerical models. During the course of this research, several more tests were conducted and these will be discussed in more detail.

To develop a fracture criterion, several fracture and rock strength parameters must be defined. Dilatancy and axial cracking of brittle rocks, loaded in compression, have been studied for many years (eg. Brace et al., 1966). Bieniawski (1967) showed that the normal stress—strain response of brittle rocks could be divided into four stages (Figure 2.1). The first portion of the curve represents the closure of existing microcracks and is usually negelected. This is followed by a linear—elastic portion (Stage I) where the elastic modulus and Poisson's ratio are usually measured. Crack initiation (CI) marks the beginning of the second stage (Stage II). This point usually occurs at the point where the

lateral strain deviates from its initial, linear—elastic, stress—strain path. For more ductile rocks, with a low yield stress, this point can be difficult to measure from the lateral strain alone as the onset of plastic deformation causes both the axial and lateral stress—strain curves to deviate from linearity. The volumetric strain, which is calculated from the measured axial and lateral strains (axial - (2)·lateral), can help in fixing this point however. The third stage (Stage III) begins at the point of volumetric-strain reversal (VR). This is the point on the stress—strain curves, between the crack initiation stress and peak strength, where the strain due to cracking begins to accelerate leading to permanent strain and dilatation. The term, crack damage (CD), shown on the stress—lateral-strain curve, will also be used to define this point as the volumetric-strain curve is not always available. It has been suggested that, at this point, cracks continue to propagate in an unstable manner even if the load is held constant (Einstein *et al.*, 1970). The fourth stage (Stage IV) begins at the point of peak strength and consists of the softening portion of the stress—strain curve. Peak strength is simply the highest stress a rock experiences before failure and softening may or may not be shown. A stiff, displacement-controlled testing machine is required to obtain the softening portion.

These points, crack initiation, volumetric reversal or crack damage, peak strength and yield stress if one exists, are all distinct points. They can be measured for the three rock types of this study from both tension and compression tests. The relative position of the points, on the stress—strain curve, may change with confining pressure, time, temperature and other environmental factors, but only the effect of confining pressure will be examined here. All tests were conducted on dry samples, at room temperature.

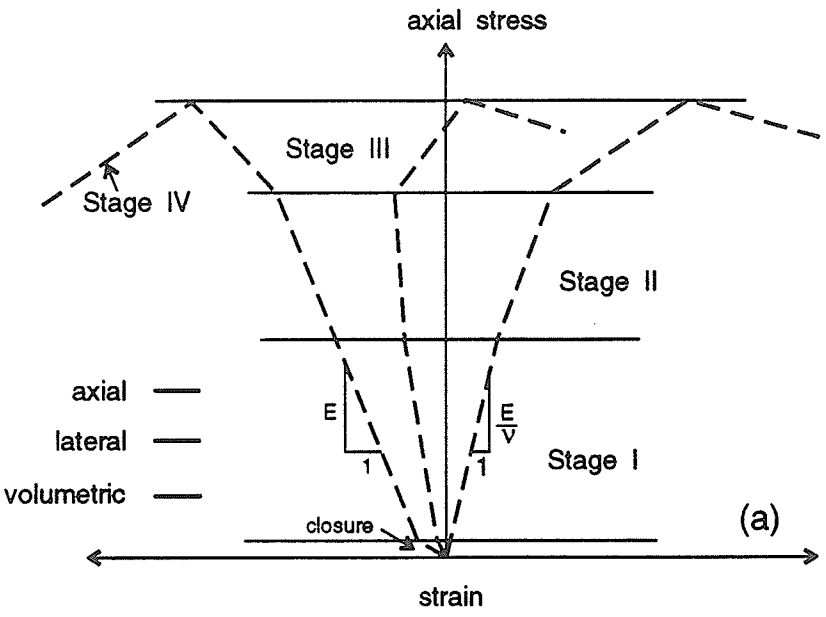

Figure 2.1 (a) The four stages of a stress—strain curve for a typical brittle rock (after Bieniawski, 1967).

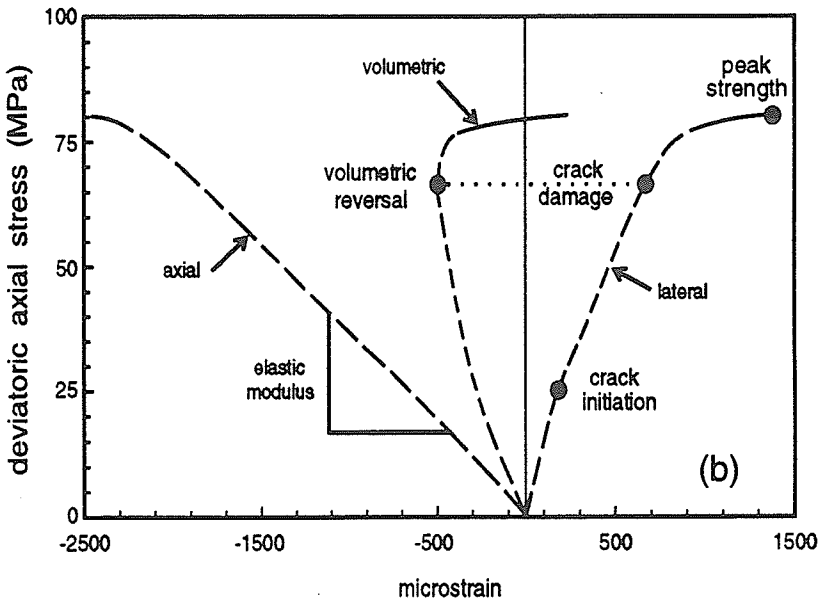

Figure 2.1 (b) An example of axial, lateral and volumetric stress—strain curves showing crack initiation, volumetric reversal or crack damage, yielding, peak strength and the elastic modulus for triaxial compression of Tyndallstone, at a confining pressure of 5 MPa.

2.1 Lac du Bonnet Granite

The most brittle of the three rocks, the granite, was obtained from the Cold Spring Quarry near Lac du Bonnet (LDB), Manitoba (Figure 2.2). It is part of the Lac du Bonnet batholith which is located on the edge of the Canadian Shield. It is commonly used as a decorative and building stone due to its color, texture, and strength.

It is a pink, relatively homogenous, medium- to coarse-grained (.5 mm - 20 mm) granite consisting of, on average, 36% oligoclase and 31% microcline feldspar, 28% quartz and 5% biotite (Lajtai, 1982). There is an indication of some foliation as well which is depicted by the lineation of the biotite grains.

Lac du Bonnet granite is a very strong, highly brittle, elastic rock. The average uniaxial compressive strength is 226 MPa while the average tensile strength is close to 14 MPa (Brazilian test data). The elastic modulus in compression is about 70 GPa and Poisson's ratio is about 0.21.

A number of triaxial compression tests were previously conducted and various strength curves have been fitted to the data to give a peak strength versus confining pressure relationship (Carter *et al.*, 1991*a*). A number of the triaxial tests were instrumented with strain gauges and the other two fracture parameters, crack initiation and volumetric reversal, can be measured from the stress—strain curves (Figure 2.3). The crack initiation point is at about 44% and crack damage is at about 71% of the strength (Lajtai *et al.*, 1991*a*). Young's modulus and Poisson's ratio were also measured from the stress—strain curves. There is little variation of the elastic modulus (Figure 2.4) and Poisson's ratio (Figure 2.5). Martin and Christiansson (1991), working at the AECL

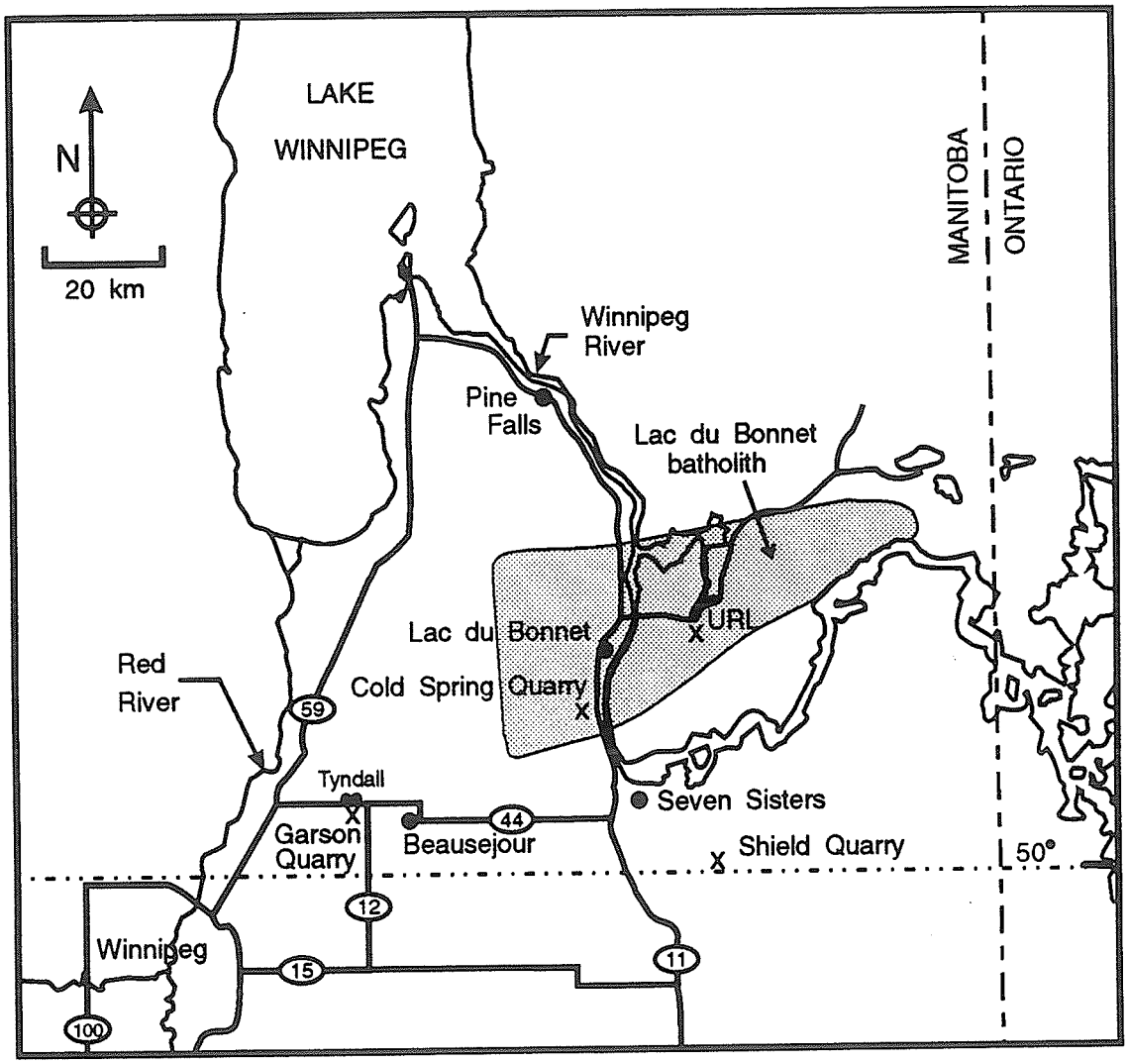

Figure 2.2 Map showing the Lac du Bonnet batholith, Cold Spring Quarry, the Underground Research Lab (URL) of Atomic Energy of Canada Ltd. as well as the Garson Quarry near Tyndall and Garson, Manitoba (after Samchek, 1983).

Underground Research Laboratory near Lac du Bonnet, also found that the modulus of the pink granite (similar to the Cold Spring Quarry granite) did not vary significantly with confining pressure.

Several cycled compression tests have also been done. These tests provide another method for finding the load at crack initiation and the load at volumetric reversal. One test was conducted in uniaxial compression (Lajtai, 1982; Lajtai *et al.*, 1990) and two more tests were performed by the author, using 28.5-mm-diameter specimens. The latter two tests were done under confining pressures of 10 and 20 MPa, respectively. The axial load was incremented for successive cycles until the specimen failed. By examining the permanent strain after each loading—unloading cycle (Figure 2.6), the crack-initiation stress and crack-damage stress were measured (Table 2.1a-c). The changing value of Poisson's ratio may also be a good indicator of crack initiation and crack damage (Table 2.1c). Poisson's ratio is nearly constant at the beginning of the test, until the crack-initiation stress is exceeded. Once the crack initiation stress has been surpassed, the ratio begins to increase slightly. This is followed by a more noticeable increase once the crack-damage stress is exceeded. The elastic modulus, on the other hand, is nearly constant throughout the tests. Another feature seen during these cycled tests is the change in the volumetric reversal point as the number of cycles increases (Figure 2.7). Once the initial volumetric reversal point has been surpassed, ensuing cycles show a decrease in the stress at this reversal point. Near the peak load, the reversal stress is almost as low as the crack-initiation stress (Martin *et al.*, in preparation).

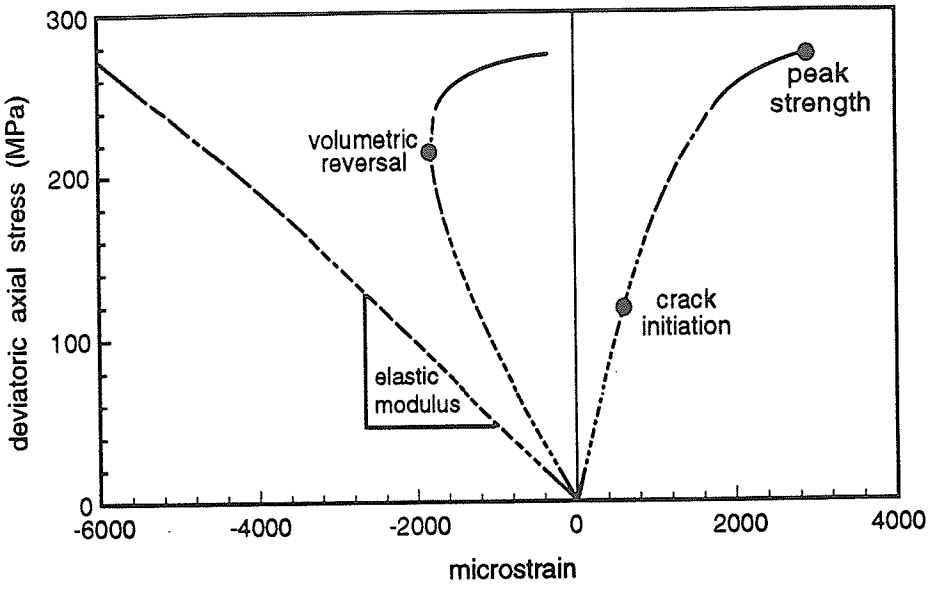

Figure 2.3 Axial, lateral and volumetric stress—strain curves for LDB granite in triaxial compression with a confining pressure of 16 MPa, showing crack initiation, volumetric reversal, peak strength and elastic modulus.

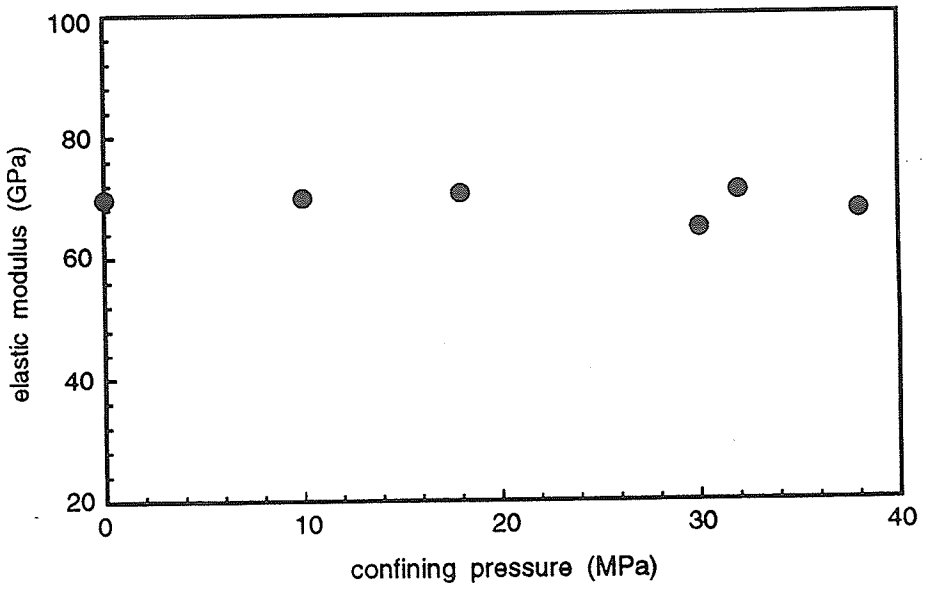

Figure 2.4 Variation in elastic modulus of LDB granite with confining pressure.

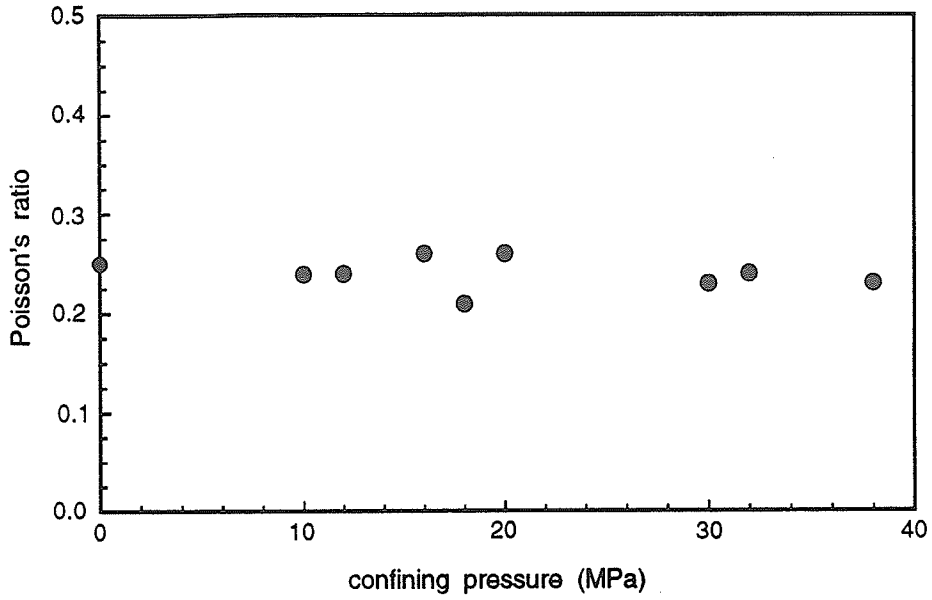

Figure 2.5 Variation in Poisson's ratio of LDB granite with confining pressure.

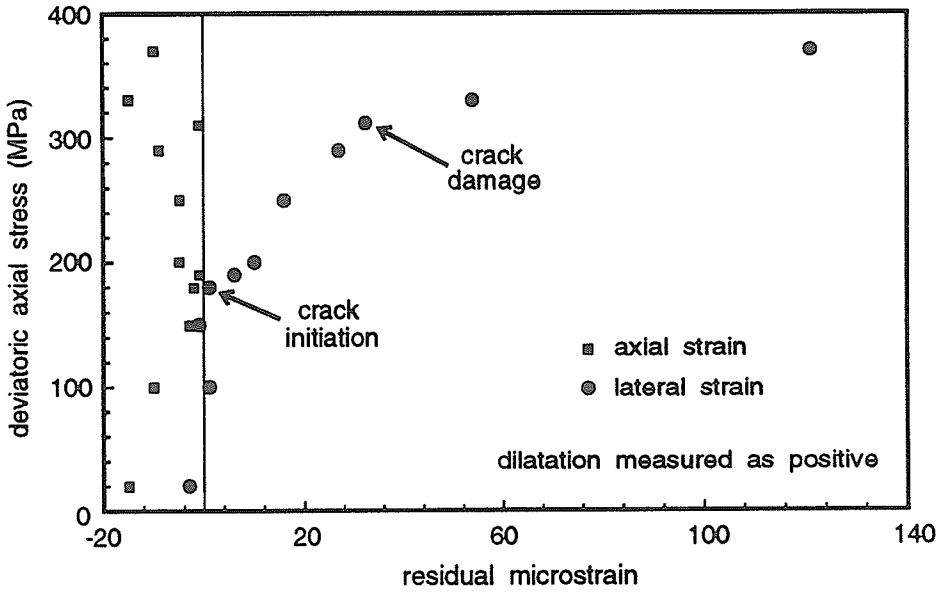

Figure 2.6 Residual or permanent axial and lateral strains for successive loading—unloading cycles for LDB granite under triaxial compression with a 20-MPa confining pressure. The changes in residual lateral strain indicate crack initiation and crack damage while the axial strain changes very little.

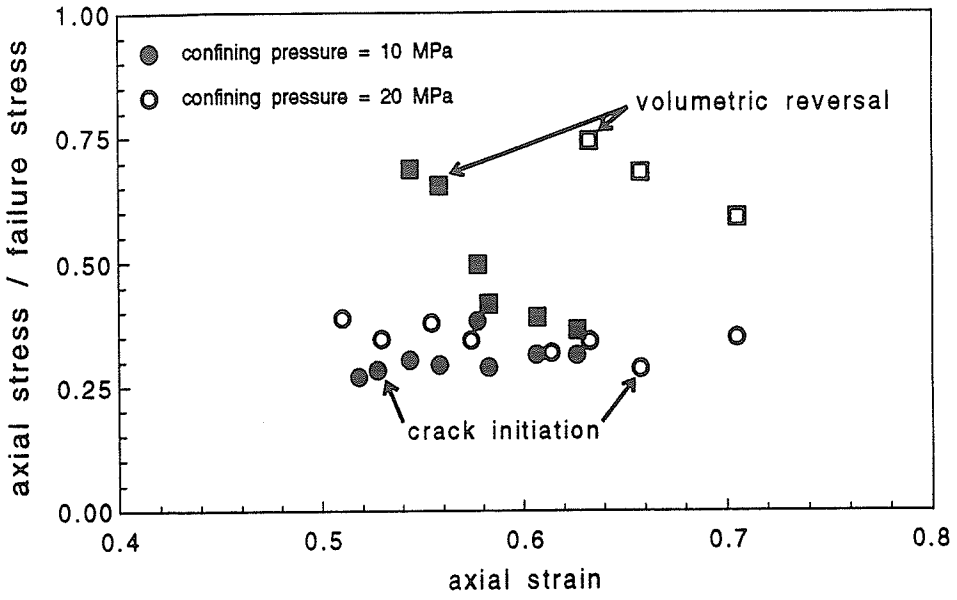

Figure 2.7 Crack-initiation stress is relatively constant for successive loading—unloading cycles (increasing axial strain at peak stress). However, the volumetric reversal stress decreases and approaches the crack-initiation stress.

Table 2.1a) Uniaxial Cycled Compression Results for LDB Granite (after Lajtai, 1982).

Dev. Axial Load (MPa)	Residual Axial Strain	Residual Lateral Strain
25	-10	2
50	-5	3
75	-6	3
100	-10	5
125	-10	9
150	-7	15
175	-5	136

Table 2.1b) Triaxial Cycled Compression (10-MPa confining pressure) Results for LDB Granite (28.5-mm-diameter core).

Dev. Axial Load (MPa)	elastic modulus (GPa)	Poisson's Ratio	Residual Axial Strain	Residual Lateral Strain
20	56	0.16	-19	-7
50	63	0.18	-24	-6
100	65	0.21	-14	-5
120	66	0.22	-7	0
150	66	0.22	-15	2
180	68	0.26	8	2
200	67	0.29	12	9
250	66	0.35	-12	31
280	64	0.49	-3	131
300	62	0.5	------	------

An indirect method of obtaining the tensile strength of rock is the Brazilian tension test (Hondros, 1959). A compressive load is applied diametrally, along a line contact, to a circular disk of rock (Figure 2.8). A tensile crack forms parallel to the applied load and the tensile strength can then be evaluated from the disk dimensions and the compressive load. A number of Brazilian tension tests were previously completed (Nowakowski, 1984; Bumsted, 1986) giving a measurement for the tensile strength of 14 MPa. Several samples were strain gauged (Bumsted, 1986) and the stress—strain curves can be used to measure crack initiation in tension (Figure 2.9). The points of crack initiation and crack damage occur at approximately 56% and 92% of the peak tensile

strength respectively (Table 2.2). The Brazilian tests have also been used to examine the size effect for granite (Nowakowski, 1984) which will be discussed in a later section.

Fracture toughness is another important parameter and can be measured using the double torsion test (Atkinson and Meredith, 1987). A thin plate of rock with a notch is subjected to a torsion (Figure 2.10) and the fracture toughness is evaluated from the plate dimensions and the applied torsion. Double torsion tests conducted on LDB granite (Svab and Lajtai, 1981) revealed an average fracture toughness of 2.5 MPa$\sqrt{m}$.

Table 2.1c) Triaxial Cycled Compression (20-MPa confining pressure) Results for LDB Granite (28.5-mm-diameter core).

Dev. Axial Load (MPa)	elastic modulus (GPa)	Poisson's Ratio	Residual Axial Strain	Residual Lateral Strain
20	65	0.20	-15	-3
100	75	0.20	-10	1
150	75	0.21	-3	-1
180	76	0.21	-2	1
190	76	0.21	-1	6
200	75	0.22	-5	10
250	75	0.23	-5	16
290	74	0.25	-9	27
310	82	0.29	1	34
330	80	0.31	-15	54
370	70	0.34	-10	121
445	66	0.4	-------	------

Table 2.2) LDB Granite Strength and Fracture Parameters.

Confining Pressure (MPa)	Crack Initiation (MPa)	Crack Damage (MPa)	Peak Strength (MPa)
0	110	185	226
10	175	250	360
12	130	200	372
16	170	240	440
18	180	310	420
20	145	255	470
30	245	380	560
32	260	415	575
38	290	410	620
Tension Test	-7.8	-12.7	-13.8

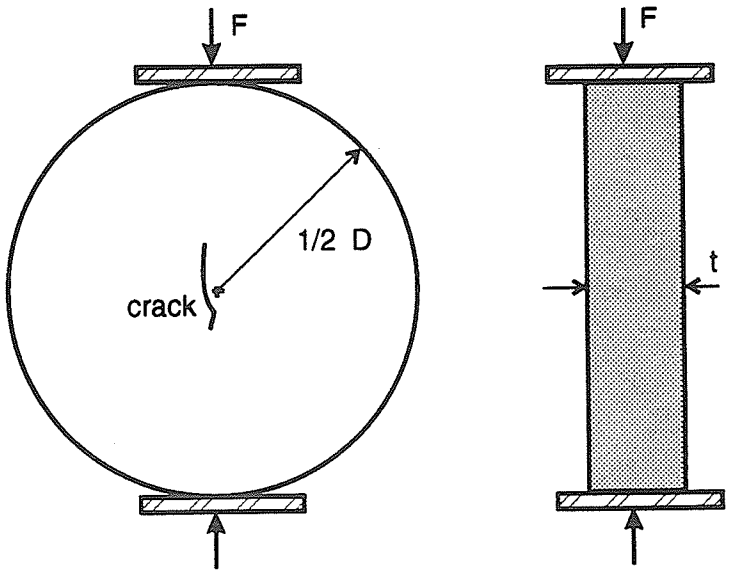

Figure 2.8 Brazilian-disk, indirect, tension test set-up (after Jaeger and Cook, 1979).

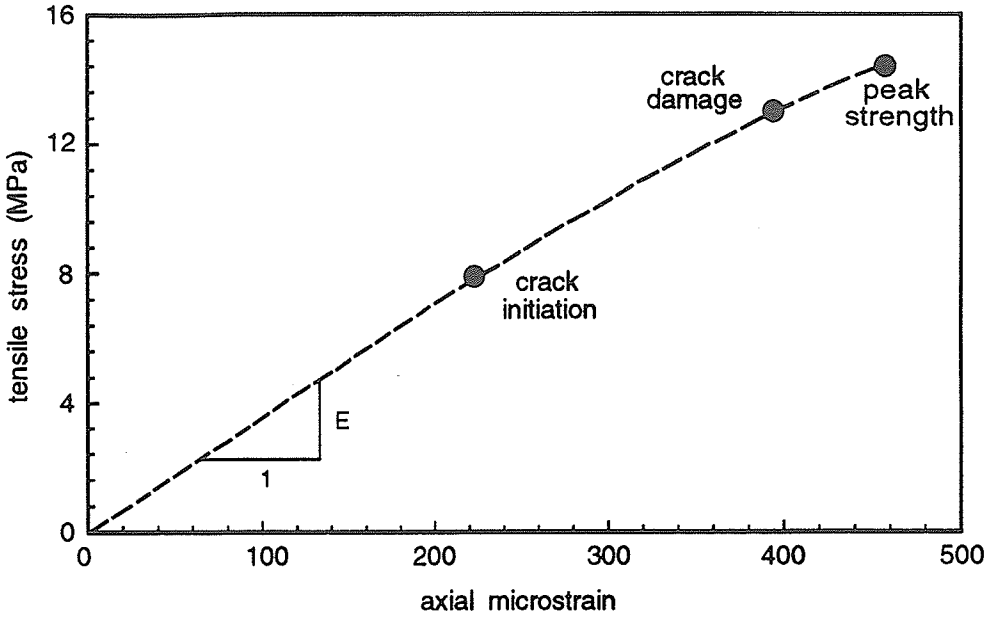

Figure 2.9 Tensile strain measured from a Brazilian test on LDB granite showing crack initiation, crack damage and peak strength (after Bumsted, 1986).

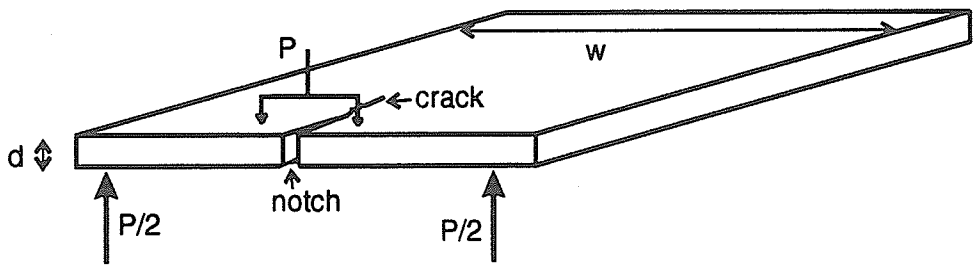

Figure 2.10 Double-torsion test set-up (after Atkinson and Meredith, 1987).

2.2 Tyndall Limestone

The limestone was obtained from a local quarry near Garson, Manitoba (Figure 2.2) which operates in the Ordovician Red River Formation. It is partly dolomitized and contains numerous fossils giving it a mottled brownish-grey appearance. For this reason it is commonly used as a decorative building stone and can be seen on the exterior of many buildings in Winnipeg, Manitoba, as well as on the inside of the federal parliament buildings of Canada.

Tyndall limestone is not as strong nor as brittle as granite but still behaves in a primarily elastic manner. There is usually a small amount of non-linearity close to the peak strength. The physical properties are highly variable throughout the quarry, although they are fairly consistent for a small area. A number of tests were conducted on one set of specimens (set 1) and the average uniaxial compressive strength was about 52 MPa while the tensile strength was close to 4 MPa (Carter *et al.*, 1991*a*). The elastic modulus in compression was about 40 GPa and Poisson's ratio was 0.33. The specimens used in this modeling exercise (set 2) had strength values which were a lot lower than the above averages, as indicated by the tension and compression tests (Table 2.3).

Five direct uniaxial tension tests, were performed, using 40-mm-diameter specimens from set #2. The specimens were glued to steel loading platens with flexible cables attached and two axial strain gauges were used to obtain Young's modulus in tension, which was calculated from the straight-line portion of the stress—strain curve at about 50% of strength (Figure 2.11). The average values for peak tensile strength, elastic modulus and Poisson's ratio are listed in Table 2.3. The average values of crack

initiation and crack damage in direct tension occurred at 60% and 87% of the peak tensile strength respectively (Table 2.4).

Table 2.3) Tension and Compression Test Results for Tyndallstone Set #2.

TEST	Strength (MPa) Mean	St.Dev.	elastic modulus (GPa)	Poisson's Ratio
Direct Tension	0.8	0.2	4.2	-----
Brazilian Tension	2.5	0.6	------	-----
4-Point Bending	9.0	2.9	------	-----
Uniaxial Compression	41.0	3.6	21.4	0.31

Table 2.4) Tyndallstone Strength and Fracture Parameters.

Confining Pressure (MPa)	Crack Initiation (MPa)	Crack Damage (MPa)	Peak Strength (MPa) Cycled	Regular
0	30	55	65	76
5	40	65	81	92
10	60	90	100	105
15	75	95	119	118
20	80	100	131	138
25	----	-----	-----	149
30	----	-----	-----	165
35	----	-----	-----	177
40	----	-----	-----	190
Tension Test[1]	-0.52	-0.78	-----	-0.9

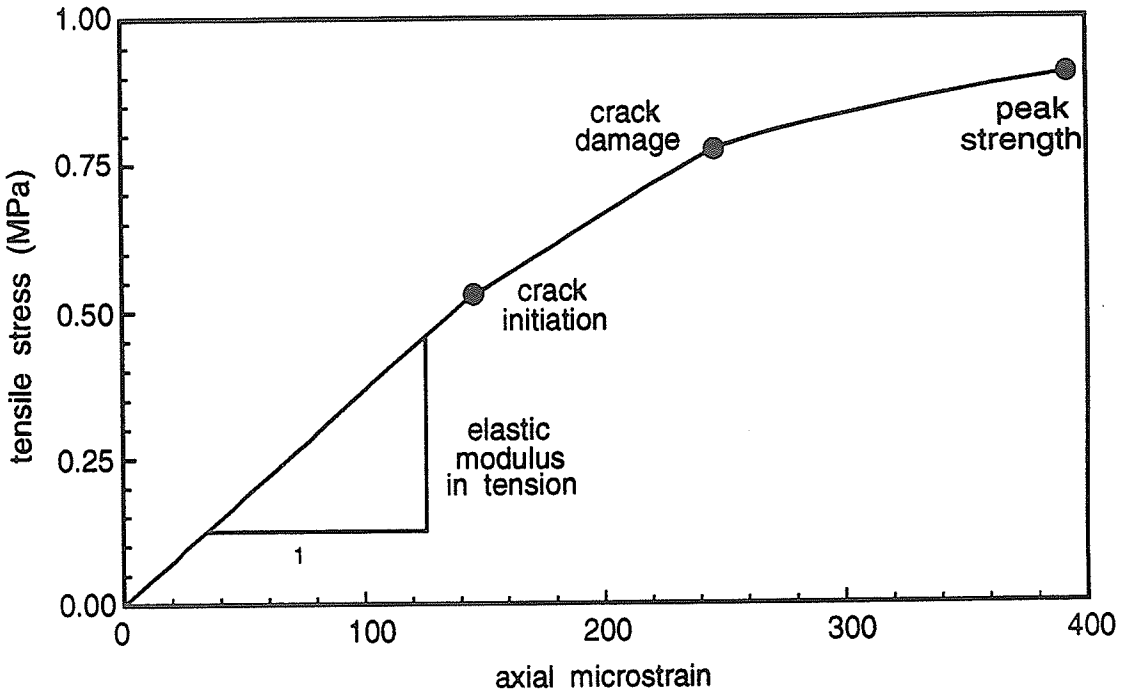

Figure 2.11 Tensile strain from a direct tension test on Tyndallstone (set #2) showing crack initiation, crack damage, peak strength and elastic modulus in tension.

Four-point-bending and Brazilian tests were also performed. Six specimens (300 mm long, 38 mm wide and 25 mm thick) from set #2 were tested in four-point bending (Figure 2.12). The bottom rollers were 254 mm apart and the top rollers 127 mm apart, corresponding to the ASTM standard requirements for four-point-bending tests on rock (ASTM C880-78). The load causing rupture of the beams in four-point bending was recorded and converted to rupture or flexure strength (Table 2.3) through:

$$\sigma_{tf} = \frac{2FL}{t^2 w} \tag{1}$$

F is the applied force, L is the distance between the bottom rollers, t is the thickness of the beam, and w is the width of the beam. σ_{tf} is the rupture strength.

Five Brazilian tests were done, using specimens which were 54 mm in diameter and 15 mm thick. The load causing failure of the Brazilian test specimens was recorded and then converted to the Brazilian tensile strength (Table 2.3) using:

$$\sigma_{tb} = \frac{2F}{\pi D t} \tag{2}$$

where D is the diameter and σ_{tb} is the Brazilian tensile strength.

Following the various tension tests, four uniaxial compression tests were performed on 40-mm-diameter specimens from set #2. Three of the specimens were instrumented with two lateral and two axial strain gauges. The elastic modulus and Poisson's ratio are evaluated from the straight-line portion of the axial and lateral stress—strain curves (Figure 2.13).

The uniaxial compressive strength of 41 MPa (Table 2.3) is over 50 times the uniaxial (direct) tensile strength of 0.8 MPa. The elastic modulus in compression (21.4 GPa) is 5 times greater than the elastic modulus in tension (4.2 GPa). The Poisson's ratio was not measured in tension; thus the value measured in the compression tests (0.31) will be used for all stress states.

Five cycled compression tests were performed using 54-mm-diameter specimens from the first set of Tyndall limestone. The strength curve for set #1 has already been established (Carter *et al.*, 1991*a*) as a number of uniaxial (Kaskiw, 1984) and triaxial (Klause, 1988) compression tests were done previously. These tests had not been instrumented; thus no data existed for the pressure dependency of crack initiation and volumetric reversal for Tyndallstone. Cycled tests were therefore performed, providing the trends for crack initiation and crack damage stress versus confining pressure. One cycled test was done under uniaxial compression while the other tests had confining pressures ranging from 5 to 20 MPa. The specimens were loaded to successively greater magnitudes for each cycle until failure occurred. By examining the permanent strain after each loading—unloading cycle, the crack-initiation stress and crack-damage stress were measured (Figure 2.14). Crack initiation occurs at 55% and crack damage at 80% of the strength (Lajtai *et al.*, 1991*a*). The changing value of Poisson's ratio can also be used to indicate crack initiation and crack damage (Table 2.5). The elastic modulus, on the other hand, is quite variable. It appears to remain relatively constant in some tests (Table 2.5 a and c) but decreases dramatically in others (Table 2.5 b, d and e). The change in axial strain could indicate yielding or possibly crushing and/or shearing.

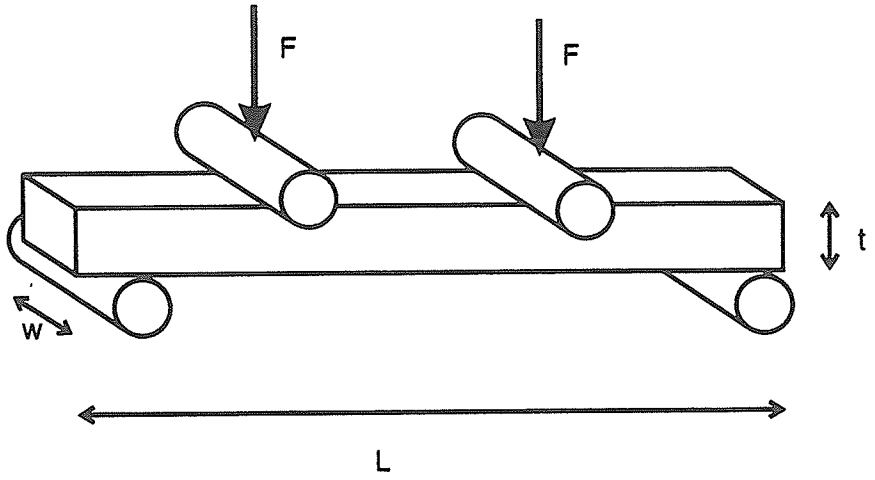

Figure 2.12 Four-point-bending test set-up.

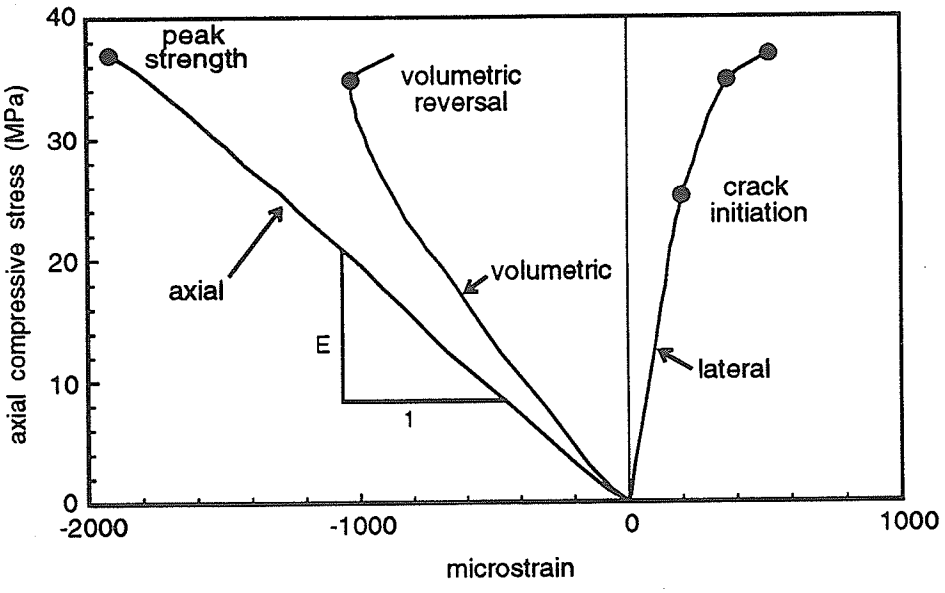

Figure 2.13 Axial, lateral and volumetric stress—strain curves for uniaxial compression of Tyndallstone (set #2) showing crack initiation, crack damage, peak strength and elastic modulus in compression.

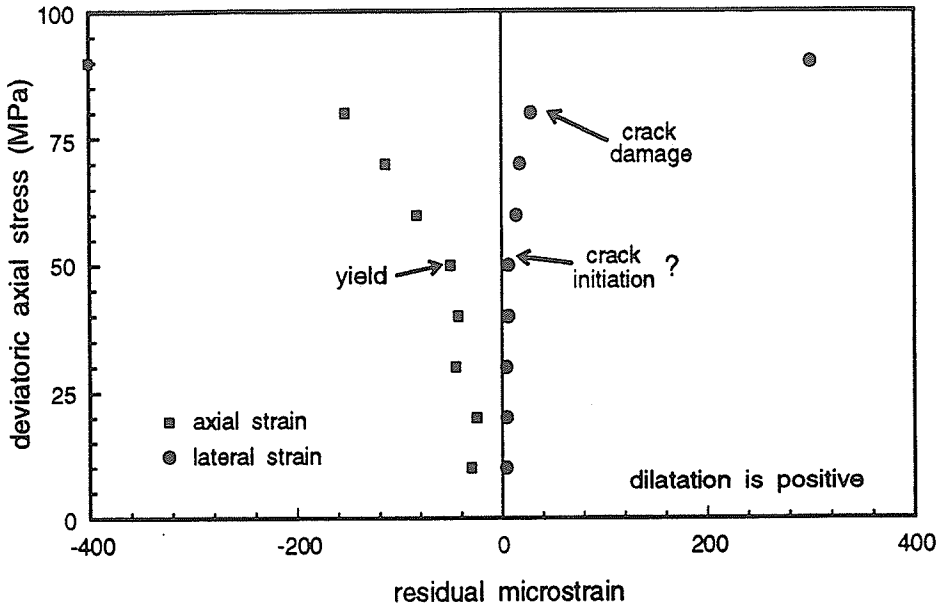

Figure 2.14 Residual axial and lateral strain for successive loading—unloading cycles for triaxial compression of Tyndallstone (5-MPa confining pressure). Both axial and lateral strains indicate changes with increasing cycles. The lateral may show crack initiation and damage but the axial must indicate yielding or crushing.

Table 2.5a) Uniaxial Cycled Compression Test Results for Tyndallstone (54-mm-diameter core).

Dev. Axial Load (MPa)	elastic modulus (GPa)	Poisson's Ratio	Residual Axial Strain	Residual Lateral Strain
30	44	0.26	-5	1
35	41	0.24	-9	2
40	41	0.24	-13	3
45	42	0.25	-17	5
50	42	0.25	-22	7
55	43	0.27	-29	10
60	43	0.27	-41	17
65	42	0.29	------	-----

Table 2.5b) Triaxial Cycled Compression (5-MPa confining pressure) Test Results for Tyndallstone (54-mm-diameter core).

Dev. Axial Load (MPa)	elastic modulus (GPa)	Poisson's Ratio	Residual Axial Strain	Residual Lateral Strain
10	56	0.23	-14	-1
15	56	0.24	-5	1
20	50	0.25	-3	-2
30	49	0.26	-18	2
40	45	0.27	-27	3
50	44	0.28	-23	4
55	43	0.28	-20	4
60	41	0.29	-40	10
65	40	0.32	-38	14
70	38	0.32	-77	50
75	36	0.32	------	-----

Table 2.5c) Triaxial Cycled Compression (10-MPa confining pressure) Test Results for Tyndallstone (54-mm-diameter core).

Dev. Axial Load (MPa)	elastic modulus (GPa)	Poisson's Ratio	Residual Axial Strain	Residual Lateral Strain
10	33	----	-30	4
20	38	0.20	-25	5
30	35	0.21	-45	5
40	37	0.22	-43	6
50	37	0.22	-50	6
60	35	0.22	-80	14
70	33	0.22	-113	18
80	30	0.24	-150	29
90	34	0.23	------	-----

Table 2.5d) Triaxial Cycled Compression (15-MPa confining pressure) Test Results for Tyndallstone (54-mm-diameter core).

Dev. Axial Load (MPa)	elastic modulus (GPa)	Poisson's Ratio	Residual Axial Strain	Residual Lateral Strain
10	86	0.22	-2	7
20	72	0.26	-23	6
30	60	0.26	-32	9
50	55	0.27	-35	10
60	52	0.27	-40	12
70	48	0.28	-59	21
80	45	0.31	-118	44
90	40	0.30	-236	103
100	36	0.33	-793	610
104	28	0.39	-------	------

Table 2.5e) Triaxial Cycled Compression (20-MPa confining pressure) Test Results for Tyndallstone (54-mm-diameter core).

Dev. Axial Load (MPa)	elastic modulus (GPa)	Poisson's Ratio	Residual Axial Strain	Residual Lateral Strain
10	120	0.24	2	8
20	85	0.23	-1	1
30	71	0.23	-35	7
40	63	0.24	-42	8
50	66	0.24	-13	3
60	52	0.24	-83	13
70	50	0.24	-90	21
80	48	0.24	-116	32
90	43	0.24	-248	58
100	39	0.26	-529	92
110	32	0.25	-------	-----

Dawson Bay limestone, which is one of the formations overlying the potash mines in Saskatchewan (Kroll, 1987), displays similar trends for crack initiation and crack damage. This limestone is finer-grained with a lower porosity than Tyndallstone and consequently it is stronger and more brittle. A number of compression and tension tests were done to determine the strength and elastic modulus (Abeda, 1989). Two of the samples were subjected to tension followed by compression, meaning the same sample was used to determine the elastic modulus in both tension and compression. The modulus and Poisson's ratio in tension (56.7 GPa and 0.28) are not significantly different from the corresponding values in compression (54 GPa and 0.25).

Crack initiation in both tension and compression can be measured from the stress—strain curves of the other Dawson Bay samples (Figures 2.15 and 2.16). Crack initiation in tension occurs at 80-85% of the tensile strength, which is 7 MPa (Abeda, 1989), while crack damage occurs at 95-100% of the strength. In uniaxial compression, crack initiation occurs much earlier, at about 45% of the strength, based on the uniaxial compressive strength of 110 MPa (Kroll, 1987). Crack damage is difficult to determine from the compression curve as the sample was not loaded to failure. The tendency for crack initiation to occur much earlier in compression than in tension (relative to the respective peak strengths) is similar to the behavior shown by the Tyndallstone and the Lac du Bonnet granite.

Double torsion tests were conducted on the first set of Tyndallstone samples (Kilgour, 1984) revealing an average fracture toughness of 1.0 MPa$\sqrt{m}$.

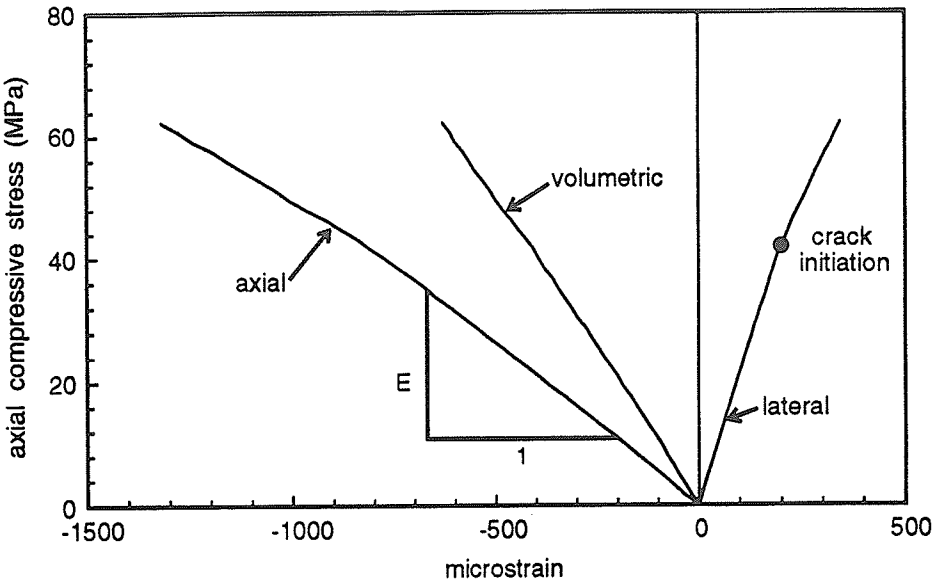

Figure 2.15 Stress—strain curves for Dawson Bay limestone under uniaxial compression showing crack initiation and elastic modulus in compression.

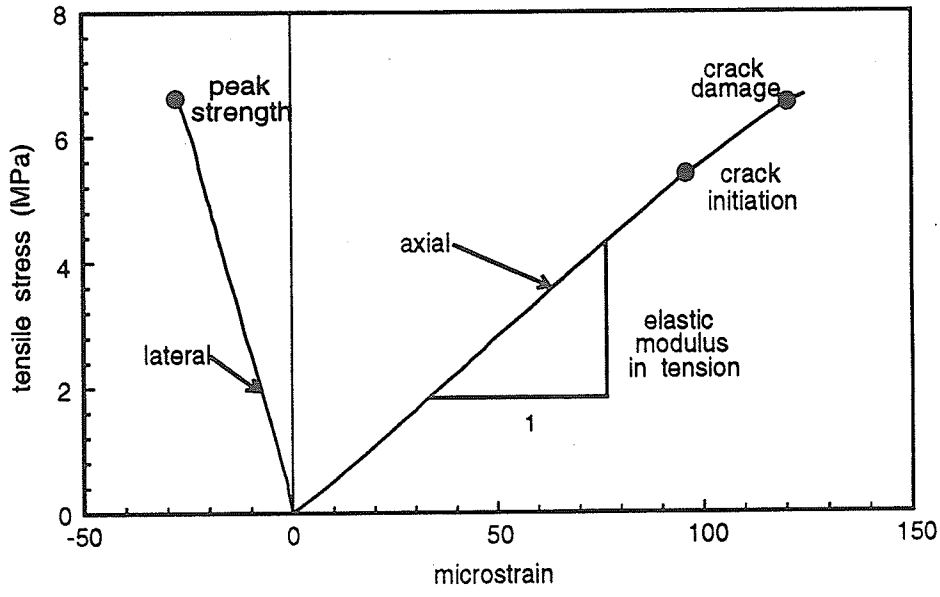

Figure 2.16 Stress—strain curves for specimen from Figure 2.12 in direct tension. The curves show crack initiation, crack damage, peak strength and elastic modulus in tension.

2.3 Saskatchewan Potash

The potash—salt rock is from the Saskatoon area of Saskatchewan (Figure 2.17a). Specifically, potash was obtained from the Lanigan and the Vanscoy mines where it is mined extensively for the potassium content which is used as fertilizer. The potash is part of the Patience Lake Member of the Middle Devonian Prairie Evaporite Formation (Figure 2.17b).

The potash is mostly coarse-grained with crystals ranging from 2 mm to 20 mm. It contains 40-45% of KCl (sylvite) with the remainder being predominantly NaCl (sodium chloride). Clays represent a very small portion (5%), usually in the form of seams and coatings (Duncan,1990).

Potash is a weak ductile rock. It is the least brittle of the three rocks and it behaves in a very non-linear manner (Figure 2.18). The strength and deformation modulus depend on the loading rate (Lajtai *et al.*, 1991*b*) but, for most standard laboratory tests, the uniaxial compressive strength is about 24 MPa, with an average elastic modulus of 17 GPa and Poisson's ratio of 0.3. The average tensile strength is between 1 and 2 MPa.

Before the laboratory tests which have been performed on potash are described, the material behavior needs to be briefly described. Potash contains two independent crystal-slip systems (Groves and Kelly, 1963). For homogeneous plastic deformation, five slip systems are required (von Mises, 1928). Thus, potash often suffers both plastic and brittle strain (Horseman and Passaris, 1981) and the stress—strain curves for a salt rock are different from those obtained for true plastic materials or for true brittle

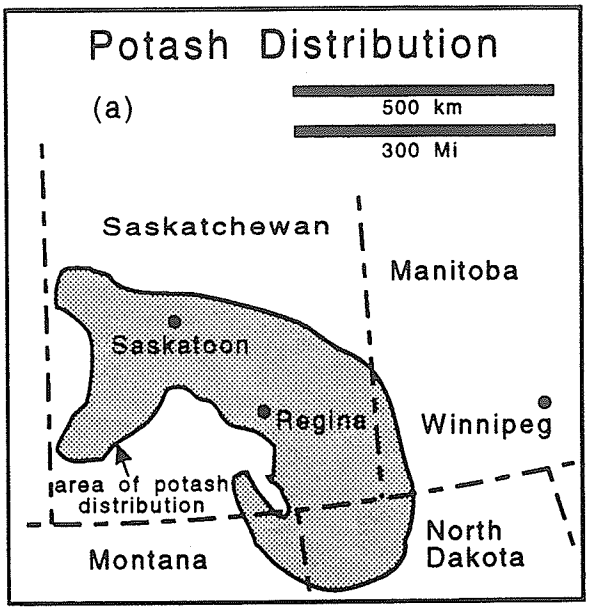

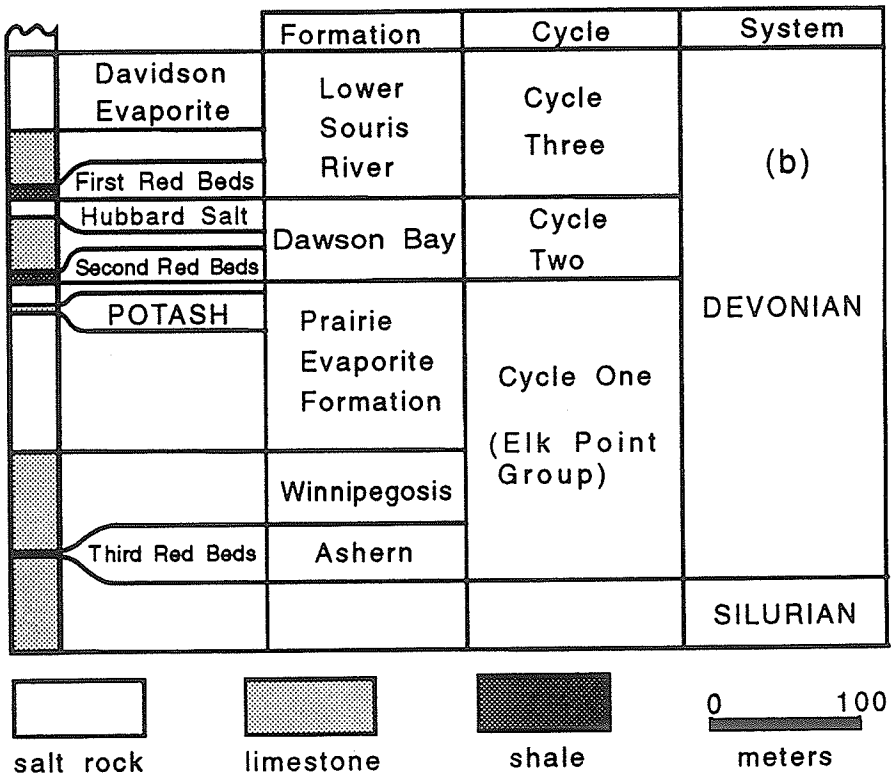

Figure 2.17 (a) Areal distribution of Saskatchewan potash. Vanscoy and Lanigan mines are located near Saskatoon while Rocanville is near the Manitoba border (after Fuzesy, 1982). (b) Stratigraphic sequence for the Saskatoon area indicating the location of the potash within the Prairie Evaporite Formation (after Lane, 1959).

materials. The curves show the influence of contributions from both the plastic and the brittle strain-producing mechanisms (Figure 2.18). A typical set of stress—strain curves displays both a crack initiation and a yield point. The first is marked by the deflection of the lateral strain curve and the second by the deflection of both the axial and the lateral strain curves. In potash, plastic deformation often starts at a lower stress than does cracking. The yield point, marking the onset of plastic deformation, is then clearly marked on both the axial and the lateral curves. Crack initiation is often poorly defined on the stress—lateral strain curve due to the non-linearity caused by yielding. Crack initiation may be more apparent on the volumetric strain curve where the entry of the brittle mechanism is often marked by an inflection point between the yield stress and the point of volumetric reversal. The point of volumetric strain reversal marks a condition where the cracks are so numerous that the specimen as a whole begins to dilate.

A number of instrumented triaxial compression tests were conducted (Duncan, 1990) providing a strength versus confining pressure relationship (Carter *et al.*, 1991*a*). The stresses at yielding and crack damage have been measured from the stress—strain curves (Table 2.6). Crack initiation is difficult to measure due to the yielding. In compression, crack initiation occurs between 20 and 60%, yielding occurs at about 37%, and crack damage occurs at about 65% of the peak strength (Lajtai *et al.*, 1991*a*).

A cyclic uniaxial compression test was conducted on Lanigan potash (Lajtai and Duncan, 1988) and the permanent or residual strain was plotted against the deviatoric axial stress (Figure 2.19). Picking the point of crack initiation is just as difficult as for

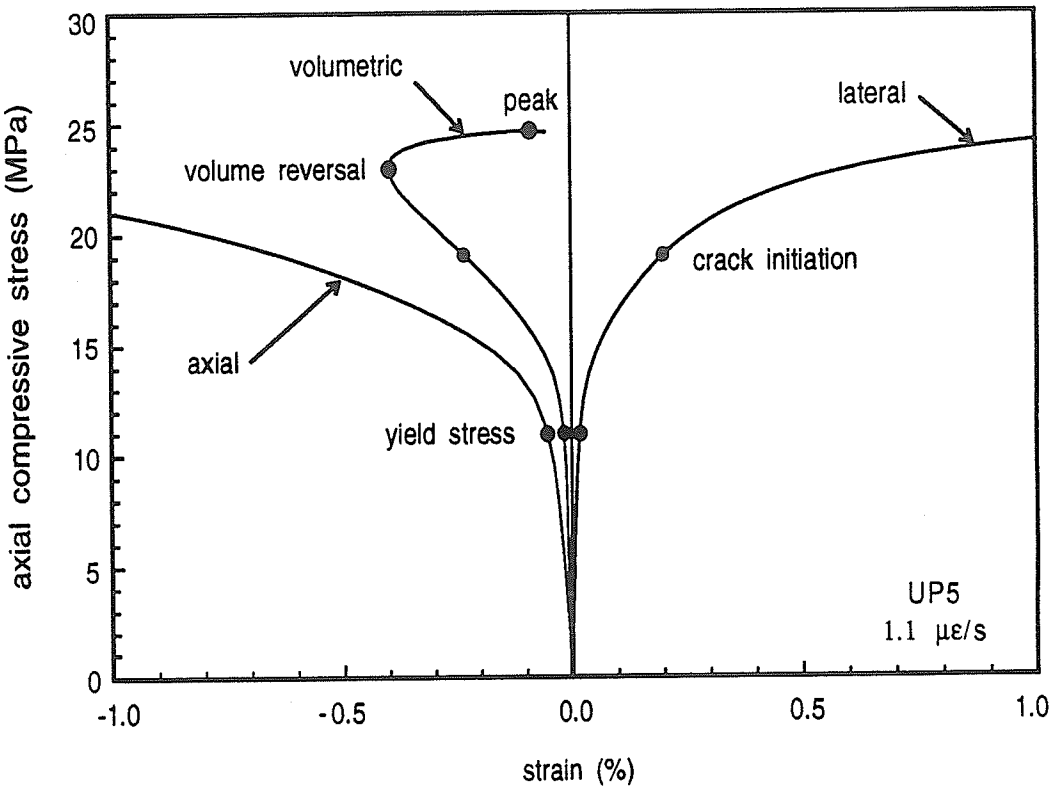

Figure 2.18 Uniaxial compression stress—strain curves for Lanigan potash showing yielding, crack initiation, volumetric reversal and peak strength (after Duncan and Lajtai, 1991). The first deflection in these curves is caused by the onset of plastic deformation rather than brittle crack initiation.

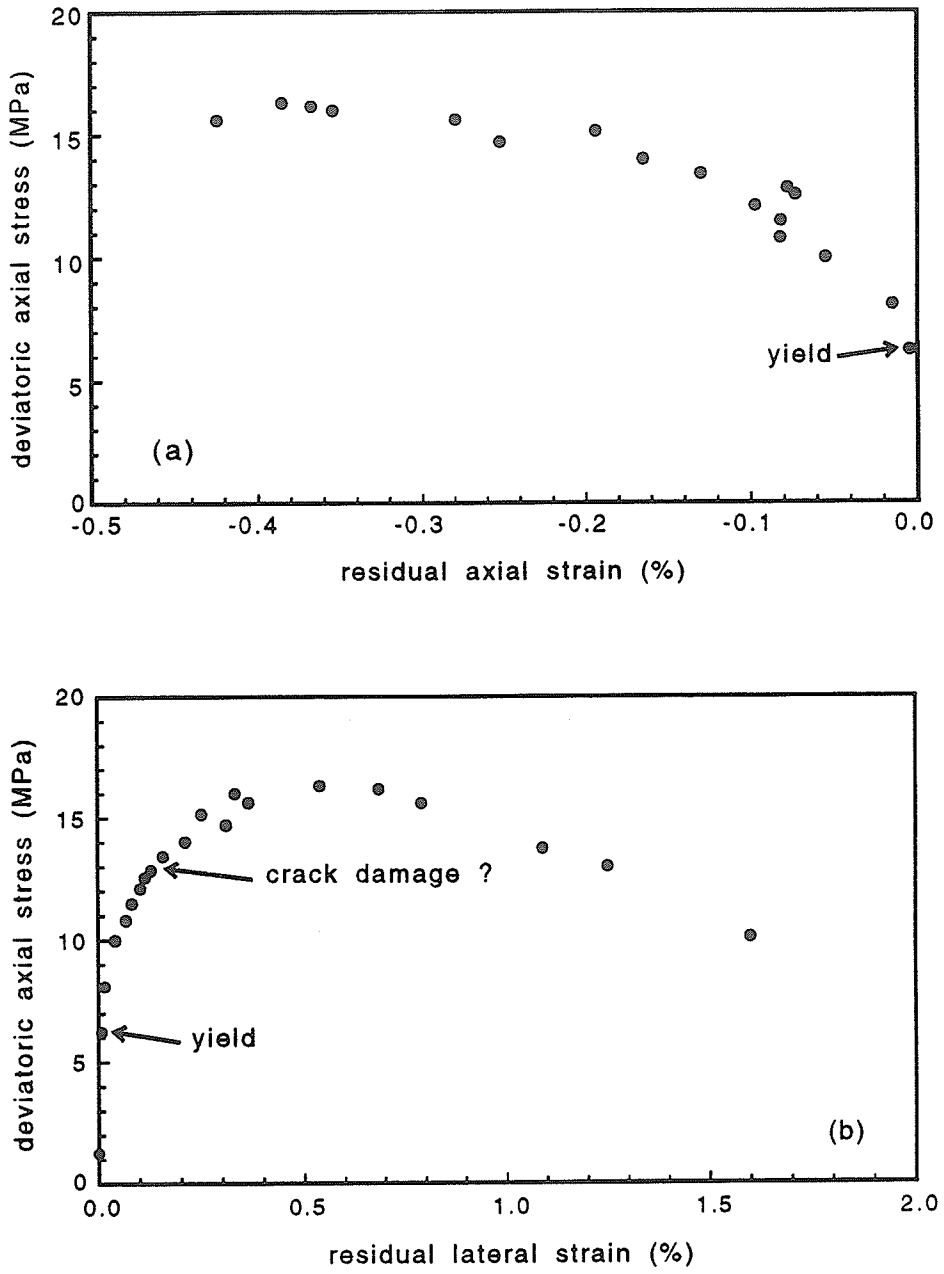

Figure 2.19 Residual (a) axial and (b) lateral strain from a cycled uniaxial compression test on Lanigan potash. Both strains indicate yielding; crack initiation and crack damage are more difficult to measure.

the regular triaxial compression tests. A yield stress is indicated by both the axial and lateral strains. The crack damage stress is also difficult to pick from these figures.

Two direct tension tests were conducted by the author using specimens of Vanscoy potash that were 40 mm in diameter and 95 mm in height, at a loading rate of about 0.01 MPa/s. Only the peak tensile strength was recorded. The first sample had a tensile strength of 1.84 MPa and the second sample had a tensile strength of 1.64 MPa. An average value of 1.7 MPa was obtained by Stimpson and Chen (1991), who performed several direct tension tests on Vanscoy potash. Potash in direct tension shows almost no crack initiation or damage prior to reaching peak strength (Carter *et al.*, 1992). Figure 2.20 suggests that there may be a small amount of cracking between 95 and 100% of peak strength. This is quite different from the behavior of the two more-brittle rocks where crack initiation and damage (non-linearity of the stress—strain curve) are both quite apparent.

Double torsion tests conducted on potash (Yamada, 1983) revealed an average fracture toughness of 0.34 MPa$\sqrt{m}$.

Table 2.6) Saskatchewan potash strength and fracture parameters.

Confining Pressure (MPa)	Yielding (MPa)	Crack Damage (MPa)	Peak Strength (MPa)
0	6.8	12.7	24.5
0.5	10	18	28
1	11	13	32
2	12	22	34
3	13	18	38
4	14	22	39.5
5	15	23	45
6	16	33	42.5
7	17	26	42
8	17	29	46
9	18	31	43
10	20	32	47
Tension Test[1]	-1.74	-----	-1.78

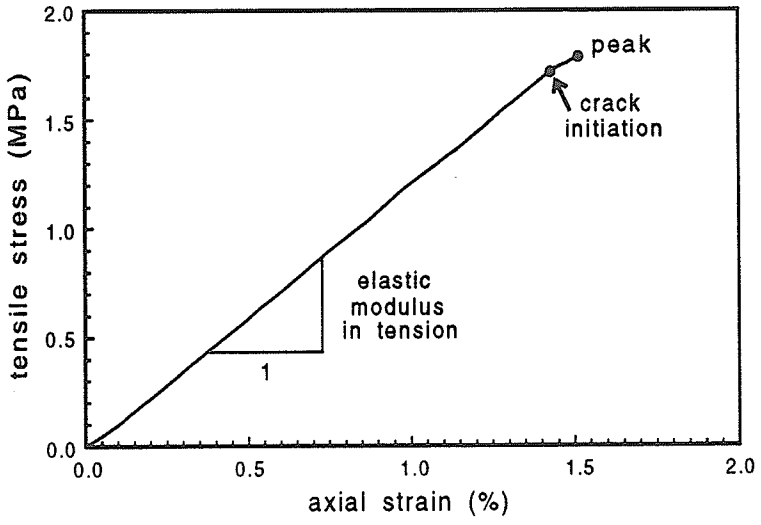

Figure 2.20 Direct tension stress—strain curve for Vanscoy potash showing crack initiation, peak strength and elastic modulus in tension (after Carter *et al.*, 1992).

A number of creep tests were conducted over the last several years (Duncan, 1990; Lajtai and Duncan, 1988) to examine the time-dependent properties of potash. The most significant concept in terms of the time-dependent fracture modeling of this study is that at loads below 8 to 10 MPa, the specimen undergoes very little cracking but at higher loads, it eventually fails due to brittle cracking (Duncan, 1990).

Both the plastic and the brittle strains depend on the stress level, the elapsed time and the loading rate (Duncan, 1990) as evidenced by multi-stage creep tests (Figure 2.21) and uniaxial compression tests at various rates (Figure 2.22). High loading rates are dominated by brittle creep whereas low loading rates show more plastic strain. For low loading rates, the change from essentially plastic to essentially brittle creep usually occurs at a stress level of about 13 MPa (Duncan and Lajtai, 1991). For creep tests below 13 MPa, much of the creep strain is plastic strain. In creep tests above 13 MPa, the early deformation is dominated by plastic straining, producing compressive volumetric strain. The brittle mechanism however gradually becomes more effective and the volumetric strain reverses direction from contraction to dilatation (Figure 2.23).

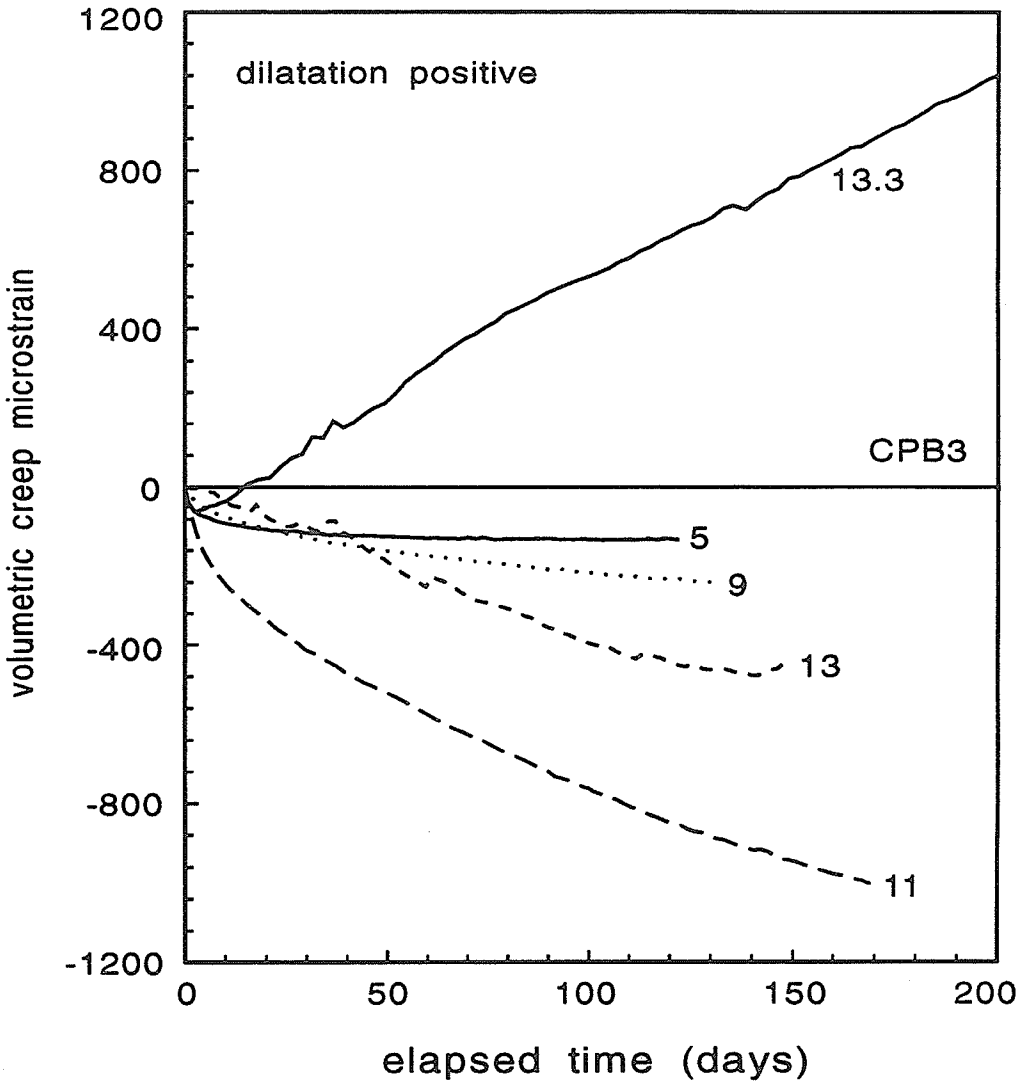

Figure 2.21 Multi-stage creep tests show how the volumetric strain changes from increasing compressive strain as the stress level increases until about 13 MPa. At stress levels above 13 MPa, the strain changes from contraction to dilatation (after Duncan and Lajtai, 1991).

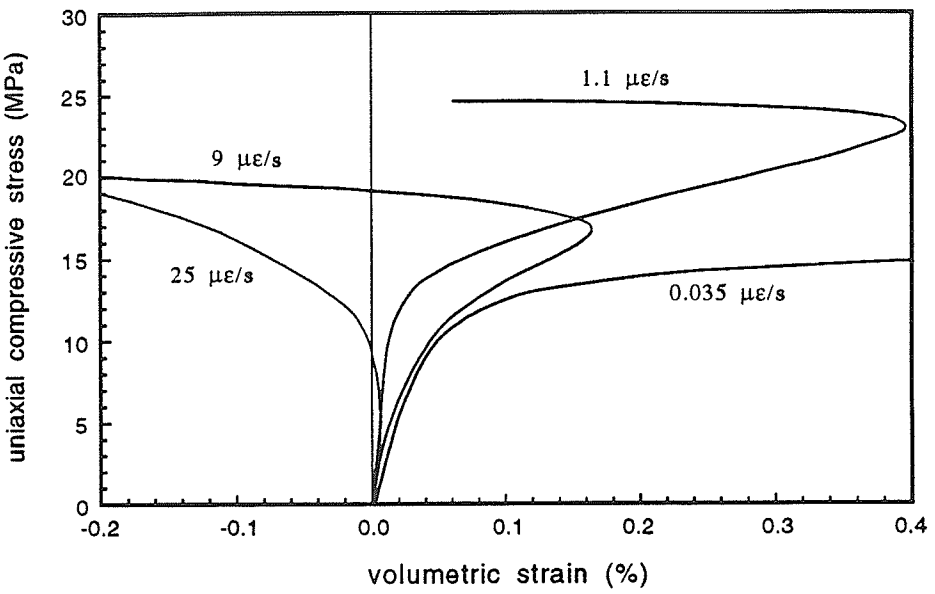

Figure 2.22 Effect of strain rate on the volumetric strain for uniaxial compression. The volumetric reversal point shifts with strain rate (after Duncan and Lajtai, 1991).

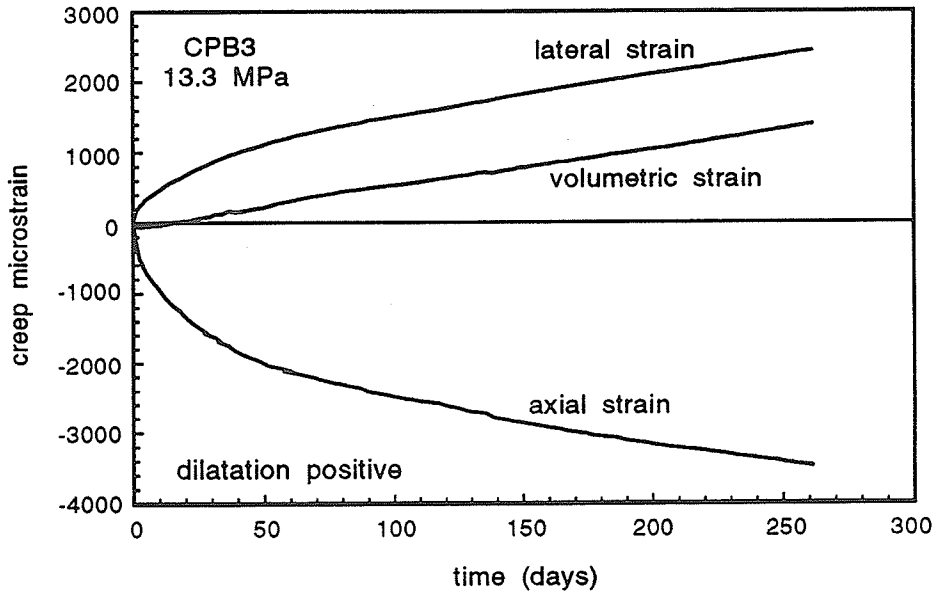

Figure 2.23 Axial, lateral and volumetric creep-strain at 13.3 MPa for Lanigan potash (after Duncan and Lajtai, 1991).

3 BRITTLE FRACTURE AND FAILURE OF ROCK

3.0 Introduction

The purpose of this chapter is to describe the basic nature of fracture and failure of rock in both tensile and compressive stress fields. Several theories currently exist for modeling rock fracture and failure, including fracture mechanics and empirical strength criteria. Both fracture mechanics and empirical criteria have also been incorporated into statistical fracture theories. The results from the tension and compression tests on the three rocks described in Chapter 2 will be used to validate these theories. As well, the topics of specimen size and stress-gradient effects will be discussed with reference to rock fracture and failure.

The difference in meaning of the terms "rock fracture" and "rock failure" can be very confusing, as many researchers often use them synonymously. The term fracture can be defined as the processes which involve: "*the separation of a material into two or more parts, at least a momentary loss of cohesion, and the release of stored elastic strain energy*" (Griggs and Handin, 1960). Failure, on the other hand, implies structural collapse and the inability of the material to sustain significant loads.

The confusion between the two terms arose from experimental testing. Most tension tests were conducted in load-controlled testing machines and, when the rock fractured, it also failed due to unstable crack propagation. However, it was shown in the previous chapter that microfractures may form prior to the achieving of peak strength in both tension and compression tests. Furthermore, many of the earlier researchers did not

realize that cracks also formed prior to failure in compression. It was thought that the rock simply failed once a shear fracture formed through the specimen (Adams, 1910). Only in the last 20-30 years has it been recognized that fracture does not always correspond to failure.

Fractures in rock occur at several scales, submicroscopic, microscopic, macroscopic and megascopic. Submicroscopic fracture involves rupture of cohesive forces between atoms. Microscopic fracture refers to cracking at the level of the constituent grains and grain boundaries, and is influenced by rock type (composition), texture, fabric, and stress inhomogeneities produced by pores, pre-existing cracks, grain contacts and residual stress. Macroscopic fracture involves fracture which is visible to the unaided eye in test specimens, hand samples, and laboratory models. Megascopic fracture includes faults, joints, sheets, large rock bursts, etc, which occur in large rock masses and which can be seen in outcrops or underground excavations.

Although all scales of fracturing have been experienced, comprehensive theories which explain, and more importantly, predict fracture of rock in both tensile and compressive stress states have only recently begun to appear in the rock mechanics literature. Fracture of materials is a common engineering problem and research in this area is carried on in several fields of engineering science. Rock mechanics, in particular, has borrowed extensively from continuum mechanics, material science, structural geology and, more recently, from fracture mechanics. Traditionally, the approach to fracture in rock mechanics has been through stress-based strength theories. Fracture mechanics, which can model both fracture propagation and failure, has become the favored method.

3.1 Fracture and Failure of Rock in Tension

Fracture in tension involves the separation of the rock, generally along a single plane, involving and activating one or a few pre-existing microcracks or flaws present in the rock. Failure implies the complete separation of the rock along this plane through displacement perpendicular to the plane. This means that failure can occur only after the crack(s) has propagated completely through the specimen.

In many tension tests, fracture initiation seems to coincide with failure as the fracture propagates through the rock almost instantaneously. Microcracks do form slightly before peak strength is reached however (Evans and Marathe, 1968; Schmidt and Lutz, 1979). Closer examination of the stress-strain curves from tension tests on Tyndallstone and LDB granite also shows that there was both crack initiation and crack damage prior to the reaching of peak strength (Figures 2.9 and 2.11). In potash, on the other hand, there was only a slight indication of crack initiation (Figure 2.17). For all three rocks, failure coincided with peak strength. This is always the case for load-controlled tension tests where the load is simply increased until failure occurs. In displacement-controlled tests, a certain amount of post-peak strain-softening has been reported to occur prior to true, traction-free cracking and failure (Labuz *et al.*, 1985; Gopalaratnam and Shah, 1985). Thus, actual failure occurs on the post-peak side of the stress—strain curve.

Figure 2.11 showed the response for a load-controlled tension test on Tyndall limestone. There is an initial linearly elastic phase, followed by a brief non-linear phase just prior to the peak strength. The non-linear phase generally indicates microcracking

and "process-zone" development ahead of the *true* crack. The process zone, a region of microcracks ahead of the actual crack tip, has been observed and documented by a number of researchers (Wecharatana and Shah, 1983; Friedman *et al.*, 1972; Hoagland *et al.*, 1973; Du *et al.*, 1990; and Schmidt and Lutz, 1979).

A true crack must not allow any stress transfer across its surfaces. In many cases, microscopic cracks, and even some visible cracks, may still transfer stress due to irregular crack paths and interlocking particles (Hillerborg, 1983). Failure of the rock can occur only after the traction-free crack has propagated through the rock, causing complete separation of the specimen into two parts. Obviously then, the terms fracture and failure should not be used to describe the same phenomenon; consequently, different theories exist for modeling fracture and failure.

3.1.1 Maximum-Stress Theory—A Failure Criterion For Rock in Tension

The original failure criterion for tension is known as the maximum stress theory. It is based on load controlled tension test data and states that failure occurs when the tensile stress reaches the tensile strength. The tensile strength coincides with the peak stress reached during the test and can be obtained through several different tests including direct tension tests, Brazilian tests, and bending tests as discussed in Chapter 2.

The maximum-stress theory is applicable only to material which is truly brittle, elastic and homogeneous with no pre-existing microcracks (Ingraffea, 1987). Another fault with this theory is its inability to account for size or stress gradient effects except in a purely statistical manner (Weibull, 1939). Large samples contain a greater range of

flaw sizes, with a higher probability of larger flaws. Larger flaws produce a lower fracture toughness (Schmidt and Lutz, 1979) and the consequence of a low fracture toughness, at least statistically, is a lower strength as well (Carpinteri, 1989). Because fracture mechanics explicitly includes crack size in its formulation, it is now used more often for modeling fracture propagation as well as the subsequent failure of the structure.

3.1.2 Fracture Mechanics for Tension

A brief introduction to the theory of fracture mechanics is necessary before directing it toward rock mechanics. The general equations of linear elastic fracture mechanics and aspects of more recent work on non-linear fracture mechanics need to be discussed with reference to brittle fracture of rock.

Fracture mechanics generally traces its origins back to the work of Griffith (1924). The basic premise of Griffith's theory, that fractures start from flaws, is fundamental to all disciplines investigating brittle fracture. The original Griffith theory is stress-based; it uses the Inglis (1913) solution for the distribution of stress around the perimeter of an elliptical cylinder.

$$\sigma_t = \frac{(P_1 + P_2)\ \sinh 2\xi_0 + (P_1 - P_2)\ [\exp 2\xi_0 \cos 2(\beta - \eta) - \cos 2\beta]}{\cosh 2\xi_0 - \cos 2\eta} \qquad (3)$$

ξ and η are elliptical coordinates, β gives the orientation of the ellipse (Figure 3.1), P_1 and P_2 are the applied compressive stresses acting at β=90° and 0° respectively. ξ_0 specifies the aspect ratio of the ellipse and is related to the ratio ***b/a*** by

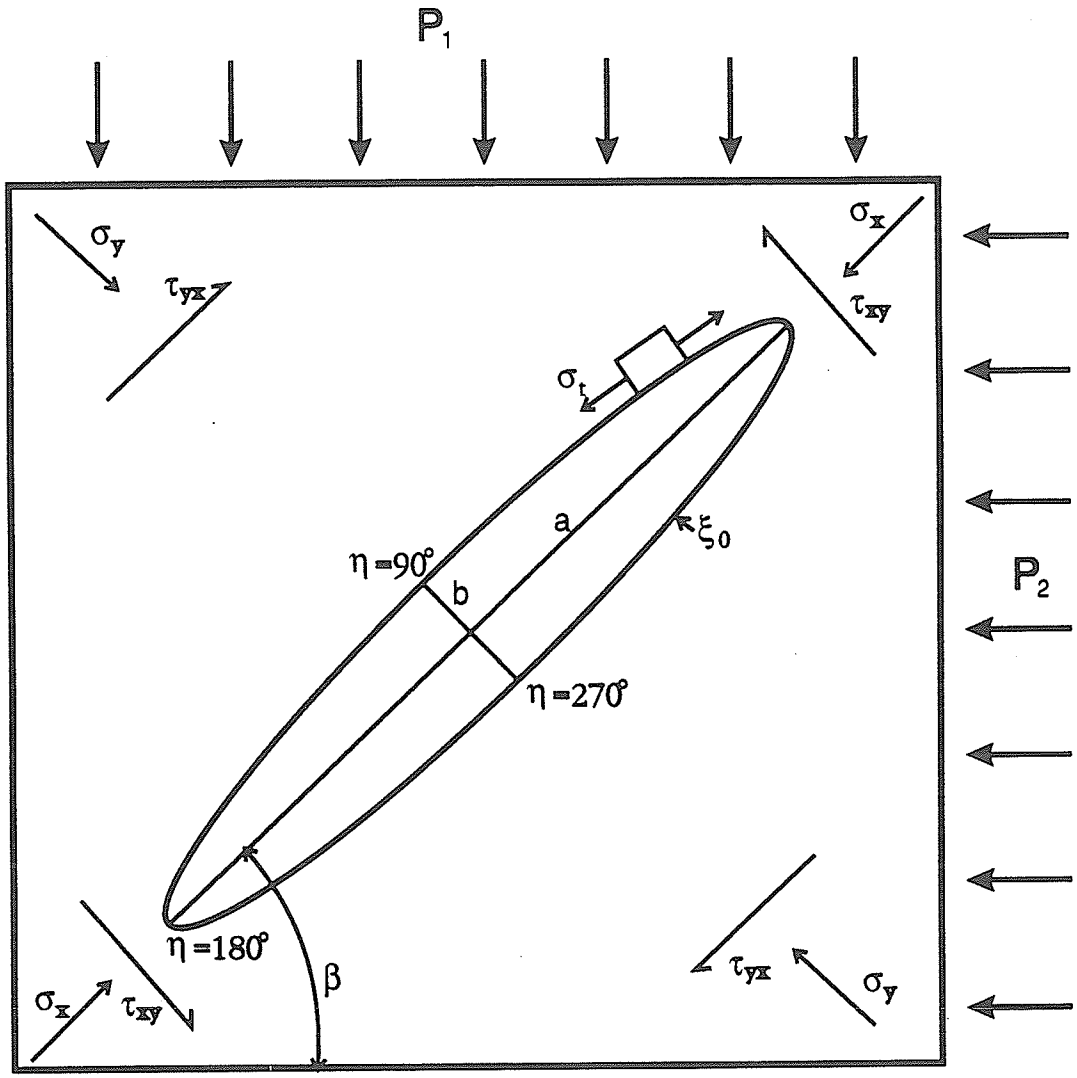

Figure 3.1 Inglis ellipse showing the relationship between far field stresses (P_1 and P_2), ellipse orientation (β) and shape (a & b or η & ξ) and the resulting circumferential stress on the cavity perimeter (after Lajtai, 1971). The cavity represents an elliptical cylinder.

$$\frac{b}{a} = \frac{\sinh \xi_0}{\cosh \xi_0} \tag{4}$$

Griffith's theory proposes that a fracture is initiated from a critical flaw when the tensile stress (σ_t) on the boundary of the flaw is greater than the tensile strength of the material. A critical flaw has an orientation such that the tensile stress concentration is maximum. Griffith (1924) simplified the original solution of Inglis (1913)

$$\sigma_t = \frac{2\,(\xi_0 \sigma_y - \eta\, \tau_{xy})}{\xi_0^2 + \eta^2} \tag{5}$$

As a result, the effect of the normal stress acting along the major axis is completely eliminated. This simplification is admissible for very flat cracks but is unacceptable for more equidimensional flaws. The model is also independent of flaw size. The discipline of fracture mechanics has evolved from Griffith's theory but now uses the *flat mathematical crack* rather than the Inglis ellipse.

The stress distribution around a flat crack subjected to external tensile stress perpendicular to the crack (Figure 3.2) is primarily derived from the work of Muskhelishvili in the early 1900's (see Muskhelishvili, 1963). Westergaard (1939) further developed this work to produce a single complex stress function which describes the stress field around the crack. Reviews are given by Paris and Sih (1965), Lawn and Wilshaw (1975) and recently by Pollard and Segall (1987). For a flat crack, subjected to a tensile load acting at infinity and perpendicular to the crack, the stresses are:

$$\sigma_{xx} = \sigma \sqrt{\frac{a}{2r}} \cos\frac{\theta}{2}\left[1 - \sin\frac{\theta}{2}\sin\frac{3\theta}{2}\right] \tag{6}$$

$$\sigma_{yy} = \sigma \sqrt{\frac{a}{2r}} \cos\frac{\theta}{2}\left[1 + \sin\frac{\theta}{2}\sin\frac{3\theta}{2}\right] \tag{7}$$

$$\tau_{xy} = \sigma \sqrt{\frac{a}{2r}} \sin\frac{\theta}{2}\cos\frac{\theta}{2}\cos\frac{3\theta}{2} \tag{8}$$

where σ, a, r and θ are shown in Figure 3.2.

A stress intensity formulation is often used to describe the stress field around the crack (Irwin, 1957; Broek, 1982). The opening mode, stress intensity factor, K_I includes the $\sigma \cdot \sqrt{a}$ term of equations 6 to 8 and is defined as

$$K_I = \sigma \sqrt{\pi a} \tag{9}$$

The opening mode (mode 1) corresponds to tension perpendicular to the crack such that the crack opens when the stress intensity factor reaches a critical value. Using K_I in equations 6 to 8, the stresses are:

$$\sigma_{xx} = \frac{K_I}{\sqrt{2\pi r}} \cos\frac{\theta}{2}\left[1 - \sin\frac{\theta}{2}\sin\frac{3\theta}{2}\right] \tag{10}$$

$$\sigma_{yy} = \frac{K_I}{\sqrt{2\pi r}} \cos\frac{\theta}{2}\left[1 + \sin\frac{\theta}{2}\sin\frac{3\theta}{2}\right] \tag{11}$$

$$\tau_{xy} = \frac{K_I}{\sqrt{2\pi r}} \sin\frac{\theta}{2}\cos\frac{\theta}{2}\cos\frac{3\theta}{2} \tag{12}$$

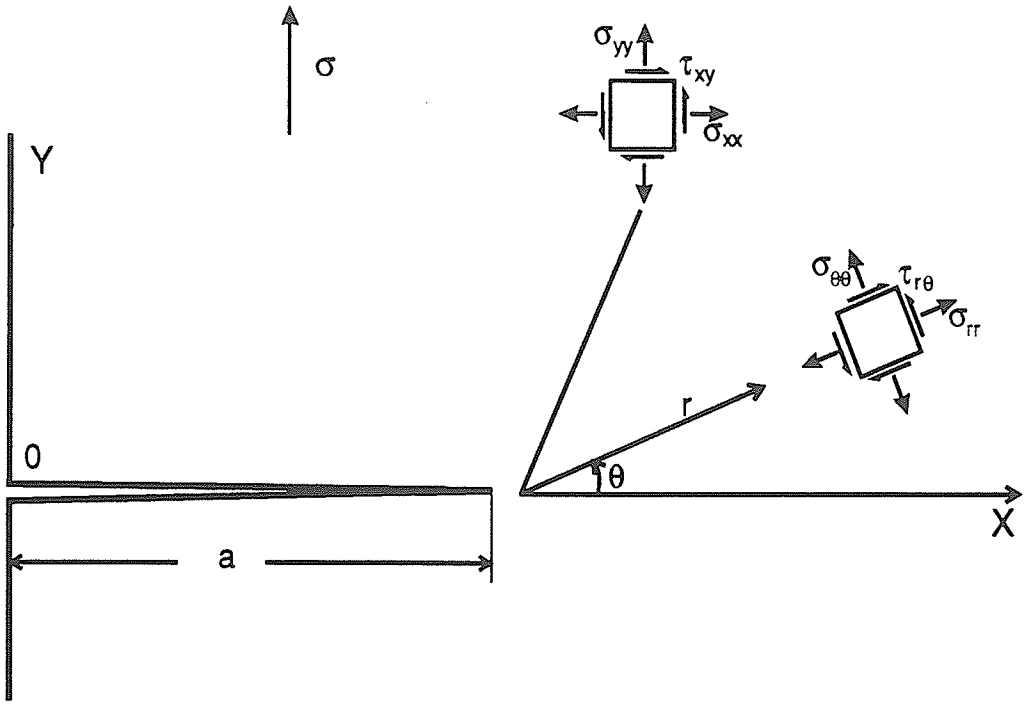

Figure 3.2 The flat mathematical crack of half-length, a. The figure shows the relationship between the crack, the applied stress and the resulting stress at the crack tip (after Broek, 1982).

For both sets of equations 6-8 and 10-12, the third orthogonal stress is:

$$\sigma_{zz} = 0 \qquad \textit{for plane stress} \qquad (13)$$

$$\sigma_{zz} = \nu\,(\sigma_{xx} + \sigma_{yy}) \qquad \textit{for plane strain} \qquad (14)$$

The main assumptions in the above derivations is that the original crack tip is perfectly sharp and the crack width is much less than the crack length. With these assumptions in equations 6-8, the stress at the crack tip becomes infinite or singular when r equals zero (Figure 3.3).

Stresses can never be truly infinite at the crack tip and it has been postulated that the material near the crack tip yields (Irwin, 1957). Most materials, especially metals, have a yield stress at which point they begin to deform in an inelastic or plastic manner. If strain hardening is not present, then the stress at the crack tip is constant and equal to the yield stress, σ_y, over the entire area where elastic stresses would be greater than or equal to the yield stress. Further away from the crack tip, beyond the yielded region, the material behaves elastically. The region of material which has undergone yielding or plastic deformation is often called the plastic zone (Figure 3.4). The size of this zone can be estimated based on energy considerations and the fact that the maximum stress must equal the yield stress when no strain hardening occurs (Broek, 1982). The first estimate of the plastic zone size is

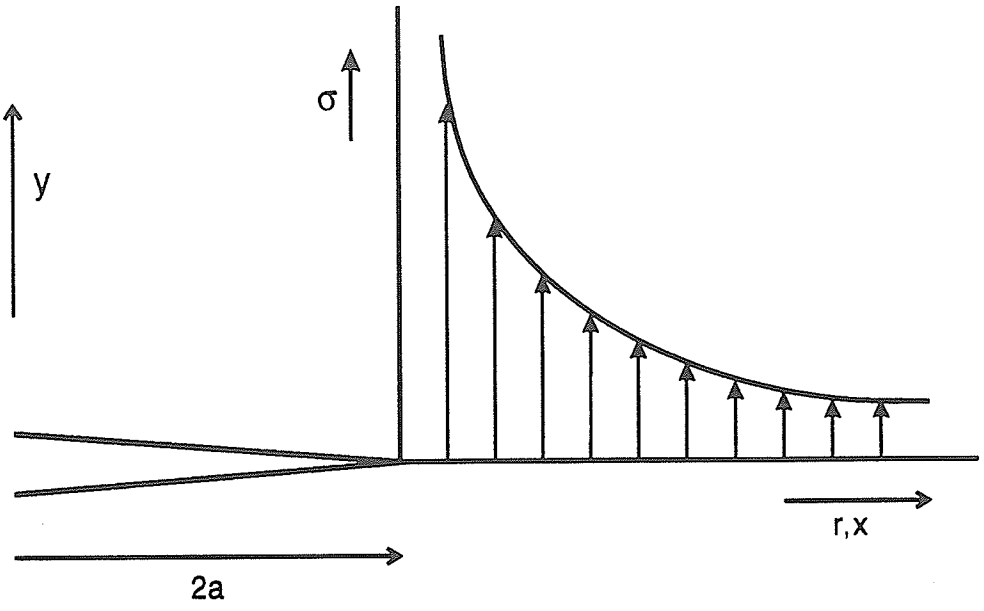

Figure 3.3 Stress at the crack tip approaches infinity as the distance from the crack tip goes to zero (after Broek, 1982).

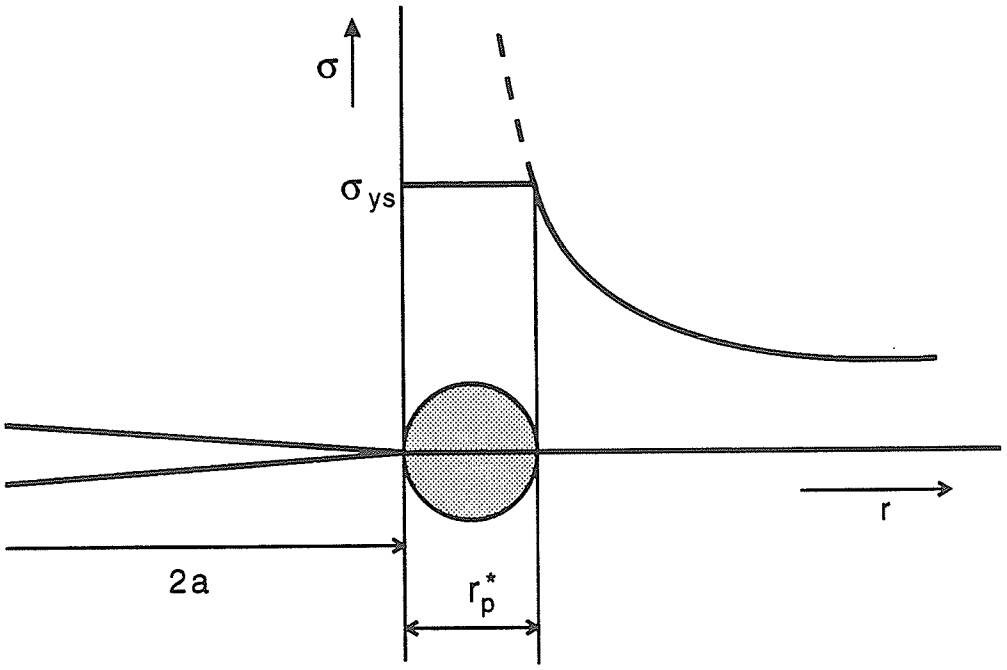

Figure 3.4 The stress at the crack tip is not infinite as a plastic (process) zone forms over the region where the stresses are beyond the yield stress for the material (after Broek, 1982).

$$r_p^* = \frac{K_I^2}{2\pi\sigma_y^2} = \frac{\sigma^2 a}{2\sigma_y^2} \tag{15}$$

for the case of uniaxial yielding where σ_y is the yield stress for the particular material, K_I or σ describes the applied stress field and r_p^* is the process zone size (Figure 3.4).

The actual size of the plastic zone is larger than this, however, due to stress transfer from the plastic region to the elastic region. Stress transfer increases the stress in the elastic region so that a larger area of material suffers plastic deformation. Irwin's concept of the effective crack length (see Broek, 1982) was used to estimate the size of the plastic zone. The new estimate, r_p, is double that of the first estimate

$$r_p = 2r_p^* = \frac{K_I}{\pi\sigma_y^2} = \frac{\sigma^2 a}{\sigma_y^2} \tag{16}$$

A slightly different approach was developed by Dugdale (1960) for ductile materials and by Barenblatt (1962) for brittle materials. The Dugdale model uses a fictitious or effective crack which is larger than the actual crack (Figure 3.5). In the model, the micro-cracked material between the actual and effective crack is assumed to carry a stress equal to the yield stress. This stress acts to close the fictitious crack which means that the true, traction-free crack is smaller than the effective crack. The stress intensity factors due to the assumed closing stresses and the remotely applied stresses must cancel for equilibrium. The size of the plastic zone, in this case, is

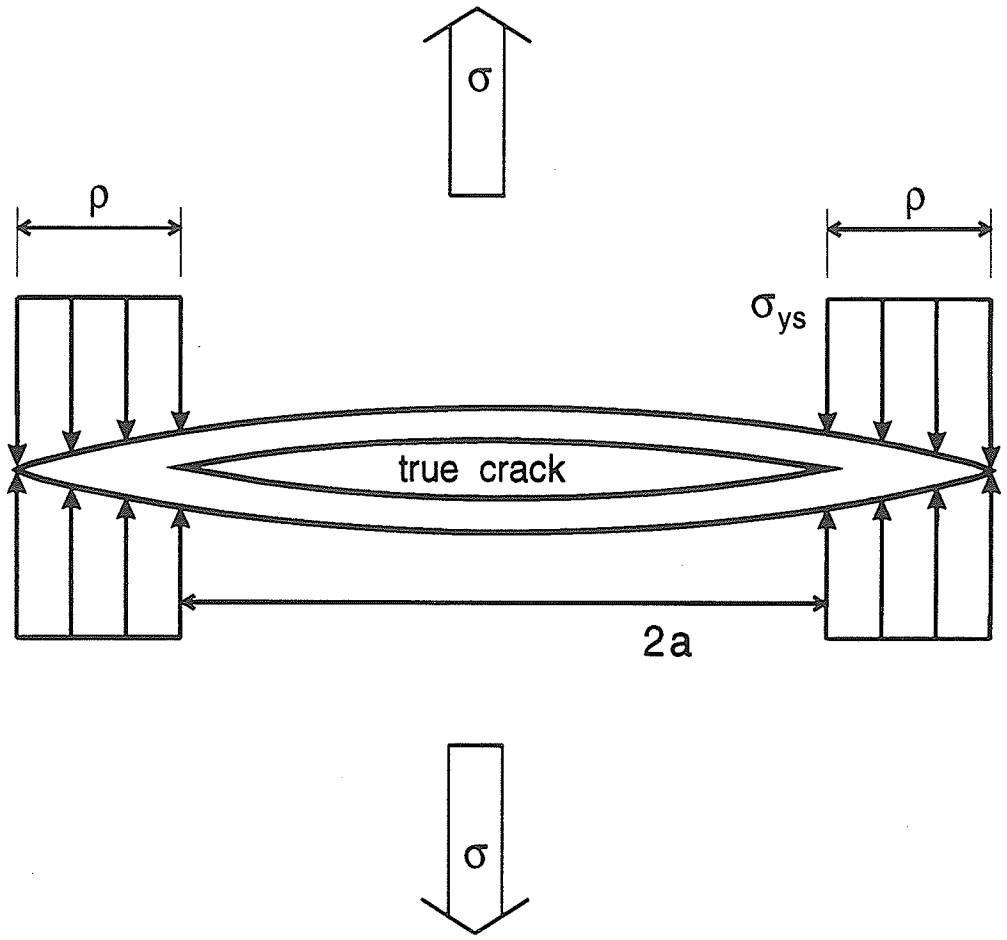

Figure 3.5 Dugdale—Barenblatt model showing the true (actual) crack and the larger fictitious crack. The closing stress acts over the plastic zone, namely, the region between the true and the fictitious crack tips (after Broek, 1982).

$$r_p = \frac{\pi K_I^2}{8 \sigma_y^2} \tag{17}$$

which is reasonably close to that of Irwin's estimate (16). The difference between the Dugdale model and the Barenblatt model is the assumed closing stress distribution. The Dugdale model uses a constant stress, σ_y, whereas the Barenblatt model assumes a linear distribution starting from zero at the actual crack tip and increasing to σ_y at the effective crack tip. The non-linear zone size for the Barenblatt model is (Labuz *et al.*, 1985):

$$r_p = \frac{9\pi}{32} \left(\frac{K_I^2}{\sigma_y^2} \right) \tag{18}$$

This size is about double that produced by the Dugdale model, suggesting that brittle materials may have a larger yield zone than ductile materials.

The previous considerations involved only uniaxial yielding where $\sigma = \sigma_y$ indicates yielding. In reality the crack tip is under a multiaxial state of stress, thus the true size and shape of the plastic zone can only be found by using all stresses in a proper yield criterion, such as the Tresca or von Mises criteria (Broek, 1982). Figure 3.6 shows the plastic zone shape for both yield criteria in both plane strain and plane stress. The difference between plane strain and plane stress is quite apparent from the plastic zone size and shape.

There is a major difference between the plastic zone behavior of ductile materials and a similar type of region in brittle materials. For brittle materials, a true plastic zone does not exist although the material at the crack tip still behaves in a non-linear fashion.

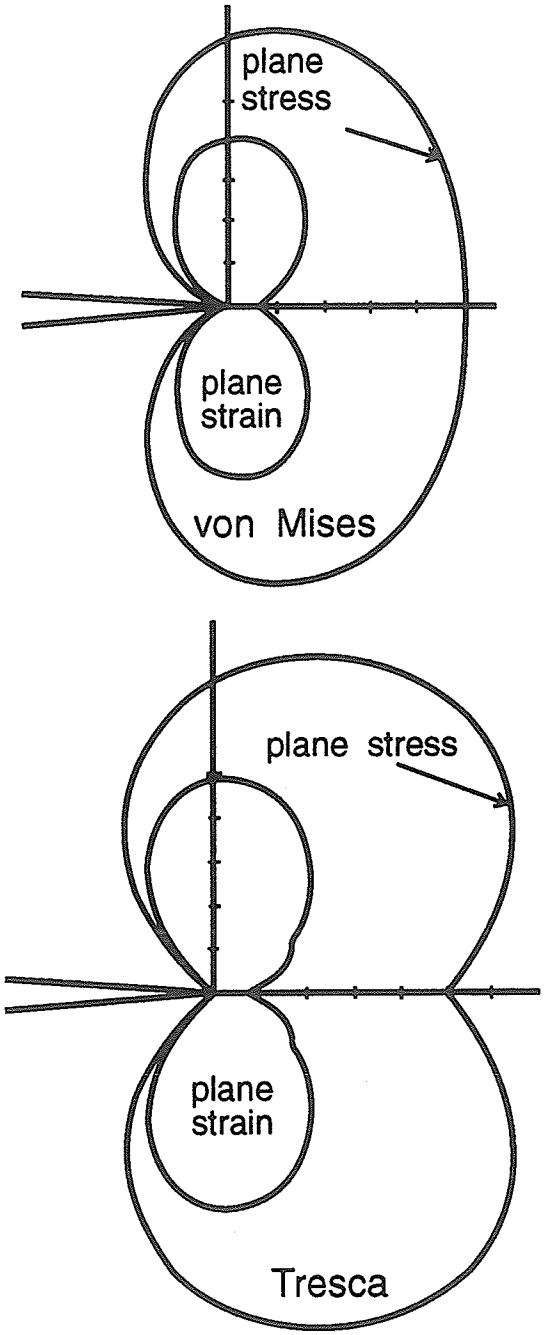

Figure 3.6 Plastic zone shapes for von Mises and Tresca yield criteria for both plane strain and plane stress (after Broek, 1982).

The non-linearity results from microcracking; the region of microcracking is called the process zone rather than the plastic zone, to differentiate between the two types of behavior (Friedman *et al.*, 1972; Hoagland *et al.*, 1973; Labuz *et al.*, 1985; Du *et al.*, 1990). Several studies have been conducted on the parameters controlling the process zone size in concrete and cementitious composites. It was found that the process zone size depends on initial crack length, specimen geometry, and loading conditions (Wecharatana and Shah, 1983). The process zone in rock was also found to depend on the grain size (Labuz *et al.*, 1985) and crack width (Wang *et al.*, 1990). Unlike ductile materials, brittle materials show very little difference in behavior between plane strain and plane stress (Hillerborg, 1983).

Due to the overall similarity in non-linear behavior between ductile and brittle materials, the process zone size in brittle materials was originally estimated from the same formulations used to measure the plastic zone size in ductile materials. The material response is fundamentally different however, which is often seen from the stress-strain curves. Metals may undergo perfect plasticity, or more commonly, plastic strain hardening, whereas brittle materials suffer microcracking (non-linearity) close to the peak strength with very little plastic deformation. Most brittle materials are not truly brittle, showing a definite strain softening response after the peak strength is surpassed (Labuz *et al.*, 1985; Wecharatana and Shah, 1983).

Due to the different material response, other models have been developed for brittle materials; starting with the Barenblatt model. Hillerborg *et al.* (1976) improved the Dugdale—Barenblatt model by employing a closing stress that is no longer constant

or linear, but varies with crack-opening displacement (Figure 3.7). This stress distribution matches the strain-softening response seen in some tension tests (Labuz *et al.*, 1985) and thus more closely represents the material response in the non-linear process zone. The size of the process zone depends on the closing stress distribution (strain softening portion of the stress—strain curve in tension) and thus should be different for various brittle materials. This model can be used to determine the process zone size in uniaxial as well as multiaxial stress states. In the multiaxial case, a yield criterion appropriate for rock and concrete such as the Mohr—Coulomb or the Drucker—Prager criterion must be used. This analysis was done for concrete (Ayari, 1988) and could also be done for any rock type. The process zone shape in concrete, using the Drucker—Prager yield criterion for both plane stress and plane strain is shown in Figure 3.8 indicating the minor differences between the two conditions for brittle materials. The size and shape of the process zone for the rocks of this study will be examined in more detail in a later section.

3.1.3 Fracture Mechanics Applied to Fracture of Rock in Tension

Fracture toughness (K_{IC}) and tensile (yield) strength (σ_t) are the two main parameters needed to apply fracture mechanics to rock fracture under tensile stresses. The other parameter required to find the stress intensity at the crack tip is the initial crack length. This is the most difficult term to define although it has been suggested that initial flaw size depends on grain size (Nur and Simmons, 1970). If no specific data is

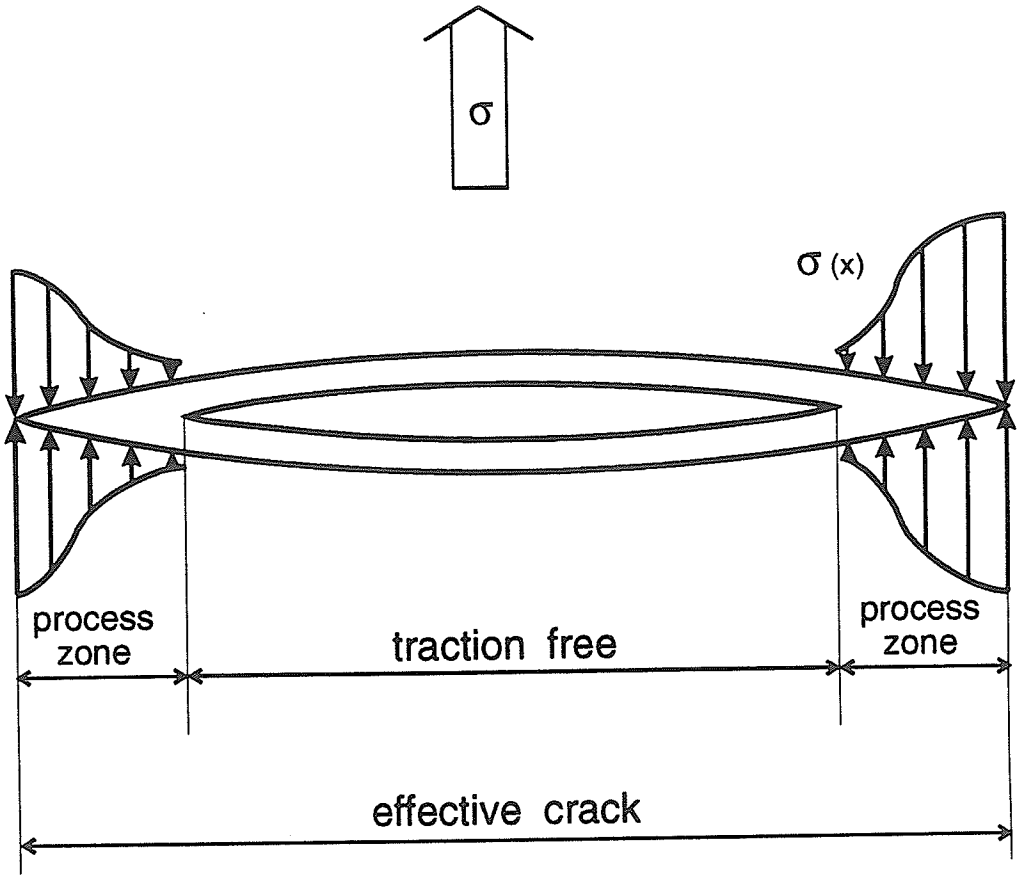

Figure 3.7 Hillerborg model for the traction-free (true) and effective (fictitious) cracks. The closing stress, acting over the process zone, is non-linear and may match the softening portion of the tensile stress—strain curve (after Hillerborg *et al.*, 1976).

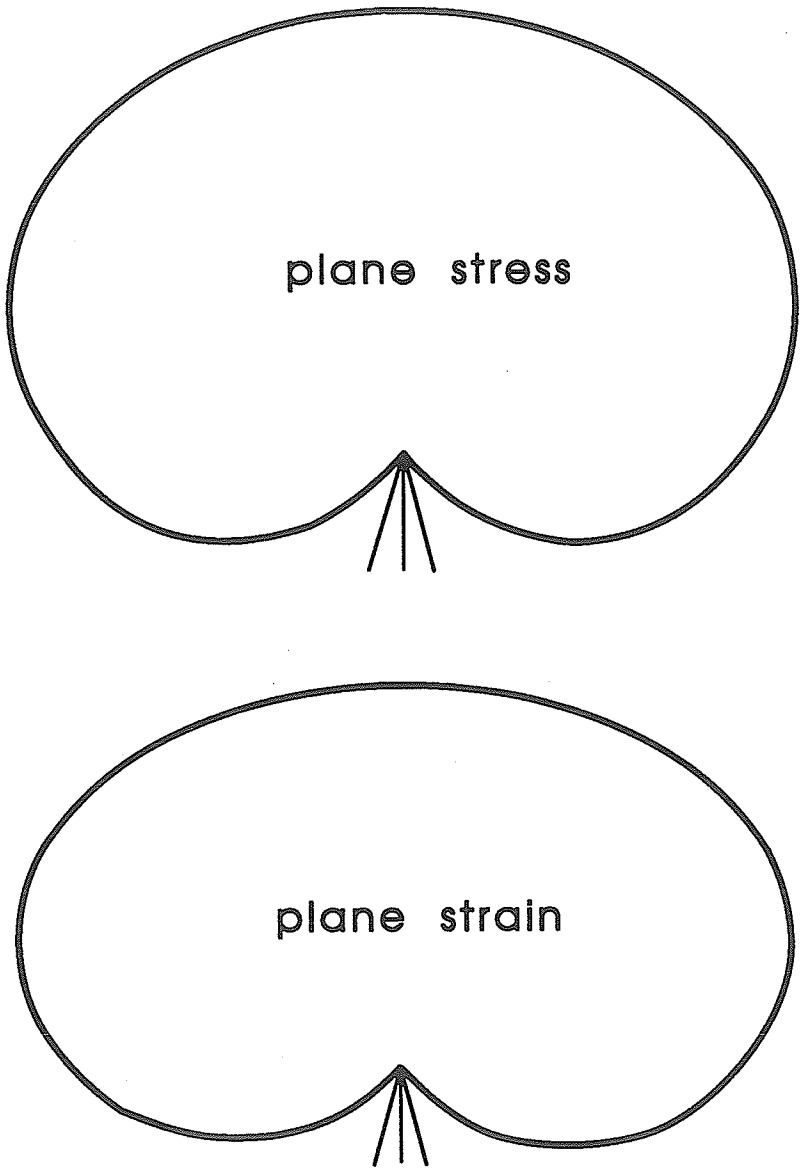

Figure 3.8 Process zone shapes for concrete using the Drucker—Prager yield criterion for plane strain and plane stress (after Ayari, 1988).

available, the average crystal or grain size, which can easily be determined by examining the specimens, is often used as a best estimate (Ingraffea and Schmidt, 1978).

Choosing the initial crack length in this manner can often lead to conflicting results however. For example, if the fracture toughness for Tyndall limestone is 1.0 MPa$\sqrt{m}$ and the tensile strength is 4.0 MPa, then the initial half-crack length should be 49 mm. This assumes that the starting crack is penny-shaped, for which the stress intensity factor is (Sneddon, 1946):

$$K_{IC} = \left(\frac{2}{\pi}\right) \sigma_t \sqrt{\pi a} \tag{19}$$

This length is quite ridiculous since the size of the sample is often smaller than this. Similar results are obtained for LDB granite, where the fracture toughness is 2.5 MPa$\sqrt{m}$ and the tensile strength is about 14 MPa. In this case the initial (penny-shaped) half-crack length would be 25 mm. For potash, which has a fracture toughness of 0.34 MPa$\sqrt{m}$ and a tensile strength of 1.7 MPa, the initial half-crack length is 31 mm.

Ingraffea and Schmidt (1978) and Schmidt and Lutz (1979) have suggested that the fracture toughness depends on crack length. For smaller cracks, the fracture toughness of the material is lower (their crack lengths start at about 5 mm). Very little is actually known about the fracture toughness in the presence of very small cracks. In fact, for multi-mineral rocks, where the minerals themselves show preferential cracking directions, it is very likely that the stress intensity factor ranges from almost zero up to critical values for the composite material itself. Lajtai (personal communication) found

that cracks in Lac du Bonnet granite, in double torsion, propagate at stress intensities as low as 1/3 of K_{IC} depending on the mineralogy at the crack tip.

Another possible factor in the conflict in the data is the presence of the process zone ahead of the crack tip. It is still unclear whether this zone increases or decreases the fracture toughness. It may actually do both (Ortiz, 1988). The size of the process zone is also important. Most researchers agree that if the process zone size is small in relation to the crack, then linear elastic fracture mechanics is suitable. Otherwise non-linear fracture mechanics (Ingraffea, 1987) should be employed. In this case, however, there are no simple analytical techniques for modeling crack growth. The crack-opening displacement is compared to a critical crack-opening displacement rather than comparing stress intensity factors to toughness (Ingraffea, 1987). Non-linear fracture mechanics will be discussed in more detail in Chapter 6.

There are a number of methods for finding the fracture toughness of rocks in tension (Freiman, 1982). Many of them, proposed quite recently, take advantage of the most common shape of rock samples, cylindrical cores (Ouchterlony, 1988). A number of other tests have been in use for many years: double torsion, notched beams, and others (Atkinson and Meredith, 1987). Atkinson and Meredith (1987) have compiled a large list of fracture toughness values for different rocks and minerals. They have also included some data on subcritical crack growth which is a major factor in the time-dependent response of rock. On the other hand, fracture toughness of cracked-material, within completely compressive stress fields, has not received much attention. The problems, noted above, associated with fracture mechanics for tensile stresses, can be

quite easily overcome; fracture in compressive stress fields is a much more complicated matter.

3.2 Fracture and Failure of Rock in Compression

Generally rock and rock structures are not exposed just to simple tension but are subjected to compressive stresses or a combination of compression and tension. The concepts of fracture and failure in compressive stress fields are not as simple as those for tension. Instead of a single or a few microcracks or flaws being activated, numerous cracks and voids are involved.

Whether under uniaxial or triaxial compressive stresses, pre-failure fracture includes the growth of tensile microcracks parallel to the direction of the maximum principal stress. Brittle solids such as rocks contain numerous flaws, cavities, inclusions and other inhomogeneities. The flaws or inhomogeneities may include such things as: suitably oriented pre-existing cracks; soft grains such as biotite in contact with stiffer grains such as quartz; slip bands, lamellae, or cleavage planes; and low-aspect-ratio cavities or pores (Tapponier and Brace, 1976; Sprunt and Brace, 1976; Simmons and Richter, 1974; Kranz, 1983). Basically any flaw, material or geometric, may promote crack nucleation and growth.

When the rock is subjected to external compressive loading, stresses build up around flaws, producing areas of tension and high compression. If the load is large enough, the tension at the flaws causes the initiation and growth of microcracks. Under uniaxial compression, these microcracks grow parallel to the axial load (Figure 3.9 a) and

may eventually extend to the ends of the sample causing axial splitting (Fairhurst and Cook, 1966). Buckling, and possibly shearing, of the thin slabs formed through splitting causes the eventual collapse of the specimen some time after peak strength has been surpassed (Wawersik and Fairhurst, 1970; Peng and Johnson, 1972).

Under triaxial compression, microcracks continue to nucleate at flaws and grow in the axial direction, which is also the direction of the maximum compressive stress trajectories. The growth of these microcracks is greatly affected by the confining pressure. The average crack length is less than in uniaxial compression and the length decreases continuously as the confining pressure is raised (Kranz, 1983). Also, the number of cracks, or crack density, increases as confining pressure increases (Horii and Nemat-Nasser, 1984). This increase only occurs up to a certain level of confining stress, depending on the rock type, after which plastic or ductile deformation increases over brittle cracking. Failure results from a combination of buckling and shearing of material between the microcracks (Figure 3.9 b), ultimately producing a shear failure plane after peak strength has been reached (Yukatake, 1989; Wawersik and Fairhurst, 1970; Peng and Johnson, 1972; Hallbauer *et al.*, 1973).

This process of stable fracture and failure under a compressive stress field is quite different from the fracture process under tensile stresses. For this reason, different theories have evolved to explain both fracture and failure in compressive stress fields. Most of the strength theories which describe rock failure are purely empirical. On the other hand, fracture mechanics has been used to model crack propagation by adapting the crack geometry for the compressive stress conditions.

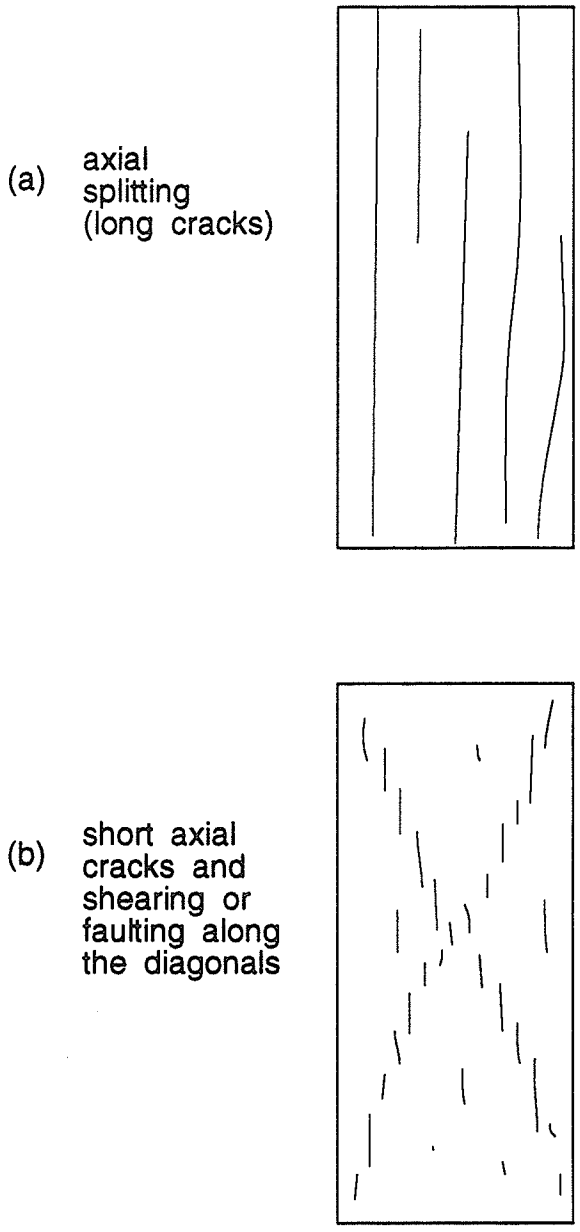

Figure 3.9 (a) The failure mode in uniaxial compression and (b) the failure mode in triaxial compression (after Peng and Johnson, 1972).

The flat starting crack, the flat ellipse from Griffith (1924) or the mathematical slit of fracture mechanics, is the centerpiece of all fracture theories. Ironically, the published literature is devoid of convincing visual evidence for fractures in rock starting from such pre-existing features under compressive loading. There have been many notable demonstrations of the so-called wing cracks propagating from *modeled*, inclined, sliding cracks (Brace and Bombalakis, 1963; Horii and Nemat-Nasser, 1984), but very few *natural* equivalents have yet been documented (Lajtai *et al.*, 1990; Stevens and Holcomb, 1980*a,b*; Costin, 1983).

Grain boundaries in polycrystalline rocks are favored as crack starters. The most effective grain boundaries are those that run in the 20- to 40-degree band measured from the compression direction (Lajtai *et al.*, 1990). The 30-degree direction corresponds to the direction of the critical orientation of cracks in Griffith's theory. The inspection of test specimens that were stressed in triaxial compression to just below their strength suggests that over 70 percent of the cracks propagate within ten degrees of the maximum-stress direction (Lajtai *et al.*, 1990; Zheng *et al.*, 1989*a*). Commonly, several cracks are seen to start at the same grain boundary, suggesting that the full length cannot be modeled as a single starting crack; in fact, there may be several potential sites at the same grain boundary which might become active independently of each other (Lajtai *et al.*, 1990). This observation has been reported by others as well (Tapponier and Brace, 1976), suggesting that the starting flaws may be located at the submicroscopic rather than the microscopic scale.

The concept of fracture occurring from a multitude of crack starters that act more or less independently offers an explanation for the parallel growth of fractures in compression. Fracture nucleation from a number of sites is possible because the process of propagation in compression is stable; the compressive stress must continuously increase to drive the process. In response to the rising stress, the less favorable sites become critical as well and new fractures are nucleated. Although the most striking feature of brittle fracture in compression is the propagation of a set of cracks parallel to the compression direction, there are a number of additional features that may be just as important, some of which are described below.

Ultimate failure of brittle rocks is often thought to occur through some type of coalescence of a suitably positioned set of parallel cracks. There are other types of interference among the parallel cracks however. One type follows from the shadowing or shielding (Kranz, 1979) effect of adjacent cracks (Figure 3.10). Horii and Nemat-Nasser (1984) demonstrated the sudden and explosive growth of fractures between two adjacent cracks. This effect should be even more important when a confining pressure, acting perpendicular to the crack, is present. A normal stress acting laterally would retard crack extension, but its effect is diminished in the stress shadow formed by two proximally growing and presumably dilating cracks. The consequence of this is the formation of several closely spaced fractures. This could explain why cracks are not uniformly distributed in the tested rock specimens, but tend to crowd in certain parts (Lajtai *et al.*, 1990).

Two proximally growing cracks are not necessary to generate additional cracks in the immediate neighborhood. Another type of crack interaction, an en-echelon pattern, (Figure 3.10) was observed while testing a block of Lanigan potash. Stable, compression parallel cracks were seen to generate offset or step-out fractures (Figure 3.11). This process was repeated with the offset crack, giving rise to another fracture. In response to increasing compression, the rock bridge between the end of the first and the starting point of the offset crack was observed to become the site of additional cracks. Eventually, the thin slabs of rock between the newly formed cracks showed signs of buckling instability (top left corner of Figure 3.11). This process was also seen in other model tests on potash and limestone which will be discussed further in the following chapters.

There is also evidence for the existence of these step-out fractures in nature where they are usually called en-echelon fractures (Pollard *et al.*, 1982). Engelder (1987) shows numerous examples of echelon joint sets. Tertiary mafic dikes on the Colorado Plateau (Pollard and Segall, 1987) also provide a good example; on the ground surface, the dikes and surrounding fractures occur in en-echelon patterns (Figure 3.12). Pollard and Segall (1987) interpret the formation of these offset fractures through twisting of the stress field. Closely spaced joints near the dike tips were interpreted to have formed in response to the tensile stresses located on either side and to the front of the tip of the dike plane; similar to a large process zone. Based on the widespread physical evidence of the complex fracture process in rock under compressive stresses, it is quite obvious that the simple fracture and failure theories for tensile stresses are not applicable. Empirical

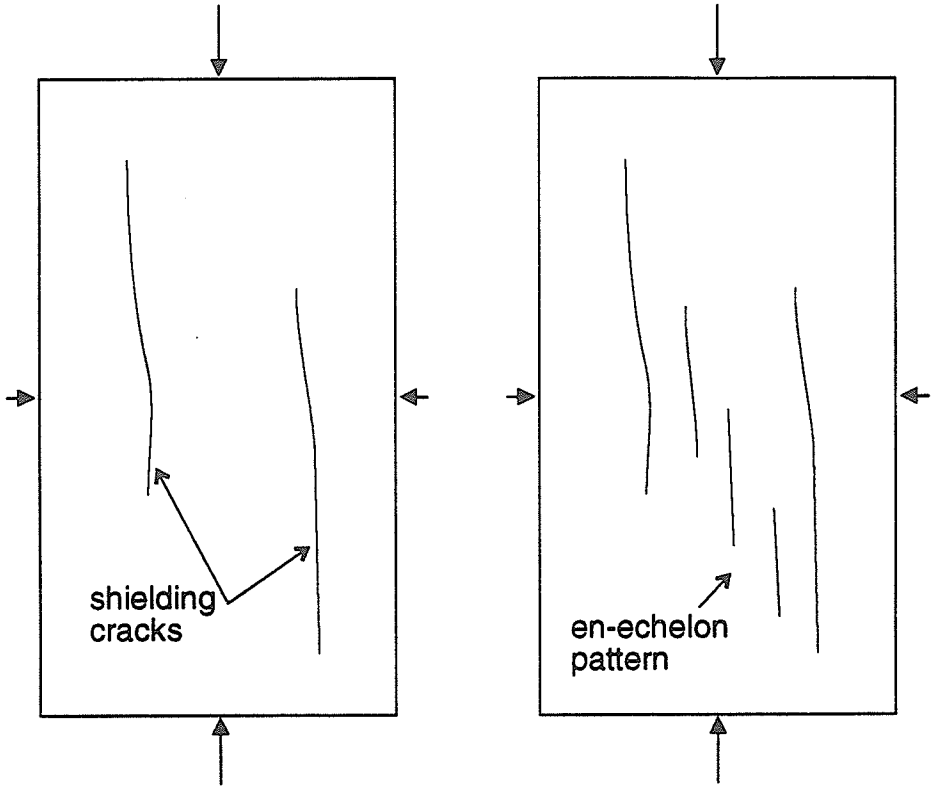

Figure 3.10 The shadowing or shielding effect of adjacent cracks allows other cracks to initiate between them. These cracks often form an en-echelon pattern, in rock subjected to compression.

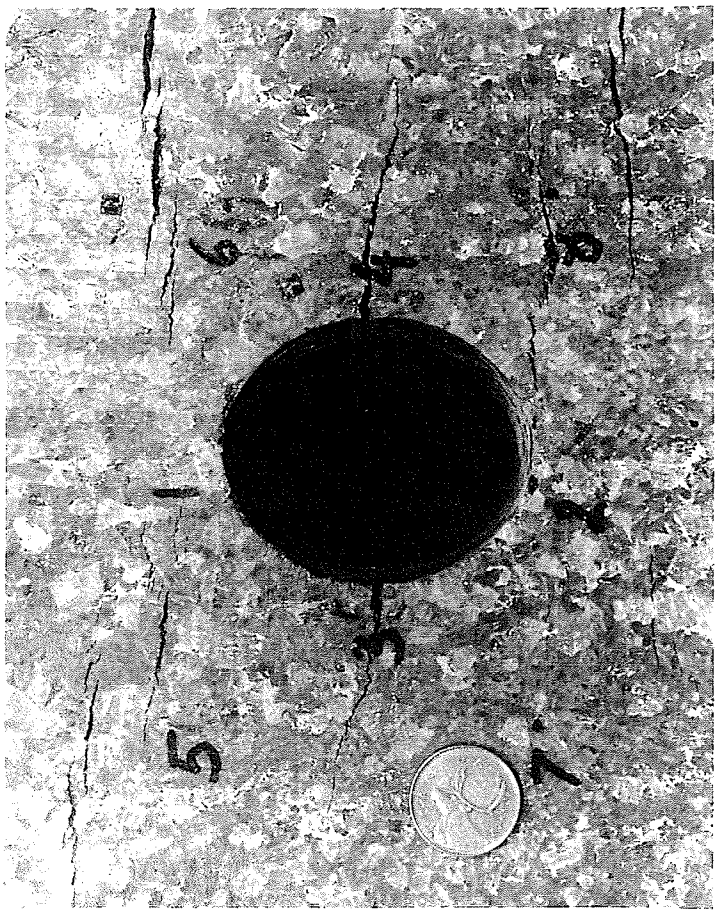

Figure 3.11 Photo of a model test using Lanigan potash to simulate a circular underground excavation. The en-echelon cracks can be seen clearly in the top left corner. The Canadian quarter, which is 24 mm in diameter, can be used for scale.

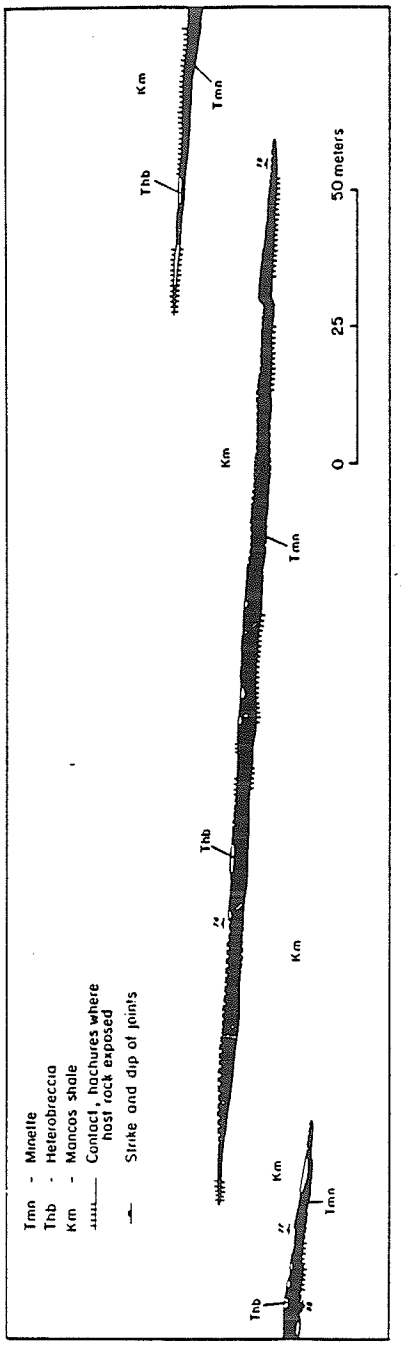

Figure 3.12 Mafic-dikes on the Colorado plateau also form an en-echelon pattern (from Pollard and Segall, 1987).

strength theories based purely on experimental data have become the norm for modeling failure of rock in compressive stress fields (Hoek and Brown, 1980). Fracture mechanics theories capable of modeling fracture in compression have been proposed only in the last few years (Horii and Nemat-Nasser, 1986; Kemeny and Cook, 1987; Sammis and Ashby, 1986; Kemeny and Cook, 1990).

3.2.1 Empirical Failure Theories For Rock in Compression

The strength of rocks has been modeled through a number of empirical criteria. Among these, the Hoek and Brown square-root parabola (Hoek and Brown, 1980) is the most widely used:

$$\sigma_1 = \sigma_3 + \sqrt{(m C_o \sigma_3 + s C_o^2)} \tag{20}$$

σ_1 represents the value of the maximum principal stress at failure for a constant minimum principal stress (σ_3), m is a curve fitting parameter and C_0 is the uniaxial compressive strength. For this study, the effect of the rock mass parameter, s, will be suppressed by setting it to unity, since the focus is on intact rock. This leaves σ_1 as function of just two parameters, m and σ_3. T_0, the uniaxial tensile strength is defined when the above strength parameters are known:

$$T_o = C_o \frac{m - \sqrt{(m^2 + 4s)}}{2} \tag{21}$$

Using the usual rock mechanics sign convention, T_o is a negative quantity, satisfying the function at $\sigma_1 = 0$.

The Hoek and Brown function has been fitted to data coming from triaxial compression testing of a wide variety of rock types with good results (Hoek and Brown, 1980). It gives a particularly good fit to data obtained from triaxial tests of hard crystalline rocks loaded at moderate to high confining pressures. The criterion utilizes the $y^2=x$ type of parabola, originally suggested for rock strength data by Leon (1934). Johnston (1985*a*,*b*) proposed that the curvature of the square-root parabola in the low-confining-pressure to tension region is not flexible enough to fit the strength data for weaker materials; the latter obey the straight-line relationship predicted by the Mohr—Coulomb theory. More variation can be achieved by replacing the square root of x with that of a variable exponent B. The strength criterion then becomes a three- rather than two-parameter function. The Johnston criterion with the stresses normalized by the uniaxial compressive strength, C_o, is:

$$\sigma_{1n}=\left(\frac{M}{B}\sigma_{3n}+1\right)^{B} \tag{22}$$

Here M and B are the controlling parameters which fix the compressive- to tensile-strength ratio according to:

$$\frac{C_o}{T_o}=-\frac{M}{B} \tag{23}$$

B often has a value between 0.3 and 1, where the latter value produces a straight line relationship between the normalized maximum principal stress at failure (σ_{1n}) and the normalized minimum principal stress (σ_{3n}). The three-parameter function is naturally more versatile and can be made to follow any rock strength distribution with acceptable

precision. Determining B and M is difficult, however, requiring a nonlinear regression procedure. Alternatively, Johnston (1985*a*,*b*) gives a relationship between B and σ_c and between M and σ_c as well as a table of results for different rocks which may be used to estimate B and M.

Curve-fitting through regression is a compromise that does not necessarily give the desired result. Often, it is desirable to force the function to fit the data in a particular range of confining pressures. Most rock failures occur at low confining pressures. Slabbing in underground cavities, for example, proceeds under a stress condition where the minimum principal stress is practically zero. Through regression analysis, neither the uniaxial tensile nor the uniaxial compressive strength calculated from the fitted functions coincides with the measured values. The regression procedure considers all data, including those at high confining pressure. Because the sharpest curvature of both functions occurs in the tensile to low confining pressure region, the risk of a poor fit is the greatest in this region. This is particularly true when the usual fitting procedure is followed for the two-parameter Hoek and Brown square-root parabola. The fitted curve may give an excellent fit at high confining pressure, but will often under- or over-estimate the uniaxial tensile and/or the uniaxial compressive strength.

Because the Hoek and Brown strength criterion does not fit very well in the tension—low-compression end of the strength curve, another empirical failure criterion called the Rocker function was developed (Carter *et al.*, 1991*a*). It is quite similar to the Johnston criterion, although it is much easier to implement, simply requiring the actual uniaxial tensile and uniaxial compressive strengths plus one fitting parameter. The

Johnston criterion, on the other hand, needs two fitting parameters which are related to the tensile- to compressive-strength ratio through equation (23).

The Rocker function is

$$\sigma_1 = C_o\left(1-\frac{\sigma_3}{T_o}\right)^R \tag{24}$$

where C_0 is the uniaxial compressive strength, T_0 is the uniaxial tensile strength, σ_3 is the minimum principal stress, R is a fitted parameter and σ_1 is the strength for a confining stress, σ_3. The exponent, R, may be regarded as a shape factor assuming values in the range of 0.3 to 1 for most rocks. Because of its simple form and the fact that T_0 and C_0 are constants, the Rocker function can be linearized for a simple linear regression procedure. The only disadvantage is that the regression may move the curve away from the desired anchor points at T_0 and C_0. The simplest way to keep the curve attached to these anchor points and get the best fit to the rest of the data is to iteratively increase or decrease R until the best fit is obtained. The best fit can be determined through several different statistical parameters such as: the error sum of squares (SSE), the residual plots, or the coefficient of determination (r^2). All three empirical strength criteria have been fitted to the three rock types of this study (Carter *et al.*, 1991*a*). The Rocker function provides a reasonable fit to all three rock types, especially in the tension—low compression region (Figures 3.12 a,b,c).

Although the Rocker function was developed independently, it is essentially identical to that of Sheory *et al.* (1989):

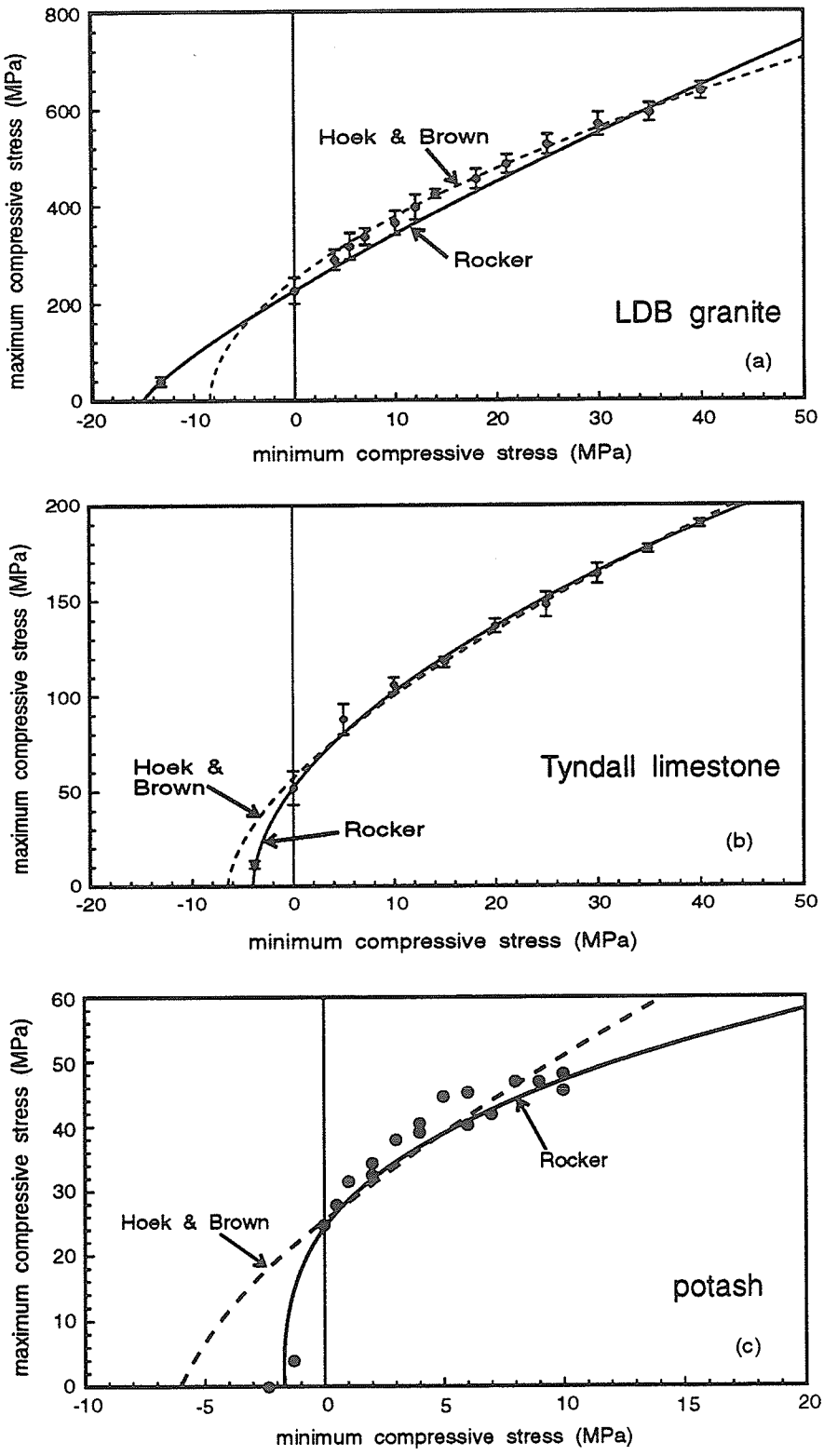

Figure 3.13 Comparison between the Hoek & Brown and the Rocker functions for triaxial strength data for (a) LDB granite, (b) Tyndallstone and (c) Saskatchewan potash.

$$\sigma_1 = C_o (1 + a\,\sigma_3)^b \tag{25}$$

The condition at $\sigma_1=0$ of $\sigma_3=-T_o$ gives:

$$\sigma_1 = C_o \left(1 + \frac{\sigma_3}{T_o}\right)^b \tag{26}$$

which is identical to the Rocker function. Sheory *et al.* (1989) also found that the more common strength criteria did not fit the triaxial strength data for most rocks. The present function was shown to fit the triaxial strength of intact rock as well as the strength of the rock mass with quite good precision.

The difficulty of fitting a single function to strength data over the whole range of loading conditions, including tension, could signal that the nature of the failure mechanism changes as the minimum principal stress moves from high compression to tension. In the intermediate range of compressive, minimum principal stress, the buckling of intact rock beams bounded by load-parallel tensile fractures seems to control the strength of most if not all rocks. This is clearly the case for the granite, limestone and potash—salt rock of this study. There is no chance of buckling instability in purely tensile loading situations; a transition must occur somewhere in the uniaxial compression to uniaxial tension portion of the strength curve. One way to overcome this problem in modeling is to use multiple criteria. The Mohr—Coulomb line with a tension cut off (Paul, 1961) is a good example of this approach. The Mohr—Coulomb strength line is compared with σ_1 while σ_3 is compared with T_0 to obtain a measure of overall stability.

The first part comes from soil mechanics while the second is an expression of the maximum stress theory. However, the double-criteria approach is inadequate to explain the fact that the principal stresses act together in causing failure. Observation of physical model tests indicate that many cracks form in low-tensile- to high-compressive-stress fields where neither the tensile nor the compressive stresses reach their respective uniaxial strength values. This also implies that these stresses must combine to cause fracturing. The Hoek and Brown, the Johnston and the Rocker criteria all imply that σ_1 influences the fracture and failure process. Although the shape of the strength line in the tension zone has never been adequately defined, assuming the existence of the line should lead to a safer structural design.

3.2.2 Fracture Mechanics for Compression

Fracture mechanics was originally developed for fracture in metals subject to tensile stresses. The theory was later applied to brittle materials with some success when the stresses were tensile. Compressive stresses produce an entirely different scenario. Most metals are quite ductile and do not fracture under compressive stresses; they yield. On the other hand, brittle materials such as rock and concrete generally fail due to accumulated brittle cracking and eventual shearing or buckling. Because fracture mechanics was originally designed for tensile loads, the present linear elastic fracture mechanics formulation ignores the stress parallel to the crack. In the case of compressive loading of rock, most cracks grow parallel to the maximum compressive stress and thus

any theory which ignores this stress can not accurately predict fracture of rock in compressive stress fields.

The Griffith (Griffith, 1924) and Modified Griffith theories of rock mechanics (McClintock and Walsh, 1962) and the discipline of fracture mechanics both model the crack starting flaw as a flat ellipse. Besides the obvious exclusion of starting flaws of other shapes, the flat flaw concept has introduced a dilemma. Flat cracks, including the flat mathematical crack, do not disturb the distribution of the crack-parallel normal stress (the axial compressive stress) and hence this component of the stress tensor is neglected. In an evaluation of the Griffith theory in compression through physical modeling, Lajtai (1971) has shown that this assumption leads to erroneous results in the case where the starting flaws, such as pores, vugs, and other voids which are common in rock (Sprunt and Brace, 1974), do not close under stress. When using the theory of the flat crack, one must accept the lack of contribution from the normal stress directed parallel to the slit. This is difficult to accept, however, as observation of fractures in laboratory specimens or in the tectonically deformed rocks of nature suggests that the dominant mode of fracture within completely compressive stress fields is consistently in the direction of the far-field maximum principal compressive stress (Kranz, 1983; Lajtai *et al.*, 1990).

The theory of fracture mechanics can account for a stress parallel to the crack by including an extra term in the original equations for stress at the crack tip (Williams, 1956; Ingraffea, 1977).

$$\sigma_r = \frac{1}{4\sqrt{r}}\left(a_1\left[-5\cos\frac{\theta}{2} + \cos\frac{3\theta}{2}\right] + b_1\left[-5\sin\frac{\theta}{2} + 3\sin\frac{3\theta}{2}\right]\right) \qquad (27)$$
$$+ 4a_2\cos^2\theta + \ldots$$

σ_r is the radial stress at the crack tip, a_1, b_1 and a_2 are constants, similar to the stress intensity factors. r is the distance from the crack tip and θ is the polar angle (Figure 3.2). The first term of (27) is singular as it is a function of $1/\sqrt{r}$. The second term, which includes a_2, is the term which accounts for the stress parallel to the crack.

This formulation produces a constant stress ahead of the crack tip equal in magnitude to the applied load but with no variation as the distance from the crack tip increases or as the crack length increases. This does not correspond well with the observed phenomenon of stable crack growth seen in rock under compressive loads. The formulations would suggest unstable crack propagation when the compressive stress produces a stress intensity equal to the fracture toughness whereas most cracks grow in a stable manner under compressive loads.

A number of other models have subsequently been developed to model fracture propagation in compressive stress fields (Horii and Nemat-Nasser, 1986; Kemeny and Cook, 1987; Kemeny and Cook, 1990; Gramberg, 1989; Stevens and Holcomb, 1980*b*; Costin, 1983). The most widely used and best-developed model utilizes a sliding crack with extensional wing cracks (Brace and Bombalakis, 1963; Nemat-Nasser and Obata, 1988); even though the dominant mode of cracking is maximum-compression-parallel (Stevens and Holcomb, 1980*a,b*).

The simplest model which represents the sliding crack mechanism is a line discontinuity, PP' (Figure 3.14), which can glide in its own plane. Sliding or shear along PP' produces opening-mode wing cracks which emerge symmetrically from both ends of the crack. The stress intensity factor for these wing cracks is (Nemat-Nasser, 1985):

$$K_I = \frac{(2a\tau^* \sin\alpha)}{\sqrt{\pi(l+l^*)}} + \left[\sigma_1 + \sigma_3 - (\sigma_1 - \sigma_3)\cos 2(\alpha - \theta)\right] \cdot \sqrt{\frac{\pi l}{2}} \qquad (28)$$

where

$$l^* = 0.27\,a$$
$$\tau^* = \frac{1}{2}\left[(\sigma_1 - \sigma_3)\sin(2\theta) - \tau_c + \mu(\sigma_1 + \sigma_3 - (\sigma_1 - \sigma_3)\cos(2\theta))\right] \qquad (29)$$

where μ is the coefficient of friction, τ_c is the cohesive resistance of the pre-existing crack, and θ, α, σ_1, σ_3, a, and l are defined in Figure 3.14. This equation is quite complex and a simplified form was used by Kemeny and Cook (1987):

$$K_I = \frac{2l_o\tau^* \cos\theta}{\sqrt{\pi l}} - \sigma_3\sqrt{\pi l} \qquad (30)$$

where τ^* was defined above, $l_o = a$ and $l = l$ from above and θ is shown in Figure 3.14. For a given state of stress, defined by σ_1 and σ_3, the stress intensity factor can be calculated and compared to the fracture toughness. When the stress intensity factor is

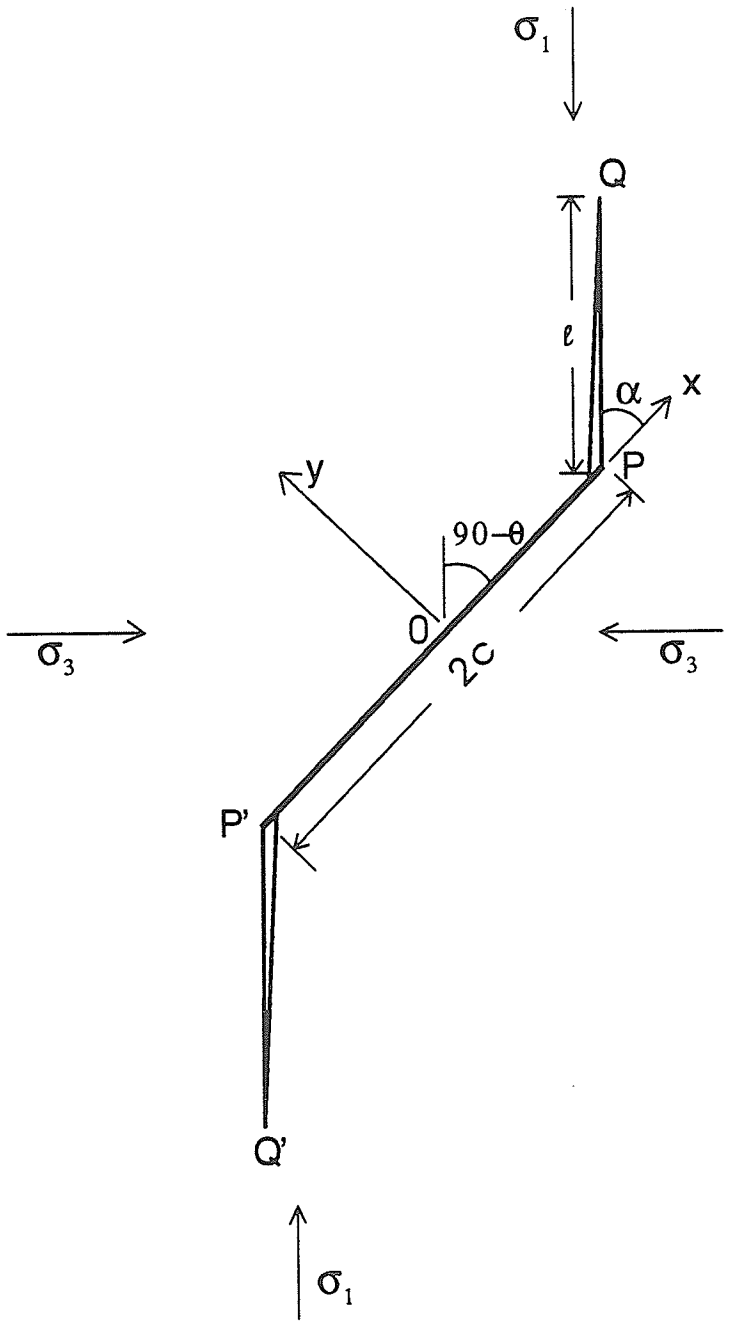

Figure 3.14 Simplified, sliding-crack model (after Horii and Nemat-Nasser, 1984). The compressive stresses induces sliding along PP' and this causes opening-mode wing-cracks to emerge from the ends of PP'. These wing cracks grow parallel to the maximum compressive stress.

equal to the fracture toughness, fracturing is assumed to initiate. Nemat-Nasser and Horii (1982) and Kemeny and Cook (1987) do not consider the formation of offset fractures as part of the failure process even though, based on physical tests, these offset fractures seem to dominate the failure process. They assume that overall failure occurs when the axial-growing wing cracks begin to propagate in an unstable manner.

Another method of modeling fracture under compressive loading is to use the splitting crack model (Ewy and Cook, 1990; Kemeny and Cook, 1990). This model is similar in principal to the Brazilian tension test (Figure 3.15). The mode I stress intensity factor for this case is (Kemeny and Cook, 1990):

$$K_I = \left[\frac{2C_1(\sigma_1 - C_2\sigma_2)\sqrt{l}}{\sqrt{\pi}}\right] \sin^{-1}\left(\frac{a}{l}\right) - \sigma_2\sqrt{\pi l} \qquad (31)$$

or for a linearly varying stress (Figure 3.15 b):

$$K_I = \left[\frac{2C_1(\sigma_1 - C_2\sigma_2)\sqrt{l}}{\sqrt{\pi}}\right]\left[\left(2 - \frac{l}{a}\right)\sin^{-1}\left(\frac{a}{l}\right) + \sqrt{1 - \frac{a^2}{l^2}}\right] - \sigma_2\sqrt{\pi l} \qquad (32)$$

where l is the crack length (Figure 3.15), a, C_1 and C_2 are constants, σ_1 is the compressive stress parallel to the crack and σ_2 is the confining stress. This method appears to model crack growth more realistically but it, too, requires time-consuming numerical procedures to produce propagating cracks.

Another method of modeling cracking and failure in compression is Damage Mechanics (Kachanov, 1982; Krajcinovic and Fonseka, 1981; Cristescu, 1986; Singh and Digby, 1989). Damage mechanics may incorporate some fracture mechanics theory

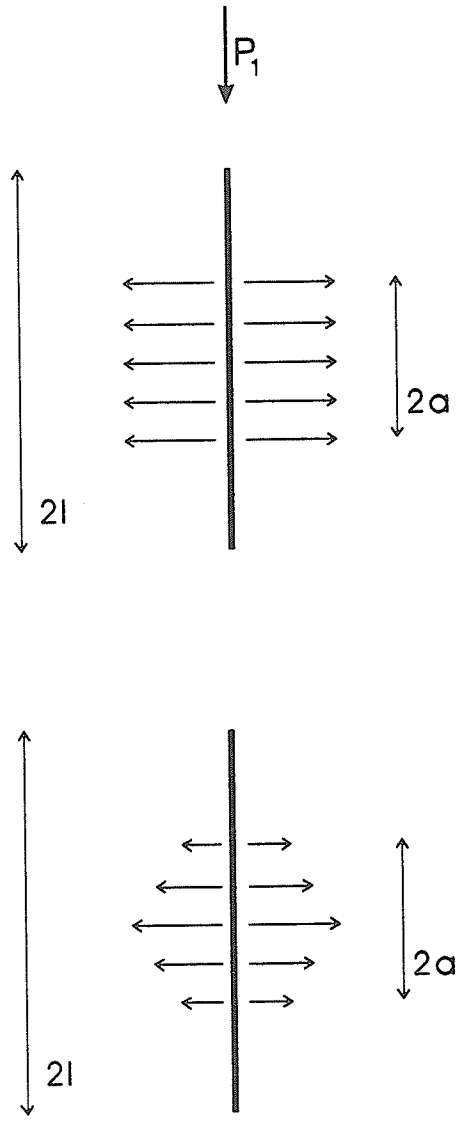

Figure 3.15 Splitting-crack model (a) with a constant stress distribution and (b) with a variable stress distribution (after Kemeny and Cook, 1990).

(Costin, 1985), some plasticity theory (Lubliner *et al.*, 1989) and/or some thermodynamics (Yazdani and Schreyer, 1988). It has generally been used to model overall stress—strain behavior rather than discrete crack propagation. It is convenient for compression as well as tension as the internal damage parameter(s) can be defined for both stress states. The term, damage, implies microcracking and damage mechanics theories usually relate the microcracking to a reduction in stiffness or elastic modulus (Costin, 1983). A reduced modulus is represented by non-linearity and strain softening on the stress-strain curve, a feature which has already been observed for many rocks (Figure 2.1). Failure occurs when the damage reaches a critical state. Although discrete crack growth has been modeled with this method (Lubliner *et al.*, 1989), it will not be used in this study.

3.2.3 Fracture Mechanics Applied to Fracture of Rock in Compression

Because fracture and failure in compression is a complex process of multiple cracks and crack interactions, simple analytical fracture mechanics formulations are not available to model even the simplest uniaxial compression test. Modeling uniaxial or triaxial compression tests requires a numerical approach such as that of Costin (1983), Horii and Nemat-Nasser (1984), or Kemeny and Cook (1987 & 1990), all of whom show a reasonable agreement between their models and experimental data.

3.3 Sample Size and Stress Gradient Effects

It was stated that fracture length, process zone size, and the size of the structure containing the crack all affect fracture growth. Size affects not only the internal fractures, it also affects the strength of the structure. The exact influence of size is still not clear, however, and some conflicting data have been presented. Evans and Pomeroy (1958) found that the crushing strength of cubes of coal decreased as the size increased. Hodgson and Cook (1970) and Gonano (1974), on the other hand, found that there was no gross size effect for uniaxial compression tests. This conflict in data could have resulted from different testing techniques, different rocks being tested, etc. The influence of stress gradients due to various testing techniques as well as the influence of material behavior (brittle or ductile) and failure mode has been well demonstrated in laboratory testing (Gonano, 1974; Gonano and Brown, 1975; Hodgson and Cook, 1970; Durelli and Parks, 1962; Lajtai, 1972). Thus, in any size effect study, the material behavior and testing procedure need to be carefully documented.

Although the influence of size and stress gradient on the strength of rocks has been widely demonstrated in laboratory experiments and physical model tests, the theoretical justification has remained highly controversial. The most widely known theory is based on the statistical distribution of flaw sizes in rock, commonly referred to as Weibull's theory (Weibull, 1939). Rather than using statistical theories, Durelli and Parks (1962) and Lajtai (1972) related the observed size effect to the stress gradients that exist in many tests of brittle materials. Durelli and Parks (1962) postulated that cracking occurs once a critical volume is reached where the stress is at least 95% of the peak

stress. Lajtai (1972) modeled the gradient effect by averaging the stresses over a critical distance along the fracture path. Gonano and Brown (1975) compared the statistical size-effect theories, including Weibull's theory, with several empirical methods and finally settled on an energy-based fracture approach which includes the concept of critical volume and critical strain energy release rate. More recently, researchers working mainly with concrete have developed dimensionless scaling factors (Carpinteri, 1982; Bazant, 1984) which relate size or scale effects to strength based on fracture mechanics principles and energy release rates. The potential strain energy of the structure is a volume term (volume of the structure) while fracture propagation energy is an area term (fracture surface area) thus producing an inherent size effect in these formulations (Bazant, 1984). Bazant and Yunping (1991) have even incorporated Weibull's theory into Bazant's (1984) size effect theory.

One of the most comprehensive studies on size and stress-gradient effects was performed by Gonano (1974) and Gonano and Brown (1975) who examined various testing procedures and theoretical models with reference to physical tests on rock. From this study it was noted that the size effects vary for different rock types (brittle or ductile) and for different tests (compressive or tensile). Tension tests showed more size effects than did compression tests, unless large stress gradients existed in compression such as for punch-bearing tests. Tests that induce high stress gradients generally show a greater size effect than tests which have very low or no stress gradients.

It was shown that very brittle rocks are subject to the greatest size—stress-gradient effects (Gonano and Brown, 1975). This was explained through the different failure

modes which exist for brittle as compared to more ductile rocks under high stress gradients. Ductile materials behave in a more plastic manner while more brittle materials suffer cracking and unstable post-peak failure (Gonano and Brown, 1975). Another series of tests, performed by Einstein *et al.* (1970) indicate that crack initiation is not affected by specimen size for simple laboratory tests such as uniaxial compression. The peak strength is affected by both the specimen size and the end-loading constraints but the crack initiation point shows only a statistical variation.

One of the conclusions reached by Gonano (1974) is that although statistical distributions of flaw sizes can induce some size effects, the real influence is the stress gradient induced by the testing method. The following section illustrates this by showing strength data for various volumes and for various tests. The data clearly indicate a dependence on test type (stress gradient) but little dependence on specimen size. The Weibull theory, which has long been used to correct for size effects, does not adequately account for the variations from the experimental tension tests.

3.3.1 Weibull Correction for Tension Tests

The Weibull (1939) theory has traditionally been used 1) to correlate tensile strength data from one type of test to another, and 2) to express the size (often as specimen volume) effect within a single test type (Jaeger and Cook, 1979). The relevance of this theory may be shown by comparing several different types of tension tests and then comparing the results for various sizes using the same type of tension test.

This comparison indicates that specimen size has less effect than test type where the different tests have very different stress gradients.

For example, to determine the tensile strength of Tyndall limestone (set #2), three different tests were used: direct tension, Brazilian and four-point bending. By fitting the Weibull distribution to each set of data, the Weibull parameter (m) can be evaluated. For the four-point-bending data, the Weibull parameter m is 1.94. The equivalent direct tensile strength, corrected for size and gradient effects, is obtained through:

$$\sigma_e = \frac{\sigma_{tf}}{[2m+2]^{1/m}} \tag{33}$$

where σ_{tf} is the (tensile) flexural strength of the four-point bending tests (mean=9 MPa). The corrected tensile strength is σ_e=2.1 MPa (Table 1). This value is much lower than the measured flexural (rupture) strength but still much greater than the mean direct tensile strength (0.8 MPa).

A closed-form solution to convert the Brazilian tensile strength (mean=2.5 MPa) to an equivalent direct tensile strength does not exist. There is, however, a numerical solution (Chandler, 1989) that gives a correction factor for the specimen volume (Figure 3.16). Using the Weibull parameter m of 2.73 and a volume correction factor (C_v) of 0.21, the corrected tensile strength is

$$\frac{\sigma_e}{T_o} = \left[\frac{V_{tension}}{V_{Brazilian}\ c_v}\right]^{1/m_{tension}} \tag{34}$$

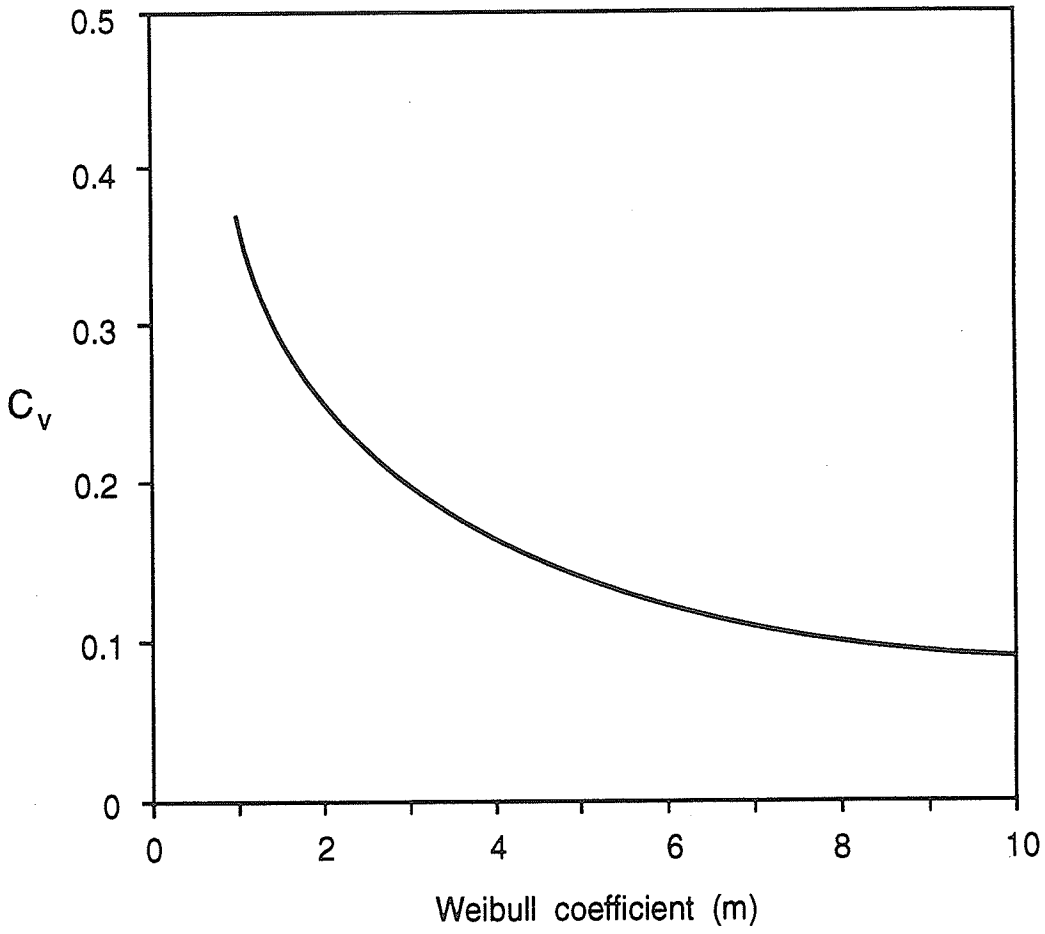

Figure 3.16 Volume correction factor as a function of the Weibull parameter (m) for the Brazilian disk, indirect tension test (after Chandler, 1989).

where T_0 is the mean direct tensile strength, σ_c is the corrected Brazilian tensile strength, V_{tension} is the volume of the direct tension samples, $V_{\text{Brazilian}}$ is the volume of Brazilian samples, and m_{tension} is the Weibull parameter for the direct tension data. The corrected tensile strength is 1.7 MPa which is about twice the direct tensile strength.

Although the Weibull theory can account for part of the variation in tensile strength obtained from the three types of tests, it would appear that the predicted values are still too far apart to let the Weibull correction substitute for performing the relevant type of tension test. The different tests may often be used to simulate the actual stress conditions in the field so it is important to be able to perform all types of tests. For the modeling exercises in the following chapters, the value of 1.5 MPa is selected as the tensile strength. It is simply the average of the three corrected tensile strengths, 0.8 (direct tension), 1.7 (Brazilian) and 2.1 (four-point-bending) as the stress conditions above the center of the hole are not exactly related to any of these three tests. The effect of material bimodularity (the elastic modulus in tension differs from that in compression) could account for some additional variation between the direct and the indirect tension tests (Stimpson and Chen, 1991) but this was not examined in this study.

The Weibull interpretation for size (volume) effect was tested against 84 Brazilian tension tests using Tyndall limestone (set #1) and involving volumes from 6.9 to 56.8 cm^3 (Weiss, 1984). According to the Weibull theory, the tensile strength T_1 having volume (V_1) is given in terms of the reference strength T_0 and reference volume V_0 by:

$$T_1 = T_o \left(\frac{V_o}{V_1} \right)^{\frac{1}{m_o}} \tag{35}$$

where m_0 is the Weibull parameter for the reference set. Using the 40 cm^3 data for the reference set, the Weibull fit is shown in Figure 3.17. Obviously the data do not support the Weibull interpretation and, in fact, no significant size effect is indicated. Brazilian testing of LDB granite (Nowakowski, 1984) produced some very confusing data (Figure 3.18). The strength initially drops with increasing size from the smallest sample size to the next three sizes which are quite close. The strength then increases again as size increases further. Newman and Bennett (1990) have done several Brazilian tests using various sizes of sandstone specimens and their data also show very little size effect.

The experimental evidence described above would tend to support the conclusion that size itself does not affect strength as much as stress gradients. Varying the stress gradients by changing the loading conditions can induce great changes in strength values. Varying the size of the rock specimens in the Brazilian test often produces very little change in strength and quite often produces conflicting data from one test series to another. For these reasons, the effect of size is often treated by examining the stress gradients produced through varying the size of the specimen.

A general fracture criterion must be capable of including the stress gradient as well as the different modes of failure in tension and compression and the different stages of fracture development. The fracture criterion to be described in the following section includes all of these features.

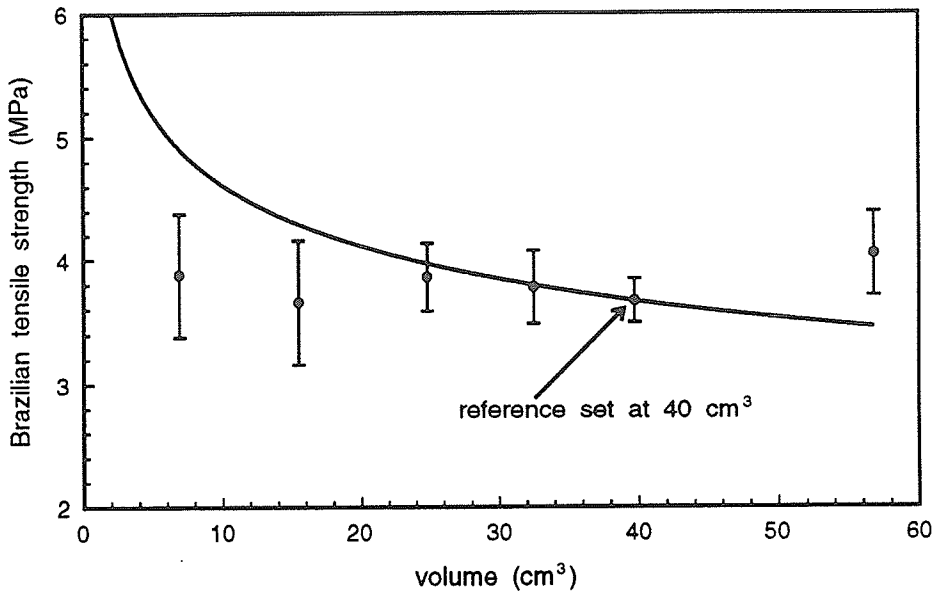

Figure 3.17 Brazilian tension test data for various sample volumes for Tyndallstone (after Weiss, 1984). Very little size effect is shown and Weibull's theory does not fit the data.

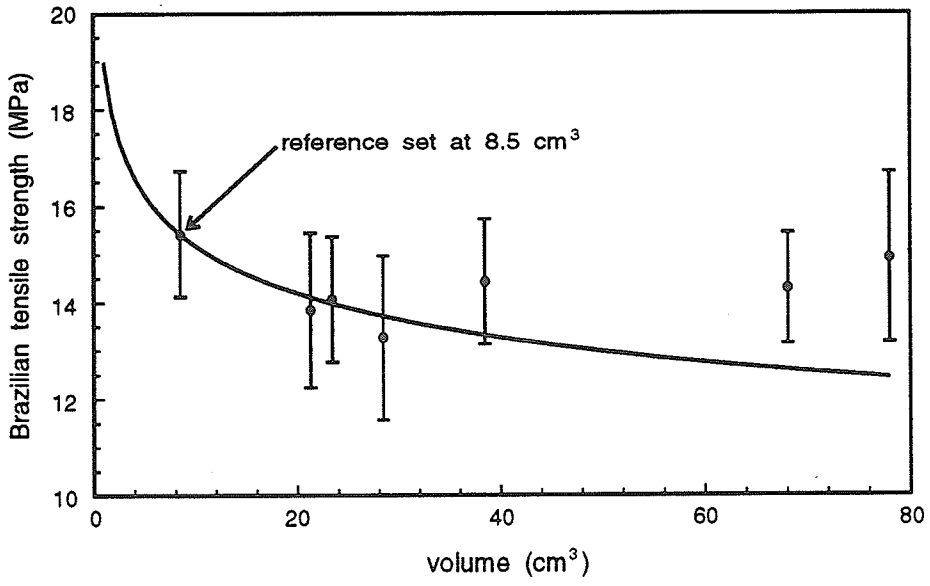

Figure 3.18 Brazilian tension test data for various sample volumes for LDB granite (after Nowakowski, 1984). Weibull's theory does not fit the data.

3.4 Rocker Fracture Criterion

It appears that no single criterion can model both fracture and failure of rock in both tensile and compressive stress fields with sufficient ease and accuracy. It was previously shown that fracture mechanics is difficult to employ for modeling rock fracture, especially in compressive or combined compressive—tensile stress fields. It was also shown that the fracture, process zone and structure size affect the progression of fracturing and the strength of the structure. The usual strength theories cannot accurately predict fracture and cannot handle the size effect. Statistical size-effect theories like Weibull's are not entirely suitable either, especially for compression. This has led to the development of a simple empirical fracture/strength criterion. In the criterion, the Rocker function, representing the fracture strength of the rock, is compared to the average principal stresses through a new formulation for factor of safety (or crack resistance), the unconfined strength ratio (*USR*).

The first step in the development of the fracture criterion is to define when the microcracks initiate, in terms of the maximum and minimum principal stresses. In both compression and tension, the point of crack damage (volumertic reversal) was shown to occur close to the peak strength (Figures 2.3 and 2.9). In compression, depending on the rock type and mineral constituents, microcrack initiation can occur very early in the loading history (Lajtai *et al.*, 1991*a*). LDB granite for example, suffers several different stages of crack initiation (Lajtai, 1982). Cleavage cracking in the weak feldspars occurs at very low loads ($<50\%$ peak strength) while the quartz only begins to crack after about 80% of the peak strength. Volumetric reversal begins at about 80% also, coinciding with

the cracking of the quartz. Yukatake (1989) found that permanent damage begins after a stress of 80-90% of the peak compressive strength for a fine- grained granite from Japan. Saskatchewan potash also has several different cracking stages, depending on the percentages of halite, sylvite and impurities (Duncan, 1990).

Crack initiation (CI), volumetric reversal (VR) or crack damage (CD) and peak strength are all a function of confining pressure. By plotting CI, CD and peak strength versus confining pressure, a pattern is apparent (Figure 3.19). The three sets of data for each rock type follow similar trends and can actually be fitted to a single Rocker function simply by adding an additional scaling factor (A) to equation (24):

$$\sigma_1 = A \cdot C_o \left(1 - \frac{\sigma_3}{T_o}\right)^R \tag{36}$$

A=1 for peak strength, A=CI/100 for crack initiation and A=CD/100 for crack damage where CI and CD are expressed as percentages of peak strength. The same function can therefore be used to monitor the process zone formation (microcrack initiation), fracture propagation, and failure, if the rock is unstable at peak strength.

One disadvantage of this formulation is that it forces all three (initiation, damage and peak strength) curves to unite at the uniaxial tensile strength, implying that all three events take place at the peak tensile strength. It has long been assumed that the points of fracture initiation and peak strength coincide in brittle rocks, especially for tension. Although this is not strictly true, the presently available data in tension do not justify a more complex formulation. Based on fairly limited data for potash, Tyndallstone and LDB granite, CI in tension is at 98%, 60 and 56% while CD is at 100%, 87 and 92%

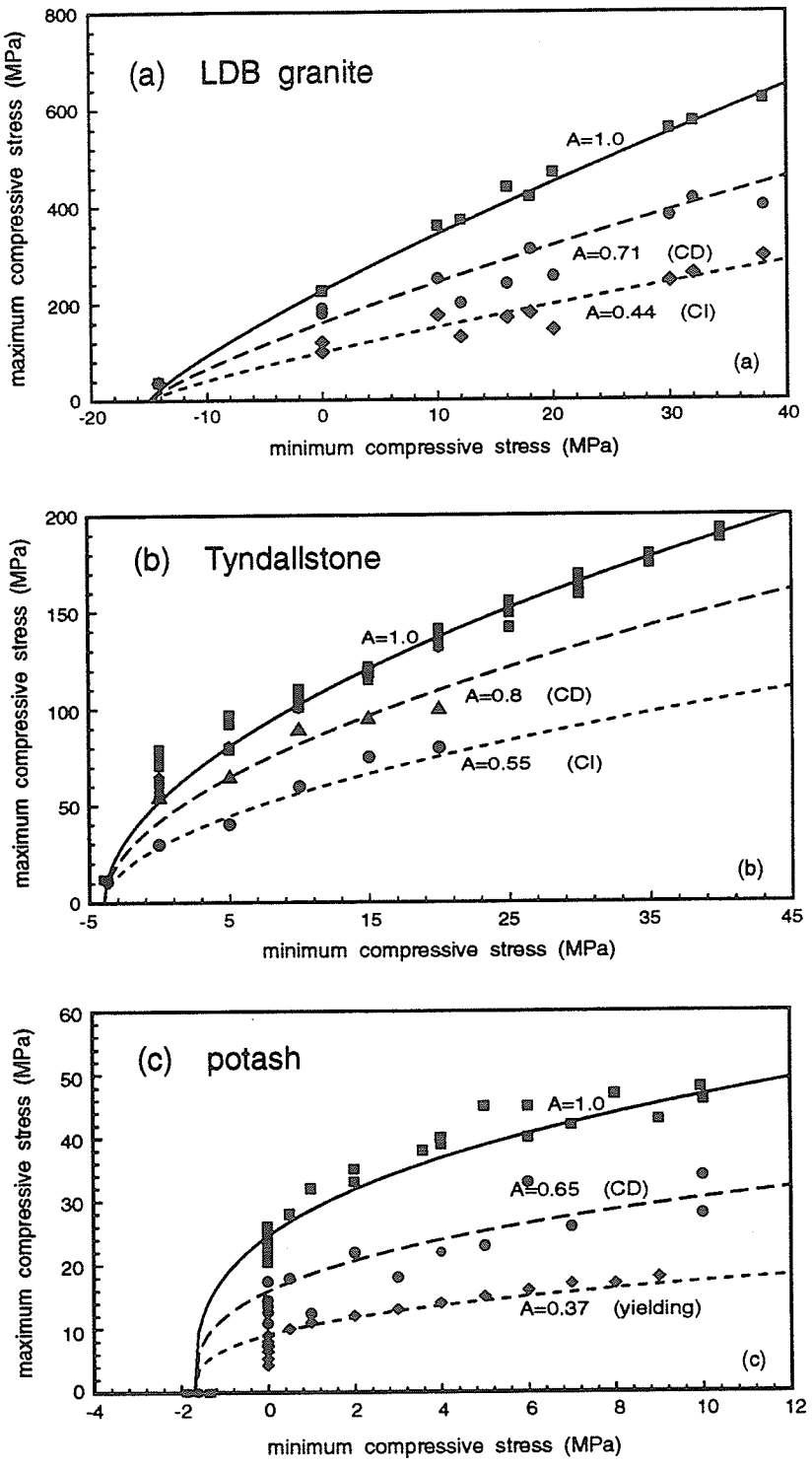

Figure 3.19 Peak strength, volumetric reversal (CD), crack initiation (CI) and yielding vary with increasing confining pressure for (a) LDB granite, (b) Tyndallstone and (c) Saskatchewan potash. The data for each rock type were fitted to a single Rocker function by varying the parameter (A).

respectively. Crack initiation is important in terms of process zone development but the crack damage stress is probably more important in terms of true crack growth; the CD stresses are all quite close to 100% of the respective, peak tensile strengths.

Once the functional form of the fracture parameters in σ_1-σ_3 space is established, the state of stress (σ_1, σ_3) can be compared with available resistance to formulate a safety factor or fracture resistance. Hoek and Brown (1980) for example define the safety factor in terms of the maximum principal stress:

$$Safety\ Factor = \frac{\sigma_{1f}}{\sigma_1} \tag{37}$$

which is valid as long as $\sigma_3 > T_0$. When $\sigma_3 < T_0$, σ_{1f} is no longer defined. This would be the case with any criterion that is based on the $\sigma_1^2 = f(\sigma_3)$ type of parabola. A possible solution for the $\sigma_3 < T_0$ condition is to express the safety factor with respect to the minimum principal stress:

$$Safety\ Factor = \frac{T_o}{\sigma_3} \tag{38}$$

For many applications, the double-criteria approach may be adequate. It has one disadvantage, however: it produces an artificial discontinuity in the safety factor distribution by causing sudden shifts in the value of the safety factor at the point where the fracture criteria change. This can be avoided by redefining the safety factor using a functional form that is valid at every point of σ_3-σ_1 space.

The role of the safety factor is to measure the state of stability; its value should reflect the severity of the state of stress when compared with available resistance. There

is no particular reason why its value should be measured with respect to either the ordinate (σ_1) or the abscissa (σ_3) of the coordinate system. In order to remain close to the generally accepted concept of the safety factor (safe when SF>1, unsafe when SF<1) but at the same time gain the advantage of a single function formulation, the unconfined strength ratio (***USR***) was proposed (Lajtai *et al.*, 1991*a*). For the state of stress, expressed through σ_3 and σ_1, one may define an equivalent strength function that represents the SF$=1$ condition (the strength line includes the state of stress). Since a single point does not fully define a strength parabola, the additional characteristic of the equivalent strength function is that it maintains the uniaxial tensile to compressive strength ratio for the rock (T_o/C_o). For the three-parameter Rocker formulation, the fractional exponent (***R***) is kept the same as well (Figure 3.20). ***USR*** then becomes the ratio between the actual uniaxial compressive strength and the equivalent uniaxial compressive strength (C_{oe}). Because the tensile to compressive strength ratio is kept constant, an expression in terms of the two tensile strengths is equally valid:

$$\textit{Unconfined Strength Ratio} = \frac{C_o}{C_{oe}} = \frac{T_o}{T_{oe}} \qquad (39)$$

For the two-parameter parabolic criteria, such as the Hoek and Brown function, ***USR*** can be expressed explicitly:

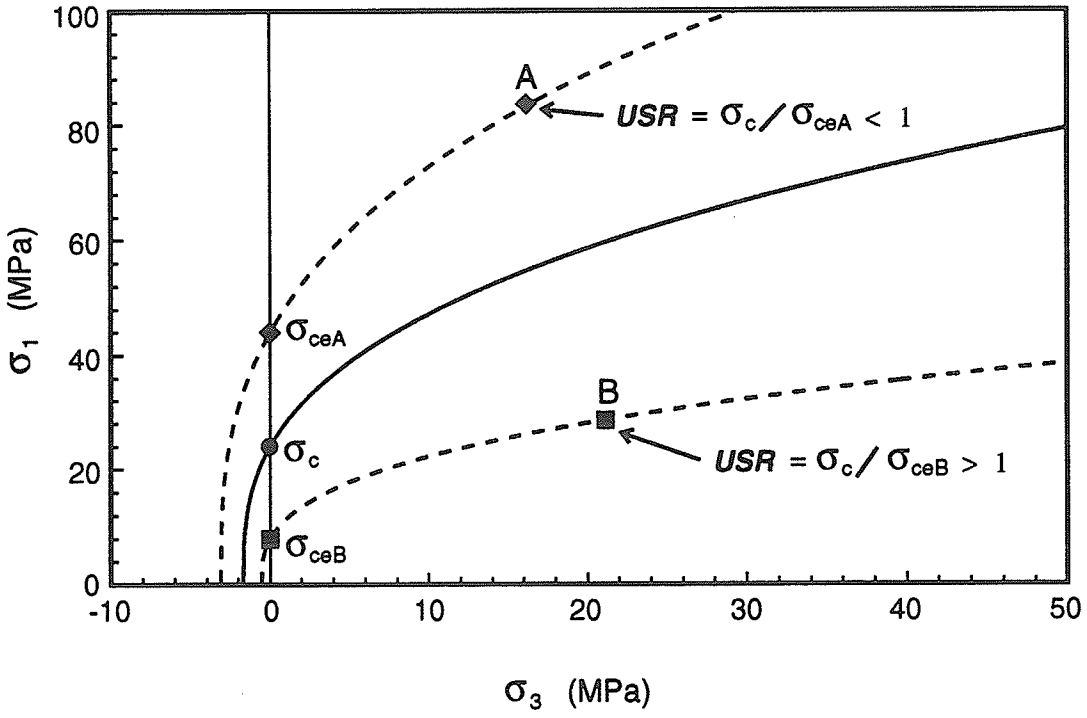

Figure 3.20 ***USR*** is defined by comparing the equivalent Rocker function, which passes through the state of stress, to the actual Rocker function for the rock. ***USR*** is greater than one (safe) if the point is under the curve, otherwise ***USR*** is less than one (unsafe).

$$USR = \frac{2C_o s}{-m\sigma_3 + \left[(m\sigma_3)^2 + 4s(\sigma_1 - \sigma_3)^2\right]^{\frac{1}{2}}} \qquad (40)$$

where the constants m and s are those given in Hoek and Brown (1980). Similarly, for the Rocker function with $R = 0.5$:

$$USR = \frac{T_o}{\frac{\sigma_3}{2} - \left[\left(\frac{\sigma_3}{2}\right)^2 + \left(\frac{\sigma_1 T_o}{C_o}\right)^2\right]^{0.5}} \qquad (41)$$

For R not equal to 0.5, USR cannot be expressed explicitly. Taking R=0.5 will always give an adequate fit in the tension field, *i.e.*, between the anchor points of T_0 and C_0, where the strength curve is uncertain. Larger errors (a poorer fit) may result at higher confining pressures, however. If a general solution is required for any fractional exponent, a numerical solution has been implemented in several computer codes (Lajtai *et al.*, 1991*a*).

The parameter s in the Hoek and Brown formulation of rock mass strength is intended to be a scaling parameter ($s<1$). By including this fractional factor in the definition of strength, the strength of the intact rock ($s=1$) can be scaled to a level that is thought to be more appropriate for the rock mass. This scaling factor is not included in the Rocker function for the simple reason that a similar effect can always be achieved by scaling down the strength parameters, C_0 and T_0 as done by Sheory *et al.* (1989), or by using the fractional parameter A.

Another method of representing crack resistance or crack potential is to find the perpendicular distance from the appropriate fracture curve to the point representing the state of stress. A point outside the CI curve has a cracking potential greater than zero indicating cracking occurs while points inside the curve have cracking potentials less than zero, meaning no crack initiation occurs.

If the state of stress is known, the minimum or perpendicular distance (Figure 3.21) can be found by differentiating the distance term:

$$CP = \sqrt{\left(\frac{\sigma_3}{C_o} - x\right)^2 + \left(\frac{\sigma_1}{C_o} - y\right)^2} \tag{42}$$

where

$$y = \left(1 - \frac{x}{T_o}\right)^R \qquad \textit{Rocker function} \tag{43}$$

Thus CP is

$$CP = \sqrt{\left(\frac{\sigma_3}{C_o} - x\right) + \left(\frac{\sigma_1}{C_o} - 1 + \left(\frac{x}{T_o}\right)^R\right)^2} \tag{44}$$

Now differentiating and setting CP to zero, the equation can be written in terms of C_0, T_0 and R which are rock strength parameters, σ_1 and σ_3 which define the state of stress, and x which defines the minimum distance from the state of stress (point) to the curve:

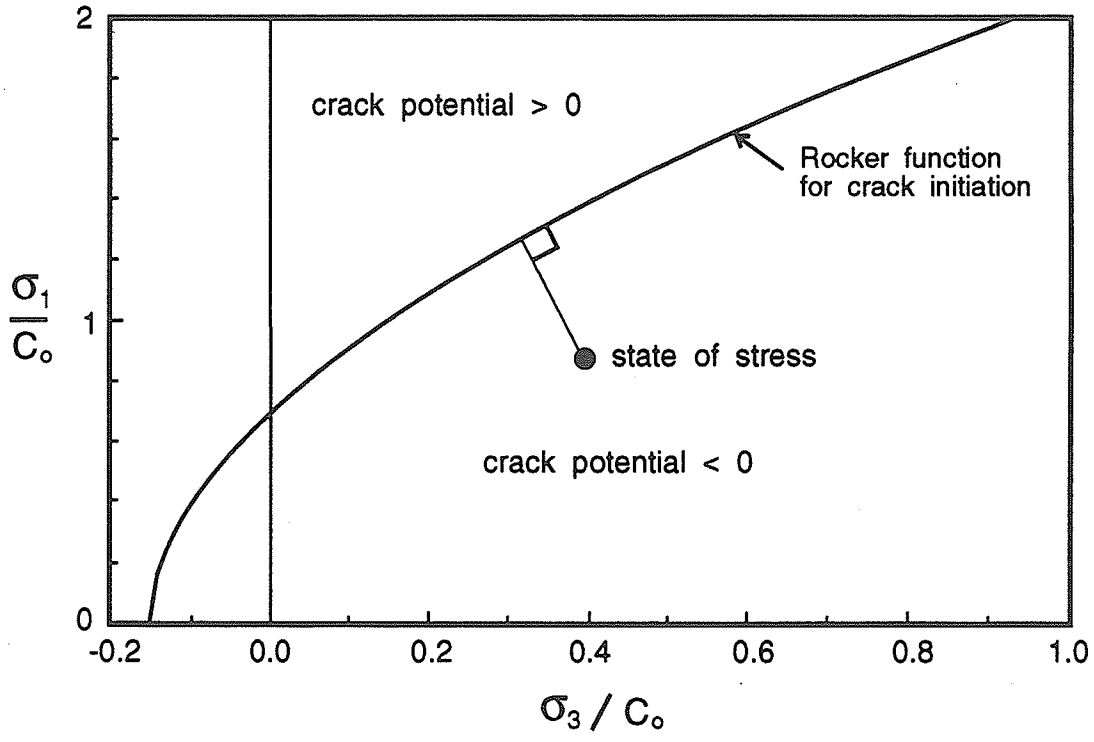

Figure 3.21 Crack potential (*CP*) is taken as the minimum distance between the state of stress and the appropriate crack resistance function. *CP* is positive (safe) when points are below the curve.

$$\sigma_3 = x + x^{R-1}\left(\frac{R}{T_o^R}\left(\frac{\sigma_1}{C_o} - 1\right) + x^R \frac{R}{T_o^{2R}}\right) \tag{45}$$

Numerically solving for x and then using (43) fully defines the minimum distance. Both definitions of fracture resistance give similar results; the ***USR*** definition, which is somewhat simpler, has been used in the following chapters.

For the Rocker fracture criterion to work on the microscopic scale, a suitable microcrack shape must be used. Due to the inability of the flat mathematical crack to disturb the crack parallel stress, especially in compression, the elliptical form first proposed by Inglis (1913) and later used by Griffith (1924) will be used to represent the cracks and pores in rocks. Microscopic examinations of most rocks indicate many irregular shaped flaws and holes in the material. However, the ellipse gives a reasonable approximation and provides a fairly simple analytical solution for the determination of the stress concentrations around these irregular flaws.

The applicability of this fracture criterion was shown by Lajtai *et al.* (1991*a*) and by Carter *et al.* (1992). Lajtai *et al.* (1991) attempted to show how different areas around an elliptical tunnel would be subjected to different amounts or levels of cracking. This is directly related to the concept of process zone size. A simple way of verifying the elliptical crack model is to map the process zone around both a flat mathematical crack and a narrow ellipse when both are subjected to tension perpendicular the major axis. The process zone size around a flat crack was mapped first, using the Rocker fracture criterion along with the stresses from the fracture mechanics formulations. This

zone was then compared to the process zone at the tip of a narrow ellipse using the Inglis (1913) solution for stresses and the same Rocker fracture criterion (Figure 3.22). The process zones are practically identical in size and quite similar in shape.

Using the maximum stress theory allows the process zone radius to be calculated using equation (18); which for LDB granite is 29 mm. Ito and Hayashi (1991) used equation (15) instead which yields a process zone radius of only 5.2 mm for LDB granite, a seemingly more realistic value. Variations in process zone size and shape are difficult to determine and have not been studied in detail. It is known that the process zone size varies significantly with the relative crack size. If the fracture toughness varies with crack size, then smaller cracks should have smaller process zones. In addition to the crack size, process zone size must depend on the specimen or structure size as well as on the specimen and crack geometry.

Schmidt and Lutz (1979) suggested that compressive stresses parallel to a crack have very little effect on the process zone size ahead of the crack. Hillerborg (1985), on the other hand, states that compression parallel to the crack could have a very large effect on the process zone. In the author's opinion compression affects not only the process zone but also the crack itself as the compressive stress parallel to the crack induces propagation and dilatation of the crack. By modeling the crack as a narrow ellipse rather than a flat mathematical crack, the effect of compression parallel to the crack can be seen on the process zone size around the crack tip (Figure 3.23).

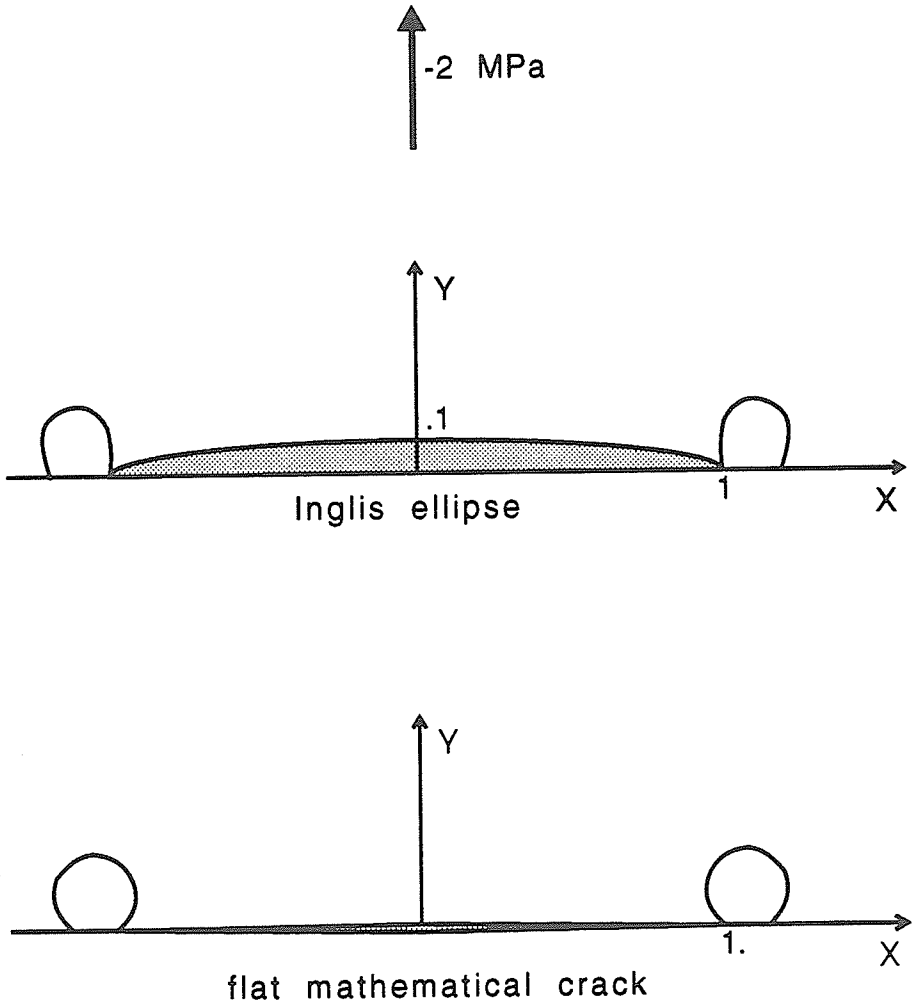

Figure 3.22 The process zones in tension for the flat mathematical crack and the Inglis ellipse are very similar, when using the same "yield" criteria.

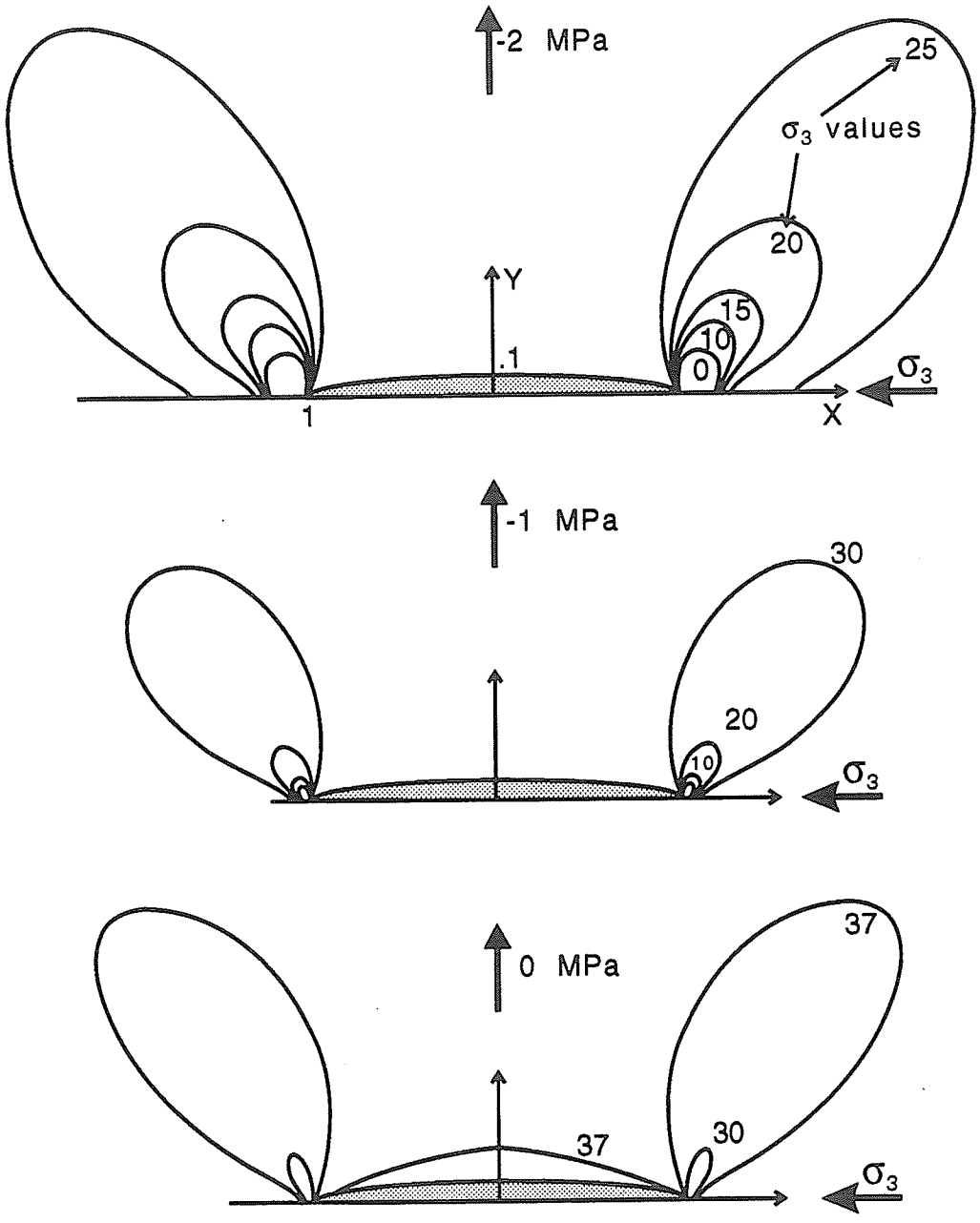

Figure 3.23 By varying the compressive stress parallel to the crack (major axis of the ellipse), the process zone can be altered. The Rocker function and the USR criterion were used as the yield function. The flat mathematical crack would not be influenced by this compressive stress. The values of the compressive stress are shown beside the process zones.

Using the finite-width elliptical cavity and Inglis's solution for the stress distribution generates a different problem, however. A compressive stress parallel to the major axis of the ellipse produces a tensile circumferential stress at the tip of the ellipse equal in magnitude to the applied stress. This stress is independent of the ellipse size. Consequently, the elliptical crack would propagate indefinitely once the stress reached a critical value. This does not occur in compression, the cracks are very stable and require an ever-increasing load to propagate them further. For this reason, the stress averaging concept was proposed (Lajtai, 1971).

Stress-averaging is similar to the point-stress criterion proposed by Nuismer and Whitney (1975) for composite materials. The point-stress model was used with some success by Nuismer and Lavor (1978) and Ito and Hayashi (1991). In this model, cracking is assumed to occur when the stress at a finite distance away from the crack tip reaches a critical value (Figure 3.24). This is similar to the concept of stress averaging, where stresses must reach a critical value over a finite distance or area ahead of the crack tip for cracking to occur.

The area of stress averaging can also be directly related to the process zone. The basic idea behind stress-averaging and the point stress criterion is that the material suffers microcracking prior to true fracture (or failure). Microcracking leads to a redistribution of stress and strain away from the area of high stress concentration. In non-linear fracture mechanics, true cracking is assumed to occur when the crack opening displacement associated with the process zone material reaches a critical value. If the process zone serves to dissipate the stress at the crack tip, then true cracking can only

occur when the average stress, over a finite distance or area, reaches a critical value. The concept and the need for stress-averaging in interpreting fracture will be supported by the physical experiments that will be described next.

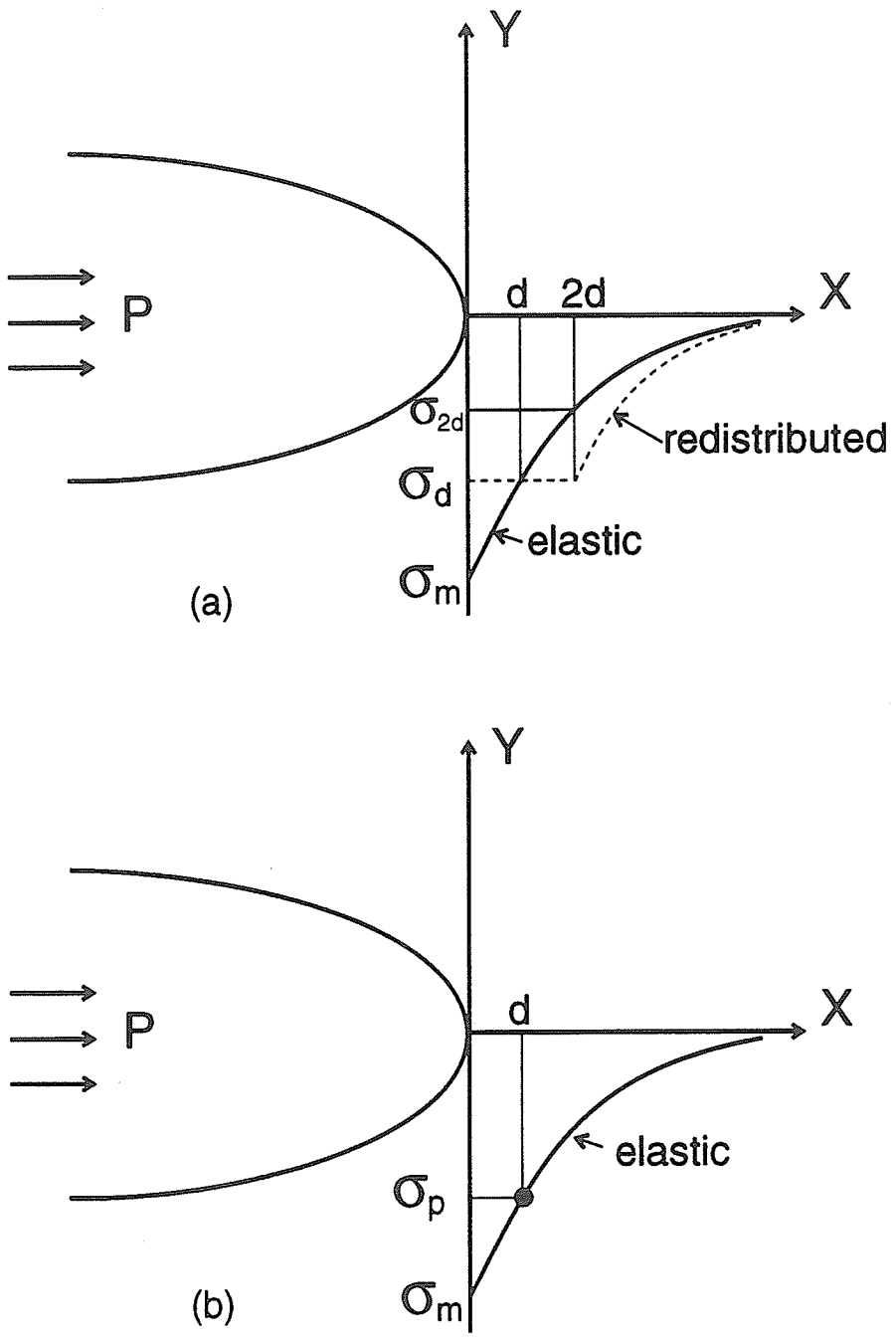

Figure 3.24 Comparison between the concept of (a) stress averaging and (b) the point-stress criterion. The average stress over a distance 2d, is σ_d, defined for point d. The actual stress at distance, d, is given by σ_p. Depending on the distance and gradient, the two values may be close.

4 MODELING SIZE-DEPENDENT FRACTURE AROUND CIRCULAR CAVITIES

4.0 Introduction

The development of a general fracture criterion for both tensile and compressive stress fields was the first step toward modeling fractures around underground openings. The fact that size or stress-gradient dependency can also be included in this criterion, by using the average stresses, makes it even more applicable to studying fracture around cavities in rock. The next step is to examine the fracture pattern around simple excavation shapes and to determine the effect of the cavity size on the fracture process.

Testing for the influence of holes on the strength of materials has a long tradition. The problem is relevant in two areas of concern for rock mechanics: a) flaws at the microscopic scale and b) mine openings (megascopic scale). Neither size is convenient in model testing and therefore both are usually evaluated using macroscopic models. The main difference between the two cases is the influence of the size, or more accurately, the stress gradients around the cavities. In the past, there have been several physical model studies performed on blocks of rock, plaster, and glass which have been related to studies of both microscopic flaws and actual mine openings.

In 1965, Hoek (see Hoek and Brown,1980) tested a block of chert under biaxial loading conditions with a circular hole cut in the center of the block. Hoek and Brown (1980) described the fracture sequence which is depicted in Figure 4.1. Vertical tension cracks first open up in the crown and invert and extend almost instantly to a length of

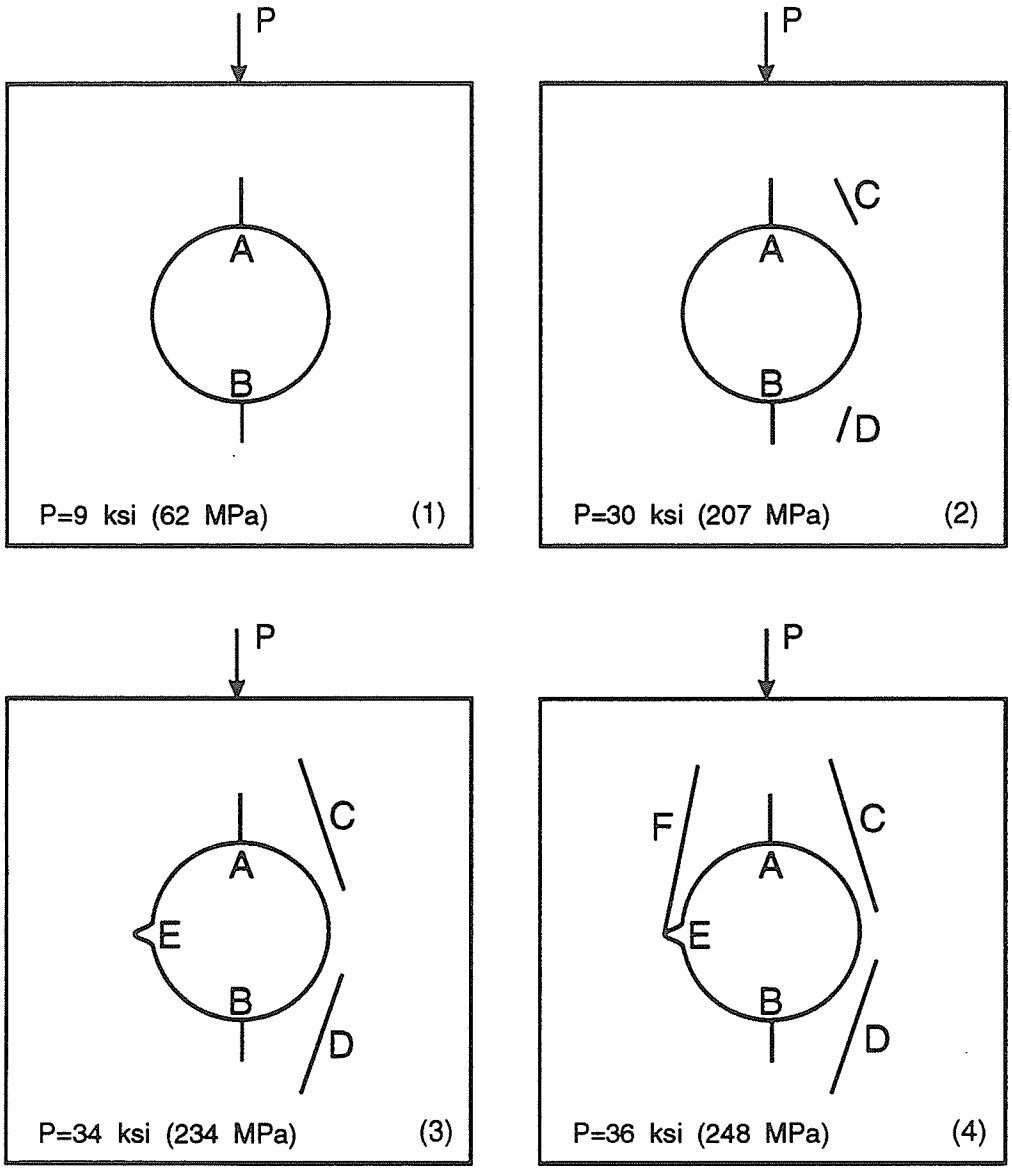

Figure 4.1 Fracture sequence around a circular cavity in chert subjected to an increasing vertical compressive stress (after Hoek and Brown, 1980).

about one third of the cavity diameter (A & B). The cracks stop and remain stable under increasing load. This is followed by another set of extension fractures occurring both above and below the crown and invert lines respectively, on both sides of the hole but remote to the tunnel perimeter (C & D). These secondary or remote fractures propagate in the direction of the compressive stress trajectories and extend away from and towards the hole. They are called extension fractures because they form in a region of moderate tensile stress, insufficient to cause tensile fracturing alone, and moderate compressive stress which drives the cracking process. The next stage of fracturing involves sidewall fractures which form on both sides of the tunnel where large compressive stresses exist (E). The block collapses when the remote cracks join the sidewall fractures (F).

Another study was performed using Plaster-of-Paris blocks containing circular cavities under various loading conditions (Nesetova and Lajtai, 1973; Lajtai and Lajtai, 1975). The fracture pattern was observed visually (Figure 4.2) and the following fracture types were identified: primary tension (1), normal shear (2), inclined shear (3), and secondary tension (4 & 5). The primary tension cracks occur first and start at the points of tensile stress concentration, the crown and invert centers. This is followed by crushing of material in the sidewalls. The crushed material initially extends in a narrow zone perpendicular to σ_1 which is called a normal shear fracture. Later, as the granulate zone expands, inclined shear fractures develop. Secondary tensile fractures occur last and cause the collapse of the cavity. By adding a confining pressure, the influence of the extension (primary and remote) fractures is diminished and the collapse process is dominated by crushing and shear fracture at the compressive stress concentrations. It

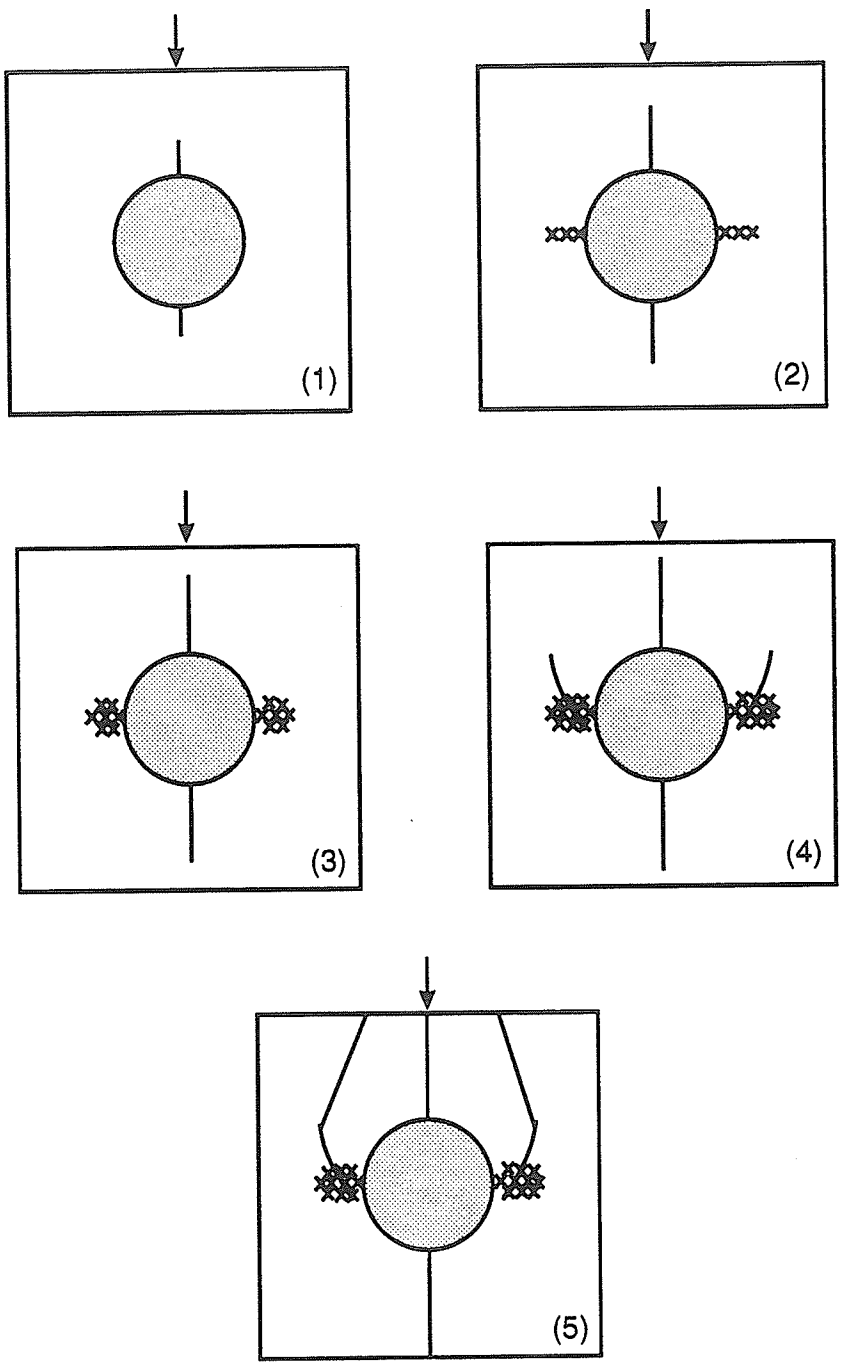

Figure 4.2 Fracture sequence around a circular cavity in Plaster-of-Paris subjected to an increasing vertical compressive stress (after Lajtai and Lajtai, 1975). The x's indicate shearing and crushing at the springlines.

should be noted that plaster is different from most rocks; it has a relatively low compressive to tensile strength ratio (5 compared to 18 for LDB granite). This could be the reason that extensive crushing at the compressive stress concentrations precedes the formation of remote fractures.

Gay (1976) completed tests on blocks of quartzite and sandstone. These blocks of rocks had circular and rectangular shaped holes cut in them and were subjected to uniaxial and biaxial loads. In general the fractures were described to develop as follows: (1) during initial loading, tension cracks formed at the center of the crown and invert and spalling occurred at the springlines at the same load; (2) as the load increased, larger inclined cracks grew, dipping at 60-80° towards the rock in front of the opening and with time formed domical cracks above the hole (Figure 4.3); (3) at very high loads, new vertical or steeply dipping inward cracks formed, followed by shear movement on these cracks and eventual collapse of material into the hole.

Another study involving plaster models was undertaken by Gonano (1974) who performed polyaxial tests on blocks with several sizes of circular and square central cavities. These tests were used to determine the size effect of the cavity on fracture initiation. Only primary and sidewall fractures were observed due to the polyaxial loading system which obscured all but the interior of the cavity. The effect of size on the initiation stress for these two fractures (Figure 4.4) was attributed to the stress gradients around the opening. Smaller cavities showed a higher initiation stress due to the higher stress gradients.

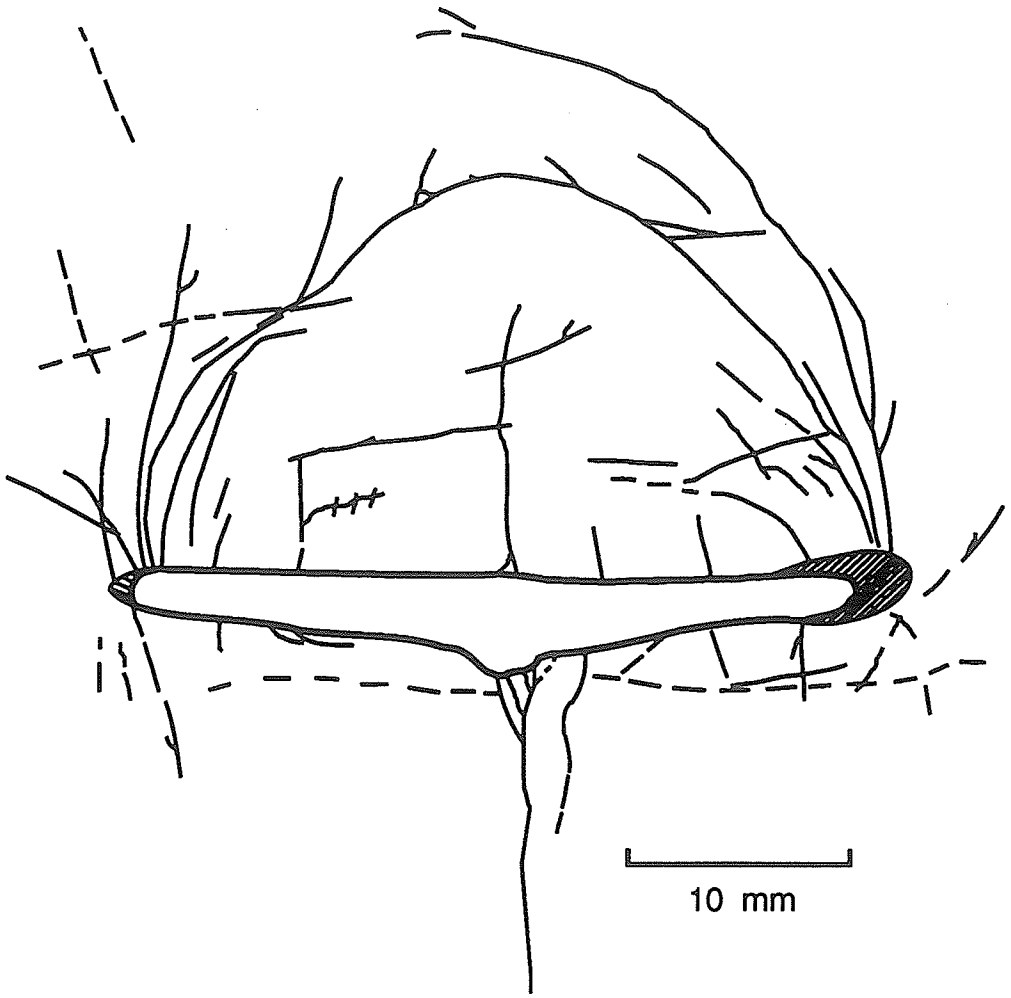

Figure 4.3 Pattern of fracturing around a long, narrow, rectangular shaped opening in sandstone subjected to a high vertical compressive stress (after Gay, 1976). Note how the "remote" fractures join to form a dome over the cavity and the central primary crack is stable beneath this dome.

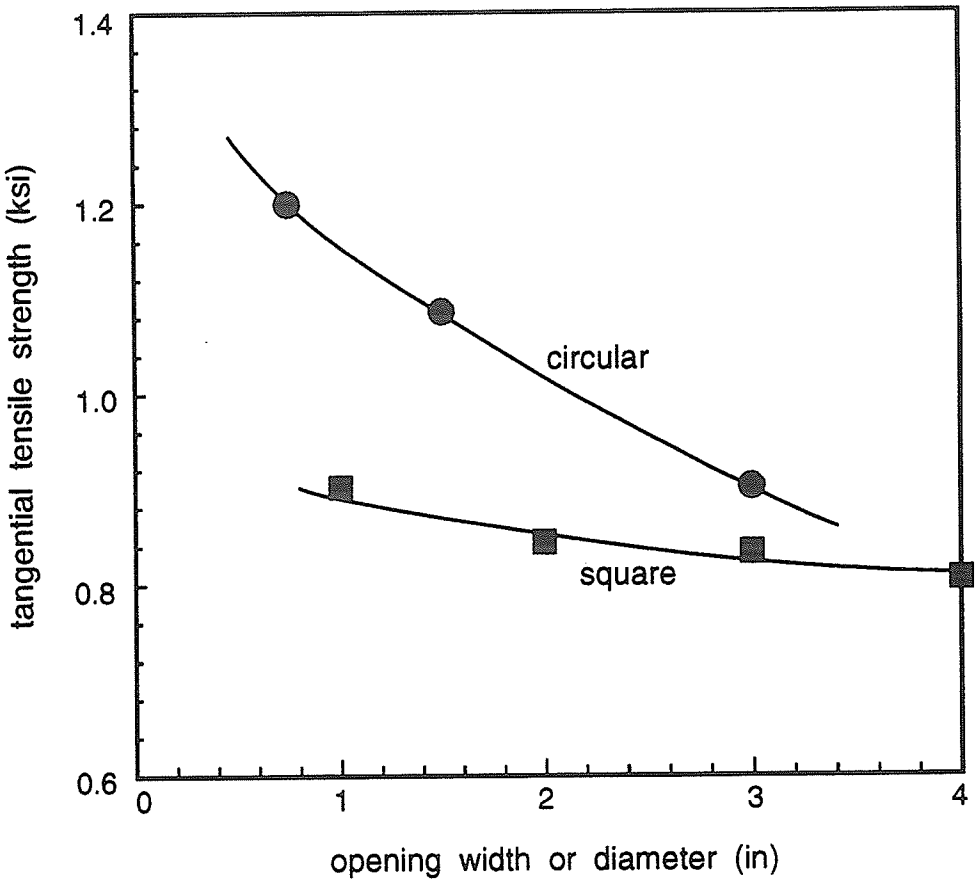

Figure 4.4 Fracture initiation stress depends on cavity size as well as cavity shape. As the cavity size increases, the fracture initiation stress decreases (after Gonano, 1974).

More recent interest into the process of fracture around cavities has evolved from studies of well-bore breakouts (Ewy and Cook, 1990; Haimson and Herrick, 1989; Guenot, 1989; Kaiser and Maloney, 1987; Zoback *et al.*, 1985). These studies involve tests on thick walled cylinders of rock with both internal and external pressure applied. This type of testing generally produces compressive stresses around the entire hole, meaning that no primary fracture occurs unless the internal pressure is high, resembling a hydro-fracturing test. Failure of the rock cylinders results from sidewall type fractures which includes successive extensional spalling fractures (Ewy *et al.*, 1987) and shear fractures (Zoback *et al.*, 1985). It was suggested that the occurrence of both types of fracture depends on the tensile to compressive strength ratio of the rock, the constitutive material behavior (Vardoulakis, 1984) and the stresses (Ewy and Cook, 1990).

Renewed interest into the fracture process around cavities has also come from more detailed studies of fractures in mines and in underground, nuclear waste storage sites. In particular, Atomic Energy of Canada's (AECL) underground research site near Lac du Bonnet, Manitoba has initiated a number of studies (Martin, 1990; Martin and Christiansson, 1991).

4.1 Physical Models Using Lac Du Bonnet Granite

In addition to the above studies, research has also been conducted at the University of Manitoba into the general fracture process and specifically into the fracture mechanism around underground cavities in LDB granite. As part of this program, a block of granite with a 36-mm circular hole cut through it was subjected to uniaxial

loading (Babulic, 1985). The results from this test were repeated utilizing additional strain gauges to improve the detection of the cracks (Carter *et al.*, 1991*b*). At a uniaxial load of 16 MPa, which is close to the Brazilian tensile strength of 14 MPa, vertical tension cracks formed in the center of the crown and invert (Figure 4.5). The primary cracks had propagated to a length of 43 mm at a 135 MPa load and remained essentially stable, only growing about 4 mm more as the load was increased to the final load of 157 MPa.

Following the formation of the vertical primary tension cracks, remote extension cracks formed at a load of 119 MPa. The quoted values of 16 and 119 MPa are averages of 2 and 4 observations respectively. The remote cracks formed above and below the crown and invert lines and extended away from and towards the opening (Figure 4.5). The remote fractures were not a single crack but consisted of a whole zone of parallel to sub-parallel fractures and microfractures. The next stage after remote crack initiation was sidewall fracturing or spalling which started at an average load of 126 MPa (Figure 4.6). At the end of the test (157 MPa), the remote fractures were seen to extend into the compressive fracture zone at the sidewall. From the earlier granite test model (Babulic, 1985), the uniaxial loads for primary, remote and sidewall fracture initiation were 15, 85 and over 100 MPa respectively.

Three more physical model tests were conducted on LDB granite by the author, one with the same size hole as the previous two tests, one with a smaller and one with a larger hole size (Table 4.1). The blocks were cut and ground into prismatic rectangular shapes with central circular holes. They were tested in a 600 000-lb loading frame under

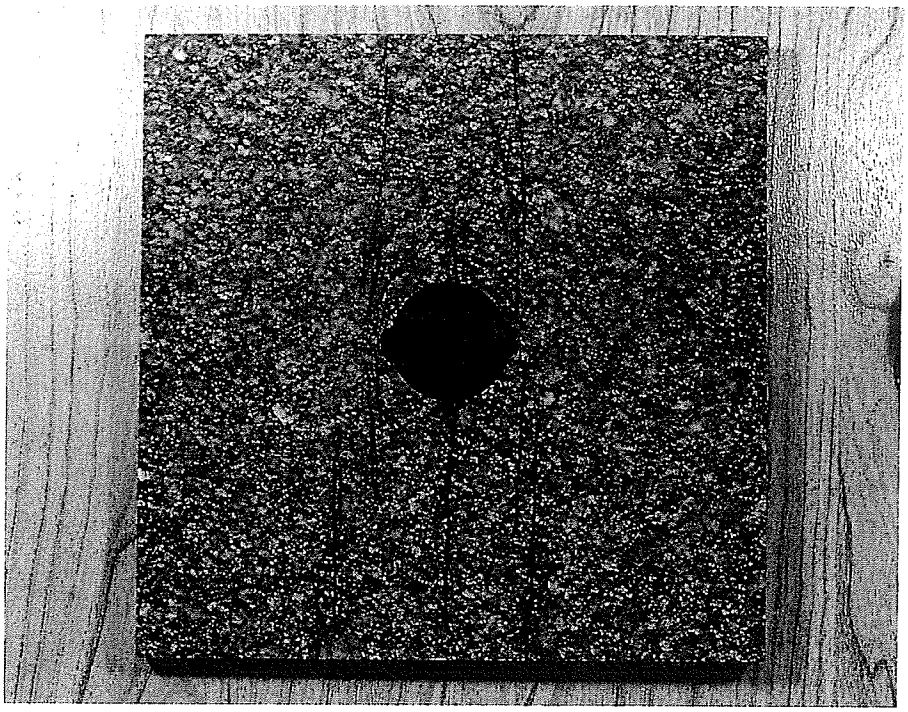

Figure 4.5 Photograph of a granite block with a central, circular cavity. The block was loaded to a peak, vertical, uniaxial compressive stress of 157 MPa. The primary fractures emanating from the crown and invert, the four sets of remote fractures and the compressional fractures at the springlines have been traced with ink for clarity. The block is 200 mm high (from Carter *et al.*, 1991*b*).

Figure 4.6 Close-up (10X) of the compressive fractures at the springlines. These fractures are extensional and the thin slabs of material, which form between the cracks, buckle or shear and "pop" out of the sidewall (from Carter *et al.*, 1991*b*).

uniaxial compression with the load applied through teflon covered steel loading platens. All three blocks were fully strain gauged (Figure 4.7) with the locations predetermined from an earlier study (Carter *et al.*, 1991*b*). One of the blocks had 35 gauges applied to its surface, including five crack propagation gauges. The crack propagation gauges (Figure 4.8) were intended to monitor the growth of the fracture but failed to give very satisfactory results; primary cracks were seen under two of the gauges before the gauges registered any change and two of the gauges were bypassed completely. The strains were measured with a Hewlett-Packard data acquisition system.

One of the main reasons for doing the physical model tests was to determine the effect of opening size on fracturing around cavities. Fracturing around small model openings is simple to monitor. It is much more difficult to examine fracturing around real underground openings. By examining the size effect in model tests, it should be possible to extend the results to actual underground openings. Thus far, all the model tests have been very similar, with uniaxial compressive loading and only a single cavity size. The fracture pattern has also been similar.

Table 4.1. Lac du Bonnet granite test block dimensions and circular cavity sizes.

Series #	# blocks tested	Block Dimensions (mm) H	W	D	Hole Radius (mm)
1	1	201	208	130	13.5
Petuhkov	1	200	200	60	18.0
Babulic	1	145	145	82	18.6
2	1	252	191	88	19.0
3	1	297	304	131	30.5

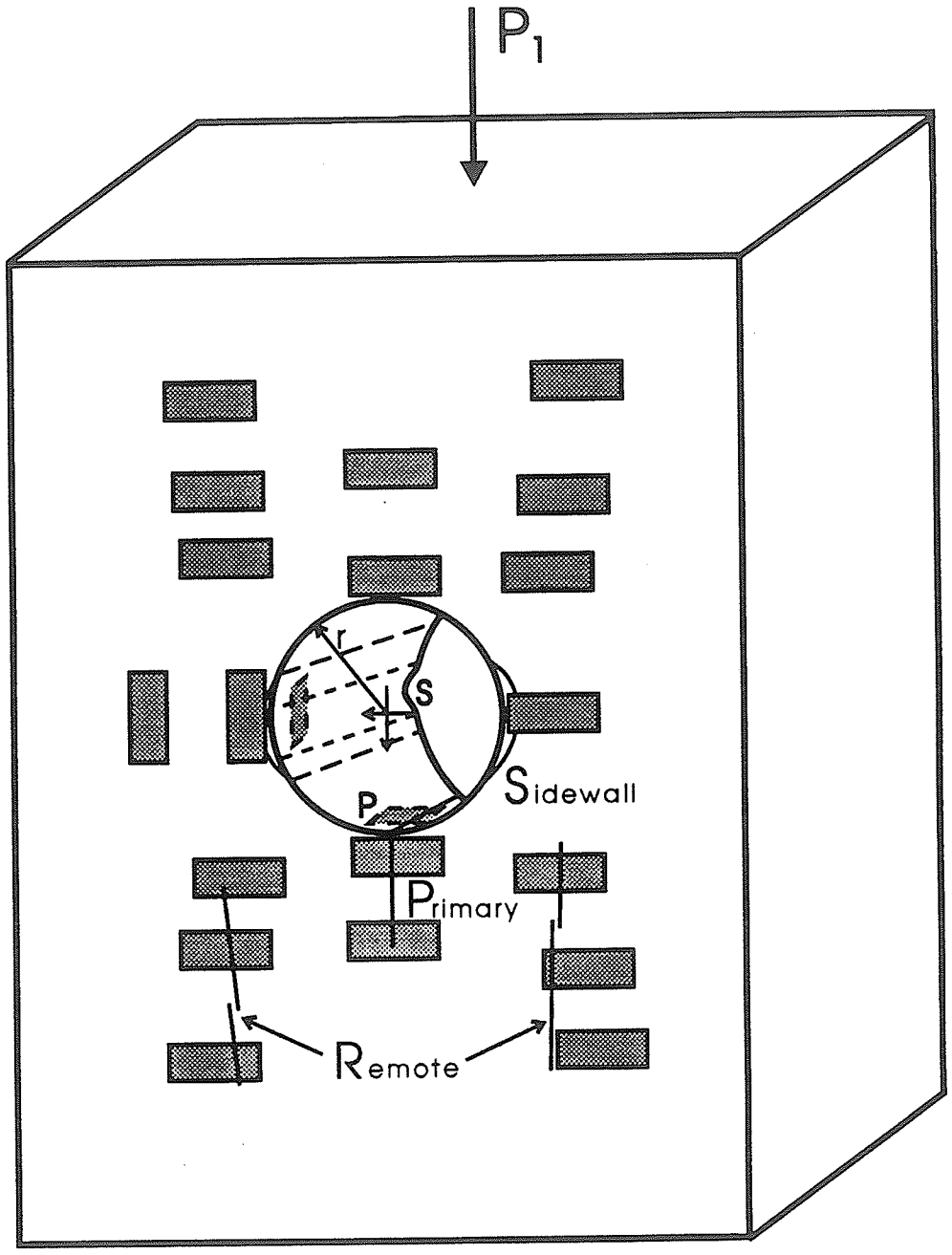

Figure 4.7 A typical pattern of strain gauge placement for the granite test blocks. A typical fracture pattern is shown in the lower half of the figure.

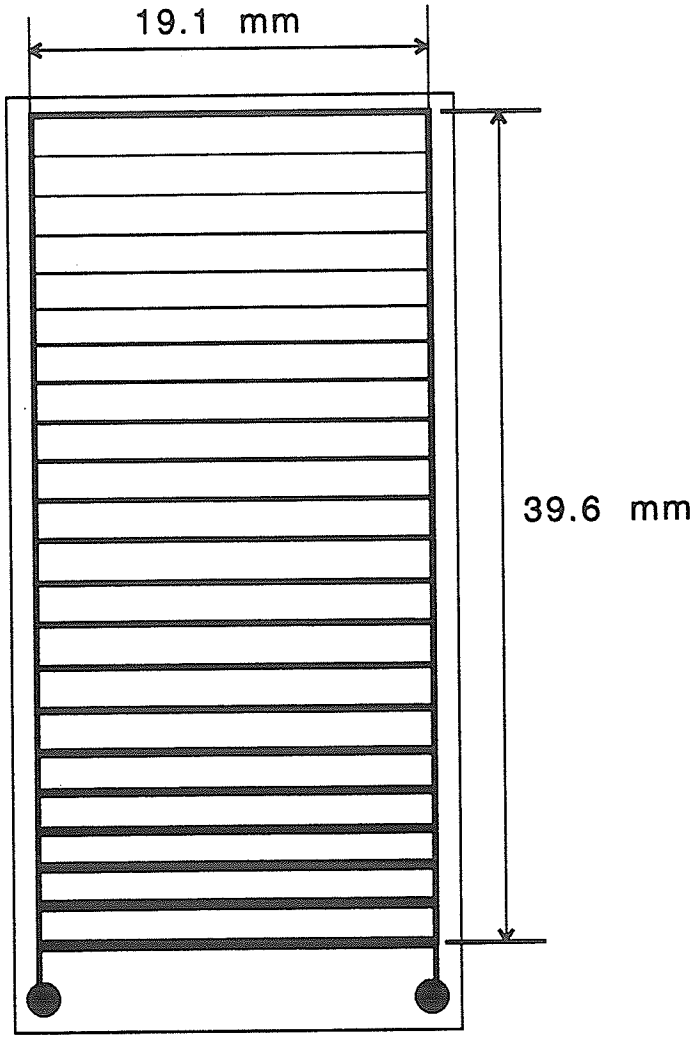

Figure 4.8 A crack propagation gauge. As the crack grows, it should progressively break the thin metal strands. This causes the resistance, which can be measured, to change.

Fracture initiation and propagation in the latter three tests follow the pattern established in the first two tests. Primary fractures initiate first, followed by remote fractures, leading to the sidewall or compressive fractures. Fracture initiation (Table 4.2) is indicated by the strain gauges. Figure 4.9 shows a typical set of stress—strain curves from one of the granite test blocks with gauges placed in the primary (P), remote (R) and sidewall (S) locations. Fracture initiation is usually indicated by the first noticeable break in the stress—strain curve. The initiation of fractures at the described stress has also been verified visually with the aid of a microscope trained on the specimen.

Table 4.2. Fracture initiation stresses for various hole sizes in LDB Granite.

Series #	Hole Radius (mm)	Primary (MPa)	Remote (MPa)	Side Wall (MPa)
1	13.5	37.0	100+	----
Petuhkov	18.0	16.0	119	126
Babulic	18.6	15.0	85	100+
2	19.0	19.7	90	108
3	30.5	14.5	64	----

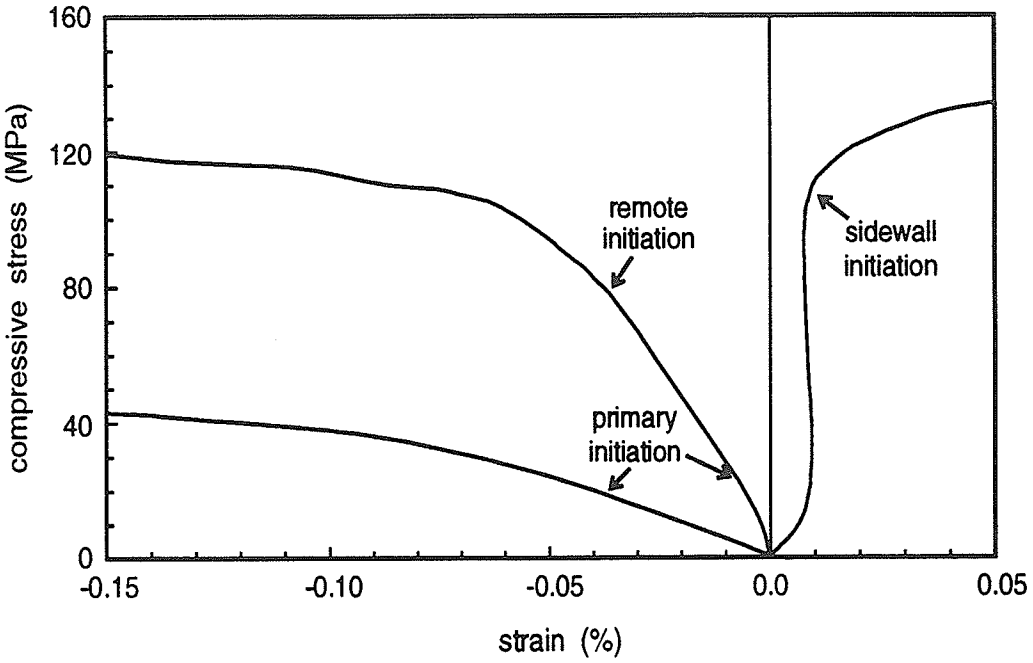

Figure 4.9 Typical set of stress—strain curves for LDB granite models. The fracture initiation stress for primary and remote fractures is taken at the point where the curves deviate from their initial linear path. The remote curve often shows a change at the time of primary initiation depending on the position of the gauge. The sidewall fracture initiation is commonly given by the inner, axial gauge and thus the initiation is difficult to determine. The abrupt change in the curve generally indicates cracking has begun and visual evidence aids the process.

Figures 4.10 a and b show the mean fracture initiation stress versus the tunnel radius for primary and remote fracturing respectively. The points represent the mean values and the error bar represents one standard deviation from the mean. The numbers below the bars indicate the number of gauges providing information on fracture initiation for that particular hole size. Although the displayed data points represent mean values, the averaging refers only to the reports of the strain gauges. Since fracture nucleation occurs at a point or over a very limited area, microstructural variations can cause substantial changes in the measured nucleation loads and this effect has not been evaluated.

4.2 Physical Models Using Tyndall Limestone

In addition to the three model tests on LDB granite, twenty-five model tests were performed using the weaker (second) set of Tyndall limestone specimens. The blocks were cut and ground into prismatic rectangular shapes with central circular holes. Nine different hole sizes were used (Table 4.3). All blocks were tested in uniaxial compression using a 250 000-lb SoilTest loading frame with stress and strain data recorded by a Hewlett-Packard data acquisition system.

The blocks were kept large enough to observe all the fractures and to allow these fractures to propagate. The block width was generally kept over five times the tunnel diameter in an attempt to eliminate edge effects. Elasticity theory (Timoshenko and Goodier, 1970) shows that the stress disturbance caused by the presence of a hole is negligible beyond a distance of four times the tunnel radius from the edge of the hole.

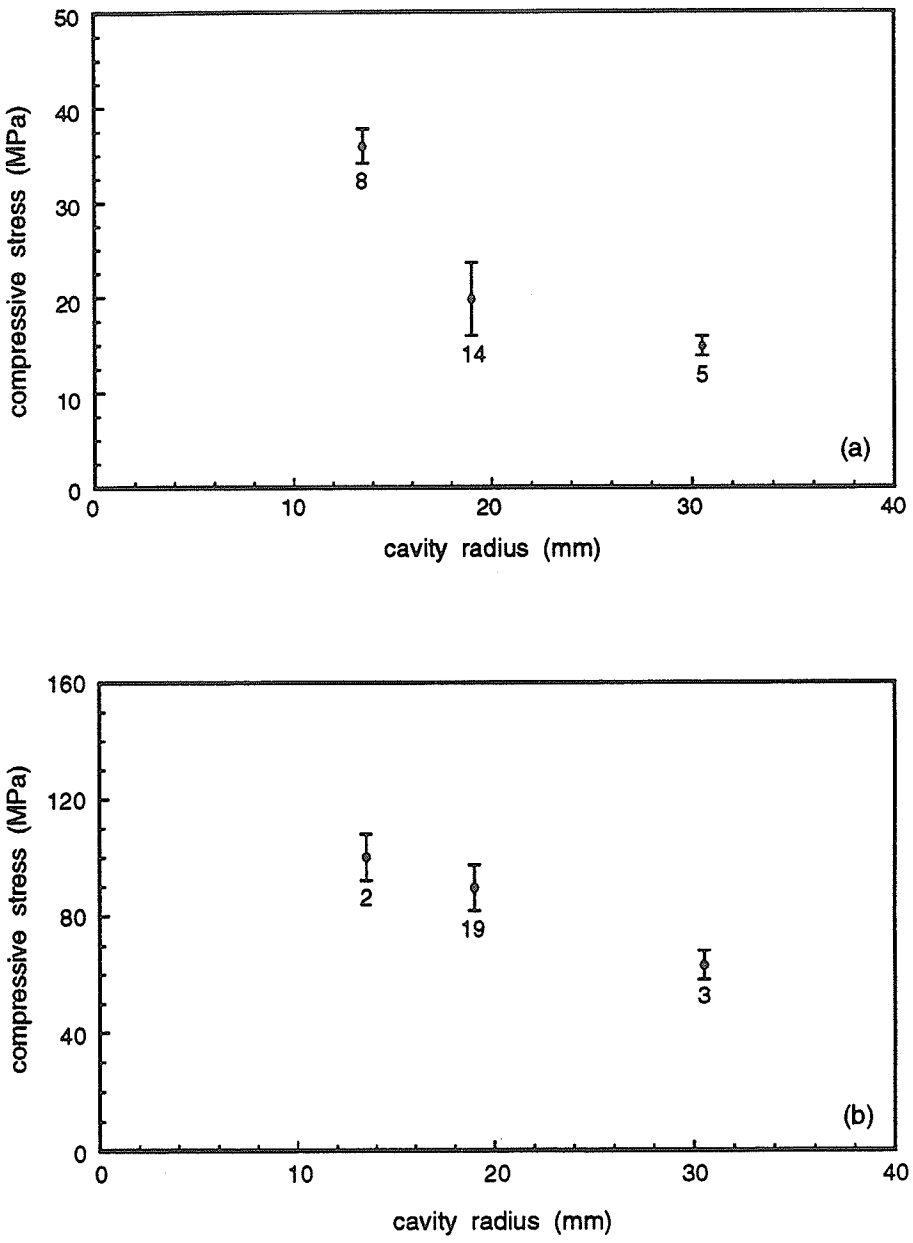

Figure 4.10 Fracture initiation stress decreases with increasing cavity size for LDB granite for both (a) primary and (b) remote fractures. The points represent mean values while the associated error bar indicates one standard deviation and the number of gauges is shown below the bar.

Table 4.3. Tyndall limestone test block dimensions and circular cavity sizes.

Series #	# blocks tested	Block Dimensions (mm) H	W	D	Hole Radius (mm)
1	2	102	86	33	1.6
2	3	152	89	84	3.2
3	3	222	117	84	6.4
4	3	230	140	84	10.7
5	3	238	140	84	13.9
6	3	241	160	89	16.3
7	4	248	197	89	19.5
8	3	254	254	89	25.0
9	1	305	305	89	31.0

The thickness was maintained more or less constant for most of the series to keep the blocks from buckling and to limit some of the edge effects. The load was applied through steel loading platens with teflon sheets between the rock and the metal platens.

Strain gauges were positioned to indicate the initiation of primary, remote and sidewall fracturing. A typical arrangement consisted of gauges inside the hole at the crown, invert and springlines and on the face of the block adjacent to the gauges inside the hole. Gauges were also placed in the four remote positions to indicate remote fracture initiation. These gauges were placed at positions 60° from the horizontal and 1.25 times the tunnel radius from the edge of the tunnel (Figure 4.11). One of the blocks from series #7 was fitted with additional strain gauges on the face in order to obtain the strain distributions away from the hole.

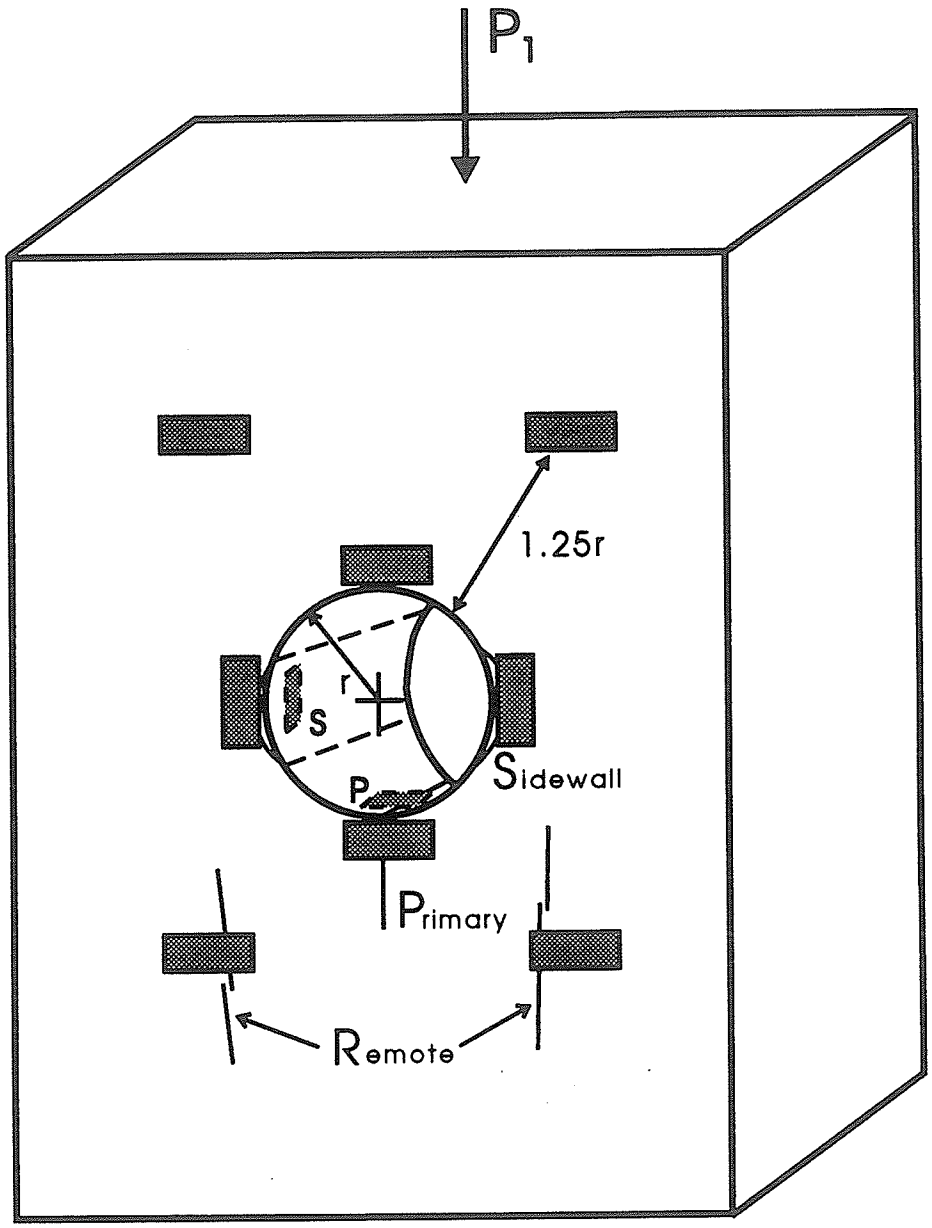

Figure 4.11 Typical position of strain gauges for the Tyndallstone models. Fewer gauges were used for individual blocks but more blocks were tested at each cavity size compared to the granite modeling.

Fracture initiation (Table 4.4) is indicated by the strain gauges. Figure 4.12 shows a typical set of stress-strain curves from one of the Tyndallstone models with gauges placed in the primary (P), remote (R) and sidewall (S) locations. As with the granite, fracture initiation is indicated by the abrupt change in the curvature of the stress-strain diagram. The initiation of fractures at the described stress has also been verified visually with the aid of a microscope trained on the specimen. All the limestone models exhibited the same general pattern of fracturing seen in the other model tests, regardless of the opening size. However, the size affected the initiation stresses, just as it did for granite.

Table 4.4. Fracture initiation stresses for various hole sizes in Tyndall limestone.

Series #	Hole Radius (mm)	Primary (MPa)	Remote (MPa)	Side Wall (MPa)	Final Collapse (MPa)
1	1.6	----	----	----	39
2	3.2	15.2	29.1	33.5	36
3	6.4	12.3	23.5	28.2	33
4	10.7	11.0	21.7	26.3	30
5	13.9	9.3	19.5	22.9	26
6	16.3	7.0	16.0	26.2	28
7	19.5	5.5	18.2	25.5	27
8	25.0	5.1	11.7	20.9	26
9	31.0	3.6	14.7	20.5	25

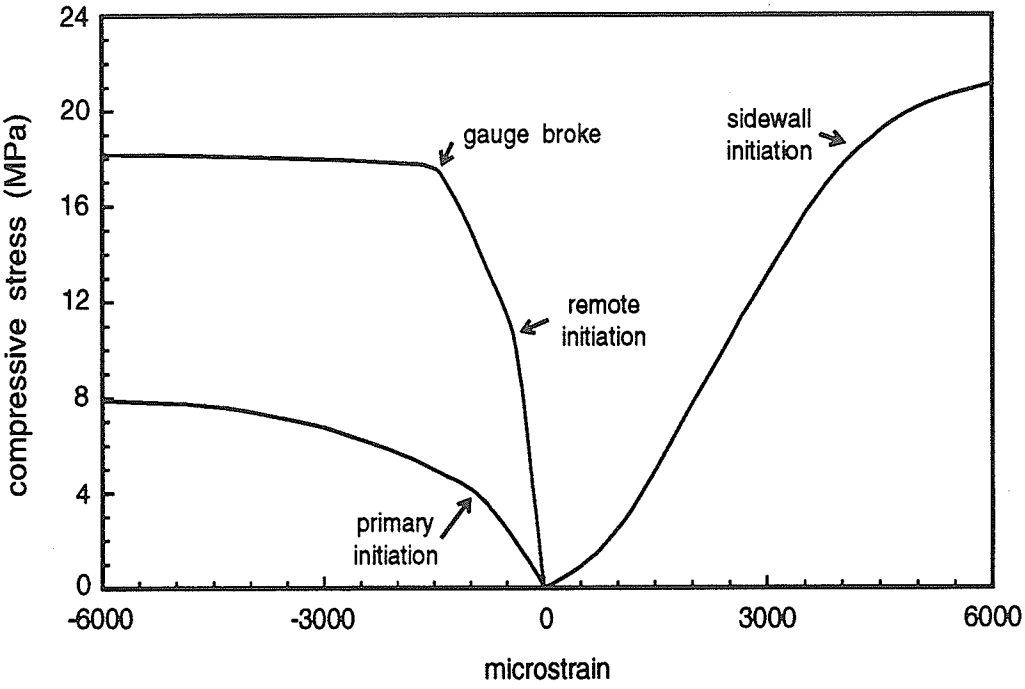

Figure 4.12 Typical set of stress—strain curves for primary, remote and sidewall gauges for Tyndallstone. Fracture initiation is indicated by the change in curvature and aided by visual observation.

Table 4.4 shows no initiation stress for series #1, as the models with the smallest hole could not be properly strain gauged. No fracture was observed during these tests. However, close examination of the failed specimen using the microscope, revealed all three fracture types. In fact, there were fractures everywhere and the failed block resembled a failed uniaxial compression sample with numerous axial cracks existing throughout the block.

Figures 4.13 a, b and c show the mean fracture initiation stress versus the tunnel radius for primary, remote, and sidewall fracturing respectively. The figures are similar to those for granite, with the points representing the mean values, the error bar being one standard deviation and the number below indicating the number of observations. The experimental data for the three fracture types show a similar decreasing trend as the cavity size increases, possibly approaching asymptotes for large hole sizes and appearing to follow an exponential decay curve:

$$P_1 = A\, e^{(B \cdot radius)} + C \tag{46}$$

where P_1 is the axial load and A, B, and C are fitted parameters. This equation was fitted to the experimental data based on a non-linear, least-squares regression routine with a suitable fit determined by the sum of squares of the error (SSE) and the residual plots. This preliminary empirical fitting procedure was done to provide some insight for the later modeling exercises. The exponential function was chosen so that an intercept at r=0 mm and an asymptote for very large hole sizes would be produced. (The granite was not modeled in this manner due to insufficient data.)

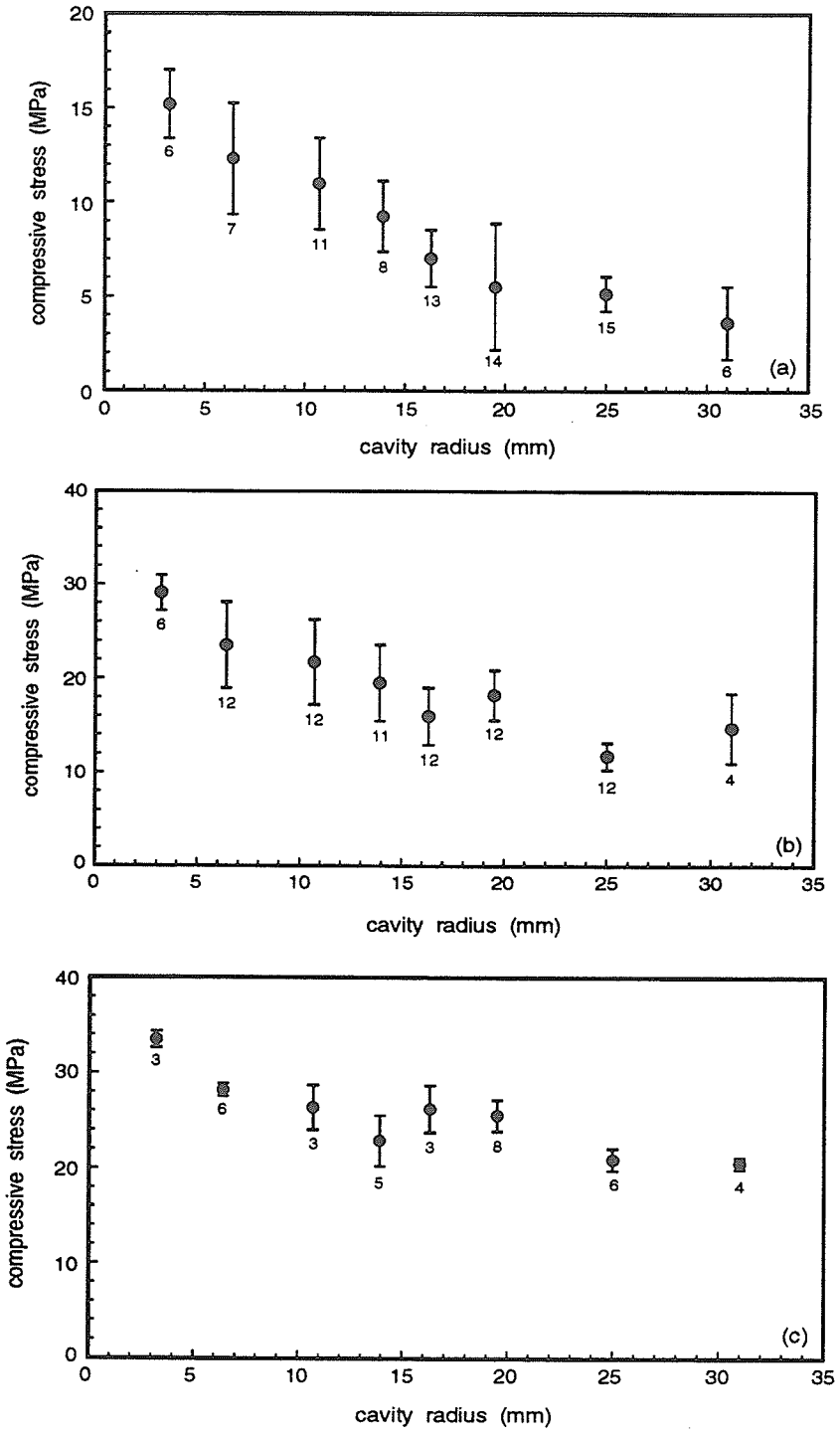

Figure 4.13 Fracture initiation stress decreases with increasing cavity size for Tyndallstone for (a) primary, (b) remote and (c) sidewall fractures. The points represent mean values while the associated error bar indicates one standard deviation and the number of gauges is shown below the bar.

The primary fracture initiation load is related to hole size through the fitted exponential function (Figure 4.14):

$$P_P = 16.9\, e^{-.061\, r} + 1.3 \qquad (47)$$

where P_P is the applied load at initiation in MPa and r is the hole radius in mm. The function gives values of 18.2 MPa for r=0 mm and 1.3 MPa for the asymptote. The primary fracture initiation load for r=0 mm is close to the crack initiation stress for uniaxial compression (26 MPa) and the asymptote at $r = \infty$ is near the tensile strength.

The remote fracture initiation stress also seems to approach an asymptote, showing a decreasing trend with increasing hole size (Figure 4.14). The exponential function which best fits the results is

$$P_R = 22\, e^{-.083\, r} + 11.7 \qquad (48)$$

where P_R is the remote fracture initiation load in MPa. Although P_R for r=0 mm (33.7 MPa) is close to the crack damage stress for uniaxial compression (35.3 MPa), the significance of this and of the asymptote (11.7 MPa) are not obvious.

The sidewall fracture initiation load also decreases with increasing hole size (Figure 4.14) and should theoretically approach an asymptote at one third of the uniaxial compressive strength. The fitted exponential function is

$$P_S = 24\, e^{-.059\, r} + 14.8 \qquad (49)$$

where P_S is the sidewall fracture initiation load in MPa. The asymptote (14.8 MPa) is close to one-third of the uniaxial compressive strength (41 / 3 = 13.7 MPa). The intercept at r=0 mm (38.8 MPa) is just below the uniaxial compressive strength.

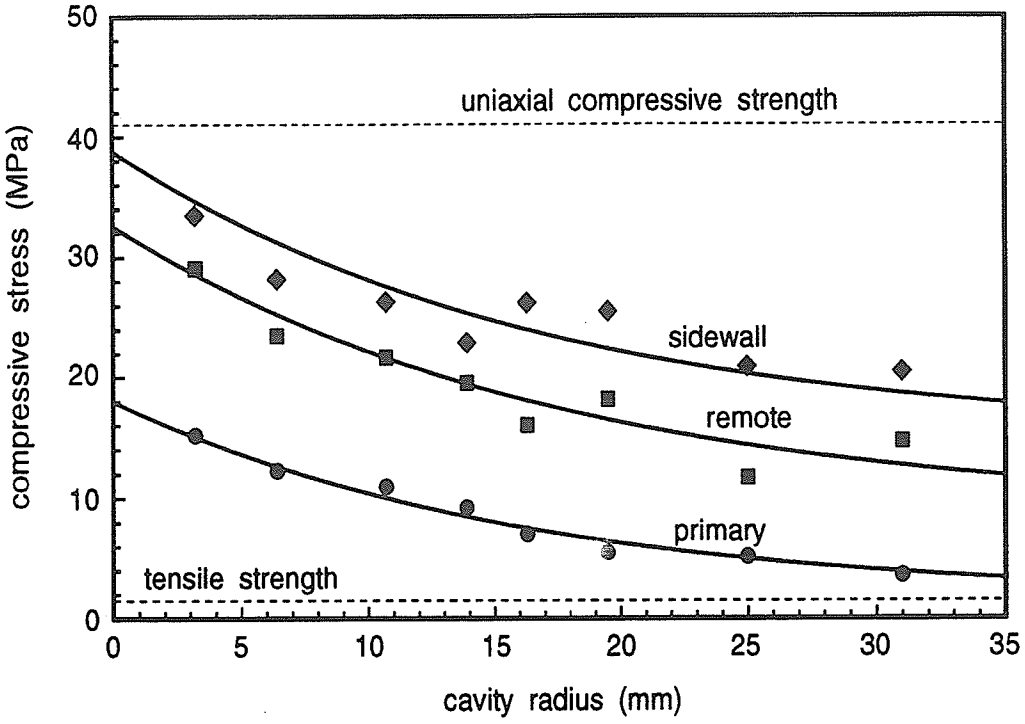

Figure 4.14 The fracture initiation stress decreases with cavity size appearing to follow an exponential decay law with an asymptote at an infinite radius and an intercept for a radius of zero (Tyndallstone).

4.3 Physical Models Using Saskatchewan Potash

To conclude this portion of the modeling exercise, tests on potash blocks were also conducted. One model test using potash (Horning, 1989) was done prior to this study. The potash block was quite large with a central circular hole of 65.5 mm diameter. The results from this test are included with the data from the current study (Table 4.5). Nine other blocks of potash from the Vanscoy mine were prepared and five different central circular hole sizes were used. All blocks were loaded in the 250 000-lb SoilTest loading frame using the same teflon and metal loading platens as were used with the Tyndallstone and granite. As well, all the blocks were instrumented with a pattern of strain gauges similar to that of the Tyndallstone models (Figure 4.11) and the strain was measured by the Hewlett-Packard data acquisition system.

Table 4.5) Saskatchewan potash test block dimensions and circular cavity sizes.

Series #	# blocks tested	Block Dimensions (mm) H	W	D	Hole Radius (mm)
1	2	112	102	50	3.5
2	2	150	110	90	6.8
3	2	225	175	85	13.3
4	2	195	170	80	19.0
5	1	245	245	80	25.0
Horning	1	230	250	120	32.7

The trend in the fracture initiation data (Table 4.6) is similar to that of the other two rock types. The smallest hole size produces the largest fracture initiation stress for all three fracture types and the fracture initiation load decreases as the hole size increases. The occurrence and pattern of fractures is also basically the same: primary, remote and sidewall fractures, initiating in that order. In some cases however, individual sidewall fractures initiated before the remote fractures (Figure 4.16) and, for the smallest cavity size, the remote fractures initiated before the primary. A typical set of stress—strain curves for the primary, remote and sidewall locations gives the fracture initiation stress for the respective fractures (Figure 4.15). For potash, visual verification of fracture initiation, using a low-power microscope, was essential as the stress—strain curves can be very difficult to interpret. Using the stress—strain curves from uniaxial and triaxial compression tests as a guide, the same procedure of distinguishing between yielding and crack initiation was used on the stress—strain curves from the model tests.

Table 4.6) Fracture initiation stresses for various hole sizes in Saskatchewan potash.

Series #	Hole Radius (mm)	Primary (MPa)	Remote (MPa)	Side Wall (MPa)
1	3.5	11.6	10.8	14.0
2	6.8	6.9	9.4	12.0
3	13.3	4.8	9.2	11.0
4	19.0	4.2	8.9	10.5
5	25.0	3.4	6.4	10.0
Horning	32.7	2.5	7.2	9.5

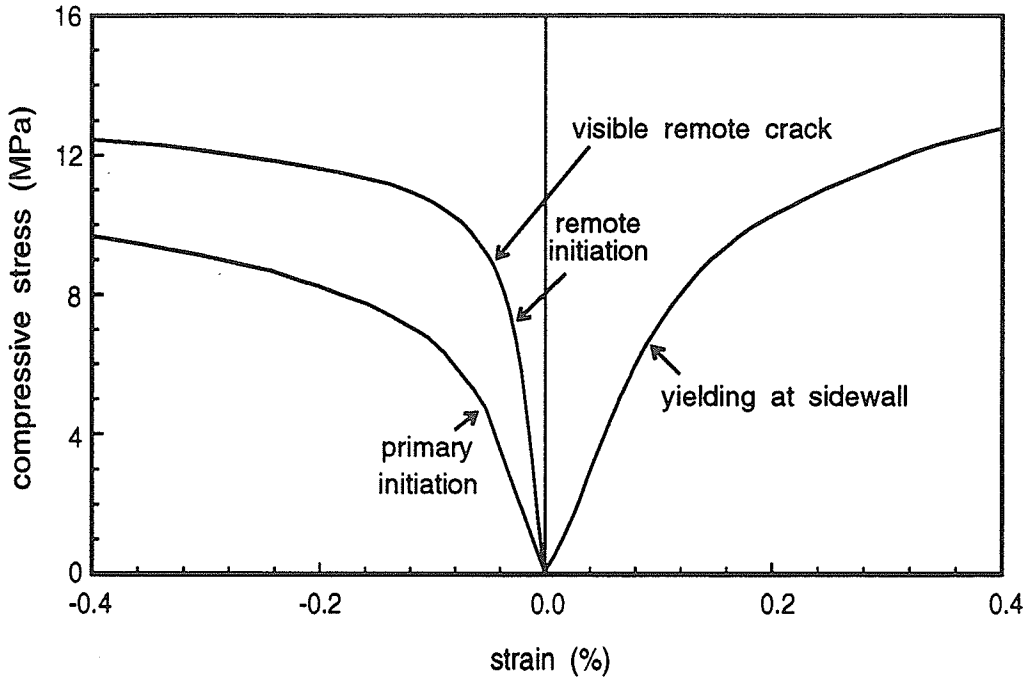

Figure 4.15 Typical set of stress—strain curves for primary, remote and sidewall gauges for potash. Fracture initiation is indicated by the change in curvature and aided by visual observation.

Figures 4.16 a, b and c show the mean fracture initiation stress versus the tunnel radius for primary, remote, and sidewall fracturing respectively. The figures are similar to those of the other two rock types. The experimental data for the three fracture types show a similarly decreasing trend as the cavity size increases, possibly approaching an asymptote for large hole sizes and appear to follow the same exponential law that the other rocks follow (equation 46).

The primary fracture initiation load is related to hole size through the fitted exponential function (Figure 4.17):

$$P_P = 16.3\, e^{-.198\, r} + 3.2 \qquad (50)$$

This function produces values of 19.5 MPa for r=0 mm and 3.2 MPa for the asymptote; the asymptote is slightly higher than the average tensile strength (1.7 MPa).

The remote fracture initiation stress also shows a decreasing trend with increasing hole size (Figure 4.17). The exponential function is:

$$P_R = 6.9\, e^{-.032\, r} + 4.4 \qquad (51)$$

Again, P_R at r=0 mm (11.3 MPa) corresponds well to the permanent damage in uniaxial compression (12.7 MPa) but the significance of this and of the asymptote (4.4 MPa) are still not obvious.

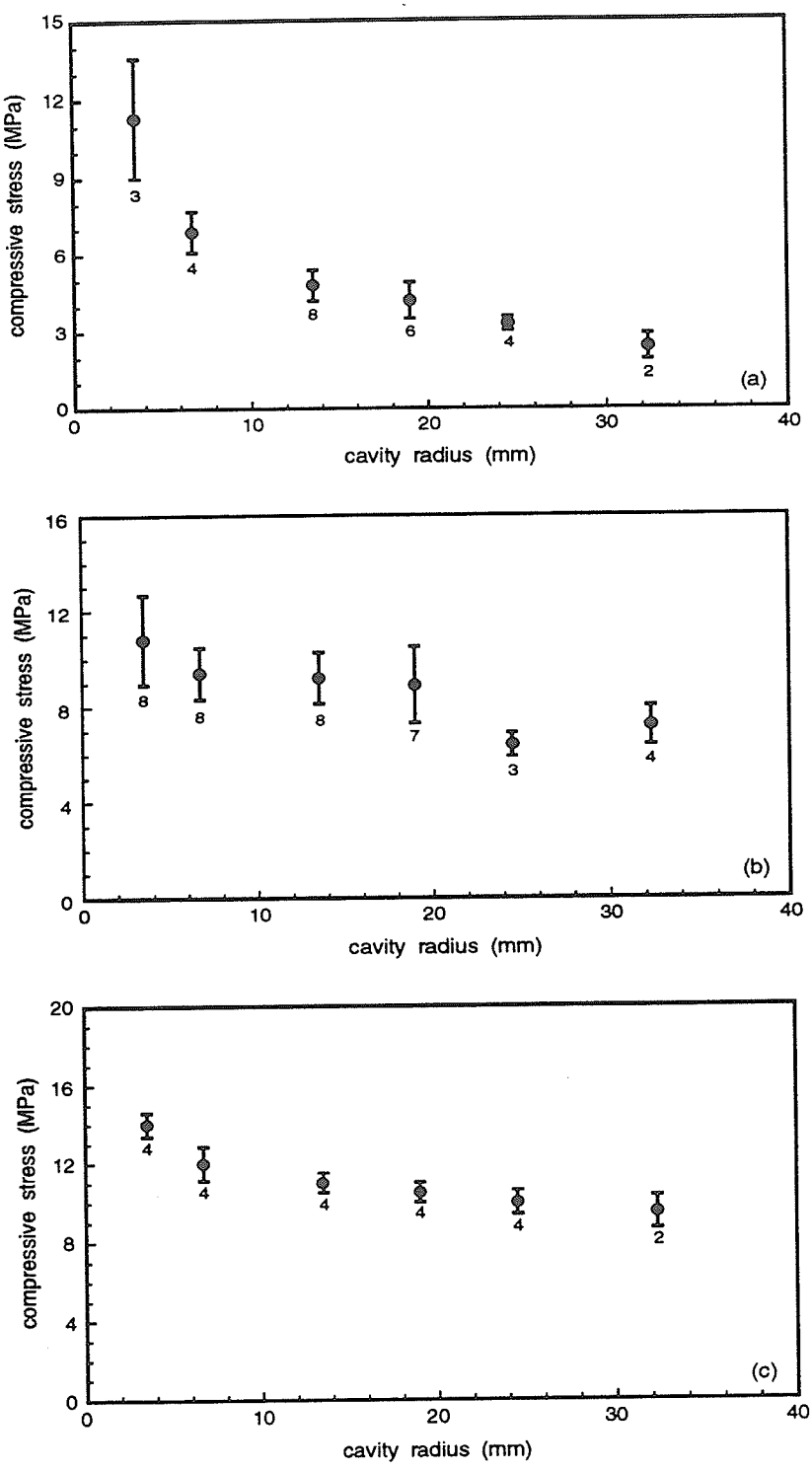

Figure 4.16 Fracture initiation stress decreases with increasing cavity size for potash for (a) primary, (b) remote and (c) sidewall fractures. The points represent mean values while the associated error bar indicates one standard deviation and the number of gauges is shown below the bar.

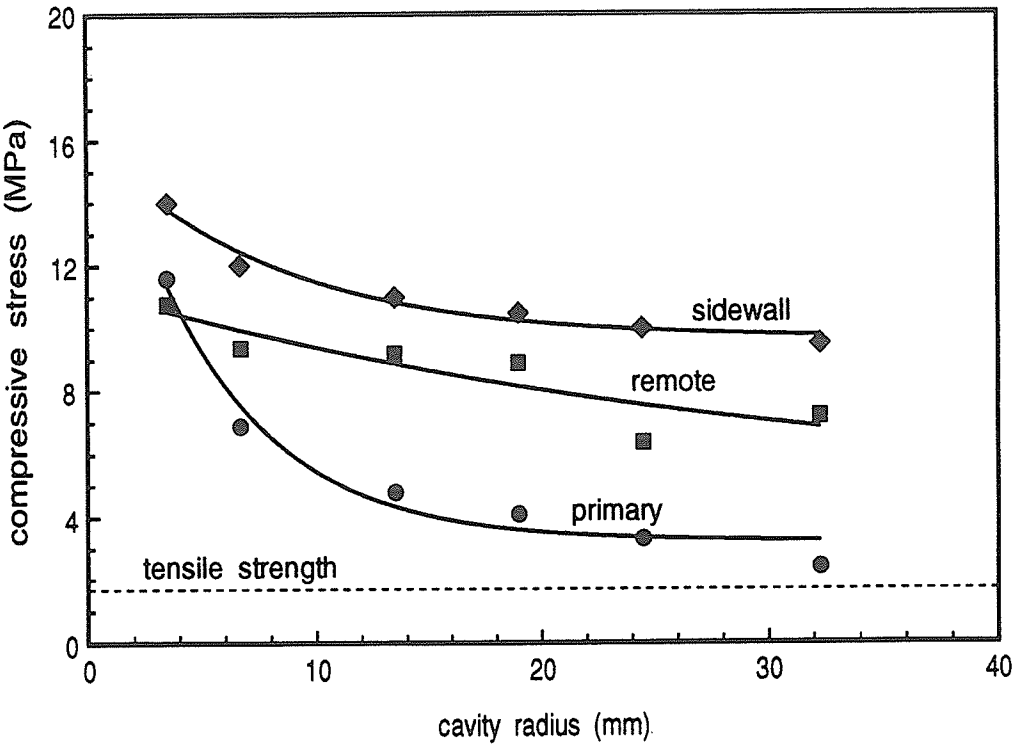

Figure 4.17 The fracture initiation stress decreases with cavity size appearing to follow an exponential decay law with an asymptote at an infinite radius and an intercept for a radius of zero (potash).

The sidewall fracture initiation load also decreases with increasing hole size (Figure 4.17) and should theoretically approach an asymptote at one third of the uniaxial compressive strength. The fitted exponential function is:

$$P_S = 6.5\, e^{-.125\, r} + 9.7 \qquad (52)$$

The determined asymptote (9.7 MPa) is close to one third of the uniaxial compressive strength (8.2 MPa).

4.4 Stress—Strain Distributions and Strength Anomalies

The above data indicate that fracture initiation around excavations in rock is strongly affected by the cavity size. Although, it was recognized quite early that the stress gradients associated with the various hole sizes produced this size effect (Lajtai, 1972, Gonano, 1974), the actual mechanisms involved are still under debate. Theoretical elastic stress and strain distributions around circular cavities were defined many years ago by Kirsch (see Timoshenko and Goodier, 1970). These distributions represent homogeneous, isotropic, elastic conditions and the possibility of measuring comparable distributions around cavities in rock is doubtful. A number of factors may influence these distributions: ductile material response; micro-fracturing—process zone development; inhomogeneities due to the multi-mineral assemblage; etc. Stress or strain transfer may occur due to the non-linear material response, causing a reduction in the stress gradient thereby changing the elastic distributions. If stress or strain transfer does occur, the high gradients associated with small holes would logically dissipate more quickly than the

lower gradients which cover a larger area. This phenomenon would be sufficient to cause some or even all of the observed size effects, as a reduction in local stress means a higher load must be applied to cause fracture.

If any of these factors affect the strain distribution, it should be apparent in the applied stress—measured strain curves and in the strain distribution curves. Therefore, the first set of curves to examine are the stress—strain curves; the simplest of these are the primary curves. The primary region is subjected to essentially uniaxial tension. It was shown in Chapters 2 and 3 that direct uniaxial tension tests on most rocks show some degree of non-linearity prior to reaching peak strength. This is also apparent in the primary stress-strain curves (Figures 4.9, 12 and 15). The non-linearity in the direct tension tests was attributed to microcracking, which could also account for the non-linearity in the primary region.

The second indication of non-linearity is in the strain distribution curves, obtained by plotting the measured strain versus distance from the edge of the hole. Figure 4.18a shows the measured tangential strain ahead of the primary crack path for Tyndallstone along with the theoretical, elastic curve for strain at a point. The three data points are based on six strain gauge measurements from one block, two gauges for each point. The average measured strain does not follow the elastic strain distribution very well. Similar measurements for LDB granite (Figure 4.18b) fit the elastic distribution somewhat better. Potash is unique (Figure 4.18c); strains measured very early in the loading cycle indicate an elastic strain distribution. At higher loads, just prior to primary fracture initiation, the measured strains no longer follow the elastic distribution, especially close to the cavity

perimeter. This is may be due to yielding prior to fracture initiation rather than microcracking and process zone development. Some of the variations in strain may also be caused by differences in mineralogy, and the fact that strain is measured over a finite area rather than at a point.

Strain measurements (distributions) are also available for the sides of the cavity for the Tyndallstone, granite and potash (Figures 4.19 a, b and c). At this location, the data follow elastic theory quite closely although these curves show only the axial strain (tangential strain). Based on simple compression tests, it is possible to have linearly elastic stress—axial strain curves while the lateral strain curves show large non-linearities. There were insufficient data to analyze the results from the lateral gauges, however.

The strains at the crown and invert at the time of primary fracture initiation were measured and can be used to determine the stress, assuming linear elasticity. Table 4.7 shows the applied stress,the measured tensile strain and the calculated tensile stress at the center of the crown and invert for Tyndallstone. The modulus from the direct tension tests (4.2 GPa) is used with the strain at initiation to calculate the tensile stress. Similar data exist for LDB granite (Table 4.8) and for Saskatchewan potash (Table 4.9). For granite the modulus in tension is 44.3 GPa while the modulus in tension for potash is 17.8 GPa (Stimpson and Chen, 1991). There appears to be a trend of decreasing strain and consequently a decreasing initiation stress with increasing hole size for all three rock types (Figures 4.20 a, b and c). There are some variations or anomolies in the measured-strain data (points do not fall on the line) but this is probrably due only to differences in mineralogy.

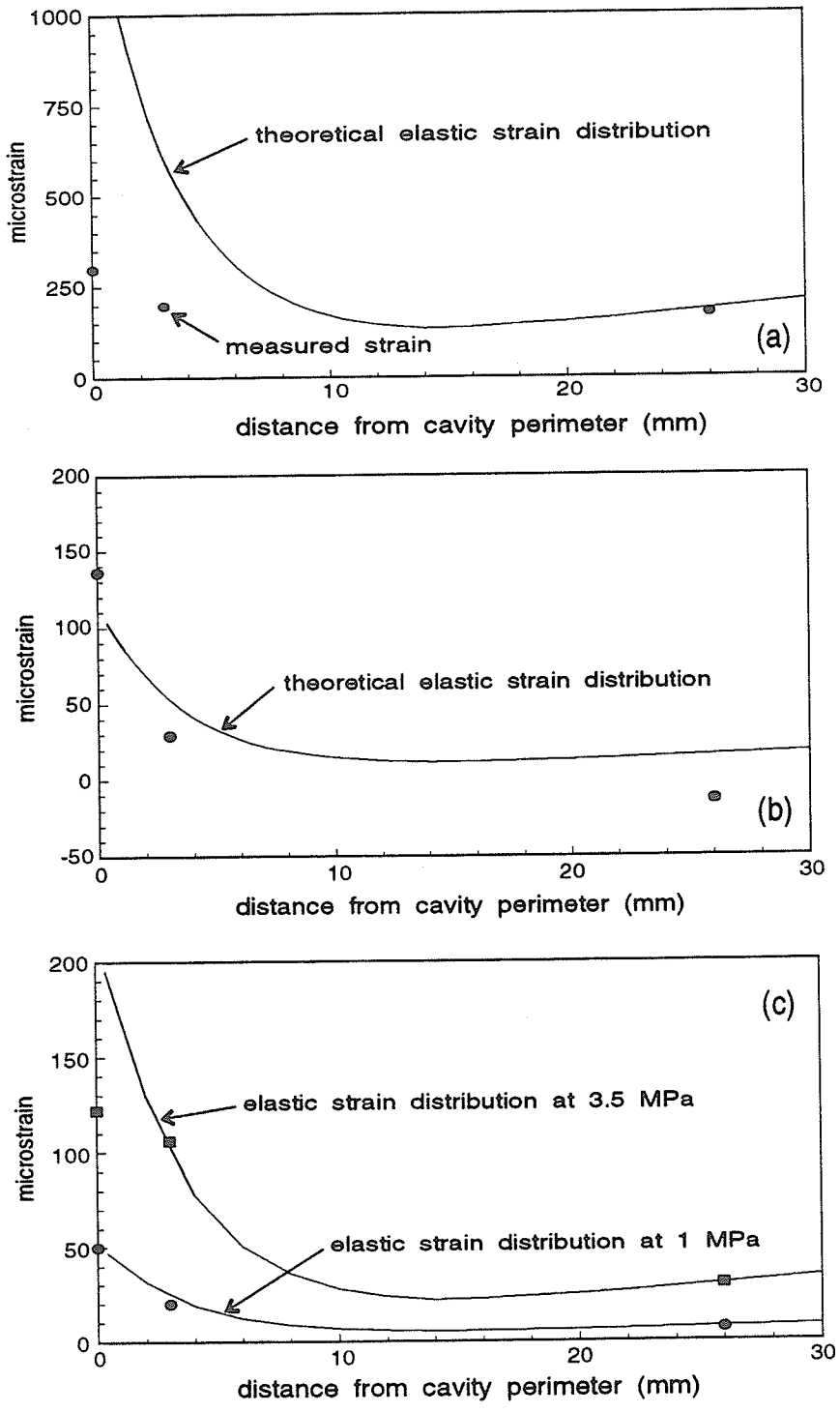

Figure 4.18 Measured and theoretically elastic tangential strain distribution along the primary crack path for (a) Tyndallstone, (b) LDB granite and (c) potash. The data for granite and potash at low stress indicate an elastic stress distribution while that for Tyndallstone and potash at higher stress indicate a reduction in strain close to the cavity perimeter.

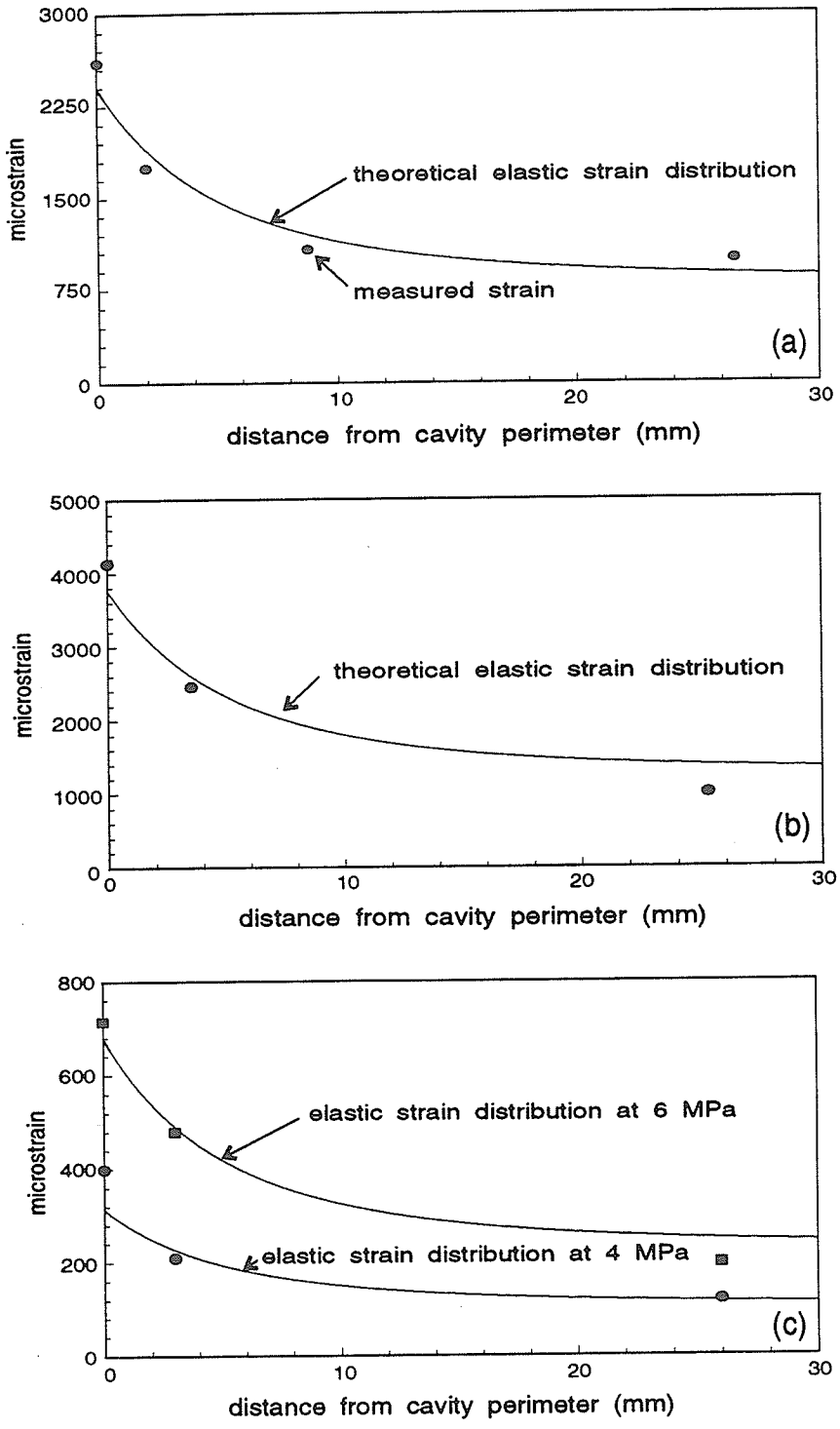

Figure 4.19 Measured and theoretically elastic tangential strain distributions along a horizontal, radial path away from the sidewalls for (a) Tyndallstone, (b) LDB granite and (c) potash. All three rocks have distributions which follow the elastic curve quite well. The data are based on axially oriented gauges which is the direction of fracture growth as well.

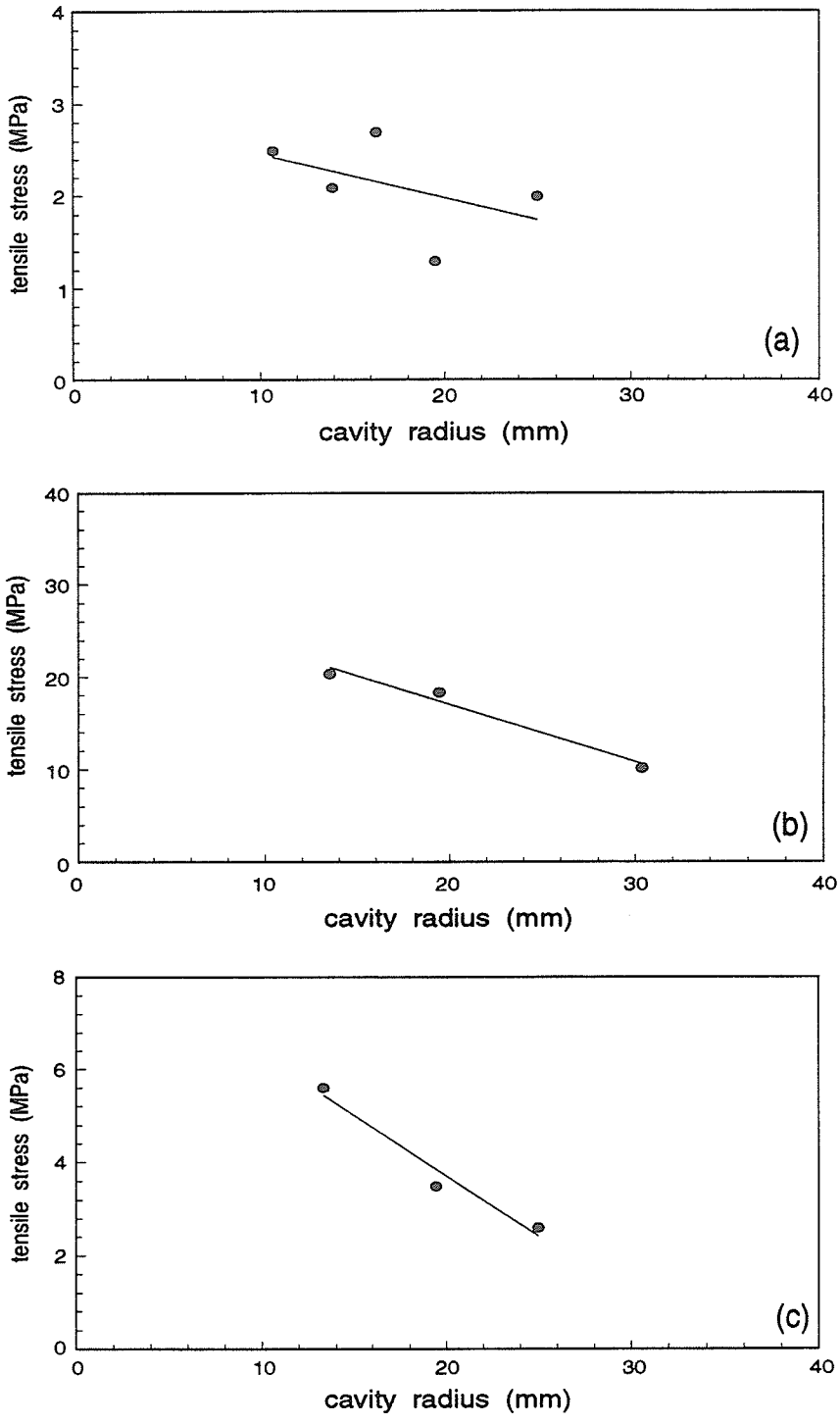

Figure 4.20 Tensile stress calculated from the measured tangential strain at the point of primary fracture initiation for (a) Tyndallstone, (b) LDB granite and (c) potash. The fitted lines indicate that the stress decreases as the cavity size increases. This indicates a decrease in strength with a decrease in gradient.

Table 4.7) Measured tensile strain and calculated tensile stress for Tyndallstone.

Hole Radius (mm)	Mean Applied Stress (MPa)	Mean - Measured Tensile Microstrain	Calculated Tensile Stress (MPa)
25.0	5.1	470	2.0
19.5	5.5	312	1.3
16.3	7.0	635	2.7
13.9	9.3	503	2.1
10.7	11.0	584	2.5

* Mean strains calculated from 4 to 6 strain gauges from three model tests per hole size.

Table 4.8) Measured tensile strain and calculated tensile stress for LDB granite.

Hole Radius (mm)	Mean Applied Stress (MPa)	Mean - Measured Tensile Microstrain	Calculated Tensile Stress (MPa)
30.5	14.5	230	10.2
19.5	19.7	415	18.4
13.5	37.0	460	20.4

* Mean strains calculated from 4 strain gauges from a single model test.

Table 4.9) Measured tensile strain and calculated tensile stress for Saskatchewan potash.

Hole Radius (mm)	Mean Applied Stress (MPa)	Mean - Measured Tensile Microstrain	Calculated Tensile Stress (MPa)
25.0	3.2	148	2.6
19.5	4.2	198	3.5
13.3	4.8	312	5.6

* Mean strains calculated from 4 strain gauges from two model tests.

Gonano (1974) found that the stress—strain curves were linear for the strain measured at the sidewalls of plaster models. At the point of fracture initiation, both the strain and the stress decreased with increasing hole size. These observations led to the conclusion that there is no stress or strain transfer (averaging); instead, the strength increases with the stress gradient; this is an inherent material property (Gonano, 1974).

Based on the model tests of this study, it is possible that both theories, stress—strain averaging and increasing strength due to increasing stress gradients, may be valid. There is definitely some degree of non-linearity in the stress—strain curves as well as in some of the strain distributions away from the hole. The measured strain and calculated stress at primary fracture initiation indicate that a degree of strengthening with increasing stress gradient also occurs.

The high fracture initiation stress seen with small hole sizes has been labelled a strength anomaly (Guenot, 1989). Several theories, such as, the increase in strength with gradient (Gonano, 1974), stress gradient averaging (Lajtai, 1972) and the pressure dependent modulus approach (Santarelli *et al.*, 1986) have all been used to account for this strength anomaly. The methods proposed by Lajtai (1972) and Gonano (1974) will be discussed in more detail later.

The pressure-dependent-modulus approach has been discarded as it cannot model the observed strength anomalies from this study or from other studies (Ewy and Cook, 1990). This theory was originally proposed for the sidewall fractures of thick-walled cylinder tests where a significant radial confining pressure exists. If the elastic modulus increases with an increase in confining pressure, an increase in strength is also obtained.

The elastic modulus for Tyndallstone and for Lac du Bonnet (pink) granite is not influenced to any great extent by changes in confining pressure (Figure 4.21). If the modulus is relatively constant, this model will not produce an increase in strength with decreasing cavity size. In the primary fracture region, the stress is essentially uniaxial tension and the modulus should remain constant. A large size effect (strength anomaly) still occurs however. These observations have led to the conclusion that the pressure-dependent-modulus approach is not suitable for modeling the strength anomaly seen in these tests.

The observed size effect could also be due, in part, to the constant-size crystals behaving differently for large cavities compared to small cavities. The radius of curvature increases with the circular cavity size, whereas the grain size is constant. This could lead to some variations in the process of cracking and failure, between the large and small cavities. This was not studied, however, and is suggested only as an alternative.

4.5 Modeling the Effects of Cavity Size on Fracture Initiation

The hole size affects the fracture initiation stress and the predominant effect is the apparent strength anomaly for very small cavities. The fracture initiation stress is much higher for very small holes compared to large holes. The difference in initiation stress must be even greater when comparing microscopic flaws to macroscopic underground excavations. Study at both micro- and macroscopic sizes is necessary and the physical model data accumulated in this study may be useful for modeling both extremes. To model these diverse sizes, present theories are now examined and new ones proposed.

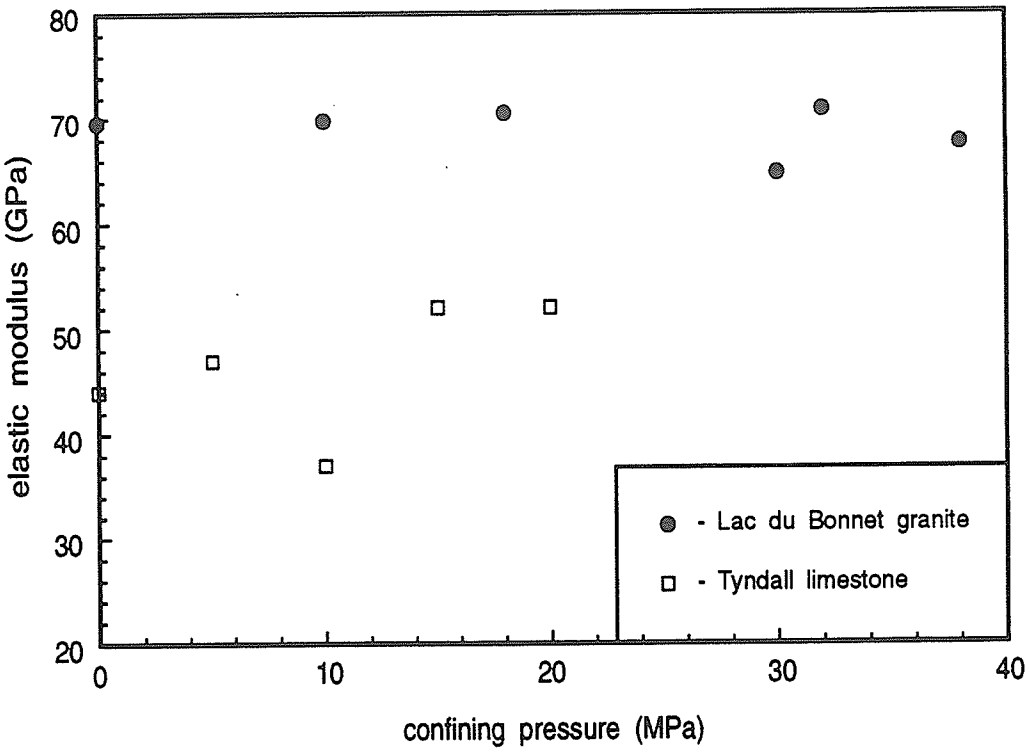

Figure 4.21 The effect of confining pressure on the elastic modulus for Tyndallstone and LDB (pink) granite is negligible over the range of confining pressures shown. There is a slight increase in the modulus of Tyndallstone but none for granite.

Theoretical modeling of fracture initiation around cavities may follow the traditional stress (safety factor) approach (Hoek and Brown, 1980) or the more recent fracture mechanics formulation and related techniques. Both methods have several shortcomings. The stress approach cannot account for the considerable size effect especially for small cavities (pores), while the fracture mechanics interpretation of the remote and slabbing types of fractures is complicated by the fact that the driving stress is compression parallel to the crack. In addition to these two approaches, the Weibull statistical model and two different strain energy density models (Gonano, 1974 and Bazant, 1984) have also been used. Another model is developed through the introduction of stress averaging, both closed-form, linear-averaging and numerical area-averaging techniques, using a multi-axial, stress-based fracture criterion. This theoretical modeling is supported by the data from the physical model tests.

4.5.1 Models Based on the Maximum Stress Theory

The presence of a cavity in an otherwise homogeneous mass of rock causes the state of stress to vary from point to point around the cavity. To evaluate the state of fracture at a specific point around the circular cavity, the state of stress must be defined and then compared with the fracture resistance of the material. For the stress-based methods, the comparison is made through empirical fracture criteria. The simplest method is based on direct stress parameters combined in the form of a safety factor. The simple, stress-based safety factor analysis works quite well for large underground cavities where the stress gradients are shallow. The *strength* parameters (often the compressive

and the tensile strengths) can be directly compared with the *stresses* existing at the point. A crack will form if the stresses are greater than the fracture resistance.

Primary fractures occur in a tensile stress field. In fact, just slightly ahead of the point of primary fracture nucleation, two of the principal stresses are negative, although the axial stress is essentially negligible. For this stress condition, the maximum stress theory:

$$\sigma_3 = \sigma_t \tag{53}$$

has been used almost exclusively in rock mechanics. The Griffith theory (Griffith, 1924) for compressive loading and its later modification (McClintock and Walsh, 1962) and extension (Murrell and Digby, 1970) are based on this criterion. However there are steep stress gradients at the cavity parimeter and these gradients cause the initiation stress to become dependent on the cavity size (Lajtai, 1971). For small cavities, the size effect invalidates the simple stress-based analysis. This can be remedied by replacing the point stress parameter (σ_3) of the safety factor formula with an average value. For this approach to work, averaging must occur over a constant distance (or area) with the averaging dimension considered as a material property.

Lajtai (1972) incorporated the size/gradient effect into a fracture criterion through stress averaging. The method uses the stress gradient to approximate the average tensile stress (σ_{3av}) for a distance of $2d$ along the primary fracture path. The average stress at a distance d from the cavity perimeter is

$$\sigma_d = \sigma_m + d\left(\frac{\partial \sigma}{\partial r}\right) \tag{54}$$

where σ_m is the maximum stress at the cavity perimeter (Figure 4.22).

For a circular hole subjected to uniaxial compression, the maximum stress along the primary crack path is $-P_P$ where P_P is the applied uniaxial load. Using the gradient over the critical distance $2d$ and replacing σ_d with T_o (a negative quantity), the load which causes primary fracture initiation in uniaxial compression becomes

$$P_P = \frac{T_o}{\frac{5d}{R} - 1} \tag{55}$$

This formulation overestimates the fracture strength for small cavity sizes because the linearization of the stress distribution underestimates the stress occurring along the fracture path (Figure 4.22).

Instead of a linear gradient, the true functional average can be found by integrating the stress distribution over the critical distance. Both the radial and tangential stress functions (Kirsch equations) can be integrated to give average maximum and minimum principal stresses, which can be used with an appropriate fracture criterion. The average tangential stress over a distance, d, along the primary fracture path is given by the integral:

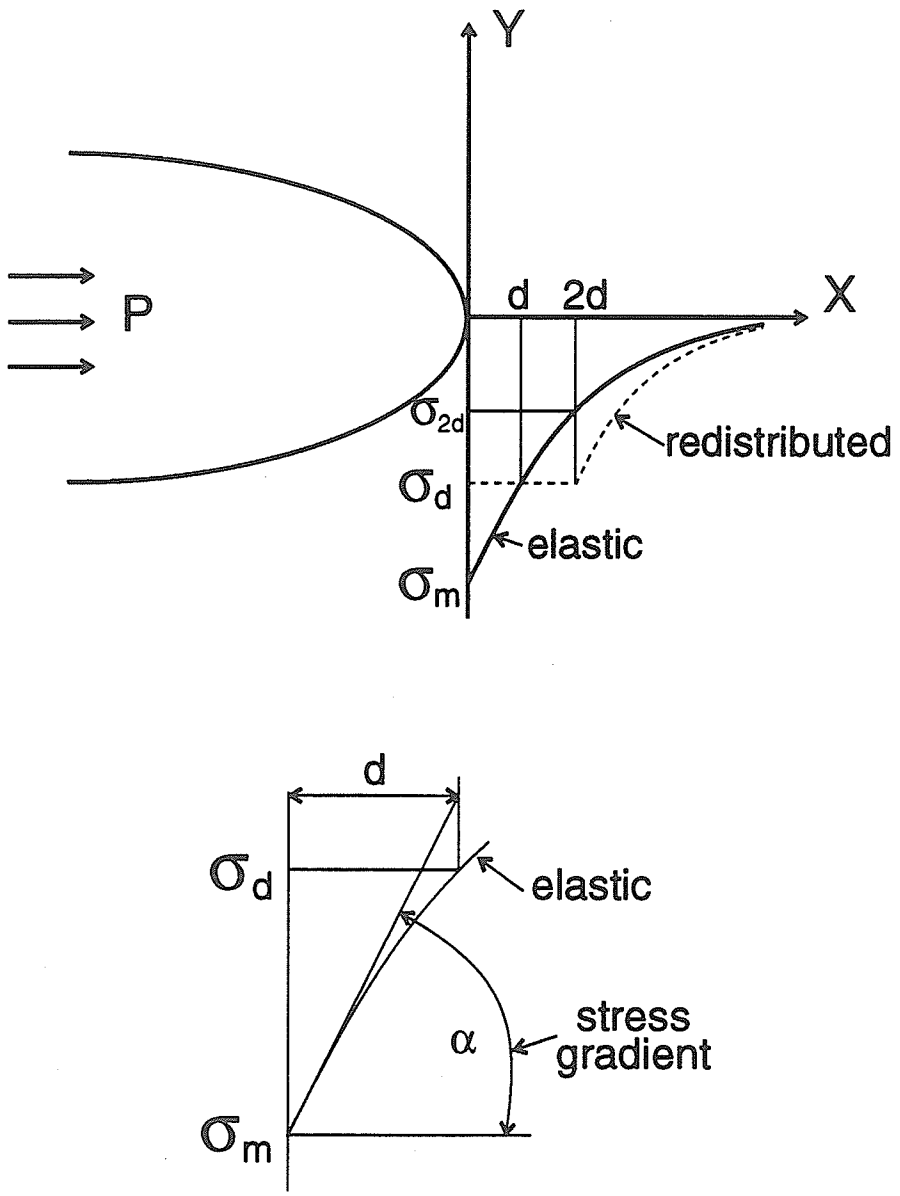

Figure 4.22 Elastic and redistributed stress distributions along the primary crack path for an elliptical cavity. A linear path along the initial gradient underestimates the average stress at a distance (d) from the perimeter.

$$\sigma_{\theta\,ave} \cdot d = \int_{R=r}^{R=r+d} \frac{P_P r^2}{2R^2} - \frac{3P_P r^4}{2R^4}\, dR \tag{56}$$

where R is the radial distance from the center of the cavity. Integrating (56) and simplifying leads to the average tangential stress:

$$\sigma_{\theta\,ave} = \frac{P_P r^2}{2d(r+d)} \left(\frac{r^2}{(r+d)^2} - 1 \right) \tag{57}$$

The same procedure for the radial stress yields

$$\sigma_{r\,ave} = \frac{P_P \left(d - 2r + \dfrac{5r^2}{2(r+d)} - \dfrac{r^4}{2(r+d)^3} \right)}{d} \tag{58}$$

where P_P is the applied uniaxial load causing primary fracture initiation, r is radius of the cavity and d is the distance from the cavity perimeter over which the stress is averaged. The simplest criterion for primary fracture nucleation would ignore the effect of the radial stress by taking

$$\sigma_{\theta\,ave} = T_o \tag{59}$$

Replacing $\sigma_{\Theta ave}$ in (57) with T_0 (negative), the size effect in uniaxial compression becomes

$$P_P = \frac{2d\,T_o}{r^2}\left[\frac{(r+d)^3}{r^2-(r+d)^2}\right] \tag{60}$$

Replacing the approximated mean stress (σ_d) from (54) with the actual mean stress ($\sigma_{\Theta ave}$) improves the model by translating the vertical asymptote towards r=0. The presence of the vertical asymptote suggests that the load necessary to cause fracture is infinite. This would be true if the rock itself were without its own stress-raising microflaws. Such microscopic structures can generate axial tensile fractures from a compressive load without macroscopic tension being present. In fact, if no cavity exists, the nucleation of axis-parallel tensile fractures should occur not at infinite load but at the crack initiation point for uniaxial compression. Although an infinite intercept is predicted, the desired horizontal asymptote near the absolute value of the tensile strength is produced as the radius approaches infinity.

4.5.2 Primary Fracture Model Based on Weibull's Theory

Weibull's theory can be used to model primary fracture initiation for various-sized cavities in a manner similar to that used by Chandler (1989) for sleeve fracture and Brazilian tests. Weibull's theory predicts that a larger volume of material will have a lower strength because of the increased probability of finding larger initial fractures. Following the same trend in thought, larger cavity sizes should have lower fracture strengths because of the increased probability of finding weaker material near the middle of the crown and invert. Although Weibull's theory is not applicable in compressive

stress fields, there are other statistical models which could be used in a similar fashion to model remote and sidewall fractures.

The first step in modeling primary fractures as a function of cavity size is to develop a volume correction factor (Chandler, 1989):

$$C_v = \frac{\int_{V_s} (\sigma_t)^m \, dV}{(\sigma_t^*)^m \; V_s} \tag{61}$$

where σ_t^* is the maximum tension in the specimen, m is the Weibull parameter and V_s is the volume of material where at least one of the principal stresses is negative (σ_t). In calculating C_v, $(\sigma_t)^m$ is integrated using a simple numerical technique. C_v is a function of m (Figure 4.23). If m is known, C_v can be found and the primary fracture initiation stress (P_P) is given by either of the following two equations:

$$P_P = T_o \left(\frac{V_{direct}}{V_{hole} \; C_{v\,hole}} \right)^{1/m_{direct}}$$

$$P_P = \sigma_{Braz} \left(\frac{V_{Braz} \; C_{v\,Braz}}{V_{hole} \; C_{v\,hole}} \right)^{1/m_{Braz}} \tag{62}$$

where V_{direct} and m_{direct} are the volume and Weibull parameter for direct tension, T_o is the direct tensile strength, V_{hole} and $C_{v\,hole}$ are the volume and correction factor for the cavity, V_{Braz} and $C_{v\,Braz}$ are the volume and volume correction factor for the Brazilian test (Figure 3.13) and σ_{Braz} is the Brazilian tensile strength. This formulation uses the two-parameter Weibull model, which results in a minimum value of zero for P_P as the cavity radius (volume) goes to infinity.

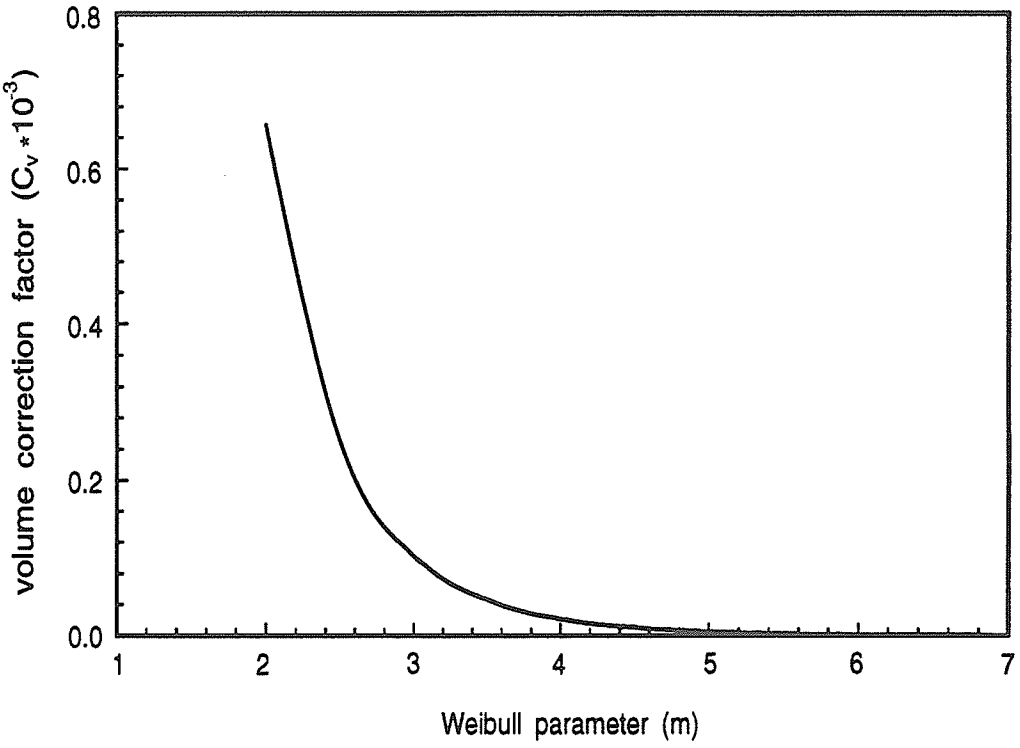

Figure 4.23 Volume correction factor as a function of the Weibull parameter (m) for primary cracking from a circular cavity under a uniaxial compressive load (for Tyndallstone).

4.5.3 Fracture Mechanics Models

In most disciplines of fracture mechanics, the stress-based type of analysis has long been replaced by the stress-intensity formulation of fracture mechanics. In fact, several closed-form fracture mechanics solutions exist for the problem of a fracture emanating from a cylindrical cavity (Sammis and Ashby, 1986; Rummel and Winter, 1983; Bowie, 1956). Primary fracture from cavities falls into this category.

Fracture mechanics is a stability theory, not a theory of fracture nucleation, meaning that an initial starting crack is required. When the material is elastic (no process zone) and the state of stress is tensile, as for primary fracture, the crack-opening-mode formulation of linear elastic fracture mechanics (LEFM) is applicable. The stress intensity factor for a crack emanating from a hole, subjected to compressive stresses (Rummel, 1987; Paris and Sih, 1965) can be found from

$$K_I = K_I(\sigma_1) + K_I(\sigma_3) = -\sqrt{r}\left[P_1 f(b) + P_3 g(b)\right] \tag{63}$$

where the dimensionless stress intensity functions f and g are (Rummel, 1987):

$$f(b) = -2\left[\frac{b^2-1}{\pi b^7}\right]^{\frac{1}{2}} \tag{64}$$

and

$$g(b) = (\pi b)^{\frac{1}{2}}\left(1 - \frac{2}{\pi}\sin^{-1}\frac{1}{b}\right) + 2\left(b^2+1\right)\left(\frac{b^2-1}{\pi b^7}\right)^{\frac{1}{2}} \tag{65}$$

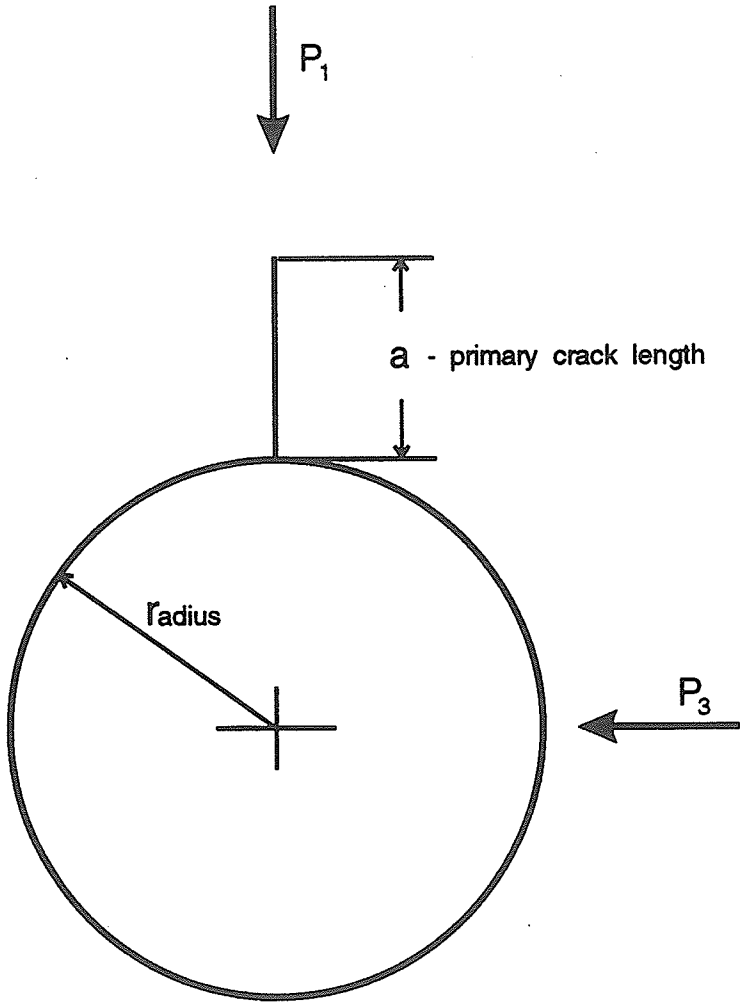

Figure 4.24 Relationship between the cavity radius (r) and the primary crack length (a) when far field loads (P_1 and P_2) are applied. An initial length ($a=l_o$) must be supplied to determine the fracture toughness as a function of crack length.

b is equal to $1+a/r$ (Rummel and Winter, 1983), a equals the crack length from the edge of the hole and r is the radius of the hole (Figure 4.24). P_1 in (63) is the maximum compressive stress parallel to the crack and P_3 is the confining stress perpendicular to the crack. The uniaxial compressive load needed to propagate a fracture in the tensile zone of the circular cavity of radius (r) can be computed after supplying an initial crack length (l_o) and the opening mode fracture toughness (K_{Ic})

$$P_P = \frac{K_{Ic}\sqrt{\pi\left(\frac{r+l_o}{r}\right)^7}}{\sqrt{2r\left(\frac{r+l_o}{r}\right)^2 - 1}} \tag{66}$$

where P_P is the applied uniaxial load (P_1 when P_3 is zero).

Sammis and Ashby (1986) use a slightly different form based on the tabulated results of Sih (1973)

$$K_I = -\left(P_1\sqrt{\pi a}\right)\left[\frac{1.1\left(1-2.1\frac{P_3}{P_1}\right)}{\left(1+\frac{a}{r}\right)^{3.3}} - \frac{P_3}{P_1}\right] \tag{67}$$

where a, r, P_1 and P_3 were defined above (Figure 4.24). The uniaxial compressive load needed to nucleate fracture in the tensile zone of the circular cavity is then

$$P_P = \frac{K_{Ic}\left(1+\frac{l_o}{r}\right)^{3.3}}{1.1\sqrt{\pi l_o}} \tag{68}$$

The two solutions produce approximately the same stress intensity factor for the same initial starting crack (l_0) and thus the latter equation will be used, as it is somewhat simpler.

These fracture mechanics formulations cannot directly model remote or sidewall fractures. Ingraffea (1977; 1979) has used a penny-shaped starting crack for remote fractures but this method requires macroscopic tensile stresses for crack propagation. However, the macroscopic tension is quite small in the remote position (Carter *et al.*, 1991*b*) and therefore the contribution of the axial compressive stress must be included in the fracture criterion as well (Lajtai *et al.*, 1990). Simple LEFM formulations are incapable of accurately modeling a fracture in this type of stress field, at least analytically.

Sidewall fractures form in an all-compressive-stress field and must be modeled with reference to microstructural flaws. In the fracture mechanics formulation, this would involve the assumption of a starting crack, either the sliding crack (Nemat-Nasser and Horii, 1982; Ewy *et al.*, 1987) or the splitting crack (Ewy and Cook, 1990). The resulting new cracks are assumed to propagate within the zone of influence of the starting

crack and, therefore, the size and the orientation of the mostly hypothetical starting crack will influence the outcome. The resulting model is no longer closed-form and must be solved numerically.

4.5.4 Critical Strain Energy Density Model

An alternative to the stress intensity form of fracture mechanics is the critical-strain-energy-release-rate approach (Gonano, 1974). This method is closely related to the LEFM approaches, as the strain energy release rate (G) is directly related to the fracture toughness (K)

$$G = \frac{\pi \sigma^2 a}{E} \quad with \quad K = \sigma \sqrt{\pi a} \quad so \quad G = \frac{K^2}{E} \tag{69}$$

where E is the elastic modulus. This method has also been used to explain the effect of size on strength for regular laboratory compression tests (Baecher and Einstein, 1981).

The basic premise is that fracture initiation occurs when the strain energy release rate in a critical volume, the volume of material subject to at least 90% of the peak stress, reaches a critical value. Consequently, for the fractures in the model tests, size-dependence is controlled primarily by strain gradient, critical volume and critical surface area (Gonano, 1974). Although these three parameters are not strictly proportional to the hole size, by plotting the primary fracture initiation stress against the hole radius, using log-log axes, a straight line relationship should be produced (Gonano, 1974), which fits the relationship:

$$\sigma = K d^{-\alpha} \tag{70}$$

where K and α are constants. α is usually less than 0.5, but statistical considerations and external strain energy can push the value towards 1.0 (in many cases α is not constant).

4.5.5 Bazant's Size Effect Model

This theory was originally developed by Bazant (1984) and is based on energy considerations of the propagating crack band front. It is essentially a form of non-linear fracture mechanics (see Appendix A):

$$\sigma_N = \frac{B f_t}{\sqrt{1 + \frac{d}{\lambda_0 d_a}}} \tag{71}$$

where σ_N is the nominal breaking or failure stress for a specific test size and geometry, f_t is the uniaxial tensile strength, d is a characteristic specimen size, d_a is the maximum grain size, and λ_0 and B are constants. Bazant and Yunping (1991) then incorporated Weibull's statistical theory into this model

$$\sigma_N = \frac{B f_t}{\left(\beta^{2nr/m} + \beta^r\right)^{\frac{1}{2r}}} \tag{72}$$

where m is the Weibull parameter, n is a dimensional similarity parameter and r is an arbitrary empirical constant. Although the second method may be somewhat better, it requires an iterative procedure of linear regression while varying r to minimize the coefficient of deviation (Bazant and Yunping, 1991). The small improvement in fit shown in their paper does not appear to be worth the extra effort involved.

4.5.6 Stress-Averaging Based *USR* Technique

The safety factor approach is more flexible than the maximum-stress theory and LEFM because it includes the influence of both the maximum and the minimum principal stress. If correction for the stress gradient is made through some scheme of stress averaging, σ_3 and σ_1, the at-the-point stresses can be replaced by the averaged stresses (σ_{3av} and σ_{1av}) in the formula for the safety factor or unconfined strength ratio (*USR*).

If linear averaging of stresses is acceptable and R=0.5 for the Rocker function (equation 24), the *USR*=1 condition can be used to express the uniaxial compressive load at primary fracture (P_P) in closed form. Substituting the averaged principal stresses (equations 57 and 58) into the Rocker definition of *USR* (equation 41) and setting *USR*=1, the compressive load for primary fracture becomes

$$P_P = \frac{T_o}{\frac{B}{2} - \sqrt{\frac{B^2}{4} + \left(\frac{C \cdot T_o}{C_o}\right)^2}} \tag{73}$$

where B and C depend on the cavity size (r) and on the distance d:

$$B = \frac{r^2}{2d}\left(\frac{r^2}{(r+d)^3} - \frac{1}{(r+d)}\right)$$

$$C = \frac{1}{d}\left(d - 2r + \frac{5r^2}{2(r+d)} - \frac{r^4}{2(r+d)^3}\right) \qquad (74)$$

If the exponent (R) in the Rocker function is different from 0.5, a numerical procedure is needed to determine the stress (P_p) for a *USR* value of 1.0.

The justification for stress averaging comes from the notion that most rocks will distribute the very high stresses and strains that exist at a mathematical point around the cavity parameter through micro-fracturing or plastic deformation. It is likely that the stresses will be distributed over a finite area rather than along a linear path.

In the area-averaging technique (Carter *et al.*, 1992), the average maximum and minimum principal stresses for a point are found by averaging over a circular region of radius d surrounding the point. The averaging is done through numerical integration by dividing the circular region into 8 sectors (at 45°) and 5 rings with the rings becoming progressively wider away from the point. The stresses are evaluated at the centroids of the 40 sectors. When a centroid falls inside the cavity, the corresponding area is deleted and the radius (d) is increased proportionately to account for the deleted areas.

The condition of $SF=1$ or $USR=1$ represents failure conditions but other values of the safety factor or *USR* could be used to represent fracture initiation and fracture damage (onset of dilatancy). These fracture parameters were defined for each of the

three rock types earlier (Figure 3.16) and will be used again in the finite element implementation of area averaging to be discussed in Chapter 6.

4.5.7 Modeling Primary Fracture From Cavities

In the physical model tests, the nucleation stress for primary, remote and slabbing fracture was found to be dependent on the size of the circular cavity. With a number of closed-form and numerical solutions being available, primary fracture from circular cavities of varying radii presents a good opportunity for evaluating and/or calibrating the fracture criteria. Since, in uniaxial compression, the remote and the slabbing fractures generally form after the primary fracture, the theoretical solution of the circular cavity employed in the present analytical/numerical model is valid only for the primary fracture. However, a theoretical solution has also been developed for sidewall slabbing and will be discussed later. Because the primary fracture does not greatly affect the stress at the sidewall (Brady and Brown, 1985), this solution may be valid for certain cases. A finite element solution to remote fracture initiation in Lac du Bonnet granite was published previously (Carter *et al.*, 1991*b*).

The strength parameters to be entered into the various theoretical models include the tensile (σ_t) and the compressive strength (σ_c) and the fracture toughness (K_{IC}). The stress-based approach also needs a value for the averaging parameter, d. This will be treated as a fitting parameter; its value will be selected to give the best fit to the physical data. Similarly, the LEFM models need an initial crack length, (l_0). It was shown

earlier that the critical lengths obtained through tension test data are often unreliable. Consequently, these values will be ignored and l_0 will be treated as a fitting parameter.

4.5.7.1 Tyndall Limestone

Tyndallstone has a compressive strength which ranges from 40 to 75 MPa and a tensile strength usually between 0.5 and 5 MPa. The fracture toughness was measured using the double-torsion test, giving K_{IC} = 1 MPa$\sqrt{m}$. This value was obtained from some of the stronger specimens. The strength parameters for Tyndallstone vary widely however and K_{IC} was not measured for the weaker set of specimens which were used in the modeling. For the fitting process, the values of 41 MPa for the uniaxial compressive strength, 3 MPa for the tensile strength, 0.4 MPa$\sqrt{a}$ for K_{IC} and 4.2 mm for l_0 gave the best fit to the data. Lowering the fracture toughness value should not cause undue concern as the stress state in the double-torsion test is quite different from the model tests, size influences the toughness (Schmidt and Lutz, 1979; Chong *et al.*, 1989) and the toughness is probably less than 1.0 for the weaker set of specimens.

In general, the physical data for primary fracture fall into the region where the size effect is quite modest. Several of the analytical models were fitted to the data first (Figure 4.25). The one marked Lajtai comes from (Lajtai, 1972) using d=1.5 mm (equation 55) and the other is based on equation (60) with d = 4 mm. Both are based on the maximum stress theory but with stress averaging included. The maximum stress theory with no averaging yields a horizontal line at the absolute value of the tensile strength. At a very small radius ($r<d$), the computed-average stress at the primary

location may become zero or even compressive. Using these two solutions, primary fracture is no longer possible if the average stress is compressive and both solutions give a vertical asymptote at a finite radius.

The two-parameter Weibull model (equation 62) was also fitted to the primary fracture initiation data (Figure 4.26) using Brazilian strength data and the associated m of 2.73 and c_v of 0.21. This model fits the data quite well except for the smallest cavity sizes. The curve tends to infinity at a cavity radius of zero and has an asymptote of zero as the radius approaches infinity. An asymptote could be generated by a three parameter Weibull model but the curve would still approach infinity at a radius of zero.

The closed-form fracture-mechanics solution (equation 68), with K_{Ic} = 0.4 MPa$\sqrt{m}$ and l_o = 4.2 mm behaves like the previous solutions (Figure 4.27). The Sammis—Ashby solution (equation 68) has an asymptote at $-\sigma_t/1.1$ as $r \rightarrow \infty$):

$$P = \frac{K_{Ic}}{1.1\sqrt{\pi l_o}} \quad but \quad \frac{K_{Ic}}{\sqrt{\pi l_o}} = -\sigma_t \quad thus \quad P = \frac{-\sigma_t}{1.1} \qquad (75)$$

It is interesting to note that by varying l_o with the cavity radius, a slightly better fit can be obtained (Figure 4.28) but the solution is no longer closed-form.

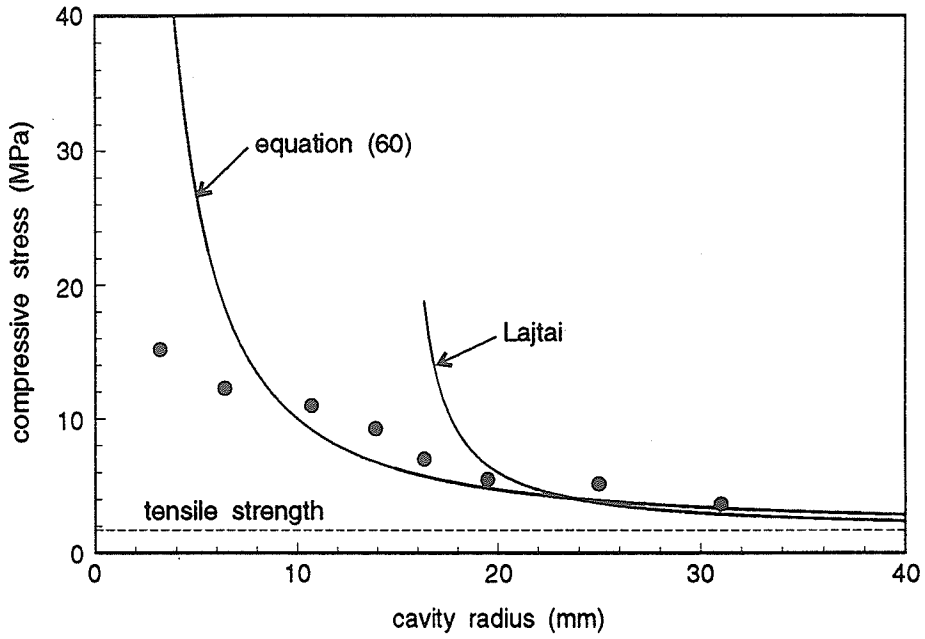

Figure 4.25 Linear averaging, using a linearized gradient and the integrated function, fitted to primary fracture initiation data for Tyndallstone.

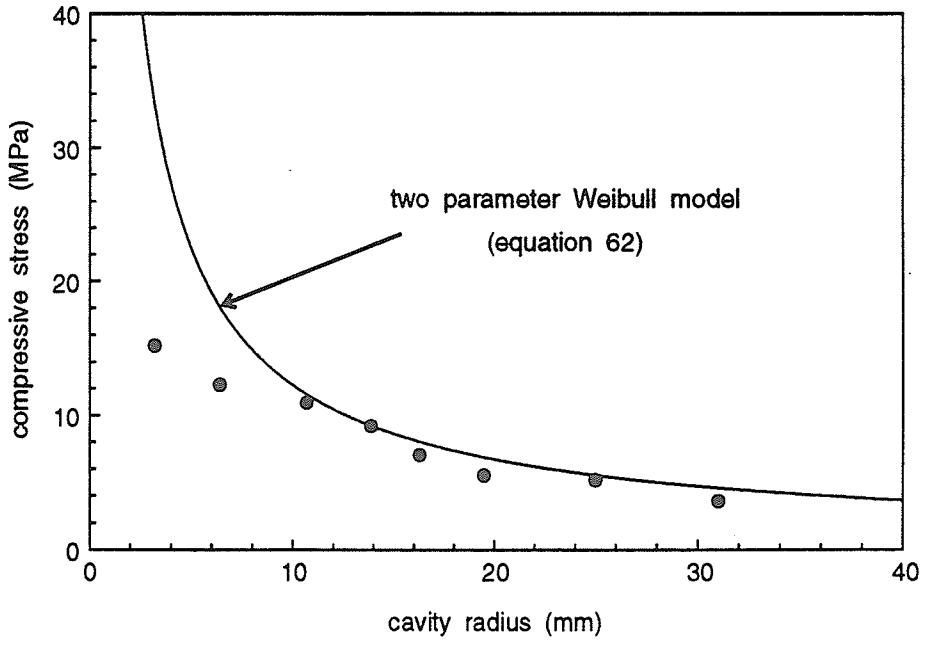

Figure 4.26 Weibull model fitted to primary fracture initiation data for Tyndallstone.

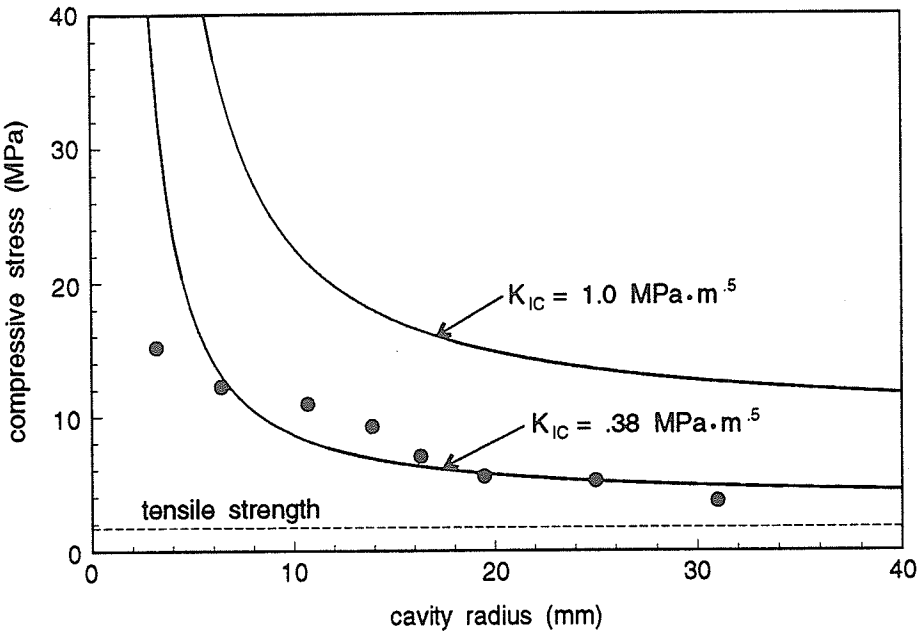

Figure 4.27 Fracture mechanics model fitted to primary fracture initiation data for Tyndallstone.

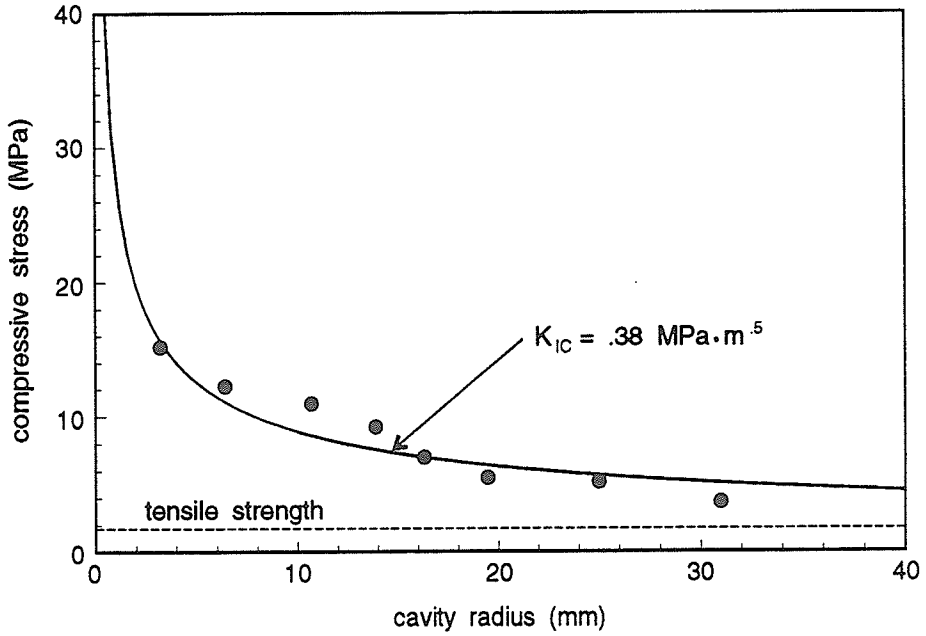

Figure 4.28 Varying the initial crack length (l_o) yields a better fit for the fracture mechanics model.

Applying Gonano's (1974) method produces a reasonable fit (Figure 4.29) although it does not appear to be better than any of the others. This relationship does not produce an asymptote for large cavity sizes and it appears that a bilinear plot would be more suitable. By varying the exponent (α), a better fit could undoubtedly be obtained.

Bazant's model (equation 71) does not fit the data very well (Figure 4.30). Equation (72) was not used due to the inability to produce the necessary parameters from the data (see Appendix A) following the method suggested by Bazant and Yunping (1991). Figure 4.30 shows a comparison between Bazant's model and a simple, empirical, exponential function. The exponential function fits much better, giving an asymptote and intercept at reasonable values. Bazant's model does not produce an asymptote.

In applying the ***USR*** concept, the condition that ***USR***=1 was used as the criterion for forming a macroscopic fracture. Microfractures usually start at higher values of ***USR*** (in terms of peak strength) and the microcrack density would be substantial at the onset of dilation (crack damage). Nevertheless, fractures of macroscopic size (visible by the naked eye) appear only at high stress, after volumetric reversal. Using ***USR***=1, the two ***USR***-based stress-averaging schemes (Figure 4.31) produce an $r = 0$ intercept at the uniaxial compressive strength (41 MPa). The proper asymptote of $-\sigma_t$ at infinite radius is also produced. The linear and area averaging schemes diverge only in the small radius region. The linear averaging (d = 4 mm) produces the right intercept but this closed-form curve goes through an unlikely maximum before reaching the axis (see the inset of Figure 4.31). All the closed-form solutions anticipate fracture initiation in the primary

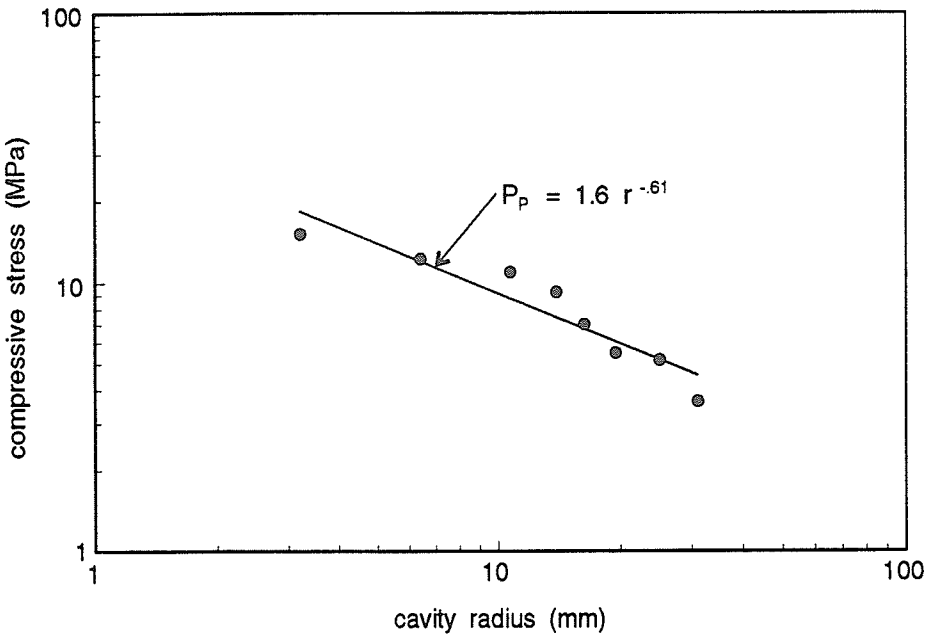

Figure 4.29 Gonano's model fitted to primary fracture initiation data for Tyndallstone.

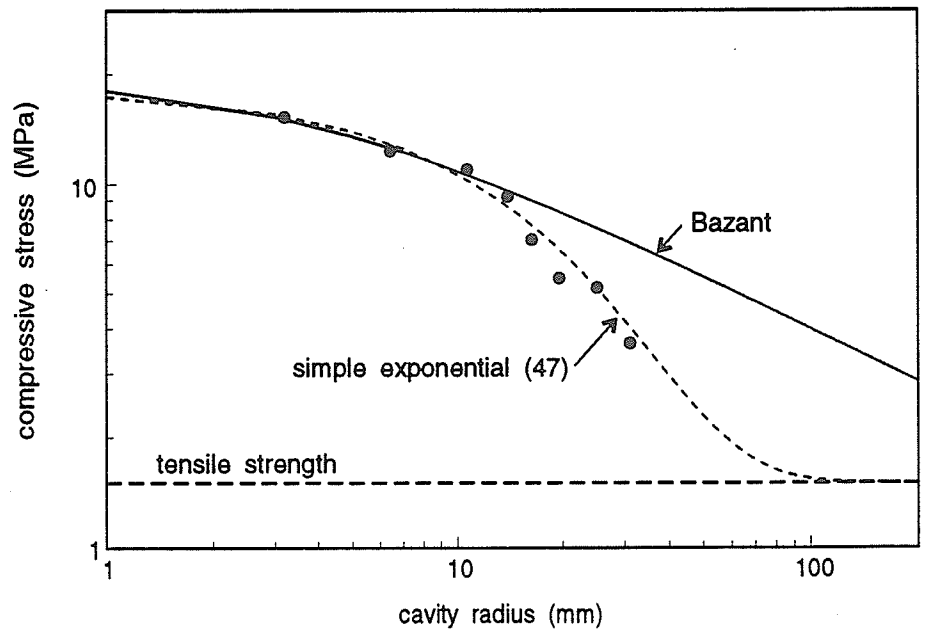

Figure 4.30 Bazant's model fitted to primary fracture initiation data for Tyndallstone. This function does not fit as well as the empirically fitted exponential.

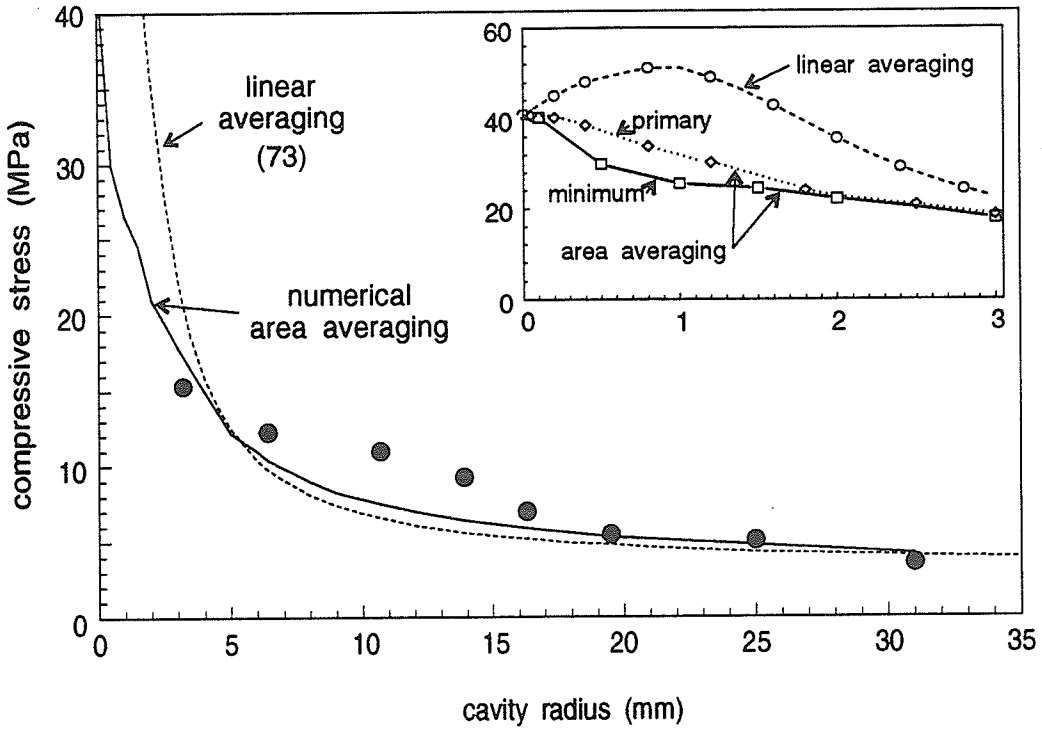

Figure 4.31 Linear and area averaging, using the *USR*—Rocker fracture criterion, fitted to primary fracture initiation data for Tyndallstone.

region only. In a numerical implementation of area-averaging (d = 3 mm), the whole area beyond the perimeter is scanned to find the lowest ***USR*** point. This analysis shows that the fracture nucleation point moves out of the primary region as the radius approaches zero. The inset in Figure 4.31 shows the results of the area-averaging scheme. The lower curve is based on the lowest ***USR*** regardless of position while the middle curve (primary) takes the minimum value of ***USR*** from the primary region.

4.5.7.2 Saskatchewan Potash

Potash is the most ductile of all the rock types with strength parameters defined earlier. Despite the ductility, the size effect follows the trend obtained through elastic analysis (Figure 4.32) and again area averaging (solid line) was the best model with d = 3.5 mm. The other stress averaging models are closely spaced and fit the experimental data well only in the $r > 5$ mm region. To have the Sammis—Ashby model follow the data trend, l_o and K_{IC} were considered as fitting parameters. K_{IC} = 0.22 MPa$\sqrt{m}$ and an initial crack length of 3.5 mm gave the best possible fit; the measured value of K_{IC} (0.34) did not fit well.

According to the numerical area-averaging scheme, the position of the nucleated fracture for small cavity radii would change from the primary region to one at the side of the cavity signalling a slabbing type of fracture. In the process of the changeover, at some intermediate radii, the fracture occupied the remote position as well. This is the reason for the irregular shape of the fitted area-averaging model in the r = 0 to 3 mm region of the graph (inset of Figure 4.32). Had the fracture stayed in the axial region,

the fracture criterion would have followed the dotted line. The transition of the first fracture from the primary to the remote region can actually be seen from the physical model data where the remote fracture occurs before the primary at the smallest radius.

The Gonano and the Bazant models were fitted to the data as well (Figure 4.33). Gonano's model fits quite well but again lacks the asymptote as the radius approaches infinity. Bazant's model does not fit the data very well and it too lacks an asymptote. Neither model fits as well as the empirically fitted exponential which is shown for comparison purposes.

For the potash rock, the effect of confining pressure was evaluated as well (Carter *et al.*, 1992). There were no physical experiments to validate these results however. In general, increasing the confining pressure shifts the location of the first crack from the primary region to the slabbing position through a transitional zone where the crack forms remote to the perimeter (Figure 4.34). At high confining pressure, the remote fractures occur close to the cavity perimeter and the order of fracture initiation changes (Carter *et al.*, 1991*b*). Sidewall fractures become the first fractures and thus remain the dominant fracture type (Carter, 1988).

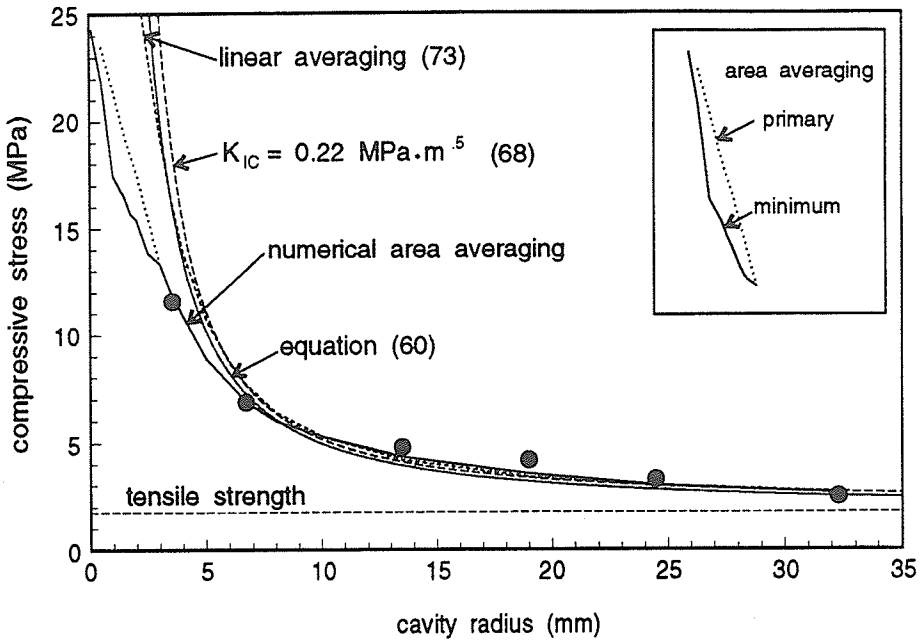

Figure 4.32 Primary fracture initiation data for potash fitted to stress averaging and fracture mechanics models.

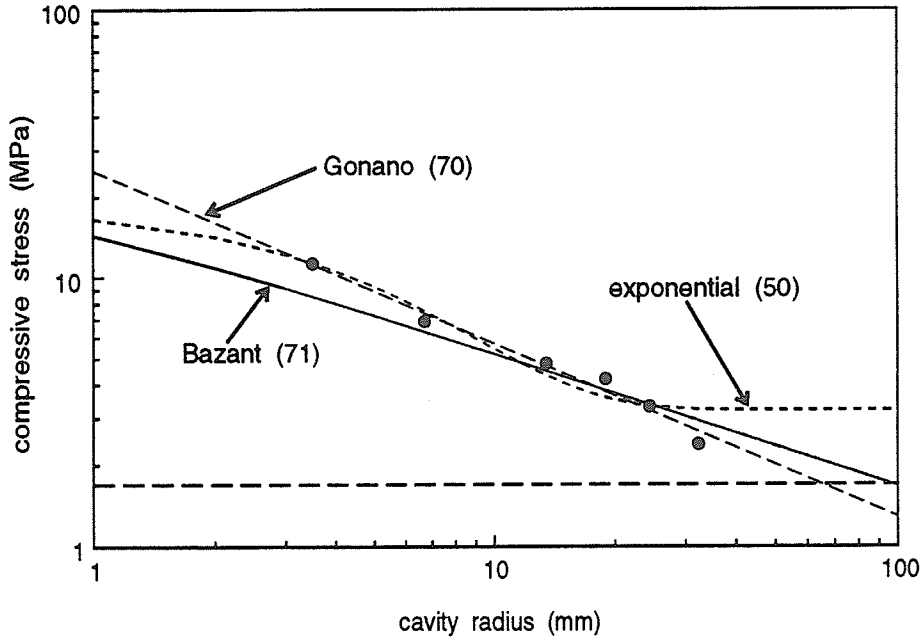

Figure 4.33 Primary fracture initiation data for potash fitted to Weibull's and Bazant's models. An empirical exponential is also shown for comparison.

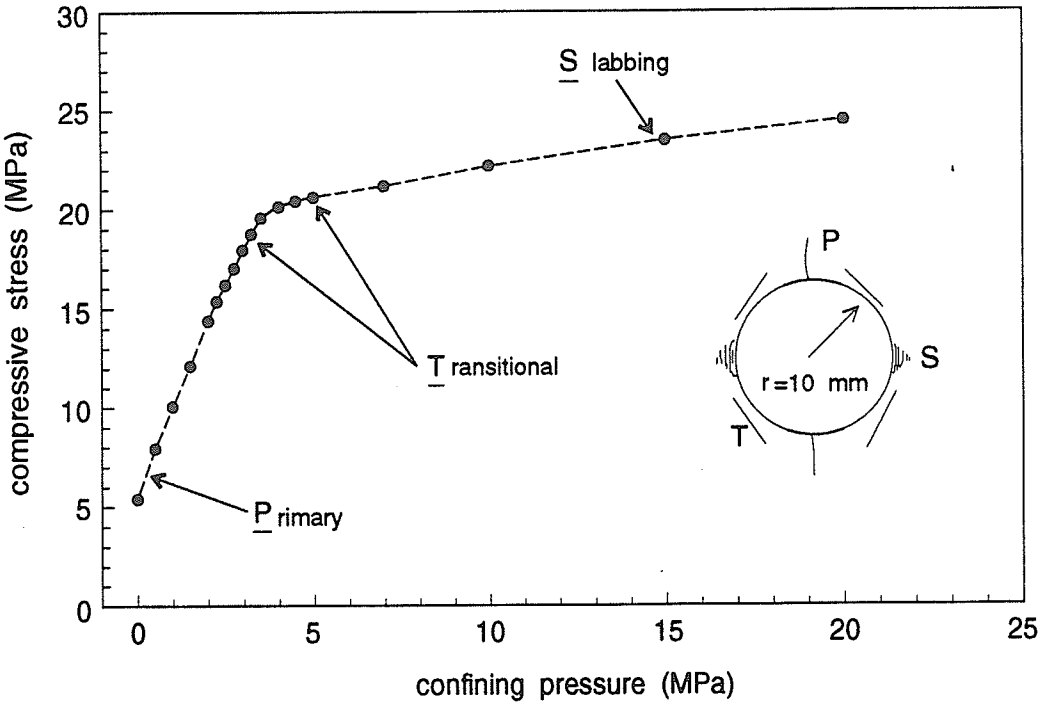

Figure 4.34 Effect of confining pressure on the location of the first fracture in potash. The stress needed to cause fracture initiation also increases. The pattern changes from primary through a transitional (almost remote) to sidewall fractures.

4.5.7.3 Lac du Bonnet Granite

With only three blocks available, the modeling is incomplete. It is included to show the fit of the area-averaging criterion when dealing with a strong, crystalline, igneous rock. The area-averaging (d =2 mm) offers the best interpretation for this rock followed by the linear averaging using d=3 mm (Figure 4.35). Once again, for small cavity radius, area-averaging would suggest that the fracture moves off the perimeter into a remote position. For the fracture mechanics model, an initial crack length of 2 mm and K_{IC} at one half of the measured value gave a reasonable fit.

4.5.8 Modeling Sidewall Fracture by Stress Averaging

The sidewall fracture initiation data can be modeled quite easily using several of the same models: the strain energy density models (Gonano, 1974 and Bazant, 1984) and the stress based models, including the stress averaging versions. Fracture mechanics is not suitable. Although statistical failure theories exist for compressive failure, Weibull's model should not be used. The strain energy density models will not provide any better results than they did for the primary fracture initiation data. The maximum stress theory produces a horizontal line at one third of the uniaxial compressive strength as the radial stress is zero at the perimeter.

Consequently, the effect of size on sidewall fracturing was modeled by the stress-averaging technique only, using integrated (average) stresses and the *USR*—Rocker fracture criterion. The radial and tangential stress distributions at the springlines (Kirsch equations) were integrated along a horizontal radial path, away from the cavity perimeter,

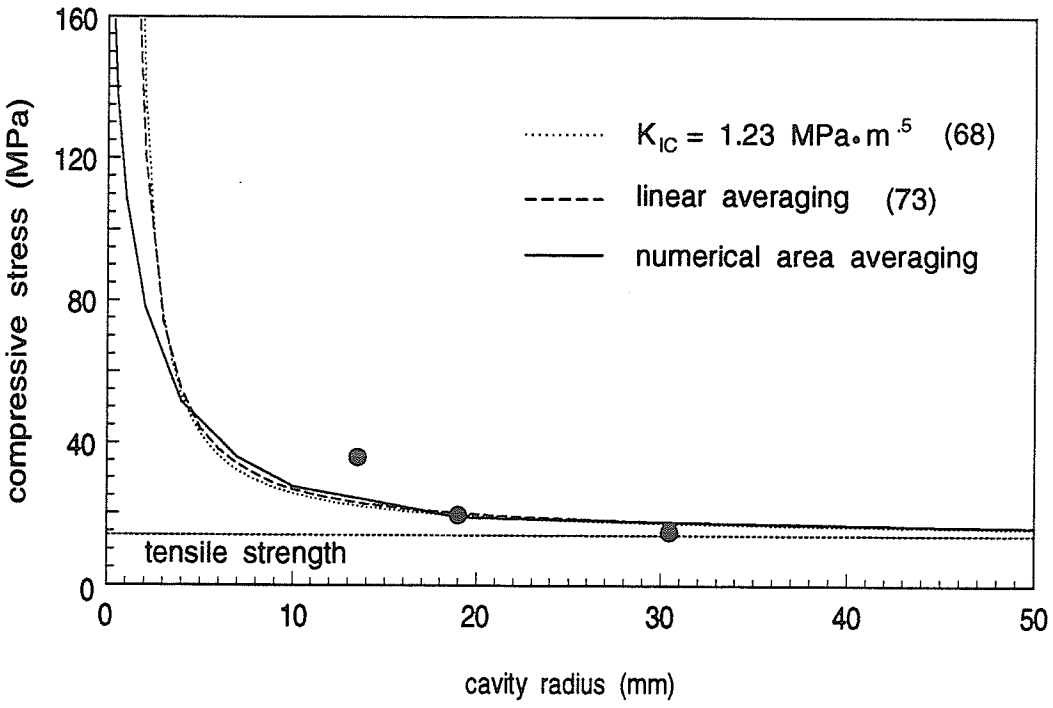

Figure 4.35 Primary fracture initiation data for LDB granite fitted to stress-averaging and fracture-mechanics models.

over a distance d:

$$\sigma_{rav} = \sigma_{3av} = \frac{P_S\, r}{d}\left[1 - \frac{3r}{2(r+d)} + \frac{r^3}{2(r+d)^3}\right] \tag{76}$$

$$\sigma_{\theta av} = \sigma_{1av} = \frac{P_S\,(r+d)}{d}\left[1 - \frac{r^2}{2(r+d)^2} - \frac{r^4}{2(r+d)^4}\right] \tag{77}$$

for the average radial and tangential stresses respectively. P_S is the applied uniaxial load causing sidewall fracture and r is the hole radius. The simplest method of predicting sidewall fracture is to equate the averaged tangential stress to the uniaxial compressive strength:

$$P_S = \frac{d \cdot C_o}{(r+d)\left(1 - \frac{r^2}{2(r+d)^2} - \frac{r^4}{2(r+d)^4}\right)} \tag{78}$$

where C_0 is the uniaxial compressive strength (a positive quantity). This assumes that the minimum principle stress is either negligible or zero as in uniaxial and biaxial compression. The model fits both the Tyndallstone and potash data quite well (Figures 4.36 and 4.37). The curves yield asymptotes of 13.7 and 8.2 MPa which are the expected values, 41/3 and 24.5/3 MPa for Tyndallstone and potash respectively. At a radius of zero, the curves intercept the stress axis at the uniaxial compressive strengths, 41 and 24.5 MPa for Tyndallstone and potash respectively.

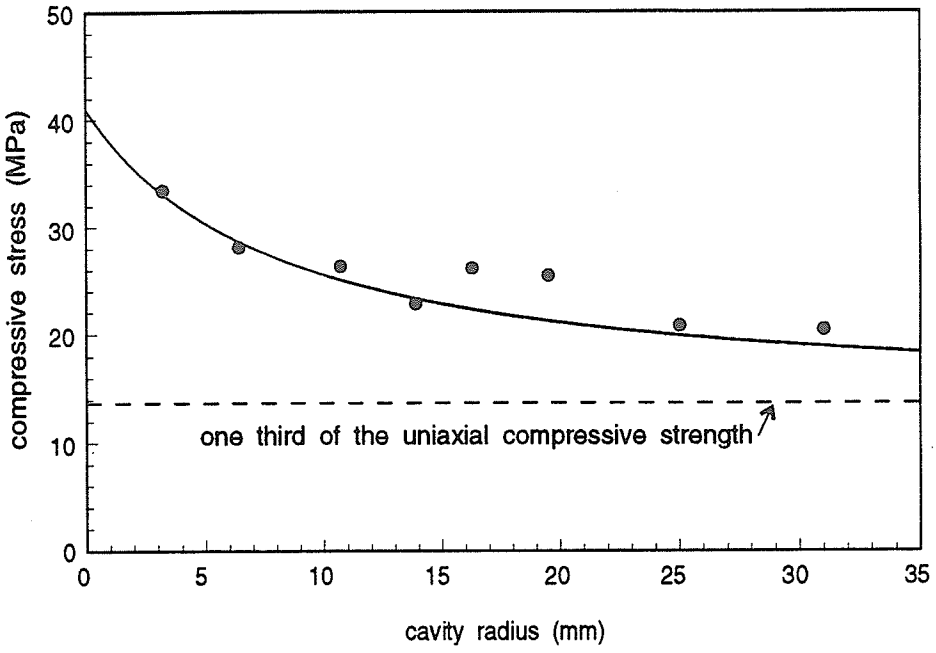

Figure 4.36 Average values of the tangential stress at the sidewalls can be incorporated into the *USR*—Rocker fracture criterion. The model fits the sidewall fracture initiation data for Tyndallstone remarkably well.

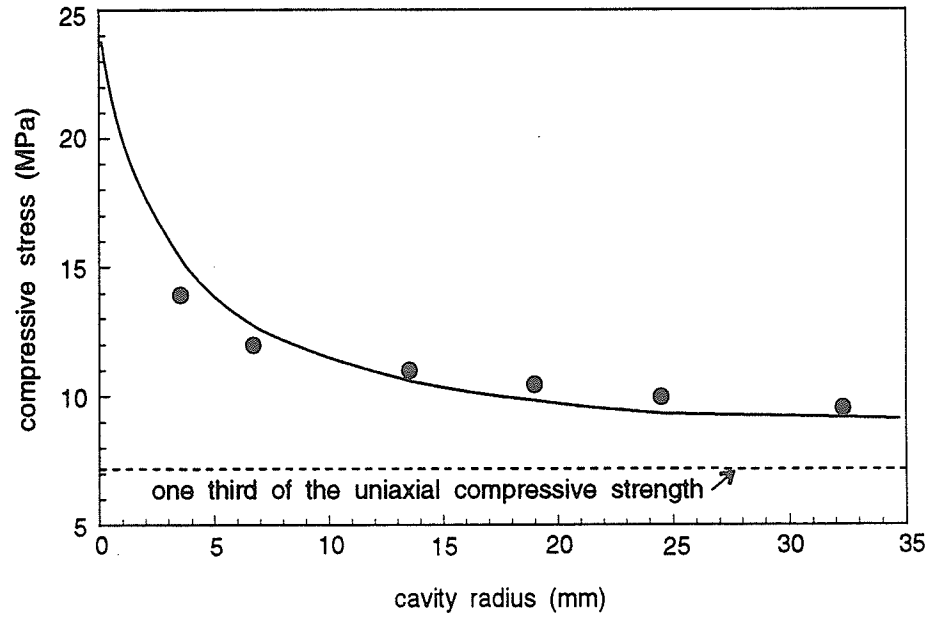

Figure 4.37 The stress-averaging model fits the sidewall fracture initiation data for potash also.

The radial stress can be accounted for by substituting both average stresses into 41, for $USR=1$ and $R=0.5$:

$$P_S = \frac{T_o}{\frac{rE}{2d} - \sqrt{\frac{r^2E^2}{4d^2} + \frac{(r+d)^2F^2T_o^2}{d^2C_o^2}}} \tag{79}$$

where

$$E = 1 - \frac{3r}{2(r+d)} + \frac{r^3}{2(r+d)^3}$$

$$F = 1 - \frac{r^2}{2(r+d)^2} - \frac{r^4}{2(r+d)^4} \tag{80}$$

However, in the physical model tests, the radial stress is the intermediate stress. The minimum principal stress is zero. Therefore this function would only be applicable if an intermediate stress was applied to the faces of the test block. Consequently, only equation (78) was used to model the data. If the exponent (R) of the Rocker function is not 0.5, a numerical procedure is required to find P_S for $USR=1$; the same procedure that was used with the primary fracture model.

At points other than the primary and sidewalls, and for cavities other than circular, the numerical-area-integration scheme can be used to determine the average stress along the fracture path or over a critical area in the crack tip region. Through this type of stress averaging, all fractures can be modeled by one simple procedure using a unified fracture criterion for both tensile and compressive stress states.

4.6 Observations on Crack Stabilization and Offset Cracks

The first crack to form in the model tests is always the primary fracture. It often nucleates and propagates in steps due to the changing mineralogy at the crack tip. In potash, the crack stabilizes as the load increases and eventually refuses to propagate any further. The length of the primary crack increases as the applied stress increases but the curve flattens out as the crack grows, reaching a horizontal asymptote (Figure 4.38). The length of the primary crack is not only a function of the stress, it is also a function of the cavity size. Figure 4.39 shows the final primary crack length, normalized by the cavity radius and then plotted against the cavity radius. The normalized crack length increases as the cavity size increases. This crack length was measured from blocks which remained intact at the end of the test; the primary fracture can easily be obscured by subsequent fractures when the block collapses completely. The primary crack growth was not studied in detail for the limestone or granite models.

The primary fracture has a very large effect on the remote fracture initiation. It is quite common to see a change in the stress-strain curve from the remote gauge when the primary fracture nucleates and as it propagates (Figures 4.9, 12 and 15). On the other hand, the primary fracture does not appear to affect the sidewall fractures. Brady and Brown (1985) show that a plane of weakness in the primary fracture position does not affect the stress at the sidewall. This can also be shown by a finite element analysis. The elastic stress at the springlines was determined as the primary fracture propagated and this stress was plotted against primary crack length (Figure 4.40). The figure shows that as the primary fracture grows, the stress at the sidewall increases a negligible amount.

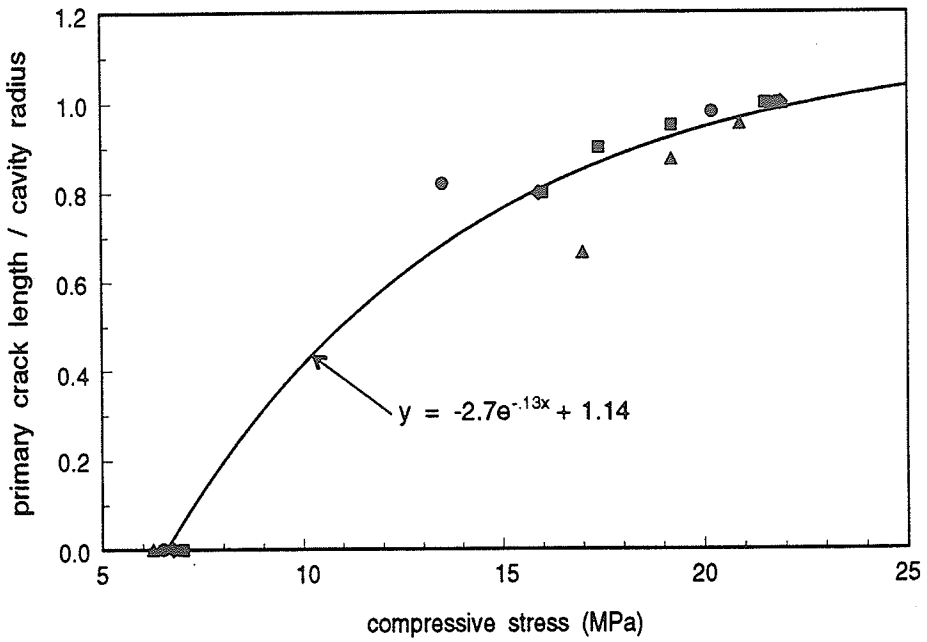

Figure 4.38 The primary crack length (normalized by the cavity radius) grows in a stable manner with increasing uniaxial stress. The curve approaches an asymptote at high stress and the crack does not propagate any further.

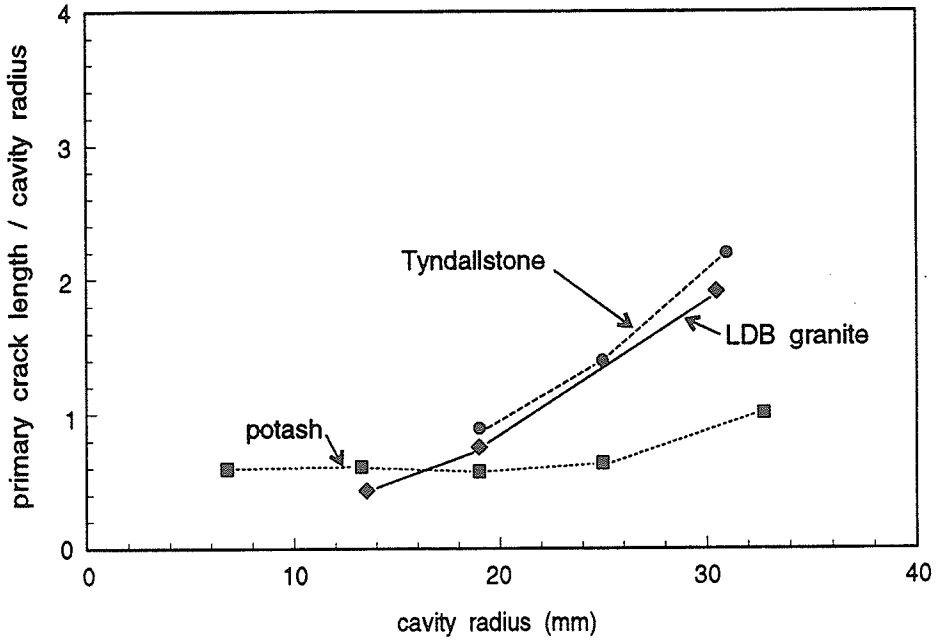

Figure 4.39 The final primary crack length (normalized by the cavity radius) is a function of cavity radius also. The final length increases as the radius increases.

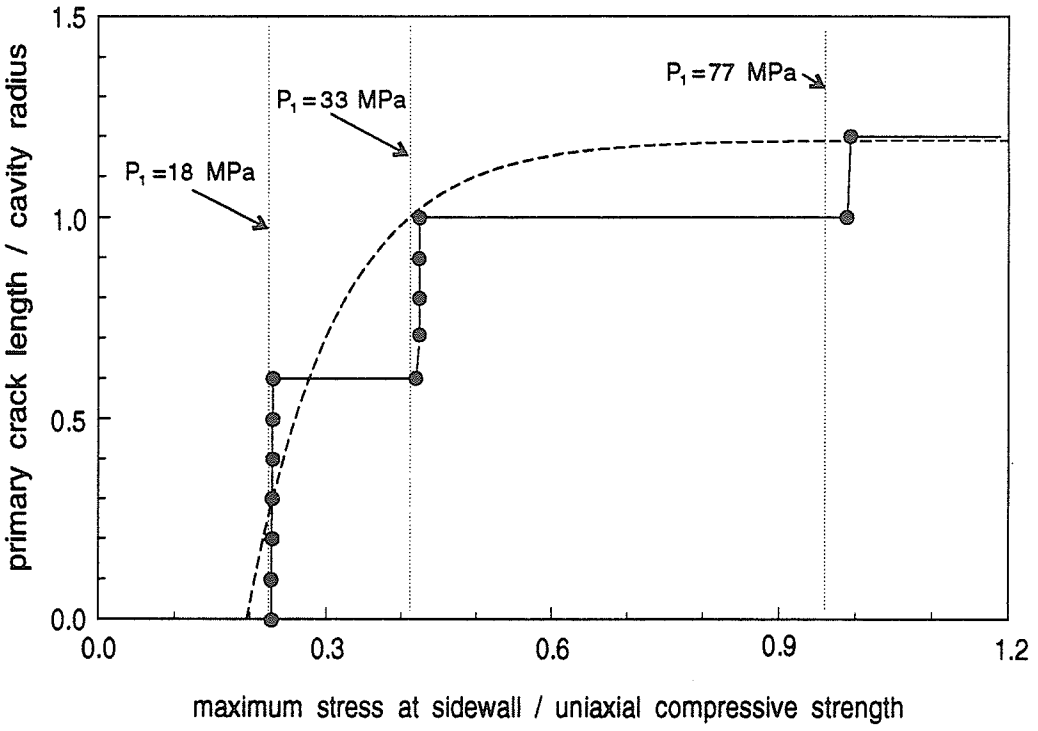

Figure 4.40 A finite element analysis produces the elastic stress at the sidewalls as the primary crack is allowed to propagate. The dotted (vertical) lines indicate the elastic stress for no primary crack (three times the applied load—$(3)\cdot P_1$). The points indicate the length of the primary crack and the evaluated stress at the sidewall. The difference between the theoretical and evaluated stresses is negligible. The crack grows at constant load, then the load must be incremented to cause further growth. The dashed line is the best fit through the final crack length at each load indicating a stable growth.

The evaluated stress is actually very close to the stress predicted by elastic theory for no primary fracture. This figure also shows that the primary crack is stabilizing; an increasing increment of applied load is required to propagate the crack and the amount of propagation at each load increment decreases.

Step-out and en-echelon crack patterns are common in these models as well as in simple laboratory compression tests (Lajtai *et al.*, 1990) and in nature (Pollard and Segall, 1987). The remote fractures are actually offset or step-out cracks from the primary crack; in this case, the primary crack includes the hole (Figures 3.11 and 4.5). Smaller step-out cracks can be found on individual primary, remote and sidewall fractures as well. These en-echelon cracks appear to be a result of the compressive stress field. Cracks grow a certain amount and then stabilize (Figure 4.38). As the load increases the crack length increases but at a decreasing rate. Assuming a stress distribution at the crack tips similar to that of a long ellipse (Lajtai *et al.*, 1990) then another crack, which is offset (remote) from the first one, will be produced once the first (primary) crack reaches a stable length. The rock finds it easier to start and propagate a new crack rather than trying to drive the original crack further. The new crack grows primarily away from the original crack but may also propagate a short distance in the opposite direction producing the rock bridges (Figure 4.41) that are commonly seen between closely spaced, offset cracks. It is also common to see further cracking, buckling and shearing of the bridge material between the first and secondary cracks (Figure 4.42). These en-echelon cracks eventually join together through this process forming a single large fracture. Many of these features will be discussed in more detail in the following chapter.

Fracturing at the sidewalls is a common feature in well bore breakouts and thick-wall cylinder experiments (Zoback *et al.*, 1985; Haimson and Herrick, 1985; Ewy *et al.*, 1987, Kaiser and Malony, 1987; Guenot, 1989; Zheng *et al.*, 1989*b*). Many of these authors have observed sidewall fracturing and explain it through shear failure due to high compressive stresses. Vardoulakis (1984) describes the fracturing at the sidewall by a bifurcation theory which states that these fractures form as spalling or splitting extensional fractures in some cases and as shear fractures in other cases depending on the compressive to tensile strength ratio. By close examination of model blocks used in this study, under the microscope at different stages of loading, it was found that most fractures began as extensional spalling fractures forming parallel to the tunnel wall. Numerous en-echelon cracks usually form first (Figure 4.6); shear fractures may develop at a later stage. The shear fractures form as displacement increases, eventually leading to the ultimate collapse of the cavity. Sidewall fractures have been observed in actual underground excavations for many years (see Hoek and Brown, 1980; Whittaker and Frith, 1990) and will be examined in further detail in Chapter 5.

Figure 4.41 Photograph of en-echelon cracking in potash showing the rock bridges between the en-echelon cracks. Loading is vertical and magnification is four times.

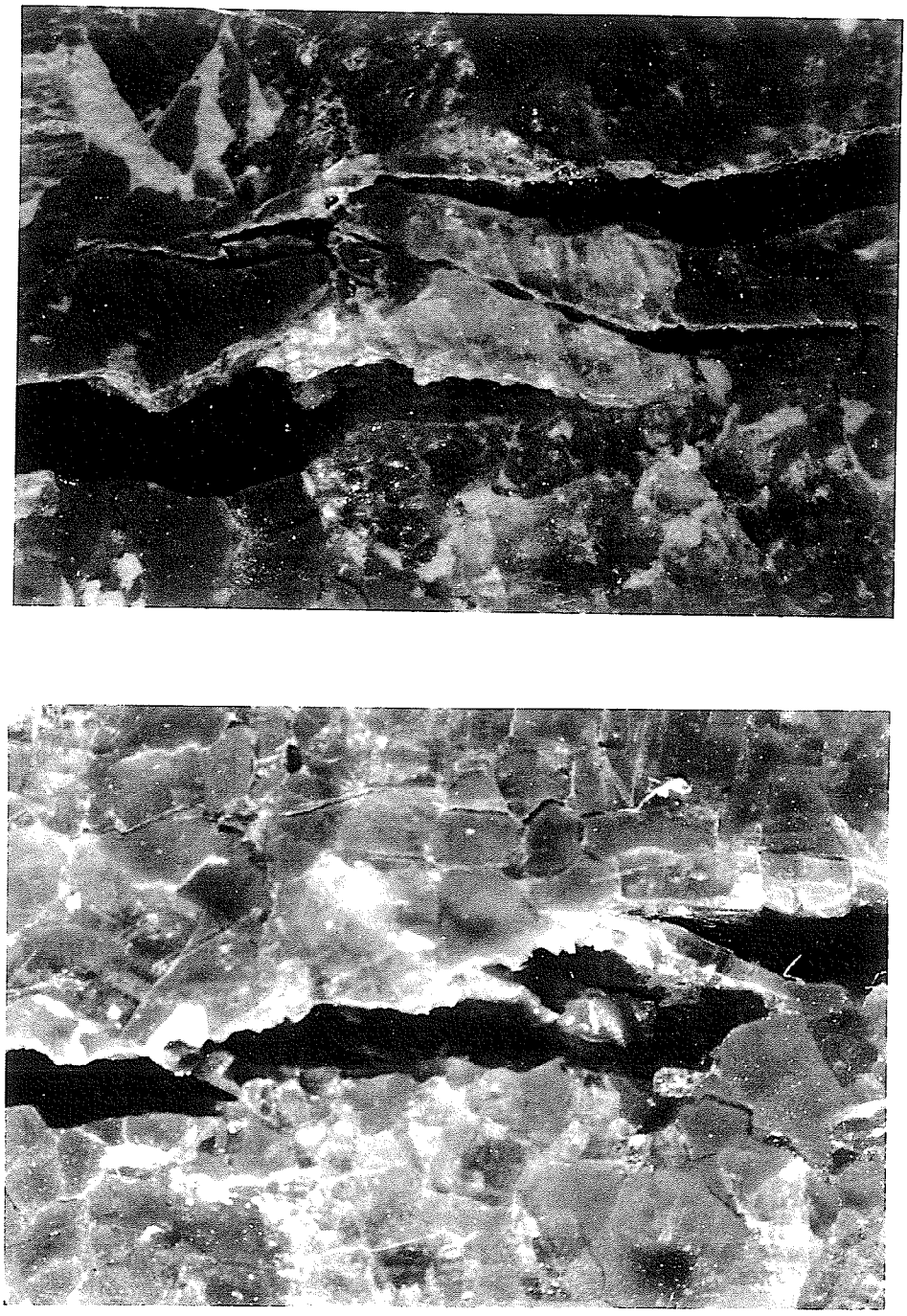

Figure 4.42 Photographs of the buckling and shearing processes which the rock bridges from figure 4.41 undergo. The final result is a single macroscopic crack. Loading is from left to right and magnification is ten times.

5 PHYSICAL MODELS OF POTASH MINE OPENINGS

5.0 Introduction

Numerous fractures exist around the underground excavations of the Cominco potash mine near Vanscoy, Saskatchewan. Many of the fractures are located in the yield pillars and within the sides of tunnels as spalling fractures. The present mining method utilizes narrow yield pillars to produce a more stable structure (Serata, 1982) which prolongs the mine life as well as increasing the extraction ratio. Yield pillars are designed to yield and/or fail as mining extraction proceeds. As a side effect, they provide a cheap *in-situ* compression test. Although the load is unknown, the evolution of fracture is clearly displayed (Figure 5.1). There are fractures in the roof and floor of the mine openings as well. Some of the most interesting fractures exist in a tunnel that was excavated perpendicular to some old collapsed workings. Many fractures are visible in the walls in this area, including some possible remote fractures around the old rooms which closely resemble the fractures seen in the model tests of this study.

The large fractures seen in Figure 5.1 develop by the union of smaller fractures. The slabs of potash bridging the large, open cracks mark positions where the original cracks terminated and new ones began. The pattern is very similar to that observed in the much smaller physical laboratory models (Figures 3.11, 4.41 & 4.42). Consequently, the parameters which control the evolution of fractures in the laboratory and the field are expected to be the same even though the fractures in the mine form in a somewhat different physical and chemical environment. The environment varies due to the presence

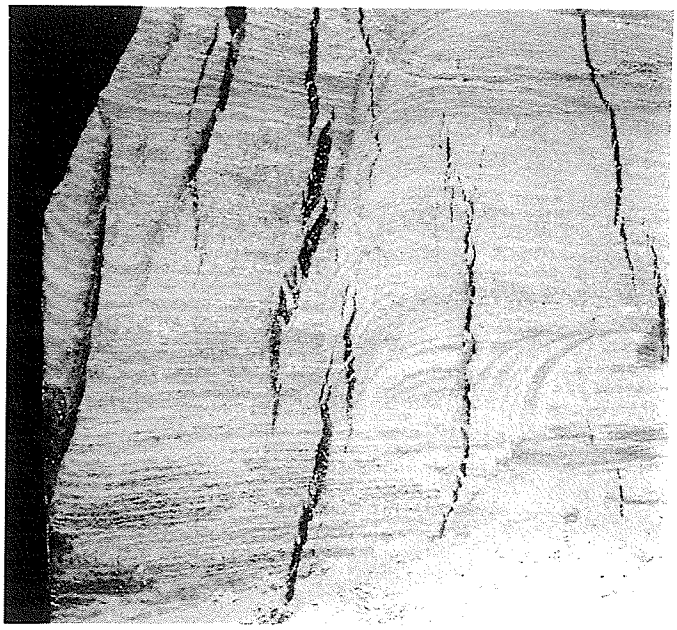

Figure 5.1 A yield pillar in the Cominco potash mine at Vanscoy, Saskatchewan. Many small en-echelon cracks join to form larger cracks. Many of the rock bridges between the cracks can be seen; some of them have already broken. The height shown is about 3 meters.

of multiple openings rather than single cavities, triaxial (possibly hydrostatic) far-field stress rather than uniaxial stress, irregularly shaped openings (almost rectangular) rather than perfectly circular holes, local stratigraphy and layering of different rock types, and varying temperature, humidity and chemistry. Another factor, which is closely connected to the stress state and the physical/chemical environment, is time.

Deformation of salt rocks, at normal room temperatures and pressures, is accomodated by both plastic and brittle strain (Carter and Hansen, 1983; Skrotzki, 1984; Skrotzki and Haasen, 1988*a*). The amount of brittle and plastic strain which occurs in potash depends on the stress level and the confining pressure (Wawersik and Hannum, 1980), as well as on time (Carter and Haasen, 1983), the strain or stressing rate (Horseman and Passaris, 1984), the loading history and the stress path (Senseny, 1984), the temperature (Handin and Carter, 1980; Skrotzki, 1984), the amount of available moisture and the chemical environment (Horseman, 1988), and the mineralogy, texture and grain size (Skrotzki and Haasen, 1988*b*). Most of the plastic strain in salt rocks results from the movement of dislocations on the two slip planes of the salt crystals (Haasen, 1985). Additional plastic strain may however come from grain boundary sliding and from the compaction of clay pods and layers that may form as much as 5 percent of the potash rock in the Saskatoon mines (Worsely and Fuzesy, 1979). The brittle stain comes from microfractures, more specifically from the lateral dilation of tensile microcracks that form sub-parallel to the maximum principal stress (Fairhurst and Cook, 1966). At the microscopic scale, the brittle fractures follow one or two of the cleavage planes of the salt crystals as well as the grain boundaries. A significant amount of strain

may also come from ductile fracture along suitable oriented grain boundaries where dislocation movements may lead to the formation of cavities (Ghandi and Ashby, 1979; Suresh and Brockenbrough, 1990).

Brittle, tensile microcracks in rocks are expected to nucleate at the various types of inhomogeneities that often concentrate around grain boundaries (Ghandi and Ashby, 1979; Tapponier and Brace, 1976). With rising stress or elapsed time, the propagating microcracks can turn into macrofractures and eventually into megascopic features that are several meters long as seen in the yield pillars of the Cominco Ltd. potash mine near Vanscoy, Saskatchewan. The whole fracture process, particularly its stress and time dependence are largely unknown for the potash mining environment. The fractures must grow both in length and width, either as the load increases on the pillars or as time increases. In a mining operation, it is usually very difficult to make the detailed observations and measurements that are necessary to separate the stress and time effects.

As suggested by the literature referenced above, abundant studies on time and stress dependence of plastic and brittle strain have been completed for both single crystals and multi-mineral rock salt assemblages, utilizing standard laboratory tests such as triaxial compression and creep. There are also a significant number of papers documenting the time dependent ductile behaviour of salt rocks in the field, including detailed measurements of cavity closure (Herget and Mackintosh, 1987; Hambley and Mraz, 1987). Conversely, very little exists in the literature describing the brittle fractures which form around excavations in the potash mines (Chen *et al.*, 1991; Haupt and Natau, 1988; Mraz, 1987). Alternatively, there are more references describing the fractures in the

more brittle rock of the usual mining environment (Hoek and Brown, 1980; Kaiser *et al.*, 1985). Fracturing around cavities has also been studied through physical modeling (Hoek, 1966; Gay, 1976; Lajtai and Lajtai, 1975; Carter *et al.*, 1991b) which simplifies the fracture monitoring procedure and allows tests to be conducted under controlled conditions.

The purpose of this chapter is to determine the effect of some of these different parameters through physical model tests, in a controlled environment. The effects of time and stress level on fracture initiation and propagation will be studied by performing creep tests on simple physical potash models. At the same time, the physical process of crack initiation and propagation in compression will be described in some detail. The influence of the local stratigraphy will be examined through a scaled model of a room at the Vanscoy mine. The final physical model will be used to monitor the fracture process in the presence of multiple openings.

5.1 Modeling Time and Stress Dependent Fracture Around Cavities

The first modeling exercise is aimed at defining the relationship between the stress level and fracture growth, including the effects of time. Fracture growth in the mining environment is rarely measured; careful monitoring of fractures through time is even less frequent. Fractures may form immediately upon excavation but it is probable that with increasing time and closure of the mine openings, fractures continue to initiate and propagate. (See also Carter and Lajtai, 1992 *a and b.*)

Potash rock is a relatively soft, ductile rock with many physical properties that are strongly time- and loading-rate-dependent (Duncan, 1990; Lajtai *et al.*, 1991*b*). A number of creep tests on potash have been done (Duncan, 1990) which show that both time and stress level affect the rock strength (Figure 2.21). Creep tests at varying stress levels indicate that there is a stress level under which the strain will attenuate and the rock will remain stable. Above this stress level, the strain continuously increases, leading to secondary and/or tertiary creep, including instability and failure.

The stress—strain diagrams (Figures 2.18 and 2.22) and the creep curves (Figures 2.21 and 2.23) give a general idea about the significance of cracking during the deformation of potash. This includes details on the entry of cracking and the volume of brittle strain produced. However they do not reveal the physical process of discrete crack growth since only the gross effect of the microcracks is documented. In the macroscopically homogeneous stress field of the laboratory specimen, all the crack initiation sites have an equal chance of becoming effective. Consequently, microcracks grow in profusion. A better environment for the study of discrete fracture is offered by the heterogeneous stress field which exists around cavities.

Model tests on blocks of rock with central circular cavities show the same trend as simple laboratory creep tests when subjected to creep at different stress levels. During model testing, both individual and total crack growth can be monitored; as the load increases or the time increases with the stress constant. This exercise is closely related to the study of subcritical crack growth in rocks and minerals (Atkinson and Meredith, 1987) which has shown that cracks can propagate with time depending on the stress and

the chemical environment. To the author's knowledge however, the time- and stress-dependence of discrete fracture growth in Saskatchewan potash have not previously been studied.

The first portion of this chapter involves both time- and stress-dependent fracture growth. Four rectangular potash models were tested under constant uniaxial loads. The models varied in size (Table 5.1) which controlled the amount of applied stress. The samples were loaded in a 35,000 lb loading frame with springs underneath the loading platen (Figure 5.2) in an attempt to maintain a constant load during the creep stage. All of the blocks had a cavity diameter between 48 and 49 mm and all blocks were instrumented with strain gauges similar to the previously described models (Figure 4.11). In addition to the strain gauges, the fractures were monitored using a low-power microscope mounted in front of the specimen. Loading was done in steps to allow time for viewing the fractures. Testing was done in a controlled-environment room where the temperature was kept at 20°C and the relative humidity at about 30%.

Table 5.1 Models used to measure stress and time dependent fracture growth.

Block #	Model Dimensions w h t (mm)	Applied Stress Peak Decay (MPa)	Time Under Load (hrs)	Grain Size (fine/coarse)
1	231 264 92	7.2 6.5	300	fine
2	208 245 100	7.2 6.3	40	coarse
3	180 204 74	11.5 10.3	3216	fine
4	167 197 69	13.9 11.9 (10)	310	fine

Note: fine grained potash has crystals in the 2- to 10-mm range, while coarse-grained potash has crystals which are in the 5- to 40-mm range.

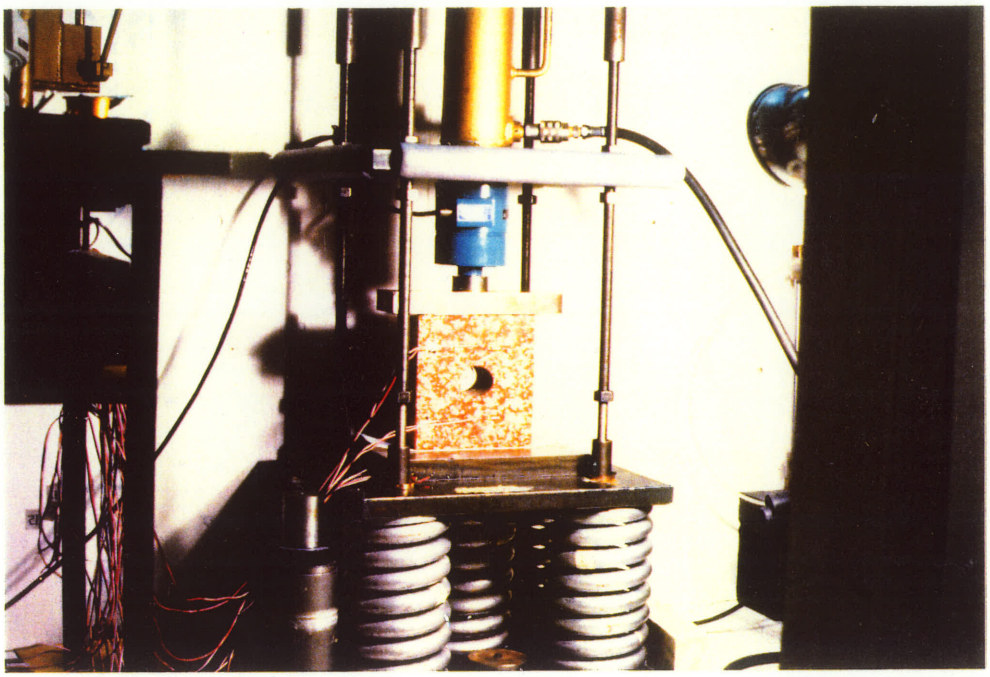

Figure 5.2 The creep-loading frame with a block of potash. The springs beneath the lower metal platen are intended to maintain a constant load.

5.1.1 Stress Dependence

In a solid block of potash (no cavity), and in response to rising stress, observable (under the microscope, at least) cracks form at a relatively high stress, about 50-80 percent of strength (Figure 2.18). However, this depends greatly on the loading rate (Figure 2.22). Cracking may start at a lower stress when the loading or the induced displacement rate is fast, in excess of 1 με/s (tests lasting less than one hour). Once the crack initiation stress is exceeded, crack density increases rapidly, indicated by the volumetric reversal which starts at about 90 percent of strength (Figure 2.18). Although individual cracks may extend and dilate with increasing stress, much of the measured dilation comes from crack multiplication; from increasing crack density rather than individual crack extension and dilation.

Testing a perforated rather than a solid block of potash extends the stress range over which both crack extension and crack multiplication can be observed. The first crack can be detected as early as 4 MPa (Figure 5.3a) in the form of a primary fracture that appears at the tensile stress concentration of the cylindrical cavity (the crown or invert under a vertical uniaxial load). The next fracture (Figure 5.3b) may form in a position that is either remote from the perimeter (above or below) or very close to the compressive stress concentrations at the sides (slabbing fracture). Individual fractures do not usually travel far. Instead, they often give rise to step-out (daughter) cracks, eventually forming an en-echelon pattern (Figures 5.3c and 5.3d). The total crack length, which is the sum of all the discrete crack lengths, increases exponentially with increasing stress (Figure 5.4). The rate of increase increases after 13 MPa (point D), approaching

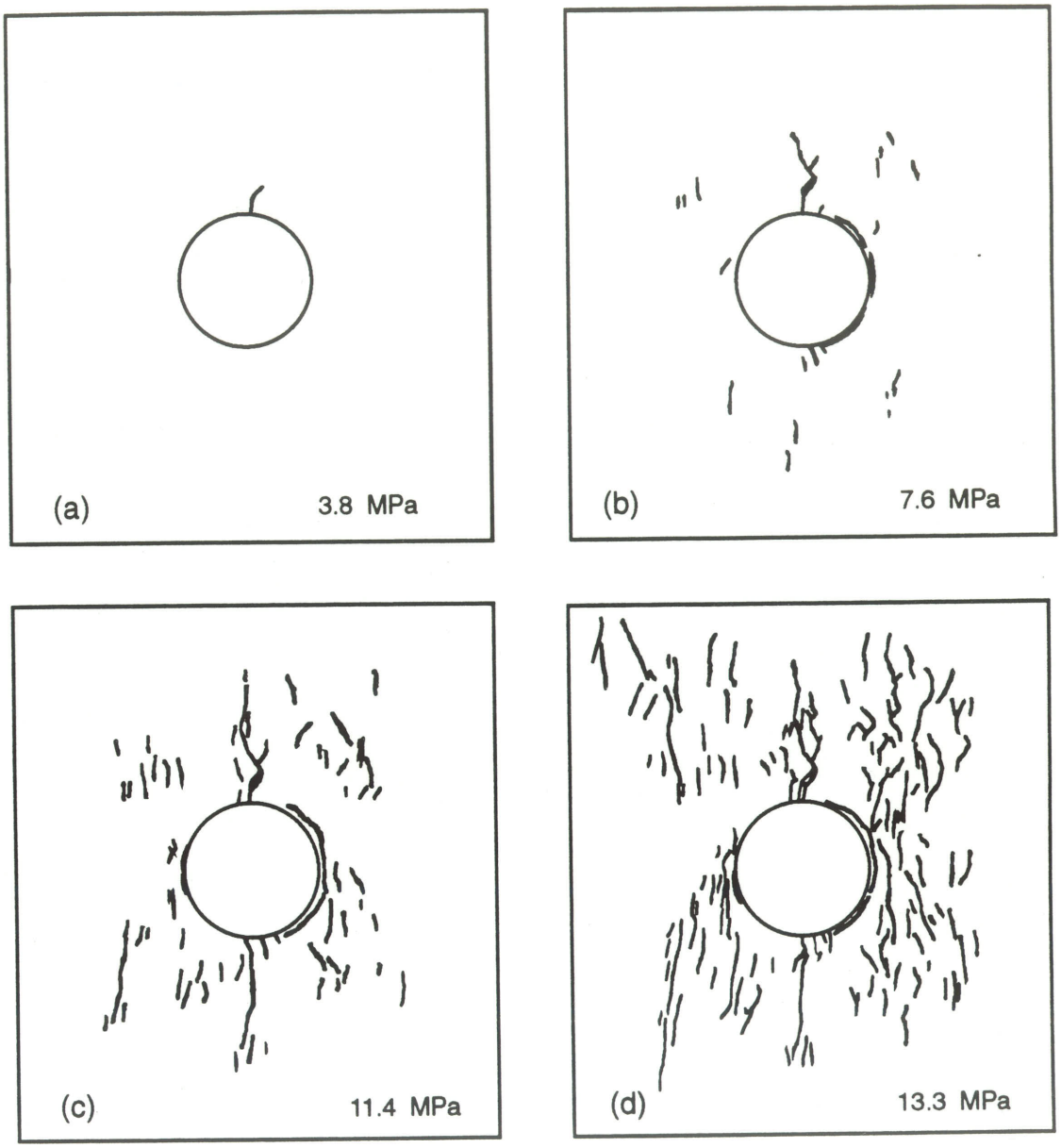

Figure 5.3 A tracing of cracks showing the stress-dependent crack growth around modeled circular cavities in potash, subjected to uniaxial compression (vertical). The primary crack forms first (a) followed by remote and sidewall cracks (b-d). The remote-crack system consists of many small en-echelon cracks covering an area from the sidewalls to the corners of the block.

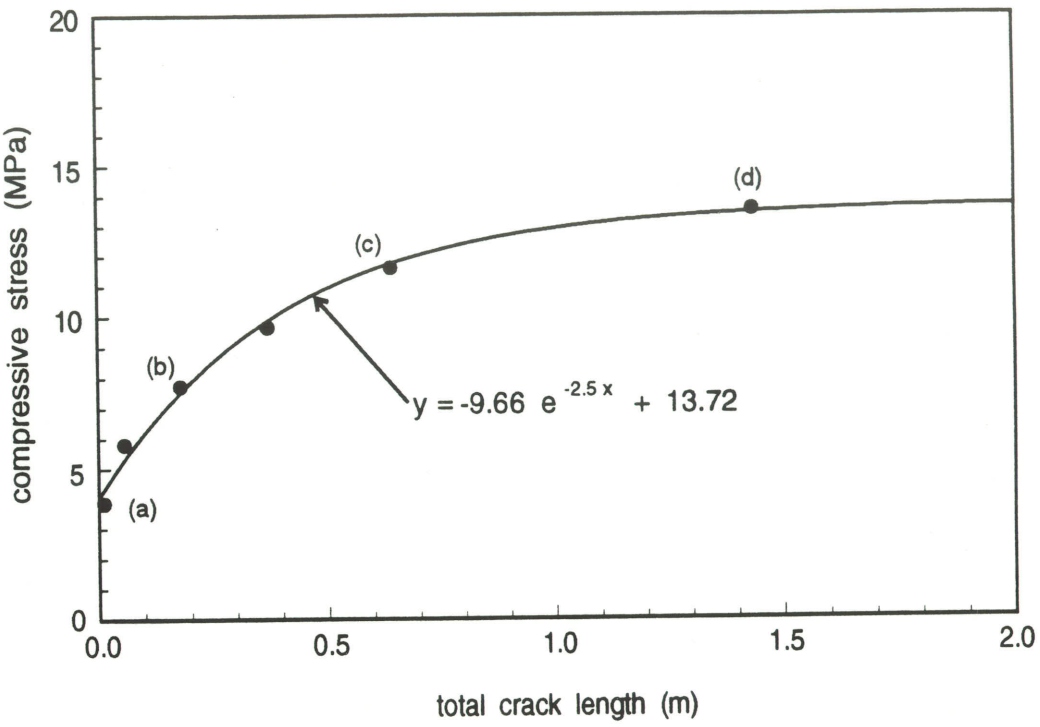

Figure 5.4 The total crack length (sum of all crack lengths) increases exponentially with rising stress. At a load between 13 and 14 MPa, the model becomes unstable.

a horizontal asymptote of 13.7 MPa, suggesting that fracture propagation would become unstable at this stress level.

The load was applied in steps to allow time for viewing and mapping the fractures with the aid of a microscope; the average loading rate was 0.2 MPa per minute. Undoubtedly, the rate of fracture evolution would change with the rate of load application but this effect was not investigated for these model tests.

5.1.2 Time Dependence

Crack growth (extension and multiplication) in potash is strongly time-dependent. In fact, there is little if any difference between the gross physical effect of time at constant stress and the effect of rising stress in short-term experiments. Not unexpectedly, the total crack length as a function of time at constant load resembles the course of the volumetric strain in conventional creep tests (Duncan and Lajtai, 1991). Figure 2.23 shows typical volumetric creep curves for various stress levels. These curves resemble those for total crack length with time (Figure 5.5).

5.1.2.1 Uniaxial Load of 7 MPa

The first test block was fine-grained and quite large in size (Table 5.1). Thus it could only be loaded to 7.2 MPa. At this stress level, there is very little crack growth beyond primary fracture initiation and the total crack length measured at the start of the experiment did not change during the test duration (Figure 5.5). After 200 to 300 hours

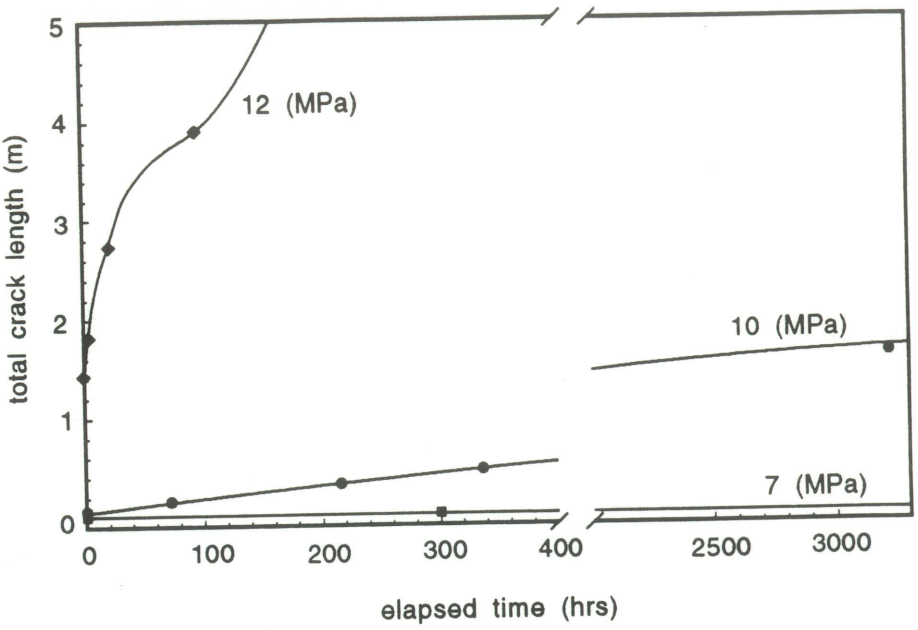

Figure 5.5 The total crack length on the surface of the potash blocks is a function of both time and stress level. At loads above about 12 MPa, the block is unstable and fails after a short time. Below about 10 MPa, the block is stable and rate of total crack length growth decreases with time.

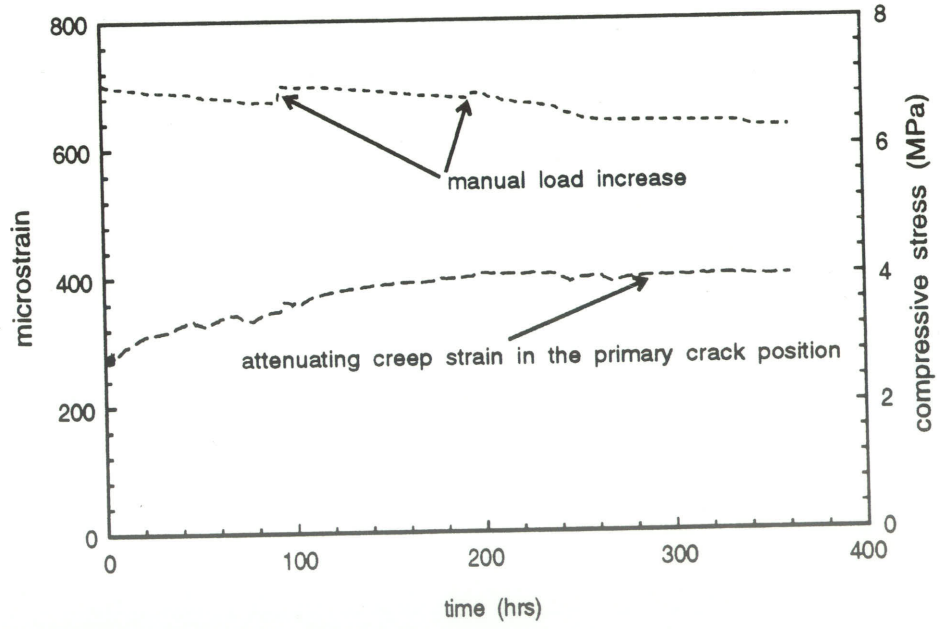

Figure 5.6 The strain at the location of primary crack initiation attenuates after about 300 hours under an average uniaxial compressive load of 6.5 MPa. The load decays slowly with time.

the stress-strain curves attenuated (Figure 5.6) with the block remaining stable. The peak load decayed down to a load of about 6.5 MPa where it was quite steady (Figure 5.6). The load was adjusted several times by manually tightening the nuts on the loading frame. This is seen in the jumps of the load—relaxation curve. The load always decayed back to its stable level quite quickly after each load increase. The creep curves were analyzed by performing a moving-point linear regression (Figure 5.7) which clearly shows that the strain attenuated between 200 and 300 hours. The slope is essentially zero at 300 hours, the point at which the test was terminated.

The second block consisted of coarse-grained potash (Table 5.1), which is generally weaker and more ductile, usually producing more erratic results (Duncan, 1990). One primary fracture was visible immediately after loading and the stress—strain curves indicated that the second primary fracture had initiated as well (Figure 5.8), although it was not clearly visible even with the microscope. Based on the stress—strain curves, the primary fractures began at about 2 MPa rather than the 4 MPa required for the first block. There were no remote cracks visible after the initial loading to 7.2 MPa or after 40 hours of creep at the stabilized load of 6.3 MPa. The test was stopped after only 40 hours as the creep curves were attenuating and, based on the previous test, it was felt that this block would also remain stable.

5.1.2.2 Uniaxial Load of 10 MPa

There was substantial time-dependent crack growth at 10 MPa. The crack pattern is shown for five sets of crack measurements (Figure 5.9). The first cracks to form were

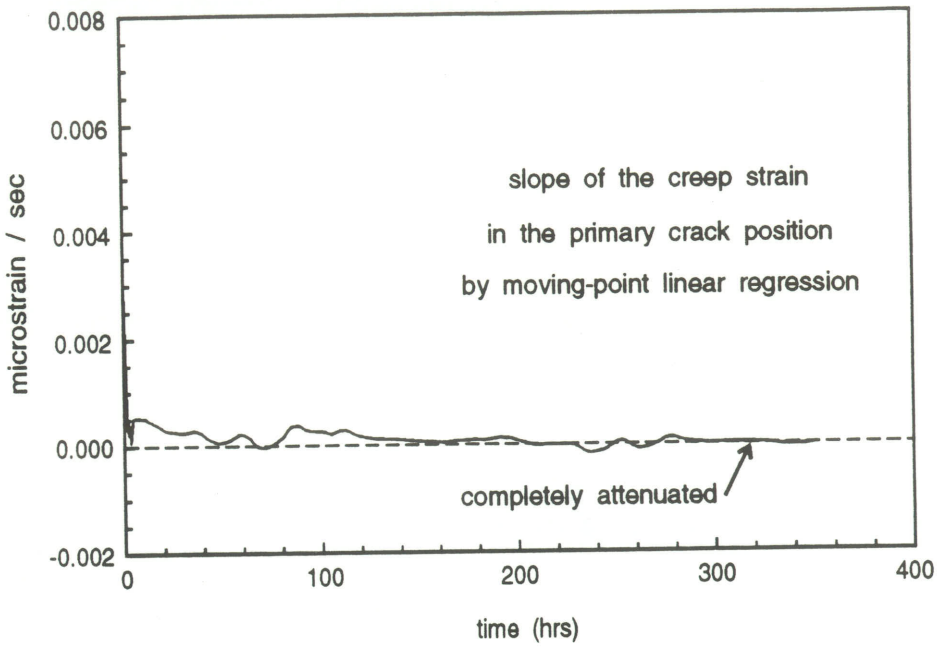

Figure 5.7 A moving-point linear regression on the primary creep strain at 6.5 MPa shows that the slope of the creep curve is zero at 300 hours.

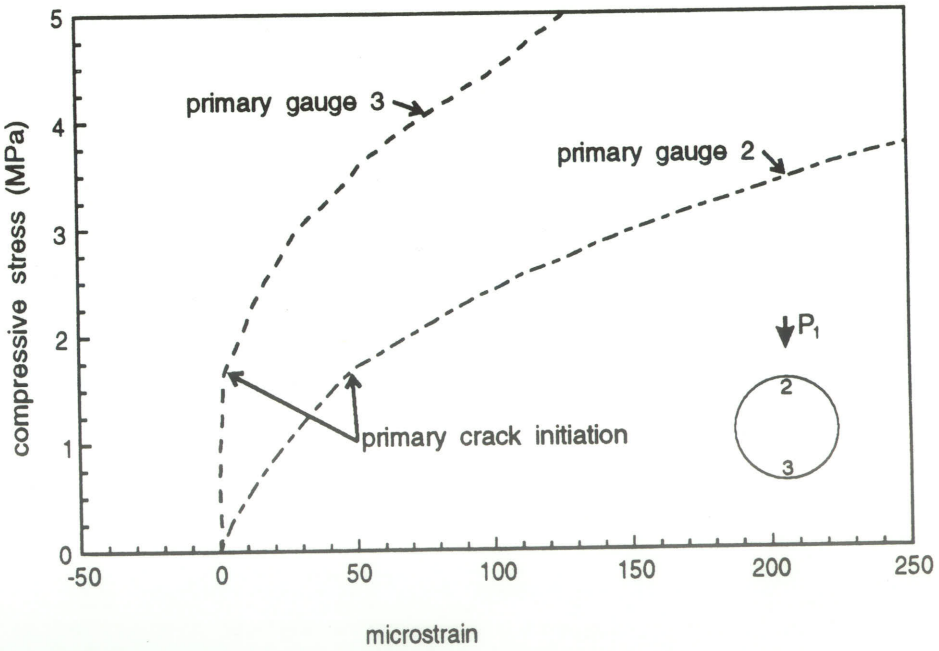

Figure 5.8 The stress—strain curves for the primary crack location indicate crack initiation at a load just below 2 MPa by the abrupt change in the curve.

the primary cracks at the tensile stress concentrations (Figure 5.9a). One primary crack initiated at about 2.5 MPa while the other initiated at about 4.5 MPa (Figure 5.10). Both fractures were visible (with the naked eye) during the initial loading process. These two cracks are very stable and propagate only a small amount over the 5-month duration (Figure 5.9a-e). The second crack to form was one of the remote cracks which initiated at a load of 7 MPa. This crack was soon followed by the formation of the other three remote fractures (Figure 5.9b). The remote fractures are not single cracks but consist of multiple, offset-crack systems covering an area from the compressive stress concentration at the sidewall to the corners of the block. Sidewall fractures can also be seen in this model (Figure 5.9c-e).

Under a constant load of 10 MPa, the rate of total crack length growth declined in time simulating a transient creep strain condition (Figure 5.11). The total crack length was calculated from the mapped overlays and was modeled by a simple exponential function which shows a decaying rate of growth as the curve tends towards a horizontal asymptote. The data fit this curve with an SSE of 44,328 as compared to 141,224 for a power function; the sum of squares of the error (SSE) is a standard measure of the least-squares fit. The decaying exponential provides a better fit than the slowly increasing power function. This is supported by the visual evidence which indicates that the rate of total crack-length growth is decreasing with time under the uniaxial load of 10 MPa.

The total crack length as measured from the mapped overlays, rather than the strain gauge data, is used to measure the relative strain in the block. There are several

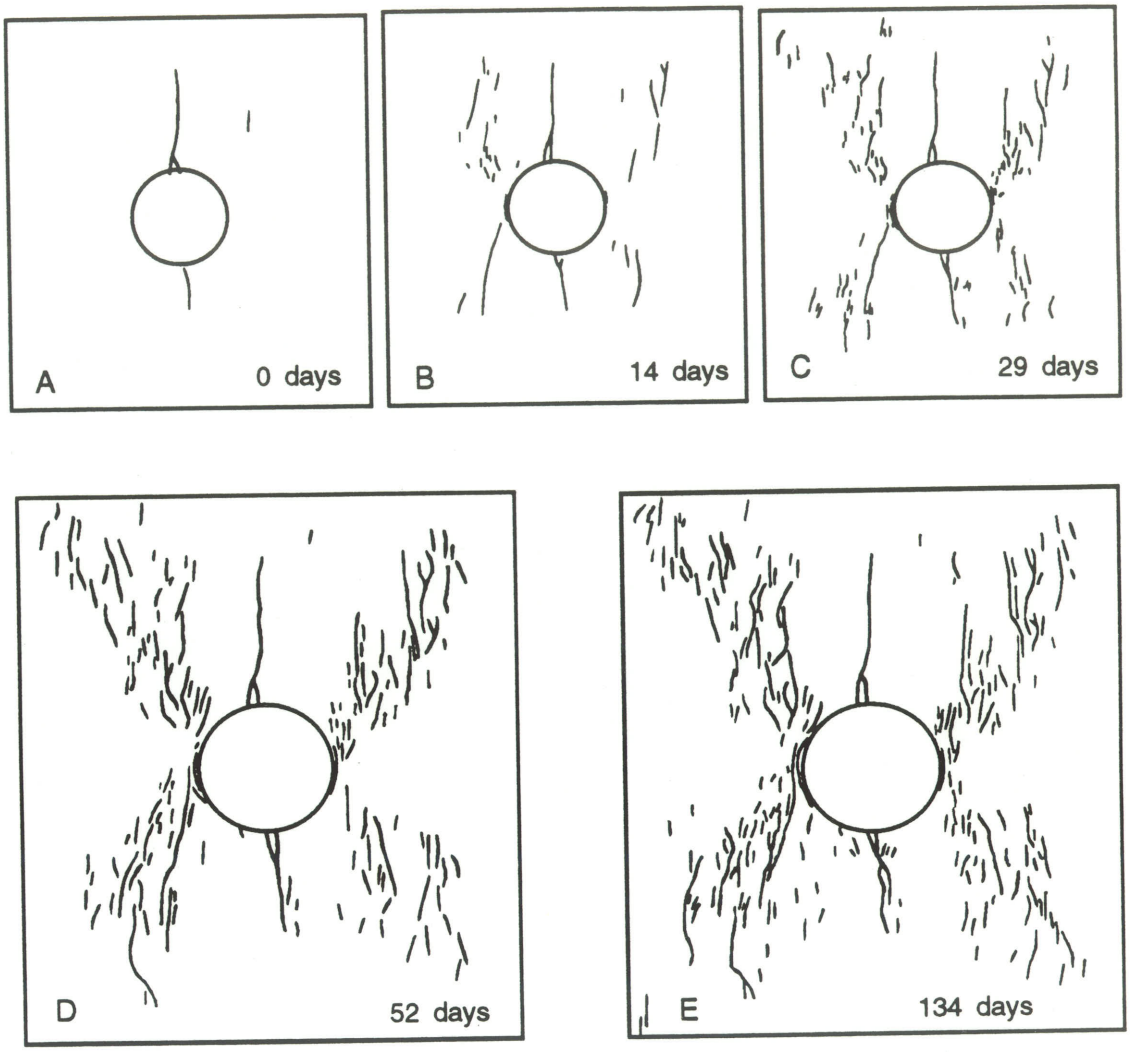

Figure 5.9 Tracings of cracks showing the accumulation of cracks around modeled circular cavities through time for a uniaxial load of 10 MPa.

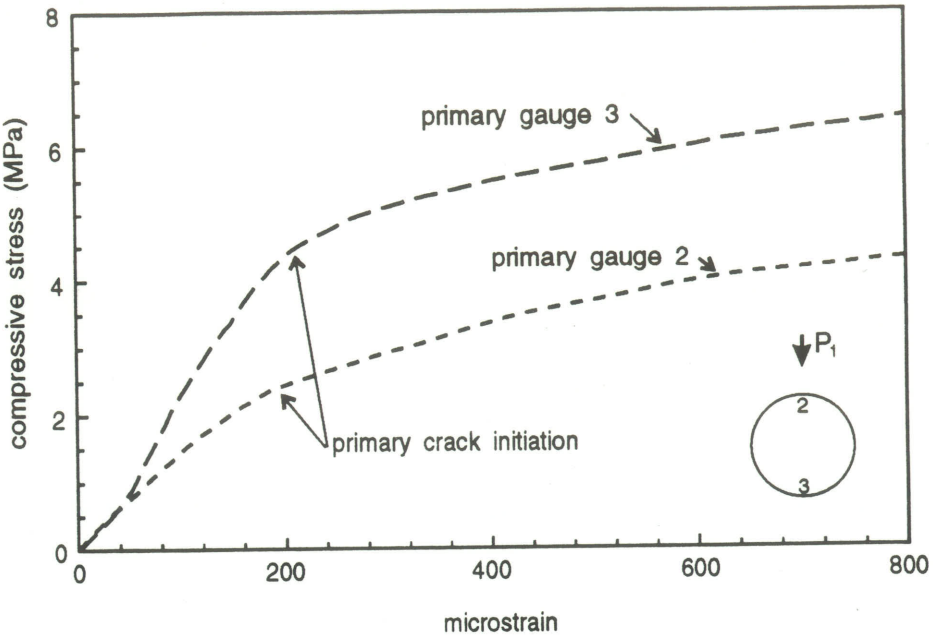

Figure 5.10 The stress—strain curves for the primary crack location indicate crack initiation, at loads of 2.5 and 4.5 MPa, by the abrupt change in the curve.

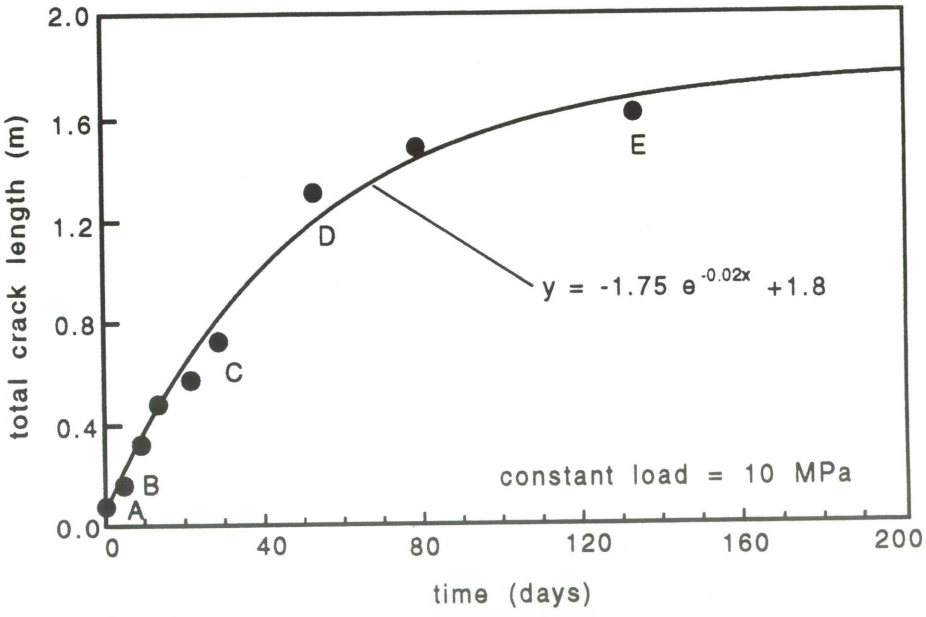

Figure 5.11 The total crack length shows a decreasing trend with increasing time at a 10-MPa stress level. The points on the graph represent the total crack length for the respective tracings in Figure 5.9. The data were fitted to an exponential curve with an asymptote.

reasons for this. The strain gauges show different stages of creep at different times because the various crack systems initiate at different times and at different stress levels. As well, the gauges are only useful for a short time, prior to breaking and/or detaching; the block remains stable even when several or all of the gauges are lost. Thus, the total crack length provides a much better picture of the average state of the entire block. Another way of measuring the state of the block is to monitor the hole closure. The circular hole acquired an elliptical shape with an increase in the horizontal diameter and a decrease (closure) in the vertical diameter (Figure 5.12). This closure is a function of time and stress and is strongly related to the surrounding deformation.

5.1.2.3 Uniaxial Load of 12 MPa

There were fewer measurements at 12 MPa as this block collapsed after only two weeks suggesting that the course of crack growth and multiplication went from the initial transient stage directly to the tertiary stage. Cracking had already progressed to a critical condition at the end of the initial loading sequence (Figure 5.3d). With increasing time, the total crack length increased further due to the multiplying offset cracks and cracking of the bridge material between offset fractures. The block disintegrated completely leaving mostly dust and grain-size particles as it collapsed in the soft, spring-loaded, creep frame.

The peak load of 13.9 MPa shown in Figure 5.3d quickly relaxed down to about 12 MPa after only 1-2 hours and continued to decay even with occasional load increases.

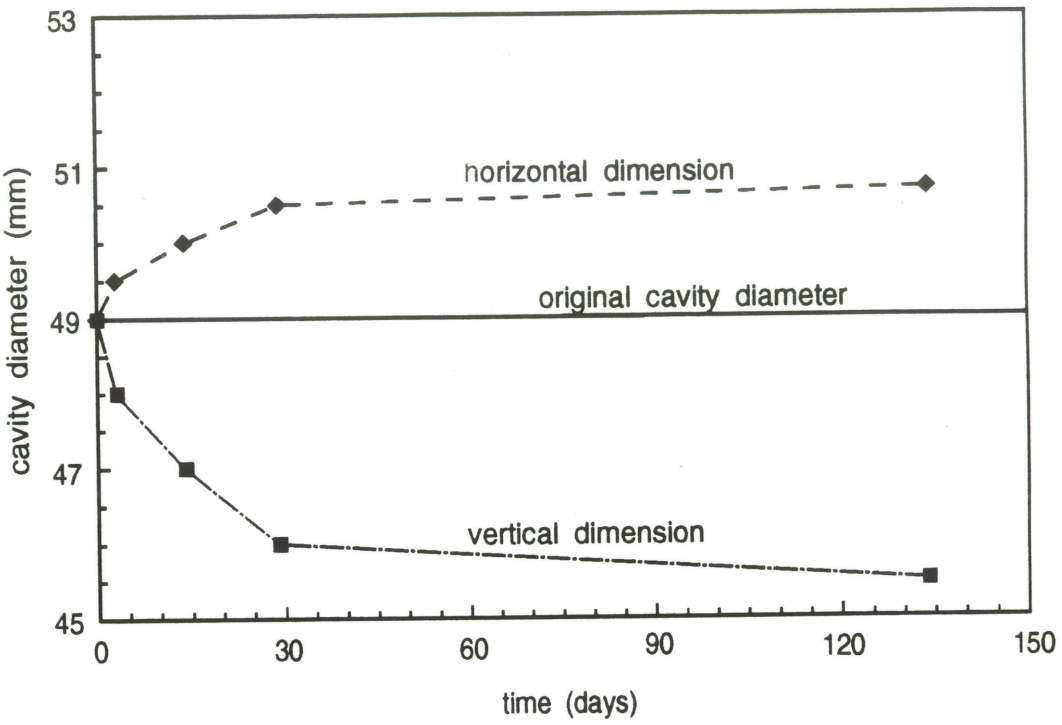

Figure 5.12 The cavity dimensions change with time. The horizontal dimension increases and the vertical dimension decreases. Both appear to be approaching a constant value.

The decay rate slowed after the first day and the load at failure, after almost 13 days, was only 10 MPa. The block was instrumented with strain gauges as were the previous three blocks. However, several extra gauges were applied to this model to determine the strain distributions away from the cavity along the primary fracture direction and along the horizontal direction at the springline. These distributions were examined previously in Chapter 4. An extra gauge was placed on the surface, at the springline location, in the lateral direction to give a better indication of sidewall crack initiation (Figure 5.13). This region is subject to highly compressive axial stress similar to a standard uniaxial compression test. Based on the uniaxial compression tests, it is often necessary to have both axial and lateral gauges to determine the crack initiation stress in potash; even then it is a difficult task. Figure 5.13 indicates that the lateral gauge is no better at providing the sidewall crack initiation data than the axial gauges. This could be a result of the yielding which is evident in the curves. The gauges were useful only during the initial loading stage as the block had cracks either through or beside the gauges after the initial loading was completed.

The cracks in this block were visually monitored during the loading stage as well as during the creep phase. The cracks were mapped, with the aid of the microscope, onto clear overlays to monitor crack growth with time. As well, several of the fractures were photographed occasionally to provide a visual record of the cracking process through time. The total crack length was measured through time and the data follow a much different trend than in the previous three models. The crack length indicates that this block progressed from primary creep directly to tertiary creep; tertiary creep is

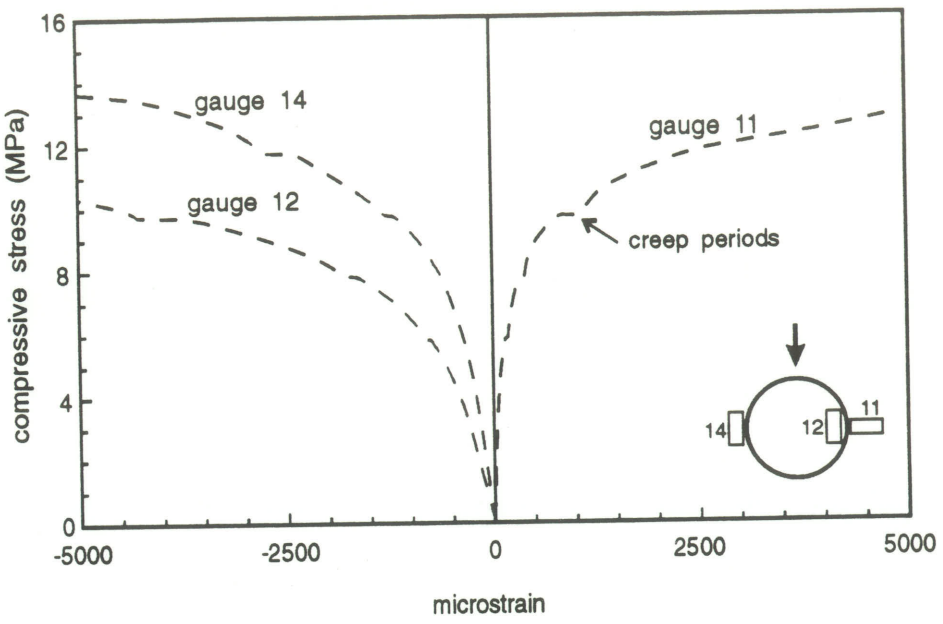

Figure 5.13 Changing the position (inside or outside the hole) and orientation (axial or lateral) of strain gauges at the springline does not help much in picking the crack initiation stress from the stress—strain curves. A difference in the amount of strain is indicated, however.

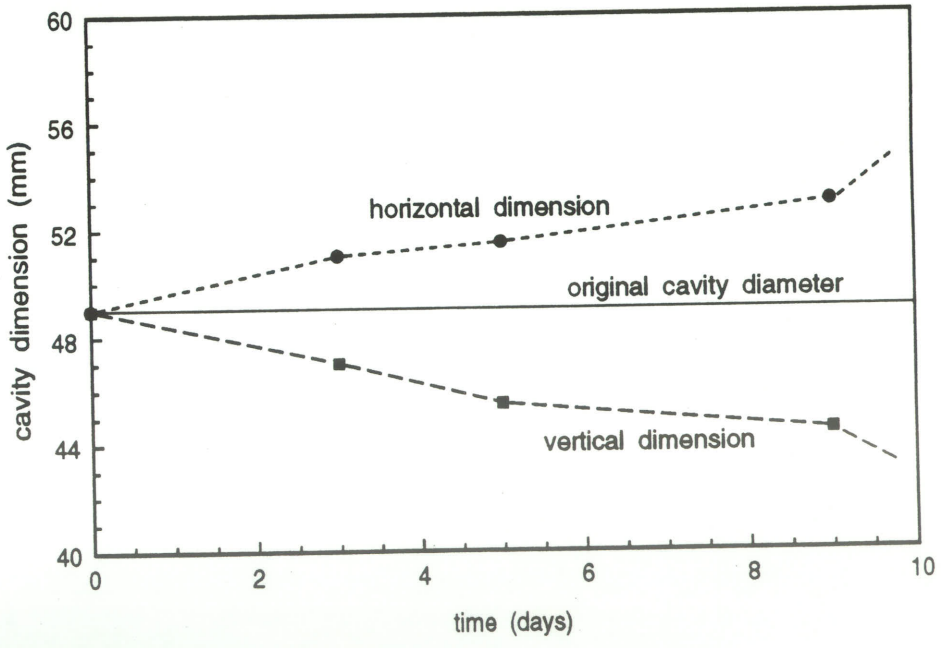

Figure 5.14 The cavity dimensions change with time. The horizontal dimension increases and the vertical dimension decreases. The model collapsed at about 13 days.

indicated by the dramatic increase in crack growth rate (Figure 5.5). The total crack length (strain) increases toward infinity at 310 hours, the time of failure. Regular creep curves for potash (Duncan, 1990) show similar trends to these four models but a complete study of creep curves and the available creep models will not be undertaken in this thesis (see Duncan, 1990 and Duncan and Lajtai, 1991 for more details on the creep of potash).

The displacement inside the hole in both the horizontal and vertical directions was also measured during the loading process and during the creep stage. Closure did not occur during the loading stage; it began only after the block was allowed to creep for a few hours. Figure 5.14 shows the rate of change in the vertical and horizontal dimensions over time. These curves follow the same trend as the strain or total crack length.

The time-dependent history of the remote crack system in the lower left corner of the block was captured through photography and the results are sketched in Figure 5.15. There are two important features to note here. The crack pattern consisting of a narrowly spaced, en-echelon (mother-daughter) crack pattern at the extreme left evolves in time to form a macroscopic extensile crack. The pattern to the right developed close to the cavity perimeter under a high compressive load and low confining stress. This type of arrangement of tensile fractures, where the individual members of the en-echelon pattern are shorter but more widely-spaced, often leads to the eventual formation of a shear fracture at the time of cavity (model) collapse.

The photographs (Figures 5.16a-f) show the changes that a single crack goes through as well as how the remote fracture system grows and joins the sidewall fracture

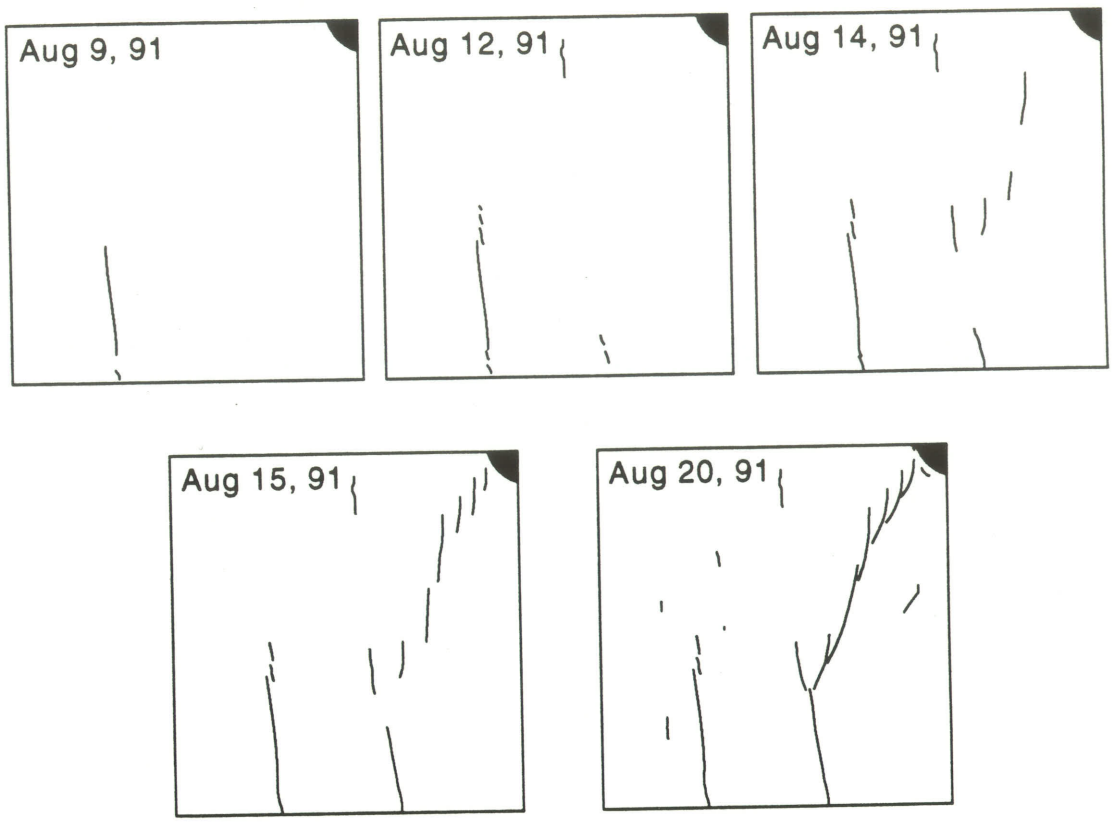

Figure 5.15 A tracing of the cracks in the lower-left remote crack region. The first crack is stable but grows in time through the union of smaller offset cracks at its tip. A closely spaced set of shorter, en-echelon cracks develops in the highly compressive stress region near the side of the cavity. The latter pattern often leads to shear fracture development.

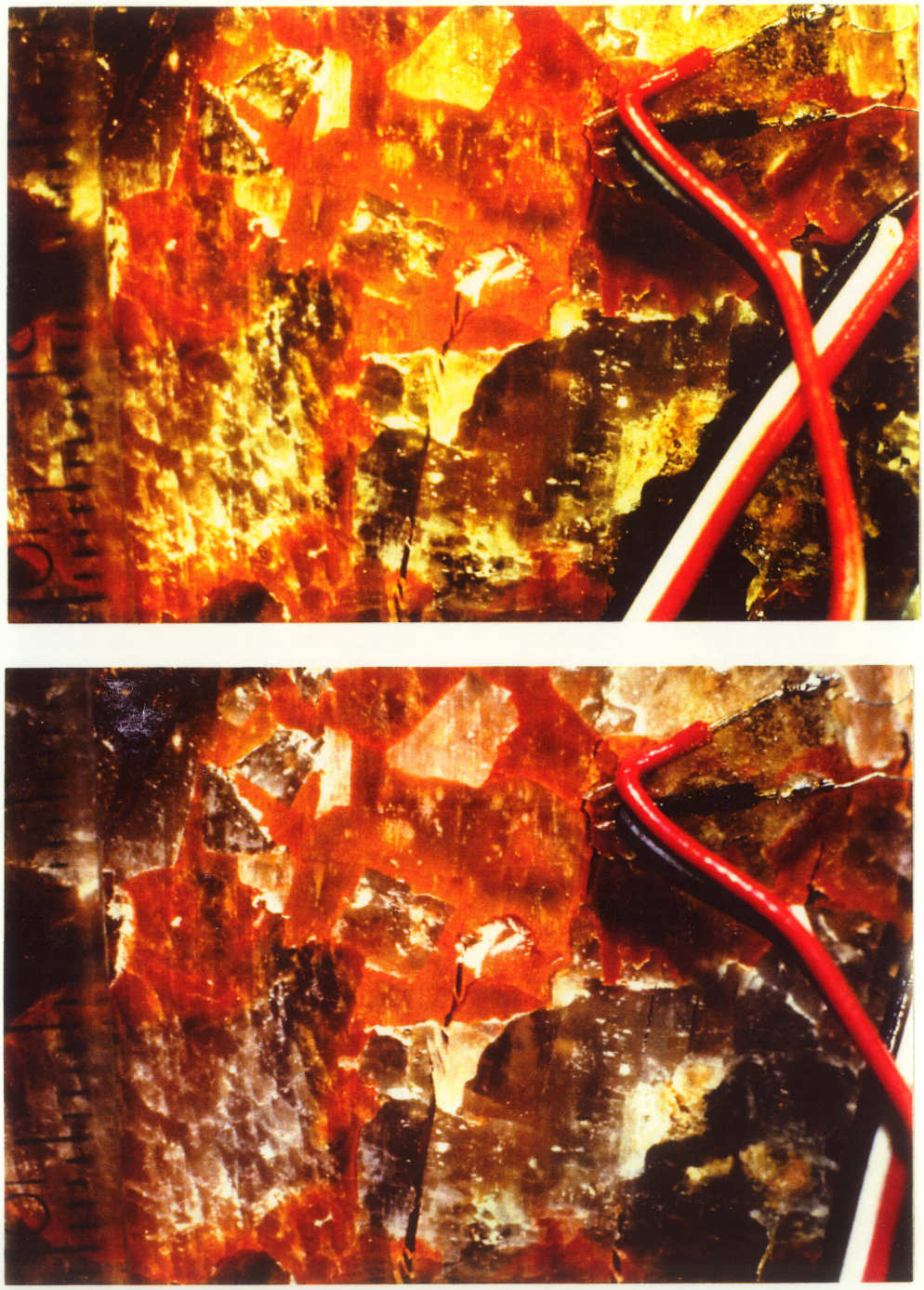

Figure 5.16 (a,b) A series of photographs showing each stage of Figure 5.15 in more detail at (a) 0 days and (b) 3 days.

Figure 5.16 (c,d) A series of photographs showing each stage of Figure 5.15 in more detail at (c) 5 days and (d) 6 days.

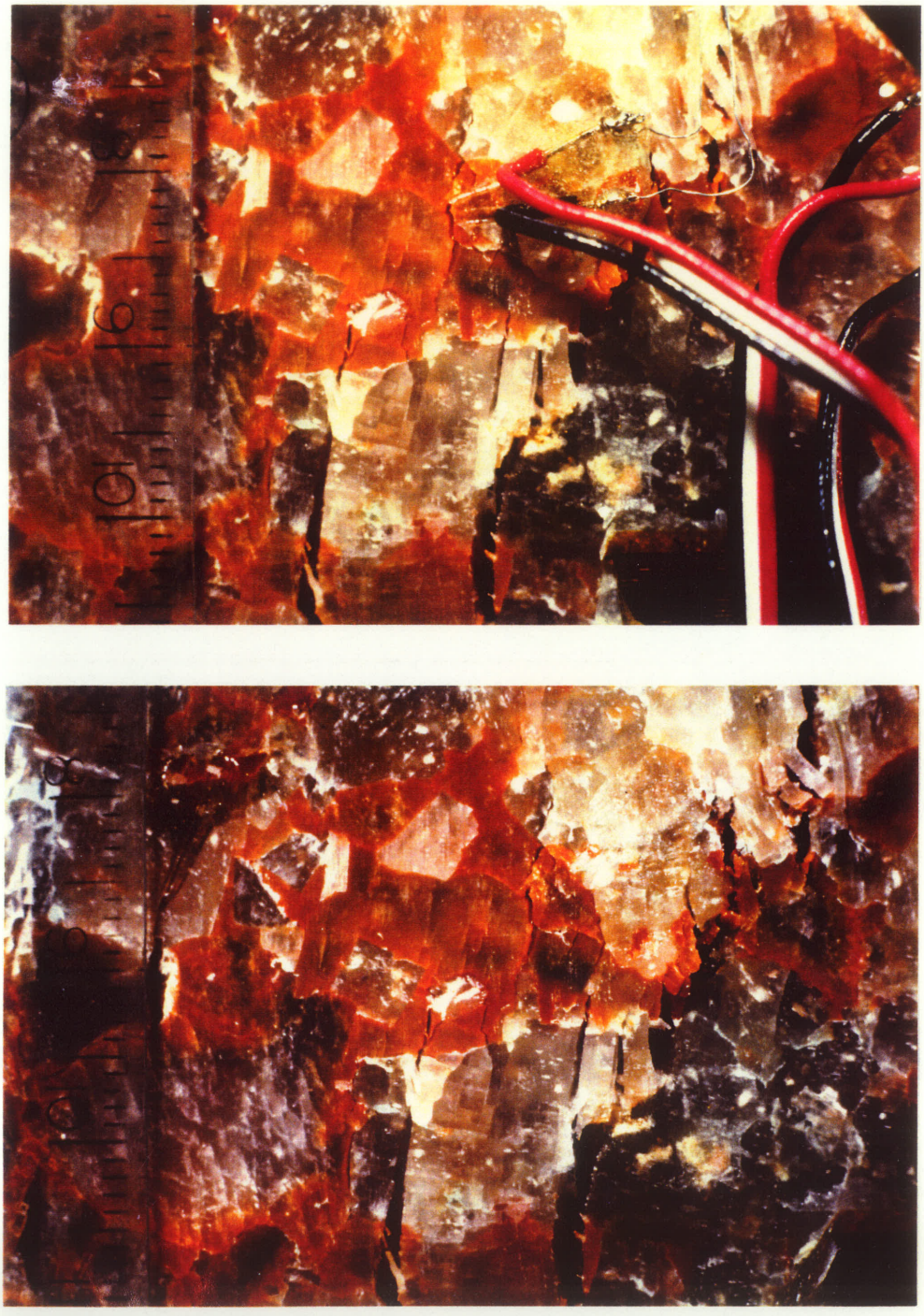

Figure 5.16 (e,f) A series of photographs showing each stage of Figure 5.15 in more detail at (e) 10 days and (f) 11 days. The model collapsed after 12 days. The scale is in millimeters (numbers are cm's).

set. Figure 5.16a shows a "single" remote crack with several rock bridges near the top and bottom of the crack which are beginning to rotate and buckle. The rock bridges indicate that this crack was not a single crack at first although it is obviously becoming one. Another crack exists just at the left edge of the glued wires and a trace of another crack can be seen in the lower right area in the shadow of the left wire. This photo was taken immediately after loading was completed.

The next photo (Figure 5.16b) which was taken 3 days after loading, shows that the first crack has remained fairly stable. The bridges have been partly destroyed and the crack has dilated slightly but the crack has not increased in length. The crack at the end of the gauge also appears to be stable. On the other hand, the crack in the lower right portion is quite active; the wire was moved aside. The crack has increased in length and dilated. As well, several other cracks are visible in the crystal immediately above this crack. The following photo (Figure 5.16c) which was taken 5 days after loading, shows that the left crack is quite stable although some further dilatation and extension has occurred. The less stable (right hand) crack from Figure 5.16b has continued to propagate and the other cracks above can now be seen clearly. There are three parallel cracks in the crystal.

Figure 5.16d (taken 6 days after loading) shows that the remote crack system has propagated up to the sidewall region. This is not a single crack but a system of many small cracks in an en-echelon pattern. The rock bridges between the single cracks are rotating and buckling which eventually leads to a single large fracture. The next photo, taken 10 days after loading (Figure 5.16e), shows the edge of the cavity and coalescence

of the remote fracture system with the sidewall fractures. Although the sidewall fractures were seen with the microscope very early in the loading history, they do not cause much damage until the remote fractures approach the area and the displacement noticeably increases. The final figure (Figure 5.16f) shows the model just before it collapsed. It is quite apparent from this photo that the system of en-echelon cracks near the cavity perimeter has become a single crack. The bridge material between adjacent cracks has been mostly destroyed through buckling and shearing. Final failure likely resulted from shearing along this weakened zone of material and cracks.

After collapse, only very small particles and dust remain! Complete collapse of underground excavations has also been seen in the Vanscoy mine (Chen *et al.*, 1991). In the mining environment however, the surrounding rock offers more confinement and the failed rock does not travel so far or disintegrate so badly.

5.2 Stratigraphically Layered Model

The actual underground excavations at the Cominco mine are located within potash rock. The rock is not pure potash but consists of sylvite, halite, clay seams and other impurities. The roof of most of the workings is halite or rock salt. Other layers of potash, rock salt, limestone and clay exist throughout the region. The regional geological stratigraphy of the area was shown in Figure 2.14. The generalized local stratigraphy for the Vanscoy mining area is shown in Figure 5.17.

A layered model, with layers similar to those indicated in Figure 5.17 was constructed (Figure 5.18). The individual blocks and layers were cut with a hand saw

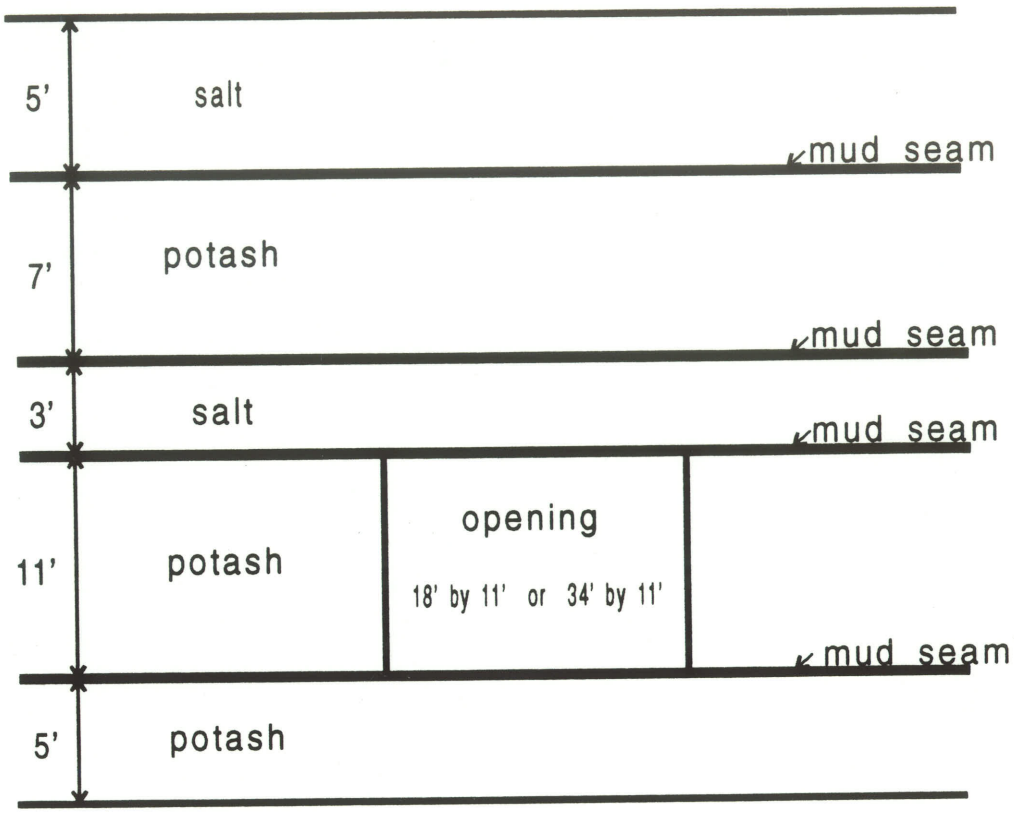

Figure 5.17 The local stratigraphy at the Cominco potash mine at Vanscoy, Saskatchewan. The normal working excavation size is also shown.

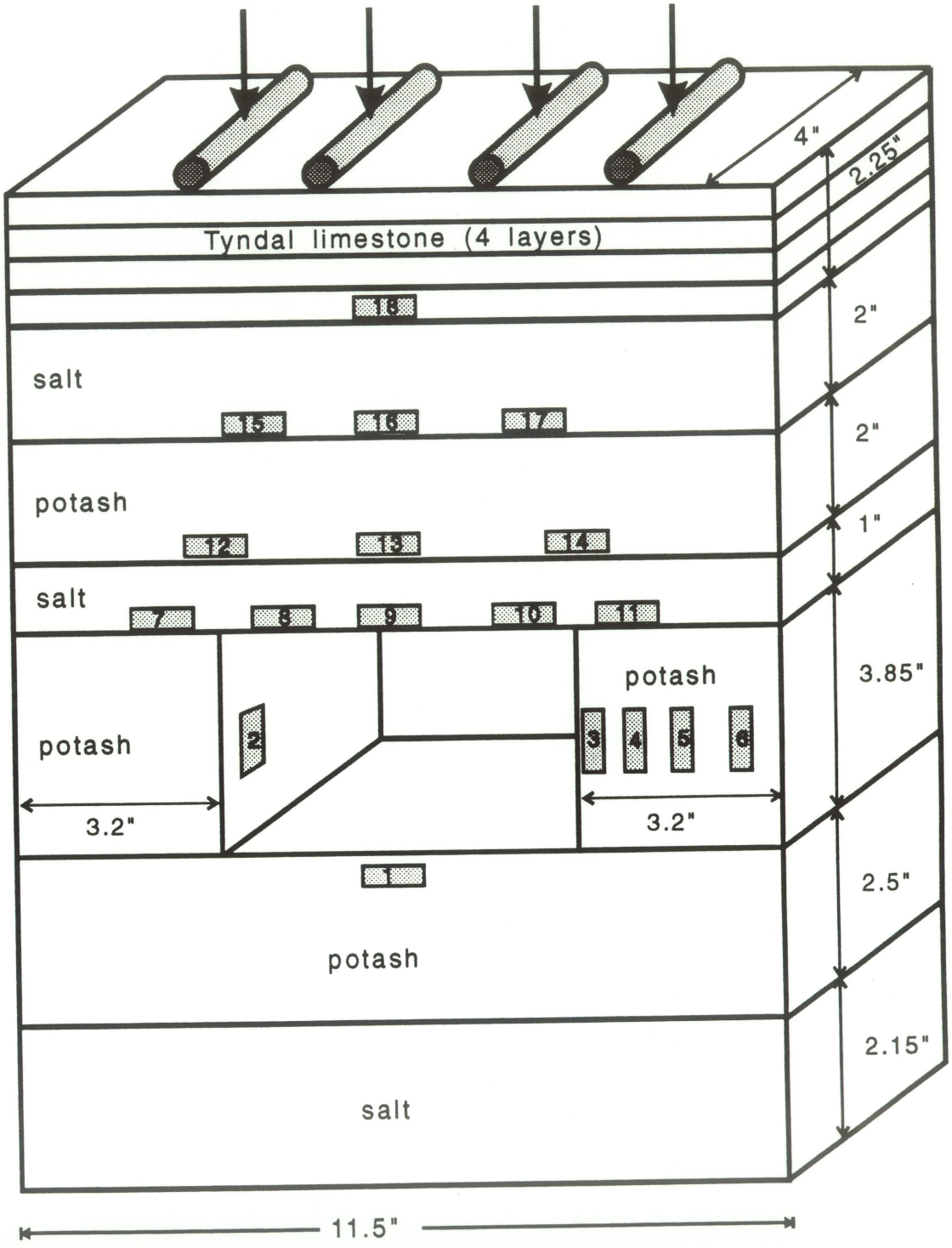

Figure 5.18 A model was constructed to simulate the actual field conditions as closely as possible. The model is about 1/36th of the actual excavation underground.

and then shaped and leveled using a diamond wheel grinder. The dimensions of the model are roughly 1/36th of the actual dimensions of the mine openings. The modeled room was made rectangular to simplify construction and because it resembles the actual opening shape to a close degree. The model was loaded in uniaxial compression, but a lateral constraint was applied to the ends of the model to keep the layers in place. This created a biaxial stress condition in some of the full layers as they bent and deformed. A fairly evenly distributed vertical load was maintained through the use of four rollers, all of which remained in contact with the upper limestone layers throughout the test. The load was increased in steps to the point where complete collapse was imminent (13 MPa on upper surface, 24 MPa on the pillars). At this time, the load was kept constant for a short period and then removed; before disintegration occurred. The model was instrumented with 18 strain gauges on one of the faces (Figure 5.18) with the strain measured by the Hewlett-Packard data acquisition system.

The fracture pattern was mapped with increasing load and evolved in the following manner. First, a single primary fracture formed in the salt back (crown) at a load of about 3.1 MPa. The crack is slightly offset from the cavity center which could simply be due to the loading, or may be a function of the presence of the strain gauges, the wide tensile stress distribution above the square opening, and/or variations in the strength (cleavage orientations) of the crystals. A second primary crack in the salt back and two more primary fractures in the potash floor formed at a load of 4.6 MPa, also offset from the cavity center (Figure 5.19a).

Following the formation of the primary cracks, "remote" cracks formed at 5.5 MPa, starting in the salt back above the edge of the pillars (Figure 5.19b). A crack in the right sidewall (pillar) formed soon afterwards at a load of about 5.8 MPa (Figure 5.19b). A fracture in the left pillar formed at 7.5 MPa (Figure 5.19c). The remote cracks above the pillars and the primary cracks in the floor extended slightly further. At 8.7 MPa, "pure" remote cracks formed in the upper salt and limestone layers on both sides of the opening (Figure 5.19c). The left-side remote crack formed near the salt - limestone boundary while the one on the right side initiated in the salt and then propagated downwards through the salt and potash and upwards towards the limestone. A crack also formed in the limestone layers above the right-side remote crack.

Between 10 and 11.5 MPa, "secondary" sidewall fractures propagated almost completely through both pillars (Figure 5.19d). These cracks developed further into the pillar away from the opening. The "pure" remote cracks also propagated further, extending from the upper surface down to the pillars.

At the final load of 13 MPa (pillar stress = 24 MPa), another sidewall crack developed further into the left pillar (Figure 5.19e). This crack extends right down into the potash layer underneath. Pure remote cracks also initiated in the potash floor beneath the pillars. During the creep phase at this high load, some further propagation occurred in the remote and sidewall regions (Figure 5.19f). The primary cracks remained stable. The left pillar became severely damaged during the creep stage and began to resemble some of the failed pillars which were photographed in the Vanscoy mine (Chen *et al.*, 1991). The right pillar is much stiffer and consequently did not suffer as much damage.

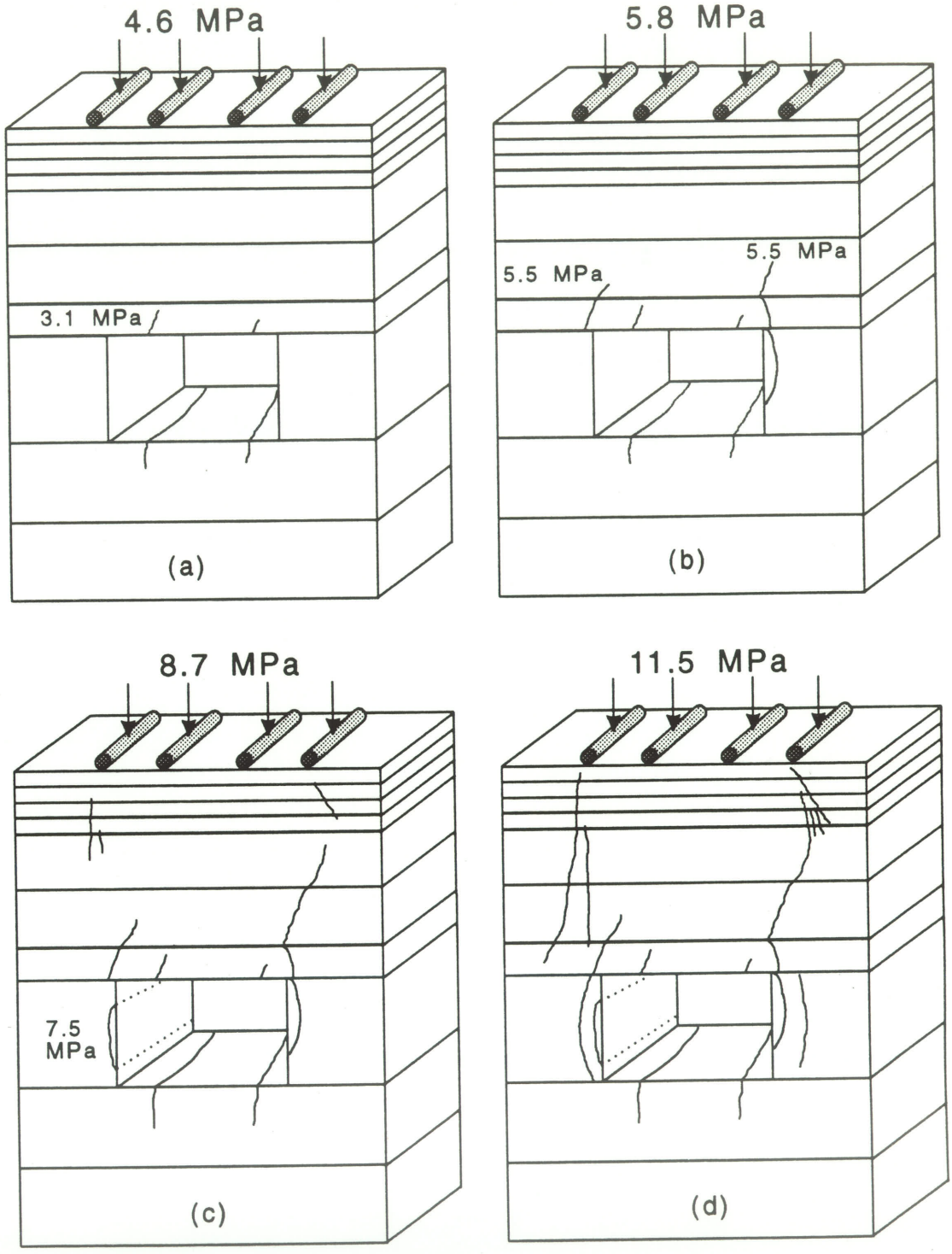

Figure 5.19 Continued on next page.

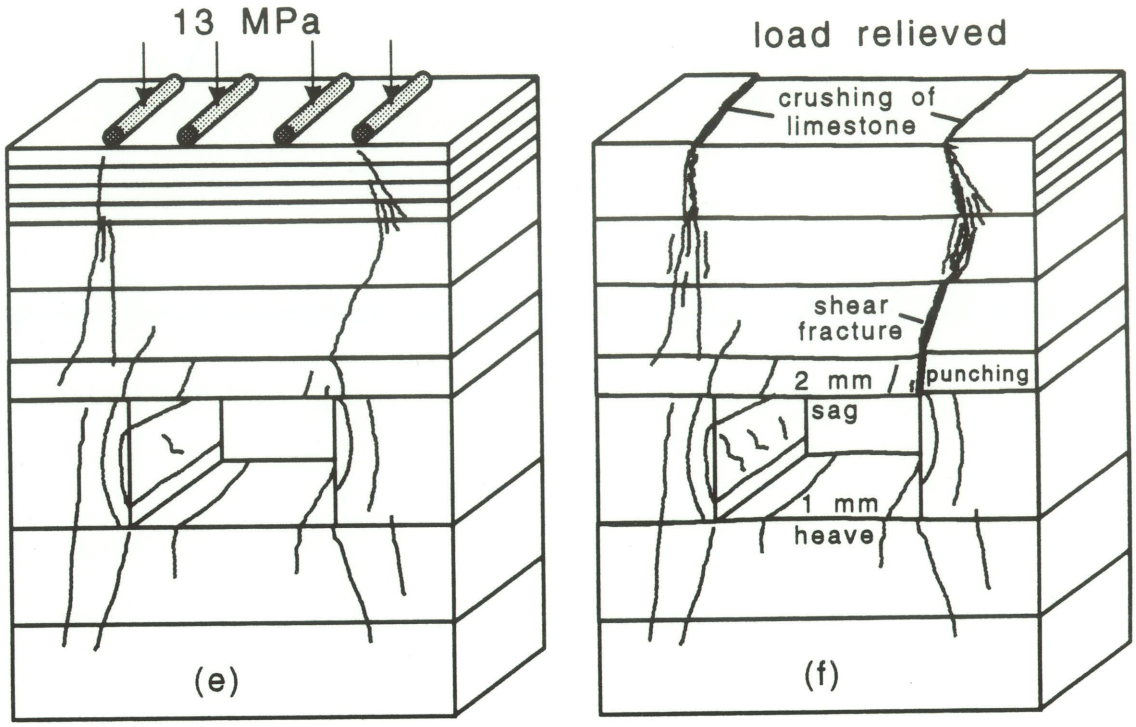

Figure 5.19 A series of tracings showing the progression of fractures in the model as the uniaxial compressive load is increased. Two primary cracks (not centered) occur in the crown and invert. These are followed by remote and then sidewall fractures. The final figure indicates crushing and shearing of the upper limestone plates. The right pillar was stiffer than the left and punched into the salt back and potash base. Sag of the upper salt back amounted to 2 mm and heave of the base was about 1 mm.

However, this higher strength and stiffness resulted in the pillar punching into both the salt back and potash floor (Figure 5.19f), which has also been seen in the mine. Above the right pillar, where punching occurred, the salt back and the layers above all suffered severe deformation and shearing along the remote fracture system (Figure 5.20). Some of the shear is probably caused by the line-loading as well.

Another common feature in potash workings is sag of the salt back and floor upheaval (Figure 5.19f). The sag and heave were measured in this model after the load was removed. In the center of the opening, the salt back sagged 2 mm while the floor heaved only 1 mm. The loading conditions and the layering are different for the top and bottom halves, possibly accounting for the variation in deflections.

The total crack length for this model was measured and then plotted against the applied stress (Figure 5.21). This figure shows a trend which is similar to that of the single circular cavity model; the total crack length increases exponentially with increasing stress approaching an asymptote at 14 MPa (stress on the full layers). If the 13-MPa load had been maintained for a significant length of time or if the load had been increased to 14 MPa, the model would likely have disintegrated.

The trend of exponential crack growth is not the only aspect of this test which resembles the previous model tests. The crack pattern is quite similar as well. Although the primary cracks are not centered in the crown and invert (there are two primary cracks in both), they still behave like the single cracks from the earlier models. They form in the tensile stress concentration, propagate away from the opening in a direction sub-parallel to the applied stress and remain stable, meaning they do not propagate far and

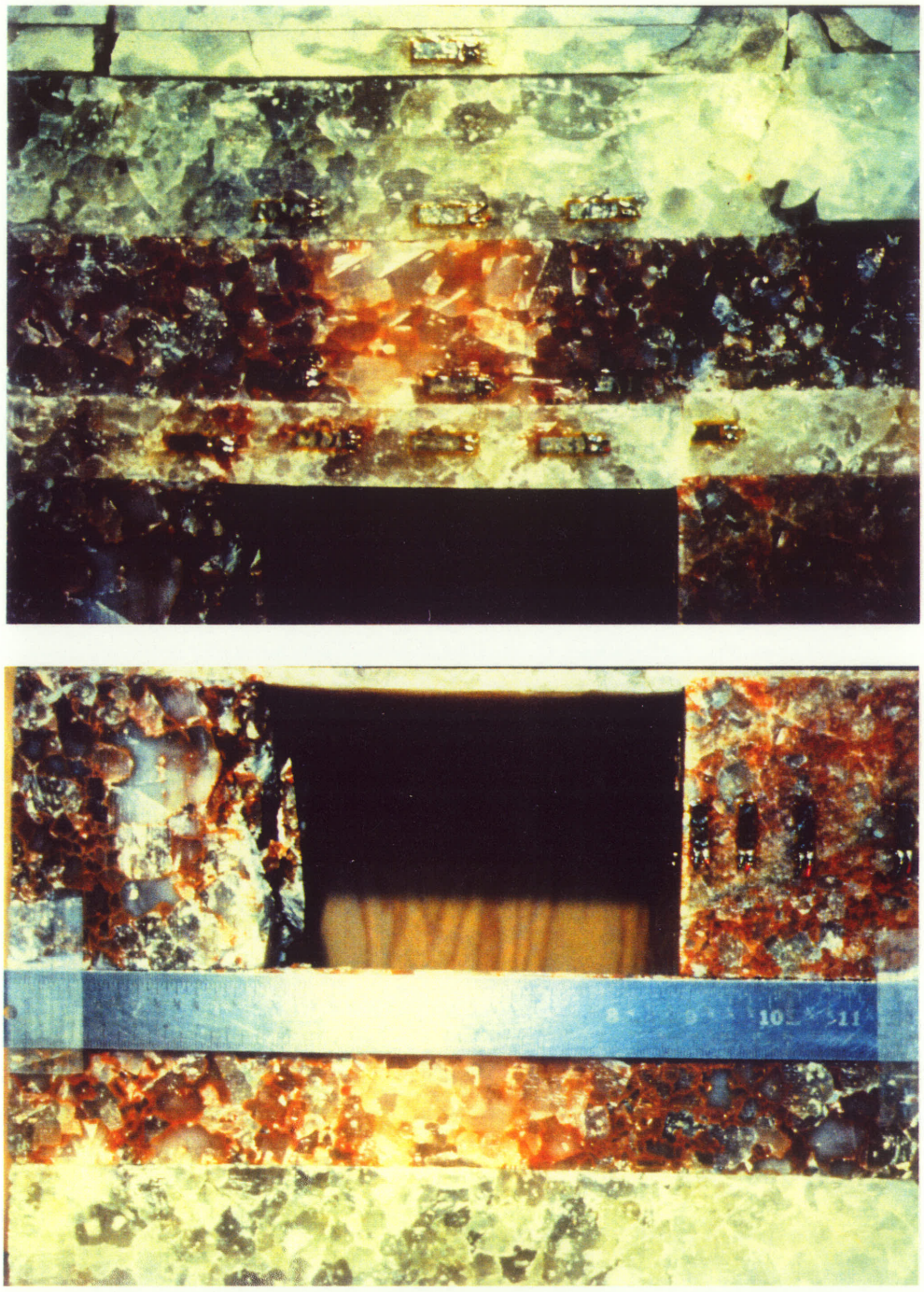

Figure 5.20 Photographs showing the rectangular model and the fractures after the load was removed. Notice the shear along the right remote and the pillar punching in the upper photo. The lower photo shows the severe fracturing in the left pillar, the sag of the salt back and the floor heave.

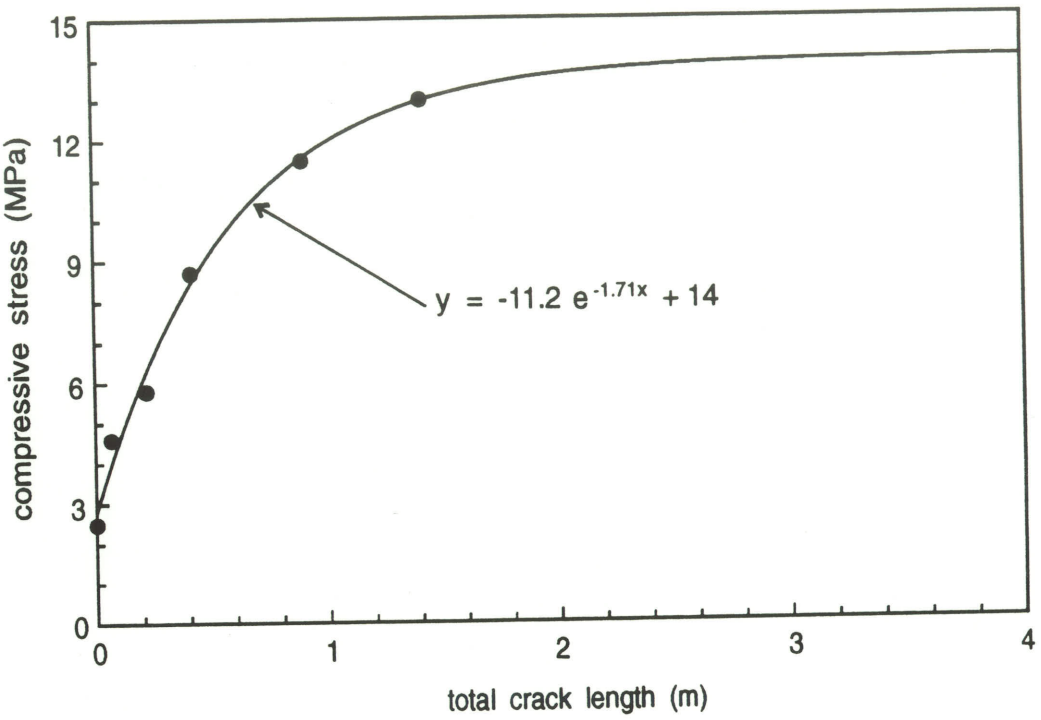

Figure 5.21 The total crack length (sum of all crack lengths) increases exponentially with rising stress. At a load between 13 and 14 MPa, the model becomes unstable.

are relatively inconsequential to the overall stability. Remote cracks form next, followed by sidewall fractures. The sidewall fractures are much more apparent for this model compared to the single circular cavity model possibly because of the increased area, the rectangular shape and/or the larger cavity size.

The limestone plates at the top of the model behave like the limestone plate below the single circular cavity modeled by Horning (1989). The fractures in the limestone appear to be part of the remote fracture system as they form during or after the remote crack initiation along the same general path. The remote fracture system is very similar to the linear arch seen in thick beam tests on rock (Ahmed, 1990). There is an indication of this arch in one of the model tests on LDB granite (Figure 4.5) and Gay's (1976) experiment also shows the linear arch features.

5.3 Multiple Opening Model

A block of potash, 630 mm wide, 343 mm high and 178 mm thick, was prepared with three horizontal, circular holes through the middle portion of the block (Figure 5.22). The central hole had a diameter of 47 mm while the two outer holes were larger with a diameter of 67 mm. The centers of the holes were all located on the same horizontal line and spaced 90 mm apart. Two limestone plates were used as top and bottom loading platens with plastic-encased plaster between the potash and the limestone, imitating a clay seam and used for leveling purposes. Teflon sheets were placed between the limestone and the metal platens of the loading frame. The model was loaded in uniaxial compression in a 1,200,000-lb MTS frame with the load evenly distribute.

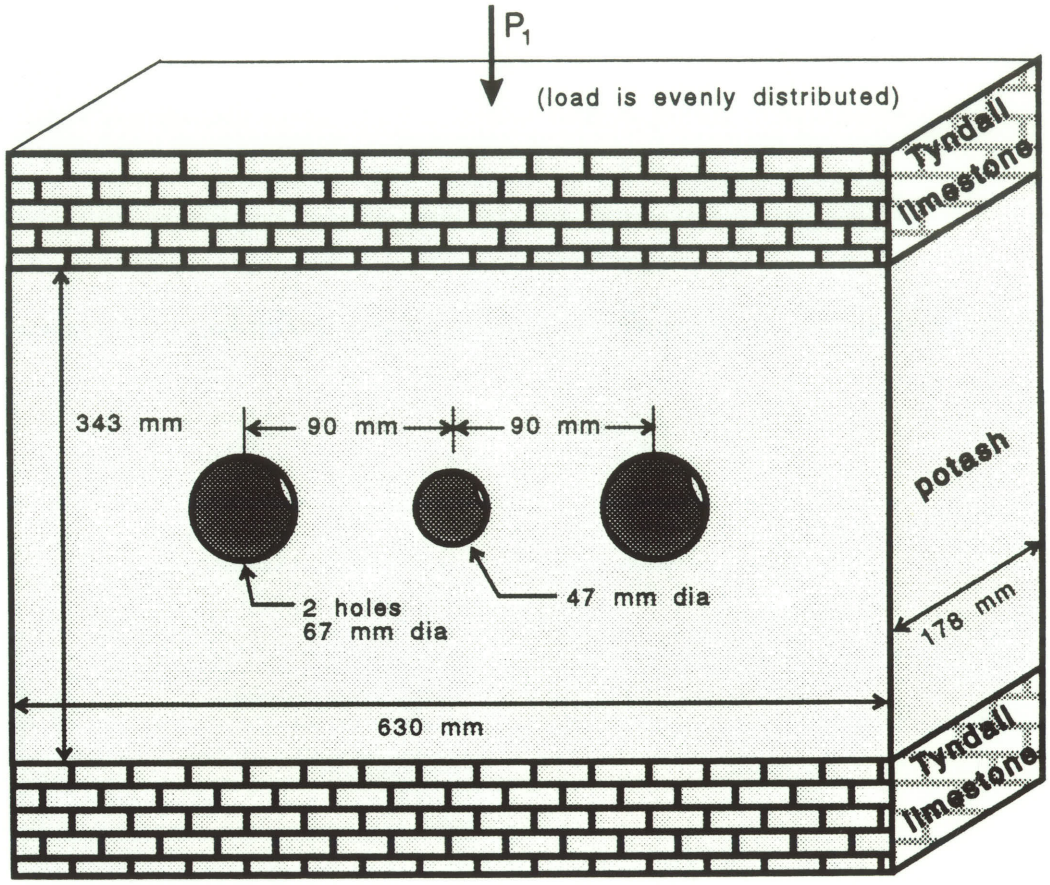

Figure 5.22 The physical model of potash with three circular cavities and limestone loading platens on the upper and lower surfaces. The cavities are horizontal and the centers lie on a horizontal line.

No strain gauges were used on this model. Instead, the fractures were monitored visually with the aid of a microscope. The fractures were mapped at various stages of loading and the entire experiment was recorded with a video camera. The load was incremented by about 100 kN (.88 MPa on the whole surface), up to a load of 13 MPa at which point the load was held constant until the model collapsed. The load was also held constant at each loading step to allow time to monitor and record the fracture process.

The fractures evolved in the following manner. Primary fractures formed in the crown and invert of the large hole to the extreme right of the block at a load between 2.6 and 3.5 MPa. Cracks then formed in the limestone loading platens at a load of about 3.5 MPa. At 4.4 MPa, there were primary cracks in the crown and invert of both outer holes as well as cracks in the limestone plates (Figure 5.23a). At 5.3 MPa, the primary fractures had propagated slightly and two remote cracks had formed on the right side of the right hand hole (Figure 5.23b).

At a load of 7.1 MPa, the remote fractures began to increase in both length and number around the two large holes (Figure 5.23c). The primary cracks of the two large holes had also propagated further (up to 90 mm). The hole to the extreme left intersected an old discontinuity which the primary crack proceeded to follow; this may have eased propagation. There were still no cracks associated with the small, middle hole. A load of 8.8 MPa resulted in a further increase in remote crack length (Figure 5.23d); the remote crack systems show an increase in the number of cracks as well as an increase in length of individual cracks. All the features associated with crack growth in compression

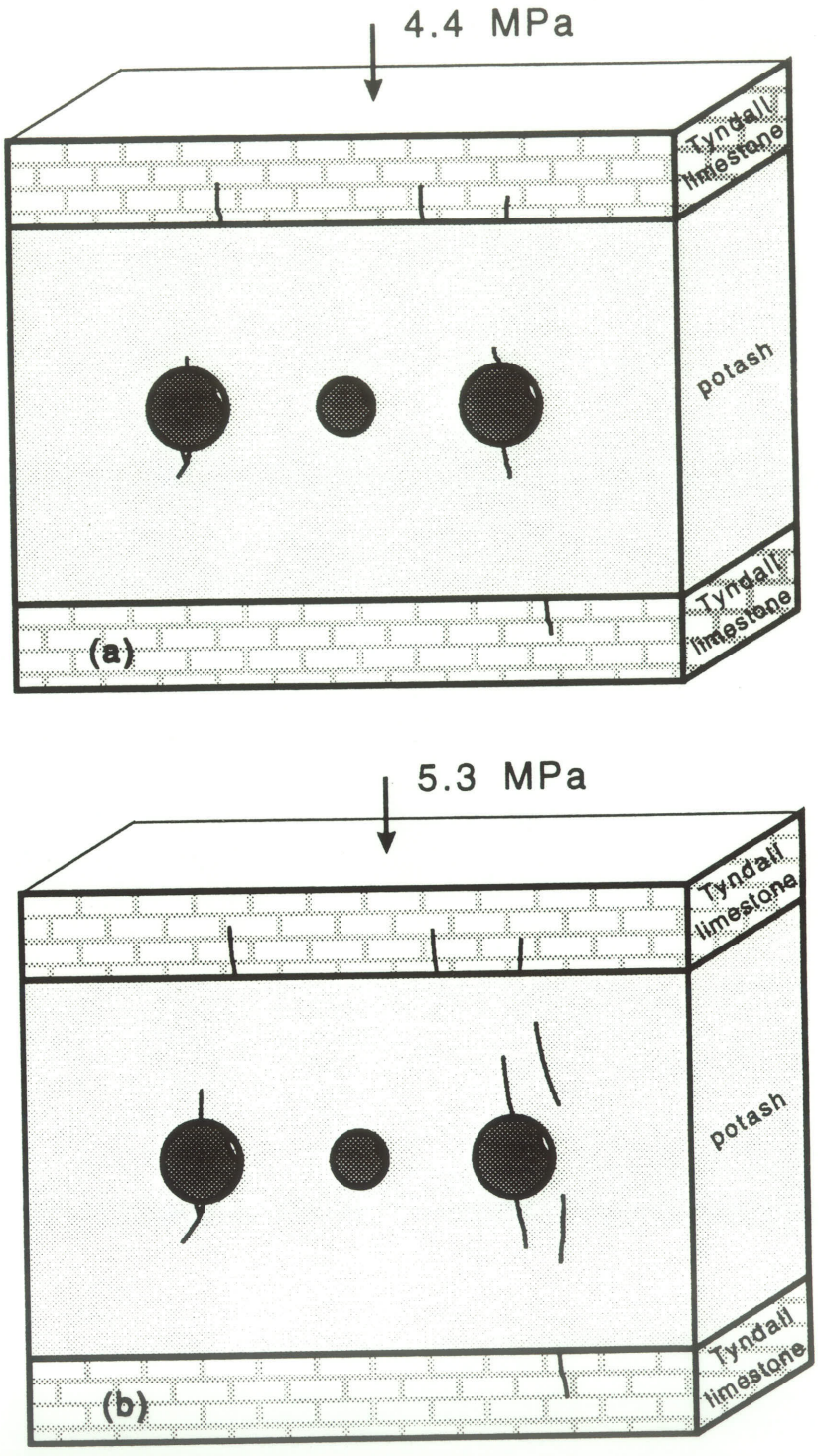

Figure 5.23 Continued on next page.

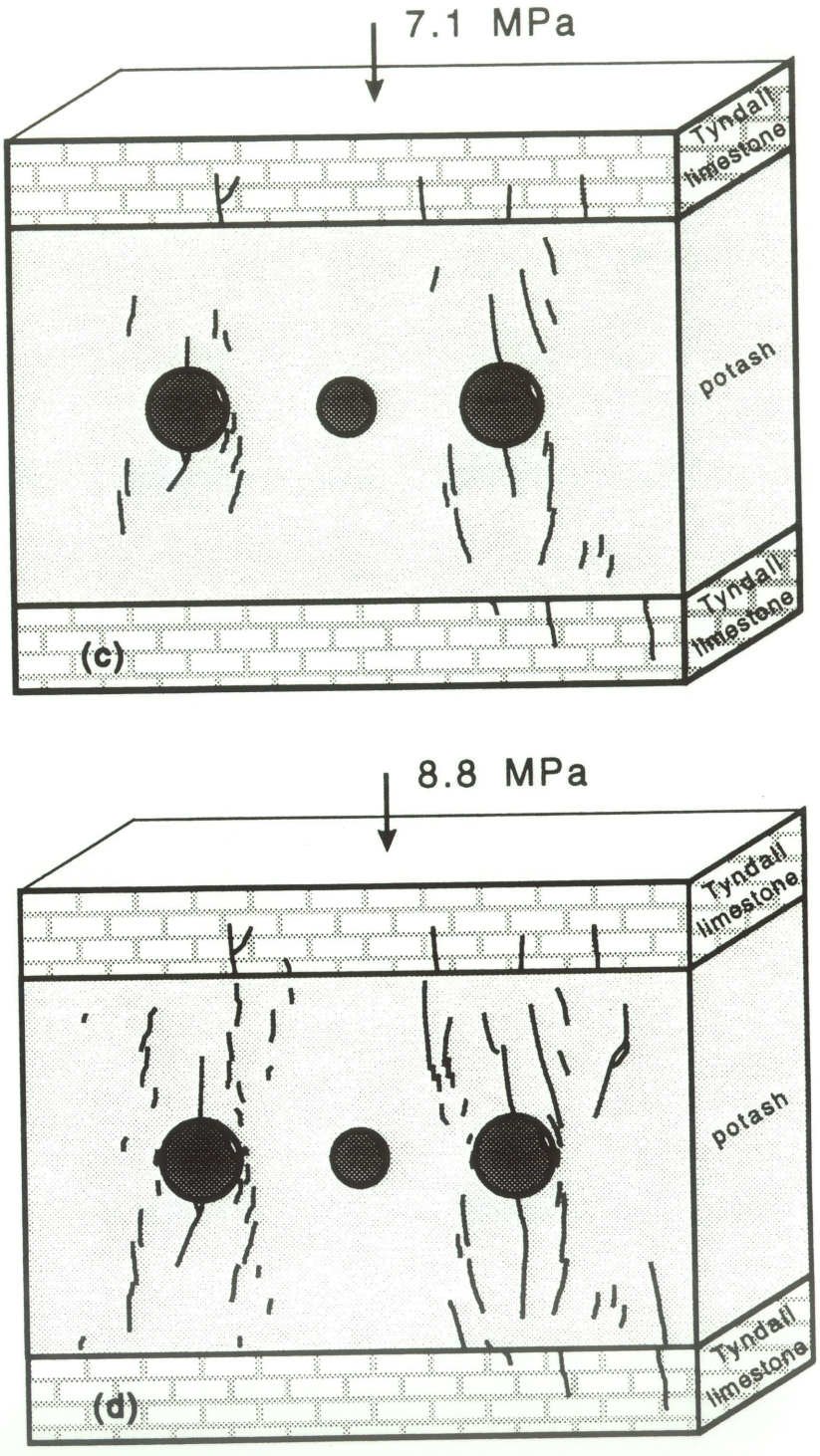

Figure 5.23 Continued on next page.

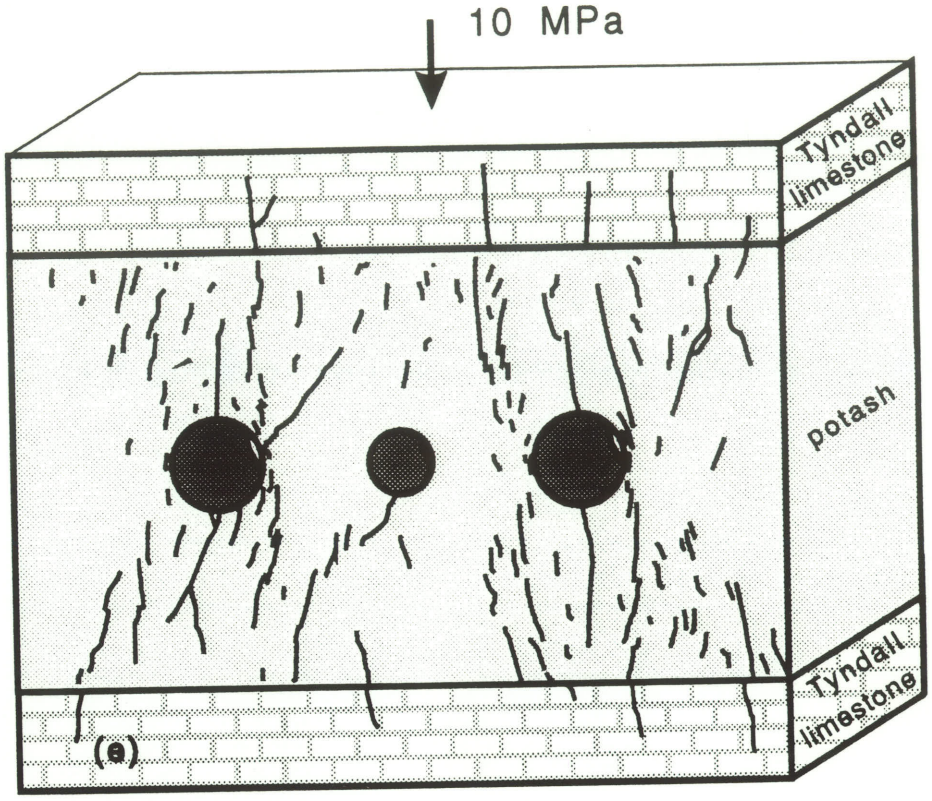

Figure 5.23 A series of tracings showing the progression of crack growth in the model as the uniaxial compressive load is increased. The first cracks are the primary cracks for the two larger holes (a) followed closely by the small stable cracks in the limestone. Next remote cracks form around the large holes (b). The usual en-echelon pattern is present. Some additional cracks form in the limestone along the path of the remote cracks. Sidewall cracks are apparent at 8.8 MPa (d). Crack growth continued beyond the stage shown in (e) and failed at 13.3 MPa.

and seen in the previous model tests are also apparent with this model. This includes stable crack growth, offset crack initiation, and coalescence of en-echelon cracks to form macrocracks.

At 10 MPa, the load was kept constant for 2 hours to evaluate the time dependence of crack growth. The block is quite full of cracks at 10 MPa (Figure 5.23e). There is some further crack growth with time although (visually) the rate appeared to be decreasing. After 2 hours, the load was increased to 11.4 MPa. Crack growth continued to increase at an accelerating rate and the surface of the block was almost completely covered with cracks. The load was increased to the final level of 13.3 MPa and this load was kept constant for a short time until the model collapsed completely.

The total crack length increases with stress level and follows a trend similar to that of the single cavity models (Figure 5.24). The data seem to follow a power curve (SSE=2.37) better than the exponential curve (SSE=3.70). This could be a result of the time dependent crack growth allowed at 10 MPa which may have caused the data to accelerate faster than the typical exponential curve. Although the exponential curve does not fit as well as the power curve, the basic trend is still similar to that of the earlier models.

The block failed shortly after the 13.3 MPa load was attained, leaving dust and grain size particles as well as some larger pieces (Figure 5.25). The pillars between the holes remained fairly well intact. The failure surfaces indicate features of both tensile and shear fractures. The initial cracks are extensile and the macrocracks (coalesced en-echelon cracks) are also extensile. The shear fracture develops as the model collapses;

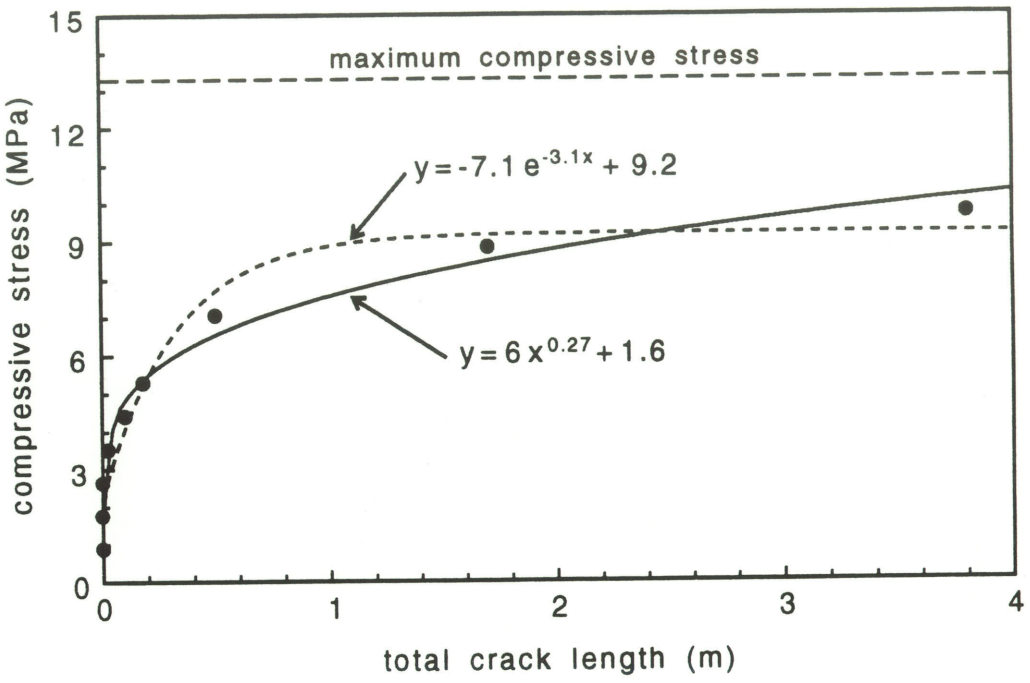

Figure 5.24 The trend of increasing total crack length with increasing stress is similar to that of the previous models. The data fit a power curve slightly better than an exponential, possibly due to two hours of time-dependent crack growth at 10 MPa.

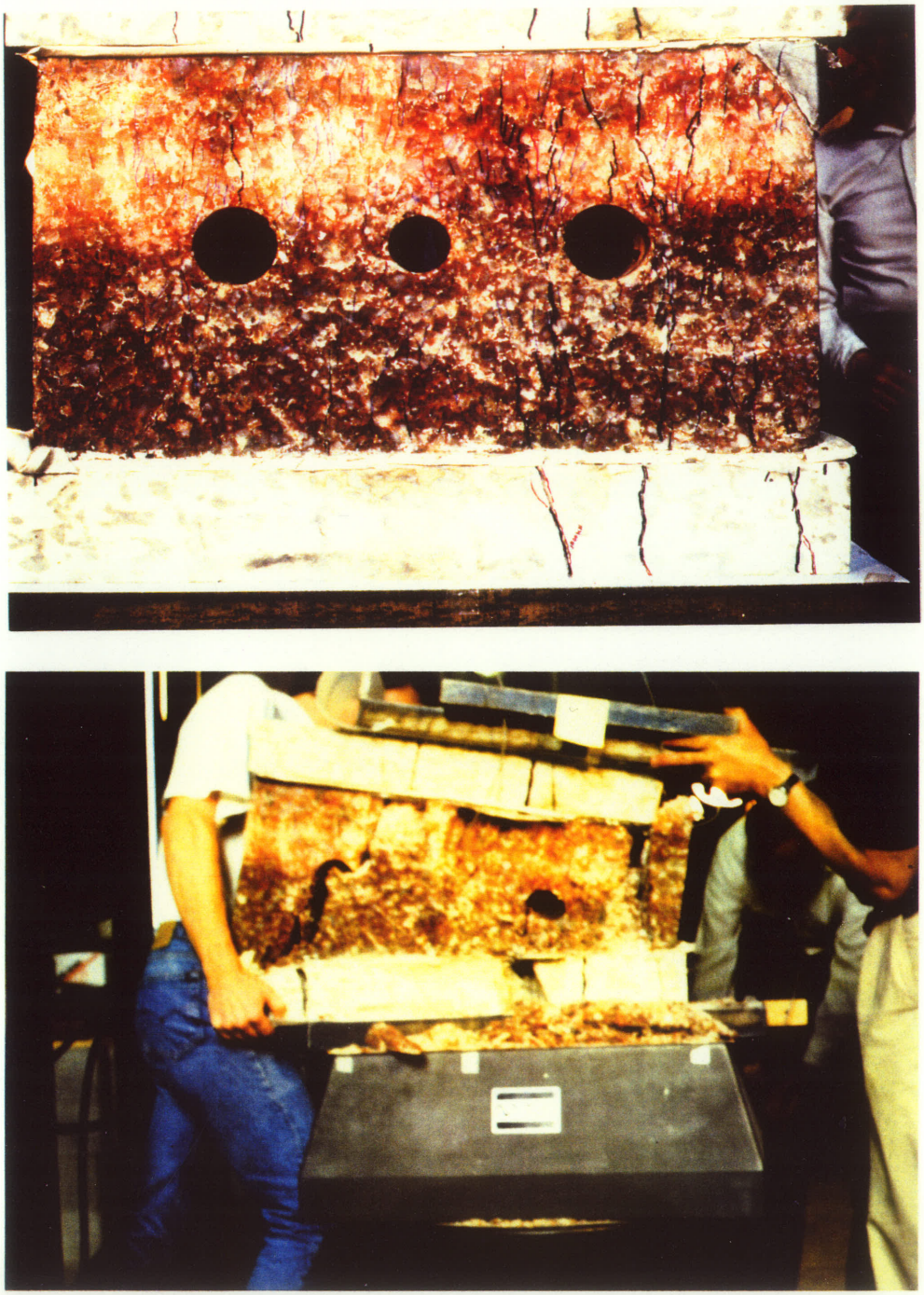

Figure 5.25 The first photo shows the intact block with three holes and limestone platens. The cracks in both the potash and limestone have been traced with a felt marker. The uniaxial load is about 12.2 MPa. The second photo shows how the model collapsed at 13.3 MPa.

the large upper blocks slide down the lower blocks following the remote crack system, from the corners toward the sidewalls of the holes.

Again there is little distinction between the trend of exponential crack growth with increasing stress for this model compared to the previous two models. The final collapse load of 13 to 14 MPa is also quite consistent. The fracture pattern around the holes is not much different either, other than the fact that the larger holes on the outer edges suffer more cracking at lower stresses than the smaller inner cavity. This feature was shown by an earlier finite element study as well (Carter, 1988). The inner cavity is initially more stable than the large cavities due to the size effect; the fracture initiation stress is higher for smaller cavities. Because there is no primary fracture, remote fractures, which are the primary fracture's off-set cracks, do not form either. Consequently, almost all the fracturing occurs around the large holes until the higher stresses are reached. At high stress (over 50% of peak uniaxial compressive strength), the entire block is subject to crack initiation. The cracks around the larger holes also tend to relieve some of the local tensile stresses which would have aided in crack initiation around the small hole. The general pattern of en-echelon extensile cracking, followed by coalescence and in some cases shearing as the model collapses is also typical of compression induced failure.

Limestone platens have been used in three different models: the single circular cavity (Horning, 1989), the layered rectangular model and this multiple cavity model. For the first two models, the process of cracking in the limestone is quite similar. The cracks in the limestone appear to be closely related to (or part of) the remote fracture

system (or the linear arch). For this latter model however, the fractures are not so closely related to the remote fractures. Some of the cracks in the limestone form long before the remote fractures exist; unlike the previous two models where the cracks formed at the same time or after the remote fractures initiated. The early cracks are scattered through the layer and are caused by the difference in deformation which is a function of material behavior (stiffness and Poisson's effect).

The cracks start at the interface between the two layers. The stiffer limestone bends due to the higher deformation above the holes compared to the edges of the block. The potash below is spreading laterally as well as being compressed vertically. These two processes combine to produce tension in the lower part of the limestone platen. The other factor is the plastic-encased plaster which was meant to simulate a clay seam. This layer further increases the lateral tensile stress as it deforms and spreads more than the potash. Other cracks in the limestone layer appear later and these are more closely related to the remote fracture system.

6 FINITE ELEMENT MODELING

6.0 Introduction

Physical modeling is an excellent way to learn about the nature of fractures forming around underground cavities. This includes initiation and propagation of a single crack, crack multiplication, crack coalescence and the mechanism of cavity collapse. With a simple loading condition, such as uniaxial compression, four surfaces of the test block and the internal surface of the cavity are accessible for instrumentation and continuous visual inspection. Although uniaxial compression is not a realistic loading condition, most multiaxial loading frames are expensive and they defeat the main purpose of the physical model, the visual display of the fracture process. A good compromise lies in resorting to numerical modeling for the more complex loading conditions, using the uniaxially loaded physical model for calibration.

In addition to all the physical model tests which have been done, both in the past and for the current study, there have been many numerical models constructed to predict the evolution of fracture: (1) in rock in general (Costin, 1987; Horii and Nemat-Nasser, 1986); and more specifically, (2) around modeled openings in rock (Carter *et al.*, 1991*b*; Ingraffea, 1977; Kowamoto and Saito, 1985). Most demonstrate the propagation of discrete fractures in brittle materials from microscopic flaws (Ingraffea, 1977; Nemat-Nasser and Horri, 1986; Ewy et al., 1987). Others treat the fracture as a shear zone or crack band (eg. Bazant, 1985) rather than as a discrete fracture. Still others examine the material behavior in terms of the damage which occurs due to microcracking (Costin,

1987) in a manner that bears close resemblance to plasticity models. Most of the modeling directed towards fractures around underground cavities has used a discrete fracture type of model rather than the crack band or the damage type. This would appear to be appropriate. In the potash mines, many fractures are visible and they primarily behave as single discrete cracks. For this reason, a finite element program which is capable of modeling discrete fractures is desired for the numerical modeling exercise.

Fractures around modeled cavities in rock are similar to those in small laboratory specimens and those in large rock masses. Indeed, many features of the cracks which form within compressive stress fields were shown in the previous chapters to be practically independent of scale. For this reason, a model which is capable of reproducing microscopic fractures in a laboratory sample should be capable of representing all fractures regardless of scale and stress state.

6.0.1 Numerical Modeling with Linear Elastic Fracture Mechanics (LEFM)

LEFM is one of the most common methods of modeling discrete fractures using finite elements. Pollard and Segall (1987) have shown that fracture mechanics can be used to model fractures occurring in nature and Horii and Nemat-Nasser (1986) have used fracture mechanics to model the stress—strain behavior of laboratory tests. Kemeny and Cook (1990), Ingraffea (1987) and Sammis and Ashby (1986) have shown that fracture mechanics can be adapted to model fracture around macroscopic cavities.

LEFM can only be used to model crack propagation, not initiation. Consequently, a method of predicting crack initiation must be developed prior to modeling the discrete

crack growth. Often, as in the case of the primary fracture, an initial crack length is assumed to exist at the beginning of the test. In other cases, crack initiation must be predicted. This is often done using one of the empirical strength or failure theories such as: 1) the maximum stress theory for tension, 2) the Mohr—Coulomb criterion, 3) the Hoek and Brown criterion and others for compression. The non-linear fracture mechanics method of crack initiation, the fictitious or cohesive crack model, represents another possiblity. Once crack initiation is predicted, a starting crack can be positioned in the finite element mesh.

A variety of cracks can be used in the finite element scheme. For uniaxial tension, a flat penny-shaped crack is sufficient. The initial crack length and the associated toughness may vary but these parameters can easily be adjusted to match the physical data. The penny-shaped crack has also been used where the stress field consists of both tension and compression. Based on the theoretical formulations, this type of crack would either ignore the compressive stress parallel to the crack or a constant stress ahead of the crack tip would be produced. Both forms conflict with the observed process of stable crack growth parallel to the compressive stress; cracks grow parallel to a moderate to high compressive stress with low or no tension perpendicular to the crack.

In finite element codes, the stress intensity factors (SIF) are derived from the crack opening and crack sliding displacements (Owen and Fawkes, 1983). If the applied loads produce relative displacement of the element-nodes surrounding the crack tip, a SIF can be obtained and compared to the material fracture toughness. The crack will propagate when the SIF exceeds the fracture toughness. If the crack does not have a

finite width (such as the flat mathematical crack), then a compressive stress parallel to the crack will not produce the required displacements; a SIF will not be generated and the crack will not propagate.

Consequently, for biaxial or polyaxial compressive stress fields, the penny-shaped crack is not usually used. Instead, the sliding crack has most often been used. Sliding cracks are rarely seen in rocks although Nemat-Nasser and Obata (1988) suggest that the inclined portion need only be submicroscopic in size to generate propagating wing cracks. The splitting crack, which was developed only recently, is based on the idea of the Brazilian indirect tension test where compressive loading across the diameter of a disk induces tensile stresses perpendicular to the load. Kemeny and Cook (1990) have derived the SIF equations for both constant and linear tensile stress distributions on the splitting crack. Ewy and Cook (1990) have used this method to produce extensile fractures in the sides of thick-walled cylinder tests. Both of these methods are quite capable of modeling fractures in compression but neither model is able to predict the initiation of offset cracks, a common feature in compressive fracturing of rock.

The number of different models necessary to propagate fractures in arbitrary stress fields makes LEFM somewhat unattractive. Most of the models require the measured material parameters, such as crack length or fracture toughness, to be adjusted so that the models will fit the experimental data. For example, in Chapter 4 the measured fracture toughness had to be lowered before the LEFM model fit the primary fracture initiation data. Often, the unknown parameters are simply assigned arbitrary values thereby

allowing the model to fit experimental evidence. In fact, most models which have two or more parameters that can arbitrarily be adjusted, can be fitted to almost any data trend.

Another problem with standard LEFM formulations, at least for the penny-shaped crack type, is the production of an incorrect angle of propagation when both stresses become compressive. A flat crack may initiate in a combined tension-compression stress field and then propagate into areas of biaxial compression. A flat crack will not produce its own local tensile stresses either. Because of the compressive stresses, a shear mode stress intensity factor is often generated causing the angle of crack propagation to vary from the direction of the maximum compressive stress. This angle of propagation can easily be fixed however by ignoring the standard methods of prediction and simply following the maximum compressive stress trajectories.

Cracks in rock always follow the maximum stress direction. If the trajectory of the stress changes, the crack will usually become offset and follow the change in direction. The method of offset cracking is not clear, although Pollard *et al.* (1982) have suggested that twisting due to the rotation of the principal stresses is one possible phenomenon. Standard LEFM formulations do not predict offset cracking, a feature which seems to be an integral part of the fracture process in rock under compression, even when one of the stresses is tensile. En-echelon crack patterns can be generated only by incorporating numerous flaws within the finite element mesh. Ewy and Cook (1990) used the splitting crack model with an array of cracks at the sidewall to produce the beginnings of an en-echelon pattern. However, this makes the modeling procedure more complicated and the original flaw or crack positions are subject to extreme bias.

The final problem with LEFM is that it is inapplicable for cracks where the process-zone size is large in relation to the crack length. There have been numerous studies on the topic of the process zone and non-linear fracture mechanics has finally emerged as the tool for modeling the process zone and true crack combination, using finite elements.

6.0.2 Numerical Modeling with Non-Linear Fracture Mechanics (NLFM)

For rock and concrete, most finite element codes use the Dugdale—Barenblatt model, which was generalized by Hillerborg *et al.* (1976), for modeling the process zone and subsequent true fracture propagation. The process zone and true crack are modeled by specifying a stress versus crack-opening displacement (COD) relationship. This relationship is usually based on the stress—strain or load—COD curve for direct tension, including the strain softening portion of the curve (Figure 6.1). The area under the curve represents the fracture energy or energy necessary to produce a true fracture. A true fracture forms only when the COD reaches a critical value (δ_c) and no stress is transferred across the crack.

Non-linear fracture mechanics has increased in popularity because 1) it includes the aspect of the process zone and the structural size effect in general, 2) it can be used to indicate crack initiation as well as propagation and 3) it leads to the use of LEFM once the crack is so long that the process zone has little or no effect. A special finite element (Figure 6.2) is often used along the path of the fracture, where the path is usually indicated by tensile stresses (Ingraffea, 1987). This isoparametric, one-dimensional,

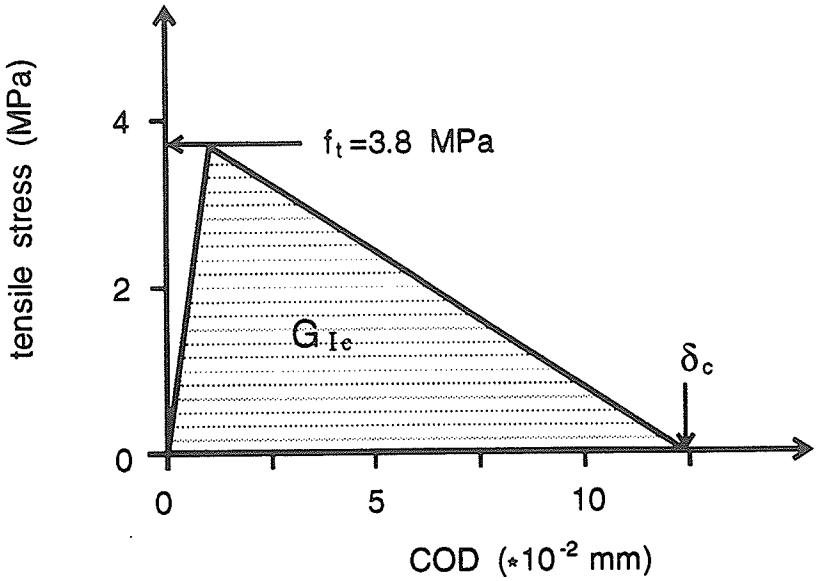

Figure 6.1 A typical process zone constitutive model for rock or concrete (after Hillerborg et al., 1976).

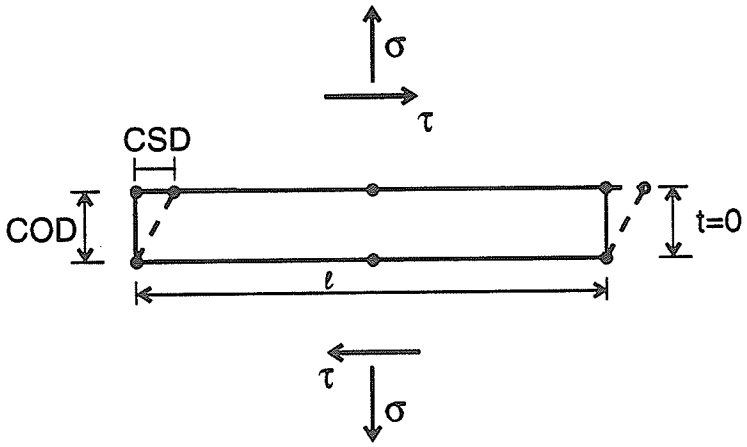

$$\begin{pmatrix} \sigma \\ \tau \end{pmatrix} = \begin{bmatrix} K_N & 0 \\ 0 & K_S \end{bmatrix} \begin{pmatrix} COD \\ CSD \end{pmatrix}$$

Figure 6.2 A quadratic, isoparametric, interface element used for modeling the process zone in rock and concrete (after Ingraffea, 1987).

interface element has several distinct features. The element is of zero thickness but does not allow contact between the adjacent elements on opposite sides. The shear stiffness (K_s) is often set to zero, which leaves only the Mode I type of cracking, a mode which occurs when the element suffers crack opening displacement. True cracking occurs when the COD reaches the critical value while the process zone exists at COD's between zero and the critical value.

The most difficult task with this type of model is to determine where and how the crack initiates and then decide on the crack path, when only compressive stresses exist. The crack path may not be too difficult as cracks always follow the maximum compressive stress direction. Determining the location and time (in NLFM, time implies critical COD) of crack initiation using these zero-thickness interface elements may be impossible. Although the location of fracture initiation often can be deduced from the geometry or from experience with physical models and nature. Crack initiation is based on the COD of the interface element. If the element has zero thickness, a compressive stress parallel to it will not induce COD. If a finite width could be used, the elements would be subject to an opening mode displacement perpendicular to the maximum compressive stress and cracking could occur. The stress versus COD relationship may not be the same for direct tension tests compared to compression tests however. If the process zone and subsequent true crack can be started, LEFM methods can be used once the crack has propagated to a sufficient length. However, all the problems associated with LEFM, such as the incorrect angle of propagation, must then be considered. Most importantly, offset crack initiation is not predicted by either NLFM or LEFM.

6.0.3 Numerical Modeling with Stress-Based Fracture Criteria

It is possible to use fracture mechanics to model single discrete fractures in rock subjected to compressive stresses. By filling the mesh with a pattern of initial flaws or cracks, en-echelon crack patterns can be generated. However, the basic progression of a single crack leading to offset cracks and a subsequent en-echelon pattern cannot be followed. For this reason, other theories and models were examined. Simple theories such as the maximum tensile stress or empirical failure theories for compression have been used in the past to indicate crack initiation and to propagate some cracks, such as the primary crack. However, these models suffer because of their lack of size dependence. Using the primary crack as an example, various hole sizes can be modeled and the same primary fracture initiation stress (the tensile strength) will be predicted for all cases when using the maximum stress theory. This is subject to mesh refinement problems as well, especially where high stress concentrations or gradients exist. The difficulties with both fracture mechanics and stress-based finite element modeling procedures provided part of the driving force behind this study. The laboratory tests, the physical model simulations and the development of a general fracture criterion were all done because a simple, generalized, discrete fracture modeling procedure was needed for analyzing the fractures around potash mine openings.

As a result, a stress-averaging based technique for finding the resistance to fracture based on experimental data was developed. This technique uses the Rocker function for crack initiation, crack damage and peak strength along with the averaged principal stresses, in the form of a safety factor term, the *USR* (unconfined strength

ratio). The function itself is immaterial. Any function which adequately describes the distribution of triaxial strength data in σ_1 - σ_3 space can be used. The *USR* is just a form of safety factor representing the state of fracture. The *USR* is used because it provides a continuous function whereas the more common definition of factor of safety in rock mechanics (equation 37) is undefined when $\sigma_3 < T_0$. Stress averaging can also be accomplished in many ways but the best appears to be a numerical, area averaging procedure. This technique can model primary and sidewall fracture from both microscopic flaws and macroscopic cavities, as shown in Chapter 4. By incorporating this criterion into a finite element code, other fractures around the cavities can also be modeled.

6.1 Finite Elements and Discrete Fracture

As part of the collaborative research between the University of Manitoba and the potash mining companies, a program called SIMEX, which stands for SImulated Mining EXcavation, was developed primarily by Dr. M.L. Ayari with later additions by Y. Yuan. This finite element code runs on a 386 or 486 IBM compatible personal computer. It is written in NDP Fortran[1], employing the PHAR LAP[2] tools for extended memory management and uses the HALO Graphics[3] package for graphical displays for both the video screen and the printer. It presently includes only elastic capabilities but both

---

[1] NDP is a registered trademark of MicroWay.

[2] PHAR LAP is a registered trademark of PHAR LAP Software, Inc.

[3] HALO is a registered trademark of Media Cybernetics.

fracture mechanics and the *USR*-Rocker fracture criterion have been included in the code for modeling discrete fractures.

There are numerous references which discuss finite element theory (Bathe, 1982; Hinton and Owen, 1979; Owen and Hinton, 1980; Zienkiewicz, 1977) thus the basic theory will not be discussed here. Many of these references discuss plasticity, visco-elasticity and visco-plasticity in addition to the basic elastic model. There are also numerous references on incorporating fracture mechanics principles into finite element codes for modeling discrete fracture (Ingraffea, 1977; Owen and Fawkes, 1983; Ayari, 1988). SIMEX and the implementation of fracture mechanics is described in detail by Ayari (1991). Discussions of more recent developments, including the implementation of the *USR*—Rocker fracture criterion can be found in Yuan *et al.* (submitted). Because the implementation of these concepts within the finite element code is still fairly recent, a brief summary of the fracture model and a description of the code will be given here.

6.2 Implementation of the *USR* Fracture Criterion into SIMEX

The first problem in numerical modeling of fractures is the mathematical representation of the physical fracture. Presently, most analytical and numerical fracture modeling exercises use the technique of engineering fracture mechanics. Here, the fracture is modeled as a slit, an elliptical void of zero width (the mathematical crack). The mathematical crack performs adequately under tensile stresses since the width of the crack has a limited influence on fracture propagation. In compression, fracture propagation depends strongly on the width of the crack; a zero-width crack (the

mathematical crack) will not propagate. Theoretically at least, a better representation of the crack is obtained by giving up on the mathematical crack and returning to the original Inglis (1913) solution for stresses around a finite width elliptical cavity (*FIWEC*).

The *FIWEC* has disadvantages also. The entry of crack width increases the number of fracture parameters from two (length and orientation) to three (length, width, orientation). Measuring the width of a propagating crack is rarely feasible although it can often be measured from physical tests or estimated. Another problem comes from the evaluated distribution of stress around an elliptical void placed in the orientation of the propagating crack. In uniaxial compression, at the crack tip (end of the major axis), the circumferential stress is always equal in absolute magnitude to the crack-parallel compressive stress. If fracture occurred according to the maximum stress theory, fracture propagation would start when the compressive stress was equal in absolute magnitude to the tensile strength of the material. Once started, the fracture would propagate indefinitely since the tensile stress at the crack tip does not depend on the length of the crack. The physical experiment demonstrated however that fracture propagation is stable; the applied compressive load must be increased to cause crack propagation.

The lack of size dependence shown by the maximum stress based elliptical model is contrary to experience; fracture nucleation and fracture propagation are both size dependent. Size dependence can, however, be successfully interpreted through stress averaging. A stress gradient exists ahead of the elliptical crack tip, thus an averaging procedure will reduce the stress and produce an apparent size effect. Stress averaging may be accomplished in many ways, one of them involves averaging stresses over a

circular region of diameter *2d* where the center of the circle is located at the reference point, for example at the elliptical crack tip (Figure 6.3).

Once the averaged stresses are defined, they are combined in a special form of the safety factor, called the ***USR*** (Lajtai *et al.*, 1991*a*). This function incorporates the condition of fracture in terms of the principal stresses. In most cases, these will be averaged stresses. The condition of fracture is $USR=1$; $USR>1$ represents a no fracture condition while $USR<1$ suggests that fracture has already occurred at a lower stress level. The actual value of ***USR*** is determined by the fracture strength of the rock, expressed in the form of a function, and the state of stress existing at a particular location. For example, if the fracture strength of the rock is modeled through the square-root form of the Rocker function (Carter *et al.*, 1991*a*), ***USR*** is defined as:

$$USR = \frac{T_o}{\frac{\sigma_3}{2} - \sqrt{\left(\frac{\sigma_3}{2}\right)^2 + \left(\frac{\sigma_1 T_o}{C_o}\right)^2}} \qquad \textbf{(6.1)}$$

$$USR = \frac{T_o}{\sigma_3} \qquad when \quad \sigma_1 = 0$$

If the Hoek and Brown criterion is selected to describe the strength of rocks, ***USR*** is computed from:

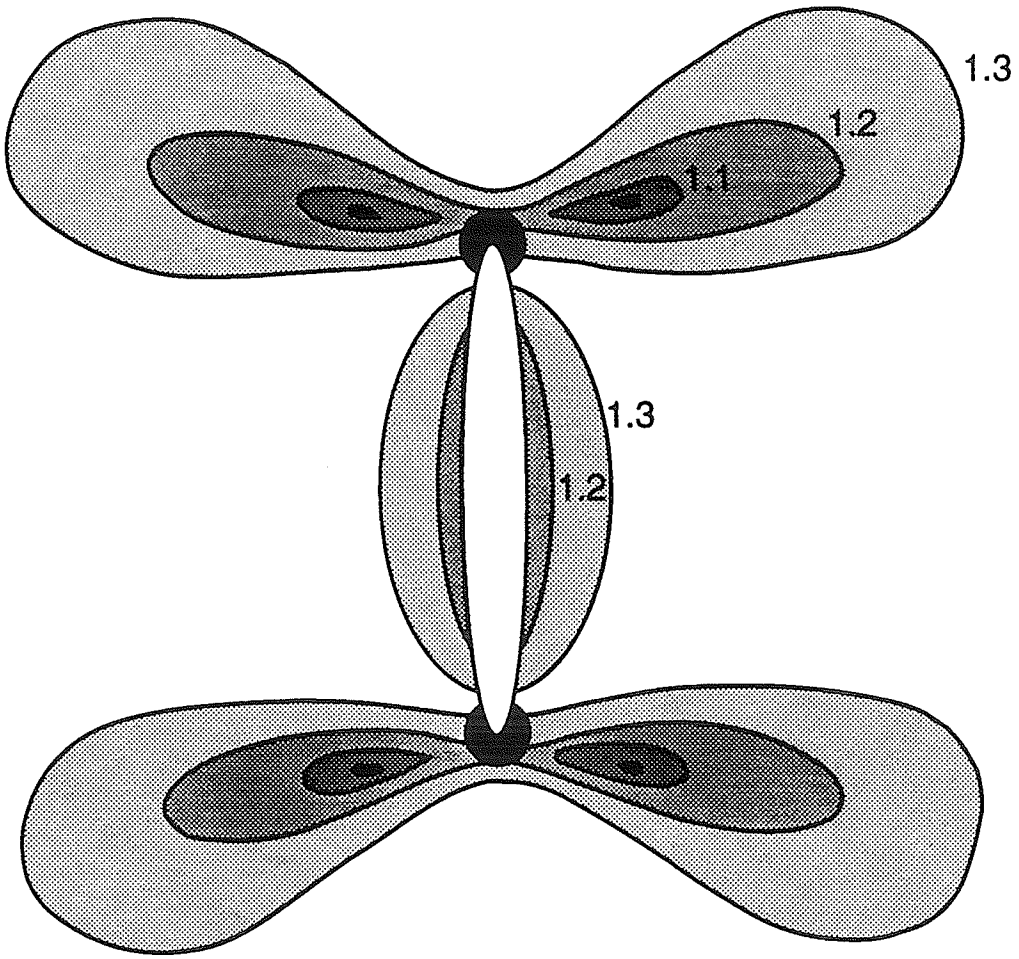

Figure 6.3 The *USR* contours around an elliptical cavity subjected to uniaxial compression parallel to the major axis. The dark circles (parts of circles) represent the area over which averaging takes place at the crack tip. By averaging the stress over a circular area at all points around the ellipse, the minimum *USR* value can be shown to move away eventually from the crack tip into remote or offset positions. The radius of the averaging area is increased at the crack tip to compensate for the lost area inside the crack.

$$USR = \frac{2\,s\,C_o}{\left[\,(m\sigma_3)^2 + 4\,s\,(\sigma_1 - \sigma_3)^2\,\right]^{1/2} - m\sigma_3} \qquad (6.2)$$

Here C_o represents the fracture strength in uniaxial compression while T_o is the tensile strength of the material. m and s are the Hoek and Brown rock strength parameters. σ_3 and σ_1 are the averaged principal stresses. For potash, the Hoek and Brown, two-parameter, square root formulation of strength has been shown to be inadequate (Carter *et al.*, 1991*a*) and the three-parameter Rocker formulation is used instead:

$$\sigma_{1f} = C_o\left(1 - \frac{\sigma_3}{T_o}\right)^R \qquad (6.3)$$

where σ_{1f} is the maximum principal stress at failure. The exponent R is 0.34 and the compressive and tensile strengths are 24.5 MPa and 1.7 MPa respectively for potash. There is no closed-form solution for USR when R is different from 0.5. However an iterative solution has been incorporated into the finite-element code.

6.3 Modeling Procedure with SIMEX

The evolution of fracture around a cylindrical cavity and in response to increasing uniaxial stress can be modeled in one session using the mouse-controlled automatic remesh features of this graphics-oriented microcomputer code. The code in its present

form is limited to elastic behavior. Subroutines for visco-plastic constitutive relationships are being built now, but they are still not available for this exercise. Therefore, potash which is not truly elastic must be modeled as such.

The first step in modeling is to construct a simple mesh of elements to represent the desired structure and then enter the required material parameters. The steps involved are quite simple with SIMEX (Ayari, 1991) because of the user interface. The mesh can be constructed through the use of a few super-elements which simplifies the initial input of nodes and their connectivity. Several super-elements can encompass hundreds (as many as the user wants) of smaller elements.

With the mesh constructed, the boundary constraints and load can be applied. The load can be applied as a pressure on the outside surface simulating the load applied to the physical models. Load can also be applied through nodal-point forces, gravity loading, or initial displacements, although only edge pressures will be used in this study. The problem can then be analyzed, producing stresses and displacements around the cavity. The possibility of fracture initiation is predicted using the averaged principal stresses with the *USR*-Rocker fracture criterion. If the load is insufficient to cause fracture initiation, the load is increased until initiation is predicted. At that point an elliptical fracture can be inserted into the mesh.

Making an elliptical cavity is a relatively simple process with SIMEX. The crack path must first be traced along a path of nodes. The program then automatically produces an elliptical opening with a user supplied crack width. The pre-cracked mesh can be refined to simplify the tracing procedure and to increase the number of elements in this

region, where the correct evaluation of stresses is important for predicting further crack propagation. The new mesh can then be reanalyzed. Either further cracking at this load is modeled or the load is increased to produce new cracks and/or propagate existing ones. This process can be continued almost indefinitely.

6.4 Single Circular Opening Under Uniaxial Compression

The mesh representing one quarter of the total model (Figure 6.4) was constructed to simulate the loading condition and the geometry of the physical models. The material properties and fracture resistance parameters were defined in Chapter 2 and 4. The first mesh contains a single circular cavity and is loaded in uniaxial compression. The hole size is 40 mm in diameter, replicating one of the physical model experiments.

A crack initiation stress of 50% and a crack damage stress of 70% of the peak strength (24.5 MPa) were used along with an averaging distance (d) of 3.5 mm. This radial distance was obtained by modeling the effect of hole size on fracture initiation from Chapter 4. The finite element modeling procedure involves step loading. For each load, the ***USR*** contours which are based on the averaged values of the principal stresses, are displayed to find the crack initiation point. At the uniaxial load of 3 MPa, this point appears at the primary fracture location (Figure 6.5). A small, finite width, elliptical half-crack is inserted here with the major axis of the crack directed along the maximum principal stress trajectory. The initial elliptical crack is usually only a few millimeters and the initial aspect ratio is about 0.01. These values are based on observations from the physical model tests.

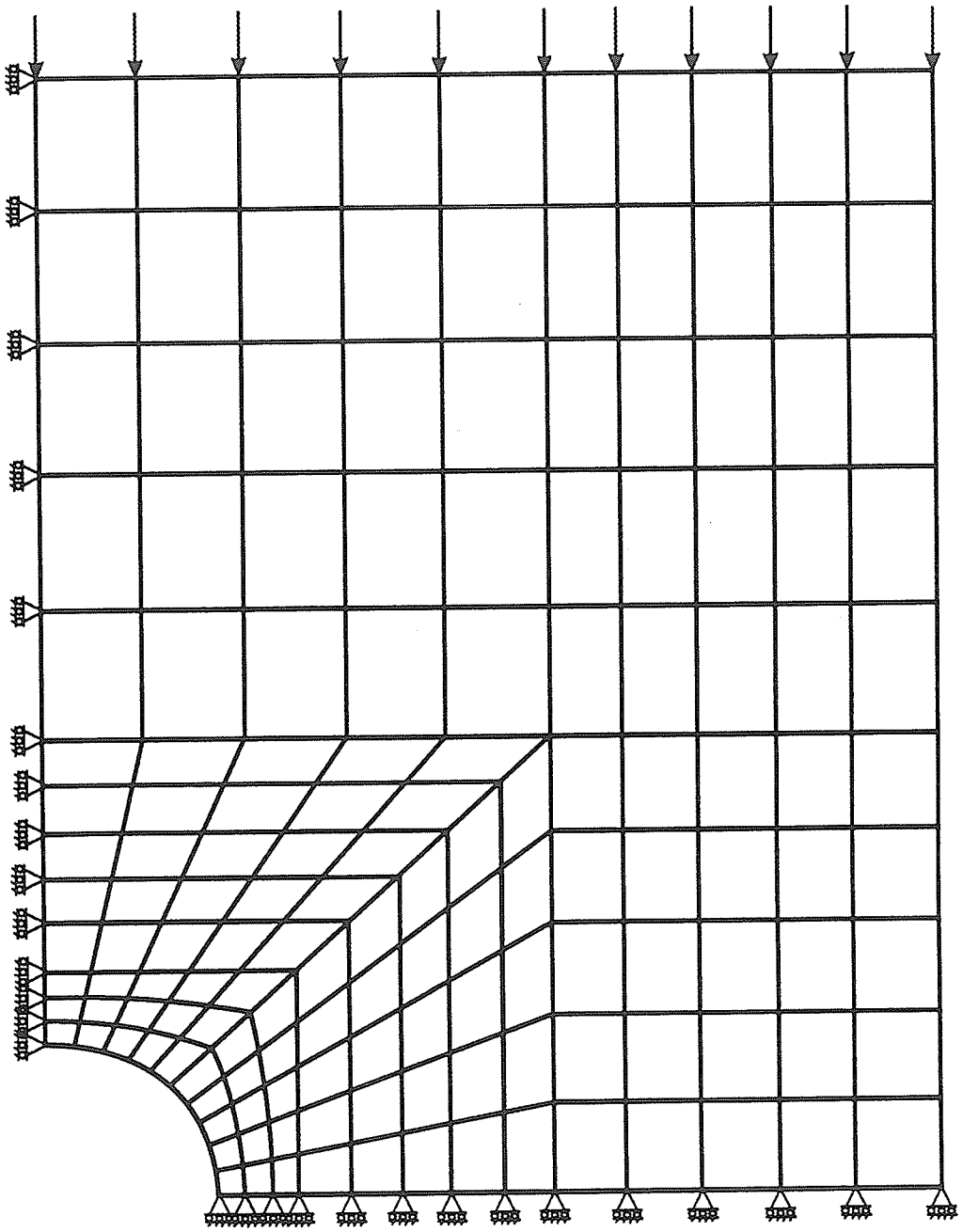

Figure 6.4 The finite element mesh simulating the physical potash models. Only one quarter of the model is needed due to symmetry. The cavity radius is 20 mm. There are 155, eight-noded quadrilateral elements prior to remeshing.

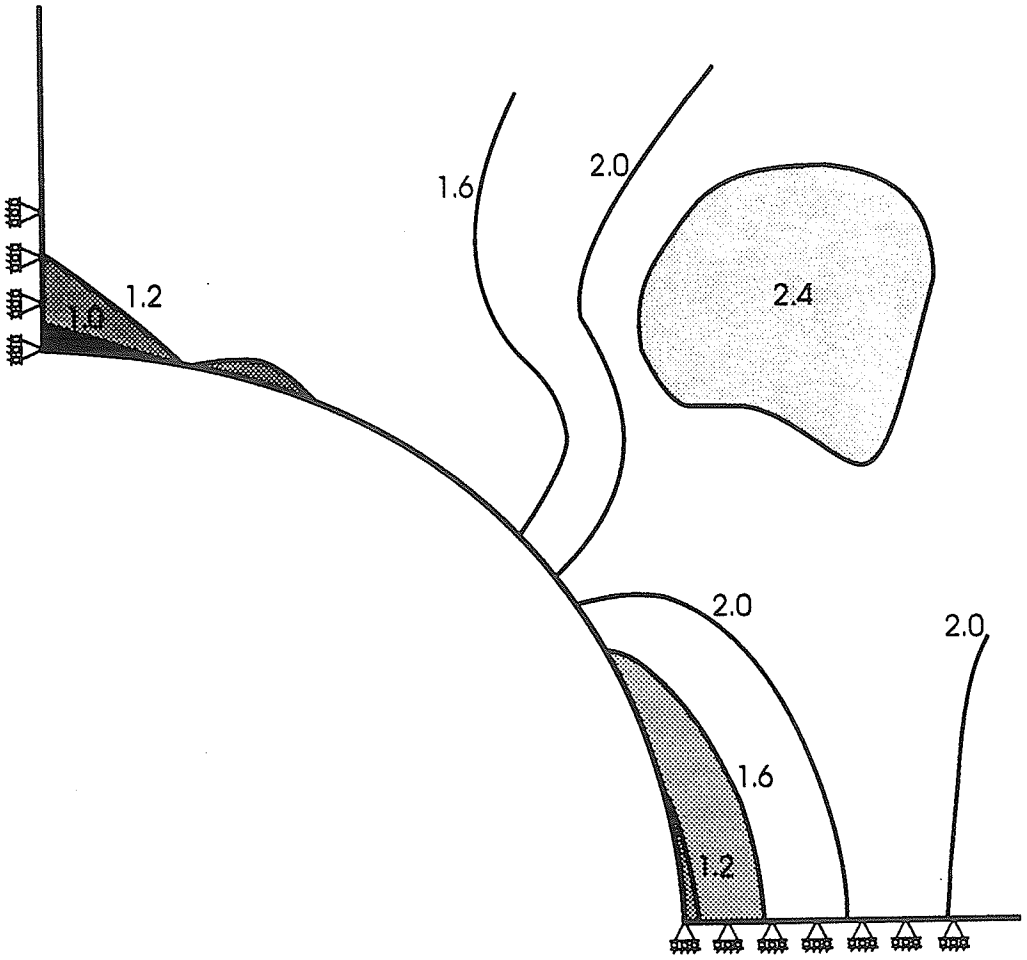

Figure 6.5 ***USR*** contours around the cavity for a 3-MPa uniaxial load. The ***USR*** values indicate that only the primary fracture should initiate as the value is less than one at the crown.

This cracked mesh is re-analyzed producing a new solution for the averaged principal stresses and the resulting *USR* distribution. The *USR* at the crack tip is again checked. If *USR* is less than unity, the crack is extended and the computational procedure is repeated. In this case, $USR > 1$, so the load must be increased to propagate the crack. For each step, the *USR* is evaluated at every Gauss point of the mesh to check for the initiation of other fractures. As the uniaxial load is increased, the primary crack propagates in a stable manner until a load of 5 MPa is reached. At this load, the *USR* contours suggest crack formation at the side of the cavity. To initiate and propagate these, first the maximum compressive stress trajectories are displayed to establish the direction of propagation. A *FIWEC* is inserted parallel to the maximum principal stress trajectories along a set of nodal points. The cracks which are inserted here are very small and they remain small. They do not propagate, instead other small cracks offset from each other must be initiated (Figure 6.6). As the load is increased, the position of fracture initiation moves away from the side of the cavity to a remote position. Cracks in this region tend to propagate further than the cracks at the side, however the pattern of stable crack growth and the initiation of offset cracks is repeated here (Figure 6.6).

The procedure could be continued beyond the stage shown in Figure 6.6 but at this stage fractures start forming in profusion as the load is increased. In general, the primary crack seems to be the least important; it forms first but quickly stabilizes with very little extension as the load is increased. The fractures at the side form close together (depending on the mesh) but they tend to remain short. The remote fractures are longer

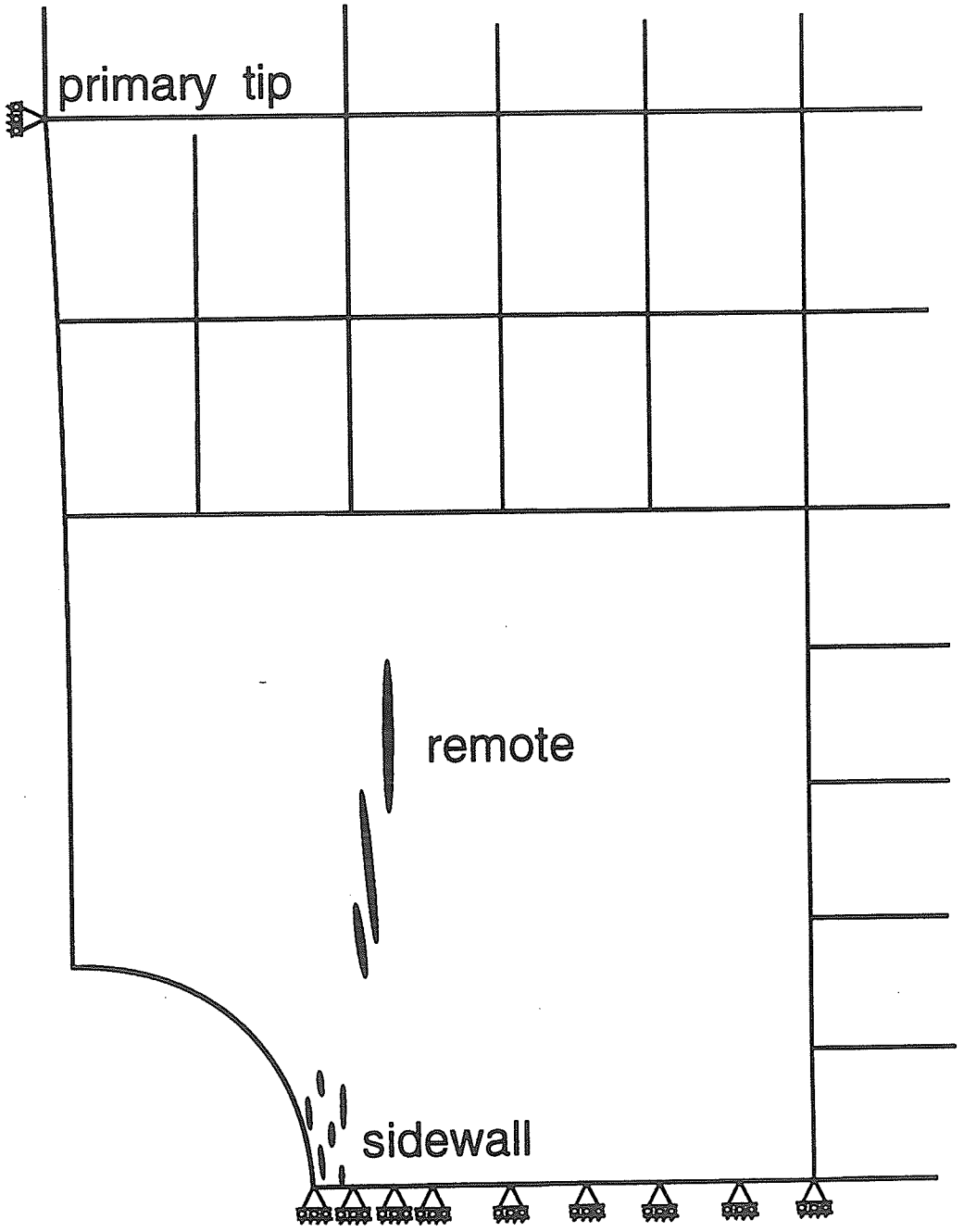

Figure 6.6 Primary, remote and sidewall cracks in the mesh at a uniaxial load of 8 MPa. The refined mesh has been deleted and the elliptical cracks have been enlarged for clarity.

and they propagate from the initiation point in both directions. The general pattern is in broad agreement with the visual observations that were made during the physical model experiment.

6.5 Multiple Circular Opening Model

A mesh was constructed to simulate one quarter of the physical model containing three circular holes (Figure 6.7). This mesh also includes the limestone loading platen on top of the potash. The material properties for the potash remain the same as for the previous model. The material properties for the limestone are based on the Tyndallstone (set #2) data. The modeling procedure was described in the previous sections, thus only the main results will be summarized.

Figure 6.8 contains a series of figures showing the progression of cracking in the model as the uniaxial compressive load is increased. The first crack to form is the primary crack at the crown of the larger, outside hole. This crack initiated at a load of about 3 MPa and propagated a short distance at this load. These cracks were observed in the physical experiment from Chapter 5 at a load between 2.6 and 3.5 MPa. An increase of the uniaxial load to 4 MPa caused this crack to propagate by a small amount.

The next increase in load to 5 MPa induced small tension cracks in the limestone loading platen. These cracks occurred at the contact between the potash and the limestone between the two cavities. These cracks reduce the local tensile stresses in the limestone and remain stable at these low loads. Similar cracks were observed in the physical test at a load of 3.5 MPa but in roughly the same area. The 5 MPa load also

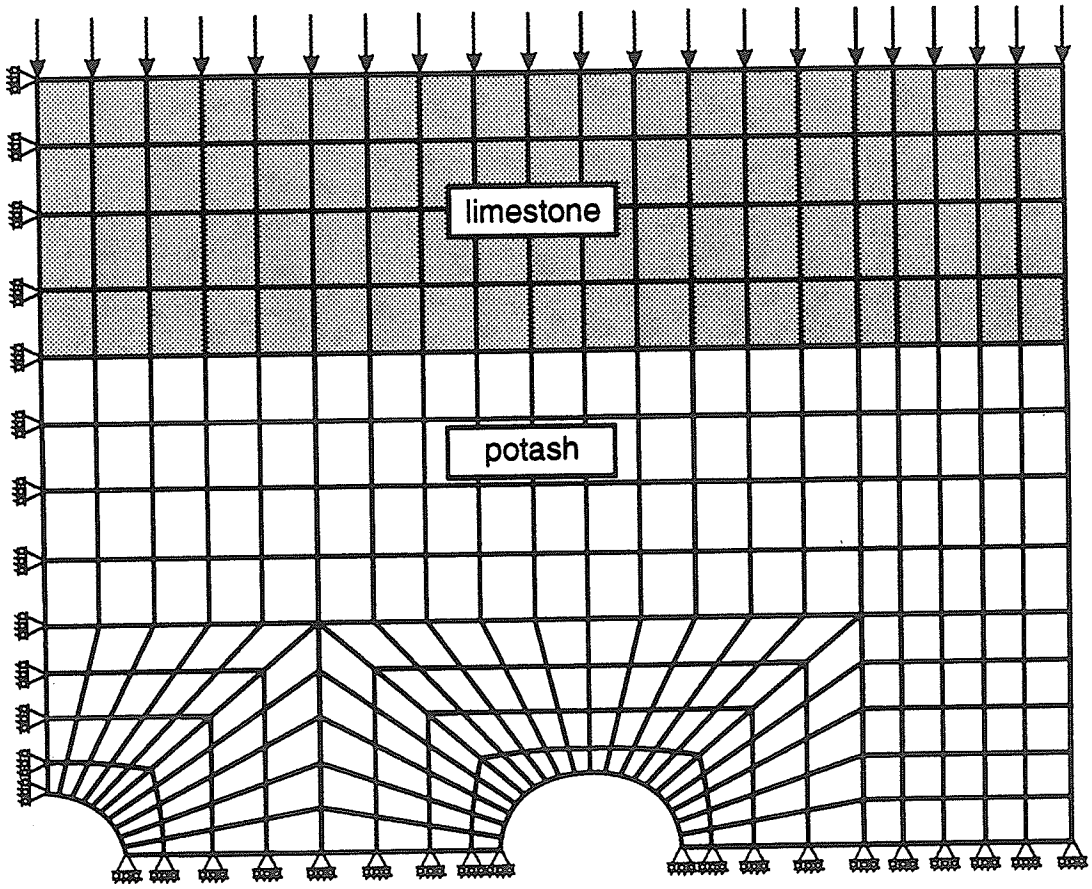

Figure 6.7 A finite element mesh simulating three singular cavities in potash with limestone loading platens. Only one quarter of the model is needed due to symmetry. The larger hole has a radius of 34 mm and the smaller hole has a radius of 23 mm. There are 305, eight-noded quadrilateral elements prior to remeshing.

caused an increase in the primary crack length. The growth of this crack appears to be stable. Although it is somewhat shorter than the observed primary crack length, the pattern is very similar.

The next load increase to 6 MPa caused a small degree of fracturing at the springlines of both the large and small hole. This is the first indication of any cracking associated with the small hole. Some tension exists at the primary fracture location of the small hole but the averaged stress is compressive. The cracks at the sidewall are small and do not propagate; they are basically the same as those described for the previous finite element model.

A load of 7 MPa causes remote fracture initiation. The first remote fractures in the physical model were observed at 5.3 MPa. These fractures are similar to the remote fractures from the previous finite element model. This load also induces further cracking at the sidewall. Modeling was terminated at this stage. Although cracking would continue with increasing load, there is still no method for determining structural stability.

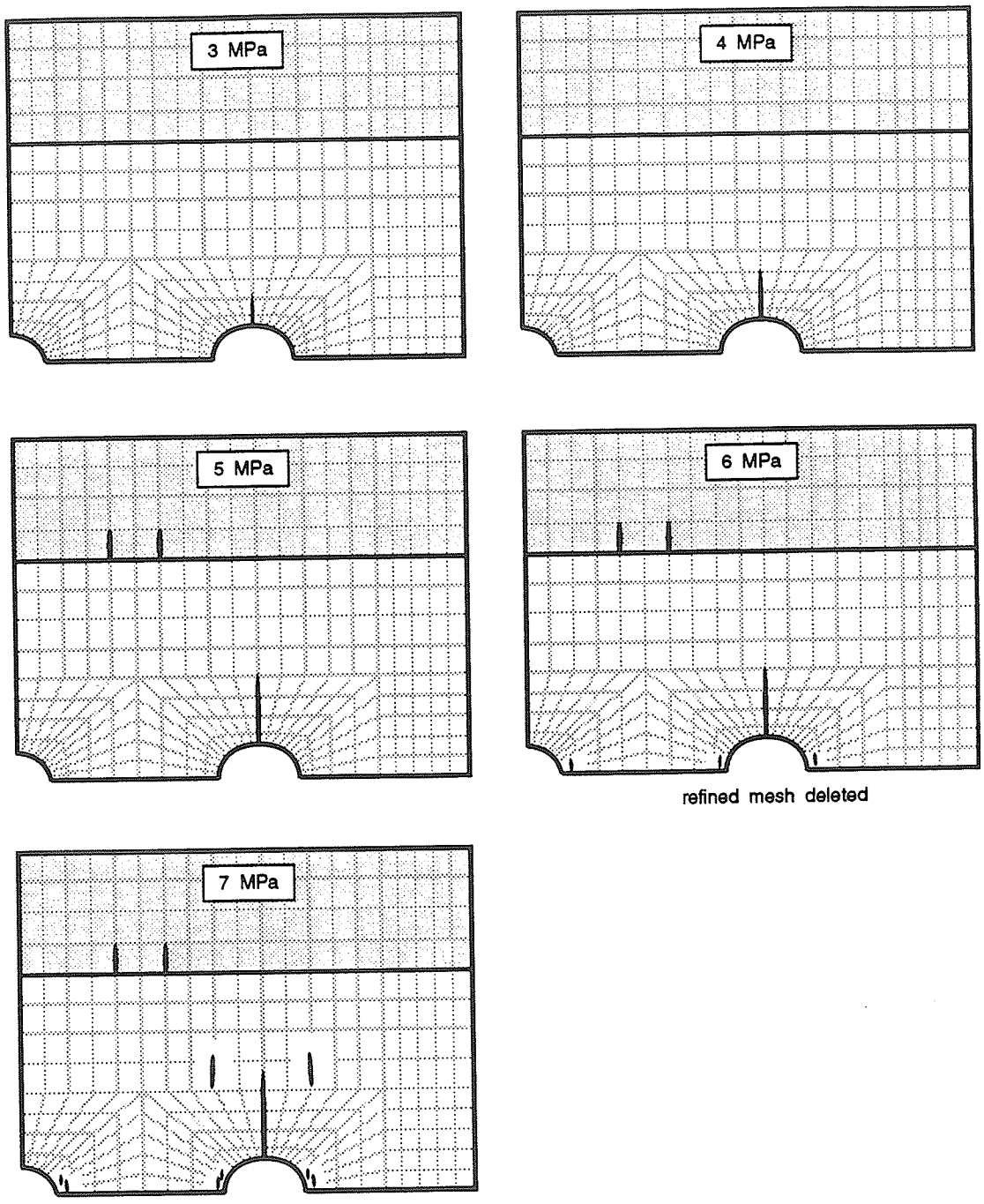

Figure 6.8 A series of figures showing the progression of cracking in the model as the uniaxial compressive stress is increased. The primary crack on the larger hole forms first, followed by stable cracks in the limestone plate. A small amount of sidewall fracturing around both holes occurs next followed by remote fracturing around the large hole.

7 DISCUSSION AND SUMMARY

7.1 General

The ultimate goal of this study was to develop a method of interpreting the fractures around underground openings in general, with special emphasis on the Saskatchewan potash. This includes initiation stress, location, orientation and direction of propagation. Due to the complex nature of the opening shapes, the combination of multiple openings and the triaxial stress state in the potash mines, a numerical procedure is required to model the fractures. Fairly simple physical models have been tested but these can serve only as a guide for predicting the actual conditions underground and as calibration for the numerical model.

Fractures in rock seem to occur at all scales and in all rock types, whether they are subjected to tensile or to compressive stresses. A numerical procedure should therefore be capable of representing fractures in both types of stress fields as well as in cases where both tension and compression exist together. The procedure must also be applicable at any scale and be able to account for the structural size effects which are often observed in experimental testing. The following is a summary and discussion of the main topics associated with the fracturing of rock in general and the numerical modeling of these fractures.

7.2 Fractures in Rock—The Physical Phenomenon

The first step toward predicting the occurrence of fractures around potash mine openings was to establish a general fracture criterion. In order to accomplish this, the strength, fracture characteristics and material properties of potash and two other rock types were examined. The other two rock types, Tyndall limestone and Lac du Bonnet granite, allowed the study to be more general and provided a range of rock behavior from relatively ductile to relatively brittle. Many of the tests necessary to define these parameters had already been completed at the University of Manitoba. The previous test data, along with the data from several additional tests conducted by the author, were summarized in Chapter 2. The data suggest that, although the rocks behave in different manners, ductile to brittle, the general stress—strain response is quite similar. The more ductile rocks have a yield stress and suffer some plastic deformation but they also crack just as do the more brittle rocks. Factors such as loading rate, stress level, and time, however, affect the quantity of strain associated with the two types of deformation.

The generally accepted description of fractures which occur in rock subjected to tension and/or compression was discussed in Chapter 3. Fractures can and do occur before failure takes place. In the laboratory, fractures range from microscopic to macroscopic size and can form as tension or extension fractures. Both types form in response to local tensile stress and are genetically similar. It has become customary in the literature however, to refer to fractures which form due to applied far-field tensile stresses as tension fractures and those which form due to locally induced tension caused by compressive far-field stresses as extension fractures. The local tension is usually due

to the redistribution of stress around microscopic flaws in the rock. Failure results when single or multiple fractures extend through the specimen, causing a significant reduction in load bearing capacity. Generally, for failure to occur, microfractures must grow to macro-size. Subsequent coalescence of several macrofractures, and possibly shearing, occur before final failure. All fractures, whether they form due to far-field tension or compression, grow parallel to the maximum compressive stress trajectory and perpendicular to the minimum stress trajectory.

A clearer picture of fracture growth in compressive stress fields was obtained from the physical model studies, namely, the simulation of a circular, underground excavation in uniaxial compression. In areas where the stress field is primarily tensile, usually only a single crack forms, possibly due to the fact that the fracture relieves the high local tension. When the stress field is compressive, the stress relief due to a single crack is quite minor and several cracks may form in close proximity.

In areas of low tension and high compression (remote positions in the model tests) several microscopic cracks often appear. They are parallel, or nearly parallel, to the maximum compressive stress direction. The initial aspect ratio is commonly between 0.1 and 0.01: they are quite long and narrow. The exact location and number of initial cracks must depend on the material flaws in the local region. The stress level is usually between the crack initiation and crack damage stress of uniaxial compression. In many laboratory tests, such as uniaxial compression, visible (naked-eye) cracks are rarely seen at the crack initiation stress; they may be visible after the crack damage stress is exceeded. Visible cracks can be seen more readily in the physical models, however. In

the case of remote fractures, low tensile stresses exist in addition to the high compression, thereby allowing visible cracks to form at a compressive stress which is lower than the crack damage stress.

The applied stress on these models was recorded as the stress acting over the upper surface, not the pillar stress. Consequently, the stress at initiation is actually higher than the recorded value. The actual stress is difficult to determine, however, due to the stress gradients, material inhomogeneities, variable elastic moduli for different crystals and slight variations in gauge position. For this reason, the initiation stress is taken simply as the stress on the upper surface. The first few cracks remain relatively stable at the initiation load although, given sufficient time and suitably humid and chemically active environments, subcritical cracking could occur, leading to static fatigue, as the data from Chapter 5 would suggest. Assuming no subcritical crack growth occurs, the load must be increased to propagate the cracks. Propagation of these first cracks may occur, but an increase in total crack length (summation of all crack lengths) often results from the initiation of offset cracks leading to the en-echelon pattern seen in Figures 3.11, 4.5, 4.41, 5.1 and 5.16a-f.

The en-echelon pattern breaks down with further increases in load as the material between the offset cracks suffers further cracking. This material then buckles and snaps off along cleavage planes or shears as the surrounding material undergoes increased displacement. Dilatation of most cracks usually occurs at the same time. The consequence of this complex process is a single fracture with some material left protruding from the walls as remnants of the bridge material between the offset cracks

(Figure 4.42 and 5.16). This process occurs not only in the model tests but also in the larger-scale potash mining excavations (Figure 5.1). The cracks are larger, but they have formed through the same process as described above. Figure 5.1 shows several en-echelon cracks and several large, single cracks which have remnants of the bridges still protruding from the walls.

In areas of low confining pressure and a high compressive load (the sidewall zone of the physical model tests), the same process still takes place. However, Figure 5.16e-f would suggest that these en-echelon cracks are generally shorter but more numerous. These cracks, including the bridge material between them, coalesce through a shearing process which produces a shear fracture rather than the long extensional or splitting fractures. The development of a shear fracture is one of the last steps before the model finally collapses (Figure 5.16f).

The comparison between the two types of stress fields, low tension or low compression perpendicular to the crack, matches that for laboratory tests in uniaxial compression and triaxial compression. Chapter 3 described the fractures in uniaxial compression as axial splitting fractures. Only a few fractures exist, but these extend through the length of the specimen, causing the material to split into columns. For triaxial compression, there are more cracks but they are shorter. Failure usually occurs by a coalescence of fractures and shearing along the weakened zone of material. The general cracking process appears to be the same, regardless of scale, for all rock types. The cracking process around cavities simply provides a clearer picture of this entire mechanism, and potash seems to be the most suitable for viewing the natural progression

from fracture initiation to specimen failure. The same fracture pattern was also seen in the physical model tests on LDB granite and Tyndall limestone.

7.3 Numerical Modeling of Fractures in Rock

All three rock types undergo brittle cracking. The fractures range in size from microscopic to megascopic; submicroscopic fractures must also exist. The pattern of fracture initiation, propagation, offset cracking, coalescence and possibly shearing is also quite well-defined, appearing in all three rock types. In order to have a general tool for analyzing fractures in rock, a numerical modeling procedure should be able to reproduce most, if not all, of these features.

The first step in the numerical modeling of fractures in rock was to define crack initiation. Crack initiation can be defined using stress-based criteria or using the strain or crack opening displacement (COD). This study uses the stress-based approach. Crack initiation as well as crack damage (volumetric reversal) and peak strength have all been measured as a function of confining pressure for the three rock types. The three data sets, one for each rock type, were fitted to a single Rocker function (equation 41) by varying the parameter A. The Rocker function was developed because the standard Hoek-Brown and Mohr—Coulomb functions did not fit all the data very well (Carter *et al.*, 1991*a*). Other functions, such as Johnston's, seemed rather complex. The Rocker function was developed independently but was eventually found to be the same as a function published earlier by Sheory *et al.* (1989). This function fits the triaxial strength

data for potash, Tyndallstone and LDB granite quite nicely. The same function also fits the crack initiation and crack damage data for all three rocks quite well.

Linear elastic fracture mechanics (LEFM) requires a method of predicting crack initiation, as do all stress-based models. Non-linear fracture mechanics (NLFM) requires the stress versus COD relationship from direct tension tests. Most stress—COD relationships are obtained from direct tension tests, but it is also necessary to be able to model fractures in compression. Although it could be done, the stress versus COD relationship has never been defined for compression and actually has not yet been defined for these three rock types in tension, either. In any case, once crack initiation is predicted, a crack can be positioned in the finite element mesh.

Models based on LEFM, as described in Chapter 6, are simple enough and can be used to model fracture propagation in tension or compression, although two or more different types of cracks are required. Chapter 3 showed that the parameters, as measured for these three rock types, do not match LEFM predictions, but such things as initial crack length and fracture toughness can always be adjusted so that results do match. For the microscopic cracks seen in the model tests of this study, it is conceivable that fracture toughness ranges from almost zero up to the critical value for the rock. The orientation of cleavage planes, flaws and grain boundaries with respect to the cracks could lead to an extremely variable fracture toughness. One question which has never been addressed is whether the toughness is the same for cracks growing in a far-field tensile stress compared to a far-field compressive stress which merely induces local tension.

Other difficulties, such as an incorrect angle of propagation and the inability to predict offset crack initiation, were fully discussed in Chapter 6.

The theory and modeling procedure of NLFM were described in Chapter 6 also. NLFM should be used in cases where the process zone is large in relation to the crack size and LEFM can then be used once the crack has grown to a sufficient length. NLFM is attractive because it does not require external crack initiation procedures and it incorporates structural and crack size effects. However, difficulties arise when no tensile stresses exist and the crack must be made to follow the maximum compressive stress trajectories. Unless the crack has a finite width, it will not disturb the stress parallel to it and accordingly will not suffer crack opening displacement. NLFM, like LEFM, does not predict offset crack initiation either.

Stress-based modeling procedures have several problems also. It was shown in Chapter 2 and 3 that rocks suffer crack initiation prior to peak strength. The point of volumetric reversal on the stress—strain curve marks a position where crack growth would continue at a constant load. Peak strength implies that the structure is full of cracks and is unable to support further load. However, "true" cracking, in tension at least, does not always occur until part way down the post-peak, strain-softening curve. In compression, shear fractures commonly develop on the post-peak side of the curve but "true" cracking may occur prior to peak strength. None of these points, such as crack initiation, are very easy to measure and it is difficult to define "true" cracking in compression. Strain-based criteria could be used but the strain is often more erratic than the stress. The other major problem with stress-based criteria is the lack of structure or

crack size dependence. This size dependence is actually a function of the stress gradient but the two often coexist, leading to the assumption that size controls the strength. Based on the data presented in Chapter 3 and 4, it seems that size itself is of little consequence. When stress gradients, which are a function of size, do exist then the size affects the strength.

The (size) stress gradient effect can quite easily be incorporated in fracture criteria, as shown in Chapter 4, by averaging the stress. The effect of cavity size on fracture initiation stress is apparent from Chapter 4 where a high stress gradient (small cavity) leads to a high fracture resistance. Numerous models were used to predict this size dependence. It was found that averaging the stresses produced the best fit to the data and provided the most reasonable values for the asymptote (fracture initiation load for very large cavities) and for the intercept (fracture initiation load for a cavity radius of zero). This procedure of using the average stresses along with the *USR*-Rocker fracture criterion was then used to model fracture initiation and propagation around elliptical cavities (Carter *et al.*, 1992). Not only is the elliptical cavity size accounted for but offset crack initiation is also predicted.

Returning to the physical models, it was stated that the stress averaging procedure produced the desired asymptote and intercepts as a function of cavity size. For the primary fracture, the desired asymptote equals the tensile strength while the intercept equals the uniaxial compressive strength. The asymptote for sidewall fractures is at one third of the uniaxial compressive strength and the intercept is again at the uniaxial compressive strength. The intercept for remote fracture is also at the uniaxial

compressive strength; little significance can be attached to the asymptote, however. All of the asymptotes could actually be much lower. Haimson and Herrick (1989), who have tested much larger cavity sizes, found that the asymptote for sidewall fractures was below one third of the uniaxial compressive strength. In theory, this value could be as low as one third of the crack initiation stress in uniaxial compression. The intercept values could also be much lower, especially for the primary fracture, which resembles the first crack in a solid block of rock. The intercept for primary fracture could be as low as the crack initiation stress. A few more tests using both very small and very large cavity sizes may define these points more accurately. For primary fracture, an intercept equal to the crack initiation stress and an asymptote close to the tensile strength can still be obtained using the stress-averaging model by simply using the Rocker function for crack initiation rather than peak strength.

Because this method of stress averaging worked so well for modeling fracture initiation around the physical cavities and also predicted offset cracking from elliptical cavities, it was incorporated into the finite element code (SIMEX). This was described in Chapter 6 along with the procedure of modeling a crack and the description of several applications. The method uses an elliptical cavity to simulate a crack and the stress at the crack tip is averaged to determine whether the crack will propagate or not. This raises two problems: 1) the elliptical crack width must be defined along with its length and 2) the averaging radius (circular area used for averaging) must be specified. The aspect ratio of the crack (width/length) is usually estimated from the observed cracks in the rock and is commonly in the range 0.1 to 0.01, depending on the rock type and stress

field. The averaging distance or radius was defined in Chapter 4 based on the numerical area averaging technique for modeling fracture initiation around cavities. The averaging distances for the three rock types are quite close. The more ductile potash requires the largest value (3.5 mm) while the mostly brittle granite has the smallest value (2 mm). Most other rocks would probably fall somewhere between these two values; Tyndallstone has a value of 3 mm.

The averaging distance was obtained from fitting the stress-averaging model to the primary fracture initiation data from the physical model tests. The cavities in this case are circular and relatively large. Based on the numerical modeling of fracture initiation from an elliptical cavity (Carter *et al.*, submitted), especially for very small aspect ratios, the averaging distance should be much lower than the value predicted for the circular cavities. The actual relationship between cavity size or aspect ratio and averaging distance was never adequately defined. However, as the finite element modeling shows, the value from the circular models actually produces fairly reasonable results and offset crack initiation and propagation are predicted.

The finite element code (SIMEX) was applied to two cases, replicating two of the physical model tests. The first model was a single circular cavity in a potash block, loaded in uniaxial compression. The second consisted of three holes (two large holes and a smaller hole in the middle) in a potash block with limestone loading platens on the upper and lower surfaces. The loading was again in uniaxial compression. The simulations reproduced the physical phenomena remarkably well. The primary, remote and sidewall fractures were all predicted at loads relatively close to the measured values.

One of the best features was the prediction of offset cracks in the sidewall and remote region. The en-echelon pattern in these regions also duplicated to a close extent the features observed in the laboratory. Fractures in the sidewall region were closely spaced and very short, while those in the remote region propagated much further before predicting offset cracks. In the second model, the limestone plate cracked in a stable manner that was very similar to that which was observed experimentally. The other cracks around the large, outer hole resemble those from the first model. In addition, very little cracking is predicted for the inner hole until very high loads are reached, a phenomenon which was also observed in the physical model. It appears that this numerical model is quite capable of modeling the fractures observed around modeled cavities for potash rock.

7.4 Future Research

The subject of fracture in rock can always use further refinement. Subcritical crack growth and static fatigue need to be addressed for potash. Crack length versus fracture toughness also requires more study. The problem of variable toughness with variations in minerals, cleavage directions, intersecting flaws and grain boundaries could be examined for individual rock types. Most fracture toughness measurements are made from bending or direct tension types of tests. It is unclear whether this toughness applies to cracks growing in a far-field compressive stress field which induces local tension. The aspect of process zone size and shape for far-field tension compared to far-field compression could also use further study. The process zone size and shape has been

studied for a number of years using various techniques in bending and tension tests. The applicability of some of these techniques (eg. acoustic emission, laser holography and interferometry, and acetylcellulose replicating film) for examining the process zone in compression should also be examined. The process zone seems to be roughly correlated to the averaging distance used in this thesis and the averaging distance seems to be a function of not only the rock type but also crack size and shape; this problem has not been addressed fully. The function of the process zone as it relates to the stress and strain surrounding the crack needs to be more clearly defined. Several authors have stated that the process zone can shield the crack from the far-field stress reducing the stress intensity and also increase the stress intensity by creating a weakened zone of material. Stress-strain curves for the three rocks of this study, which include the strain softening portion of the stress-strain curve, also need to be generated. Direct tension tests still have not been done on LDB granite.

The next topic involves the physical model tests. Several model tests could be done using both very small and very large cavity sizes to arrive at a better definition of the asymptote and intercept. The linear-integration averaging technique used to model the fracture initiation stress could be extended to the elliptical cavity. Physical modeling of various elliptical cavity sizes or aspect ratios could help define the relationship between averaging distance and crack size/shape. Much more work could be done with the physical models of potash, analyzing in more detail: 1) time- and stress-dependent cracking and closure, 2) fractures in the mine, in terms of time, propagation rate, crack density, and 3) the correlation between the fractures in the mine and the model tests.

Numerical modeling is probably the biggest area where further studies can be undertaken, some of which are currently being done. Using the present finite element model, it should be possible to model crack growth around the potash mine openings using any opening shape or combination of openings with various stress fields. Plasticity and visco-plasticity capabilities are currently being added to the program. This is important as the deformation, including brittle cracking, of potash is time- and rate-dependent. The addition of the other capabilities should allow the time-dependent cracking and plastic deformation to be more carefully modeled. A method of predicting structural instability due to accumulated cracking in the finite element simulation also needs to be examined. The last question is, can fracture mechanics, either LEFM or NLFM be made capable of predicting offset fractures in compressive stress fields?

8 CONCLUSIONS

1) For both uniaxial and triaxial tests, the stress—strain curves for Saskatchewan potash generally show yielding, crack initiation, crack damage or volumetric reversal and peak strength. Tyndallstone may or may not show yielding; LDB granite does not show yielding.

2) For each of these rock types, a single Rocker function can be fitted to the crack initiation, crack damage and peak strength data, in σ_1 - σ_3 space, by varying a single parameter. The Rocker function fits the peak strength data, in the tension and low confining pressure region, better than the traditional Hoek and Brown function.

3) The unconfined strength ratio (*USR*) can be used to represent the state of fracture. The fracture states are: i) no cracking, ii) initiation of microscopic cracks, iii) crack damage, which is usually the beginning of macroscopic cracking and iv) post-peak softening, which includes macrocrack coalescence and shear fracture development.

4) Cracks grow in compression by a complex process of propagation of individual cracks, offset or en-echelon crack initiation, cracking of the bridge material between the en-echelon cracks, buckling and shearing of the cracked bridge material, coalescence of the en-echelon cracks to form a macroscopic crack and sometimes shearing along this weakened zone of cracked material.

5) In a highly compressive stress environment such as the sidewall of a cavity, the en-echelon cracks are short and closely spaced, almost always leading to a shear fracture.

6) Fracture growth is stable in compression. An increasing amount of load is required to produce equal increments of crack propagation.

7) Total crack growth in potash is time-dependent as well as stress-level-dependent. A stress between 13 and 14 MPa will cause the potash model to collapse in a short period of time. Stress levels below about 10 MPa may induce significant cracking but the rate of total crack length growth decreases in time and the model remains stable.

8) Fracture initiation around a cavity, in a finite block of rock, depends on the size of the cavity. Small cavities require a greater load to initiate fracturing than do larger cavities.

9) In general, the fracture sequence around cavities is independent of cavity size, for the range of sizes tested. Primary tension fractures form at the center of the crown and invert, remote extension fractures form away from the cavity perimeter on either side of the primary crack, and sidewall fractures form at the springlines as extensional cracks in a high-compressive stress environment.

10) Cavity shape has little effect on the fracture pattern.

11) The presence of multiple cavities has little effect on the sequence of fractures.

12) The effect of cavity size on primary fracture initiation stress is best modeled by averaging the maximum and minimum principal stresses over a small area in the region of cracking. The model predicts an asymptote at the tensile strength and an intercept at the uniaxial compressive strength.

13) The effect of cavity size on sidewall fracture initiation stress is best modeled by averaging the tangential stress in the region of cracking. The model predicts an

asymptote at one third of the uniaxial compressive strength and an intercept at the uniaxial compressive strength.

14) Linear elastic and non-linear fracture mechanics can both be used to model fractures in rock. However, neither model predicts the initiation of offset cracks.

15) A finite-element implementation (SIMEX) of stress averaging and the *USR*-Rocker fracture criterion can be used to predict the fractures seen around modeled openings in potash, including offset or en-echelon crack patterns.

REFERENCES

Abeda, W.K. (1989). Comparison of the moduli of elasticity of the Dawson Bay Formation in uniaxial tension and compression. B.Sc. Thesis, Geological Engineering Department, University of Manitoba, Winnipeg, Canada.

Adams, F.D. (1910). An experimental investigation into the action of differential pressure on certain minerals and rocks, employing the process suggested by Professor Kick. Journal of Geology, Vol 18, pp. 489-525.

Ahmed, M. (1990). A Study of Possible Failure Mechanisms for Mining-Induced Seismicity in Saskatchewan. Ph.D. Dissertation, Civil Engineering Dept., University of Manitoba, Winnipeg, Canada, p. 217.

Atkinson, B.K. and Meredith, P.G. (1987). The theory of subcritical crack growth with application to minerals and rocks, In: Fracture Mechanics of Rock. Ed. B.K. Atkinson, Academic Press, London, pp. 111-166.

Ayari, M.L. (1991). SIMEX - Simulated Mining Excavation: Theory and User's Manual. Internal Report, Geological Engineering Department, University of Manitoba, Winnipeg, Canada.

Ayari, M.L. (1988). Static and Dynamic Fracture Mechanics of Concrete Gravity Dams. Ph.D. Dissertation, University of Colorado, Boulder, Colorado, p. 159.

Babulic, P.J. (1985). Fracture propagation around a circular opening in granite. B.Sc. Thesis, Geological Engineering Department, University of Manitoba, Winnipeg, Canada.

Baecher, G.B. and Einstein, H.H. (1981). Size effect in rock testing. Geophysical Research Letters, 8, No 7, pp. 671-674.

Baeza, L., Rosenthal, J. and Kvapil, R. (1987). Geomechanics at El Teniente mine. Proceedings of the 28th U.S. Symposium on Rock Mechanics, Tucson, Arizona, pp. 1153-1160.

Barenblatt, G.I. (1962). The mathematical theory of equilibrium of cracks in brittle fracture. Advances in Applied Mechanics, Vol 7, pp. 55-129.

Bathe, K.J. (1982). Finite Element Procedures in Engineering Analysis. Prentice-Hall.

Bazant, Z.P. (1984). Size effect in blunt fracture: concrete, rock, metal. Journal of Engineering Mechanics, American Society of Civil Engineers, Vol 110, No 4, pp. 518-535.

Bazant, Z.P. (1985). Mechanics of fracture and progressive cracking in concrete structures, In: Fracture Mechanics of Concrete: Structural Application and Numerical Calculation. Editor-in-Chief: G.C. Shah, Martinus Nijhoff Publishers, pp. 1-94.

Bazant, Z.P., Gettu, R. and Kazemi, M.T. (1991). Identification of nonlinear fracture properties from size effect tests and structural analysis based on geometry-dependent R-curves. International Journal Rock Mechanics and Mining Science & Geomechanics Abstracts, Vol 28, No 1, pp. 43-51.

Bazant, Z.P. and Yunping, X. (1991). Statistical size effect in quasi-brittle structures: Part II - nonlocal theory. Journal of Engineering Mechanics, American Society of Civil Engineers, Vol 117, No 11, pp. 2623-2640.

Bieniawski, Z.T. (1967). Mechanism of brittle fracture of rock. International Journal of Rock Mechanics and Mining Science, Vol 4, No 4, pp. 395-430.

Blejwas, T.E. (1987). Planning a program in experimental rock mechanics for the Nevada Nuclear Waste Storage Investigations Project. Proceedings of the 28th U.S. Symposium on Rock Mechanics, Tucson, Arizona, pp. 1043-1051.

Bowie, O.L. (1956). Analysis of an infinite plate containing radial cracks originating at the boundary of an internal circular hole. Journal of Mathematics and Physics, 35, pp. 60-71.

Brace, W.F. (1964). Brittle fracture of rocks. In: State of Stress in the Earth's Crust. Elsevier, New York, pp. 111-174.

Brace, W.F. and Bombalakis, E.G. (1963). A note on brittle crack growth in compression. Journal of Geophysical Research, Vol 68, pp. 3709-3713.

Brady, B.H.G and Brown, E.T. (1985). Rock Mechanics For Underground Mining. George Allen & Unwin Publishers, London, p. 527.

Broek, D. (1982). Elementary Engineering Fracture Mechanics. Martinus Nijhoff, The Hague, Netherlands, 3rd edition, p. 469.

Bumsted, J. (1986) The elastic constants of Lac du Bonnet granite in tension and compression. B.Sc. Thesis, Geological Engineering Department, University of Manitoba, Winnipeg, Canada.

Carpinteri, A. (1982). Application of fracture mechanics to concrete structures. Journal of the Structural Division, Proceedings of the American Society of Civil Engineers, Vol 108, ST4, pp. 833-848.

Carpinteri, A. (1985). Scale effects in fracture of plain and reinforced concrete structures, In: Fracture Mechanics of Concrete: Structural Application and Numerical Calculation. Ed. G.C. Shah, Martinus Nijhoff Publishers, pp. 95-140.

Carpinteri, A. (1989). Decrease of apparent tensile and bending strength with specimen size: two different explanations based on fracture mechanics. International Journal of Solids & Structures, Vol 25, No 4, pp. 407-429.

Carter, B.J. (1988). Remote Fracturing Around Underground Openings. M.Sc. Thesis, Civil Engineering Department, University of Manitoba, Winnipeg, Canada.

Carter, B.J. (1992). Size and stress gradient effects on fracture around cavities. Rock Mechanics and Rock Engineering, accepted for publication.

Carter, B.J., Duncan, E.J.S. and Lajtai, E.Z. (1991*a*). Fitting strength criteria to intact rock. Geotechnical and Geological Engineering, Vol 9, pp. 73-81.

Carter, N. and Hansen, F. (1983). Creep of rock salt. Tectonophysics, Vol. 94, pp. 275-333.

Carter, B.J. and Lajtai, E.Z. Time and Stress Dependence of discrete fracture in potash rock. Submitted to: Rock Mechanics and Rock Engineering.

Carter, B.J. and Lajtai, E.Z. Stress and time dependent fracture around cavities in physical models of potash—salt rock. Submitted to: EUROCK'92, International Symposium of Rock Mechanics.

Carter, B.J., Lajtai, E.Z. and Petuhkov, A. (1991*b*). Primary and remote fracture around underground cavities. International Journal of Numerical and Analytical Methods in Geomechanics, Vol 15, pp. 21-40.

Carter, B.J., Lajtai, E.Z. and Yuan, Y. (1992). Tensile fracture from circular cavities loaded in compression. International Journal of Fracture, accepted for publication.

Chandler, N. (1989). An Energy Approach to Sleeve Fracture Stress Measurements. Ph.D. Dissertation, Civil Engineering Dept., University of Manitoba, Winnipeg, Canada.

Chen, R., Brisbin, W.C. and Stimpson, B. (1991). Mining induced deformation in potash yield pillars. Internal Report, Geological Engineering Department, University of Manitoba, Winnipeg, Canada.

Chong, K.P., Li, V.C. and Einstein, H.H. (1989). Size effects, process zone, and tension softening behavior in fracture of geomaterials. Engineering Fracture Mechanics, 34, No 3, pp. 669-678.

Costin, L.S. (1983). A microcrack model for the deformation and failure of brittle rock. Journal of Geophysical Research, Vol 88, No B11, pp. 9485-9492.

Costin, L.S. (1985). Damage mechanics in the post-failure regime. Mechanics of Materials, Vol 4, pp. 149-160.

Costin, L.S. (1987). Time-dependent deformation and failure. In: Fracture Mechanics of Rock. Ed. B.K. Atkinson, Academic Press, London, pp. 167-215.

Cramer, M.L., Dischler, S.A., Erb, D.B., Berlin, G.T., Wittreich, C.D. and Bauer,R.E. (1987). Geomechanical testing development for the Basalt Waste Isolation Project. Proceedings of the 28 U.S. Symposium on Rock Mechanics, Tucson, Arizona, pp. 1053-1062.

Cristescu, N. (1986). Damage and failure of viscoplastic rock-like materials. International Journal of Plasticity, Vol 2, No 2, pp. 189-204.

Du, J.J., Kobayashi, A.S. and Hawkins, N.M. (1990). An experimental-numerical analysis of fracture process zone in concrete fracture specimens. Engineering Fracture Mechanics, Vol 35, pp. 15-27.

Dugdale, D.S. (1960). Yielding of steel sheets containing slits. Journal of Mechanics and Physics of Solids, Vol 8, pp. 100-108.

Duncan, E.J.S. and Lajtai, E.Z. (1991). The creep of Saskatchewan potash rock in uniaxial compression. Internal Report, Geological Engineering Department, University of Manitoba, Winnipeg, Canada.

Duncan, E.J.S. (1990). Deformation and Strength of Saskatchewan Potash Rock. Ph.D. Dissertation, Civil Engineering Dept., University of Manitoba, Winnipeg, Canada, p. 323.

Durelli, A. and Parks, V. (1962). Relationship of size and stress gradient to brittle failure stress. Proceedings of the 4th US National Congress on Applied Mechanics, pp. 931-938.

Einstein, H.H., Baecher, G.B. and Hirschfeld, R.C. (1970). The effect of size on strength of a brittle rock. Proceedings of the 2nd Congress, International Society of Rock Mechanics, Belgrade, 3-2.

Engelder, T. (1987). Joints and shear fractures in rock. In: Fracture Mechanics of Rock. Ed. B.K. Atkinson, Academic Press, London, pp. 27-70.

Evans, P.H. and Marathe, M.S. (1968). Microcracking and stress-strain curves for concrete in tension. Materials and Structures (RILEM), No 1, pp. 61-64.

Evans, I. and Pomeroy, C.D. (1958). The strength of cubes of coal in uniaxial compression. Mechanical Properties of Non-Metallic Brittle Materials, Walton Ed., Butterworth, London, pp. 5-28.

Ewy, R.T. and Cook, N.G.W. (1990). Deformation and fracture around cylindrical openings in rock, Parts I and II. International Journal of Rock Mechanics and Mining Science & Geomechanics Abstracts, Vol 27, No 5, pp. 387-427.

Ewy, R.T, Kemeny, J.M, Zheng, Z. and Cook, N.G.W. (1987). Generation and analysis of stable excavation shapes under high rock stresses. Proceedings of the 6th Congress, International Symposium on Rock Mechanics, Montreal, pp. 875-881.

Fairhurst, C. and Cook, N.G.W. (1966). The phenomenon of rock splitting parallel to free surfaces under compressive stress. Proceedings 1st Congress, International Society of Rock Mechanics, Lisbon, pp. 687-692.

Freiman, S.W. (1982) A critical evaluation of fracture mechanics techniques for brittle materials. Fracture Mechanics of Ceramics, Vol 6, pp. 27-45.

Friedman, M., Handin, J. and Alani, G. (1972). Fracture-surface energy of rocks. International Journal of Rock Mechanics and Mining Science & Geomechanics Abstracts, Vol 9, pp. 757-766.

Fuzesy, A. (1982). Potash in Saskatchewan. Saskatchewan Energy and Mines, Report 181.

Gay, N.C. (1976). Fracture growth around openings in large blocks of rock subjected to uniaxial and biaxial compression. International Journal of Rock Mechanics and Mining Science & Geomechanics Abstracts, Vol 13, pp. 231-243.

Gendzwill, D.J. (1983). Elastic properties of carbonate rocks over the Cory mine. In: Potash Technology - Mining, Processing, Maintenance, Transportation, Occupational Health and Safety, Environment, Proceedings of Potash '83, Pergamon Press, Ed. R.M. McKercher, pp. 299-304.

Ghandi, C. and Ashby, M.F. (1979). Fracture-mechanism maps for materials which cleave: F.C.C., B.C.C. and H.C.P metals and ceramics. Acta Metallurgica, Vol. 27, pp. 1565-1602.

Gonano, L.P. (1974). Stress Gradient and Size Effect Phenomena in Brittle Materials. Ph.D. Dissertation, James Cook University, Northern Queensland, Australia.

Gonano, L.P. and Brown, E.T. (1975). Stress gradient phenomena and related size effect in brittle materials. Proceedings of the 5th Australian Conference on Mechanics of Structures & Materials, Melbourne, Australia, pp. 205-218.

Gopalaratnam, V.S. and Shah, S.P. (1985). Softening response of plain concrete in direct tension. American Concrete Institute Journal, May-June, pp. 310-323.

Gramberg, J. (1989). A Non-Conventional View on Rock Mechanics and Fracture Mechanics. A.A. Balkema, Rotterdam.

Griffith, A.A. (1924). The theory of rupture. 1st International Congress of Applied Mechanics, Delft, pp. 55-63.

Griggs, D. and Handin, J. (1960). Observations on fracture and a hypothesis of earthquakes. Geological Society of America Memoirs, 79, pp. 347-364.

Groves, G. and Kelly, A. (1963). Independent slip systems in crystals. Phil. Mag., 8, pp. 877-887.

Guenot, A. (1989). Borehole breakouts and stress fields. International Journal of Rock Mechanics and Mining Science & Geomechanics Abstracts, Vol 26, No 3, pp. 185-195.

Haasen, P. (1985). Dislocations and the plasticity of ionic crystals, In: Dislocations and Properties of Real Materials. Inst. of Metals, pp. 312-332.

Haimson, B.C. and Herrick, C.G. (1989). Borehole breakouts and in situ stress. Proceedings of the 12th Annual Energy-Sources Technology Conference & Exhibition, Drilling Symposium, American Society of Mechanical Engineers, Vol 22, pp. 17-22.

Hallbauer, D.K., Wagner, H. and Cook, N.G.W. (1973) Some observations concerning the microscopic and mechanical behavior of quartzite specimens in stiff, triaxial compression tests. International Journal of Rock Mechanics and Mining Science & Geomechanics Abstracts, Vol 10, pp. 713-733.

Hambley, D.F. and Mraz, D.Z. (1987). Behavior of a wide opening in a deep potash mine: a case History. 28th US Symposium on Rock Mechanics, Tucson, pp. 883-892.

Handin, J.W. and Carter, N.L. (1980): Rheology of rocks at high temperature. Proceedings of the 4th International Congress on Rock Mechanics, pp. 97-106.

Haupt, M. and Natau, O. (1988). Performance and results of geomechanical measurements in a rock salt gallery. 2nd International Symposium on Field Measurements in Geomechanics, A.A. Balkema, Rotterdam, pp. 635-644.

Herget, G. and Mackintosh, A.D. (1987). Mining induced stresses in Saskatchewan potash. Proceedings of the 6th Congress, International Society of Rock Mechanics, Montreal, pp. 953-957.

Hillerborg, A. (1985). Numerical methods to simulate softening and fracture of concrete, In: Fracture Mechanics of Concrete: Structural Application and Numerical Calculation. Editor-in-Chief: G.C. Shah, Martinus Nijhoff Publishers, pp. 141-170.

Hillerborg, A. (1983) Analysis of one single crack. In: Fracture Mechanics of Concrete. Ed. F.H. Whittmann, Elsevier,. Netherlands, pp. 223-249.

Hillerborg, A., Modeer, M. and Peterson, P.E. (1976). Analysis of crack formation and crack growth in concrete by means of fracture mechanics and finite elements. Cement and Concrete Research, Vol 6, pp. 773-782.

Hinton, E. and Owen, D.R.J. (1979). An Introduction to Finite Element Computations. Pineridge Press, Swansea, UK.

Hoagland, R.G., Hahn, G.T. and Rosenfield, A.R. (1973). Influence of microstructure on fracture propagation in rock. Rock Mechanics, Vol 5, pp. 77-106.

Hodgson, K. and Cook, N.G.W. (1970). The effects of size and stress gradient on the strength of rock. Proceedings of the 2nd Congress of the International Society of Rock Mechanics, Belgrade, 2, pp. 31-34.

Hoek, E. (1965). Rock fracture under static stress conditions, Nat. Mech. Eng. Res. Inst. Report MEG 383, CSIR, S. Africa, 1965.

Hoek, E. and Brown, E.T. (1980). Underground Excavations in Rock. Institution of Mining and Metallurgy, London.

Hondros, G. (1959). The evaluation of Poisson's ratio and the modulus of materials of a low tensile resistance by the Brazilian (indirect tensile) test with particular reference to concrete, Aust. J. Applied Science, Vol 10, pp. 243-264.

Honisch, K. (1988). Rock mass modelling for large underground powerhouses. Proceedings of the 6th International Conference on Numerical Methods in Geomechanics, Innsbruck, A.A. Balkema, Vol 3, pp. 1517-1522.

Horii, H. and Nemat-Nasser, S. (1986) Brittle faulting in compression: splitting, faulting and brittle ductile transition. Philosophical Transcripts of the Royal Society of London, A 319, pp. 337-374.

Horii, H. and Nemat-Nasser, S. (1984) Compression-induced microcrack growth in brittle solids: axial splitting and shear failure, Journal of Geophysics, B4, pp. 3105-3125.

Horner, R.B. (1983). Earthquakes in Saskatchewan: a potential hazard to the potash industry. In: Potash Technology - Mining, Processing, Maintenance, Transportation, Occupational Health and Safety, Environment, Proceedings of Potash '83, Pergamon Press, Ed. R.M. McKercher, pp. 185-190.

Horning, B. (1989). Physical modeling of fractures around a cavity in potash. B.Sc. Thesis, Geological Engineering Department, University of Manitoba, Winnipeg, Canada.

Horseman, S. (1988). Moisture content - a major uncertainty in storage cavity closure prediction. Proceedings 2nd Conference, Mechanical Behavior of Salt, Hanover, Germany, Trans Tech Publications, pp. 53-68.

Horseman, S. and Passaris, E. (1981). Creep tests for storage cavity closure prediction. Proceedings of the First Conference on the Mechanical Behavior of Salt, Edited by H.R. Hardy and M. Langer, Pennsylvania State University, University Park, Pennsylvania, pp. 119-157.

Inglis, C.E. (1913). Stresses in a plate due to the presence of cracks and sharp corners. Institute of Naval Architecture, London, 55, pp. 219-230.

Ingraffea, A.R. (1987). Theory of crack initiation and propagation in rock. In "Fracture Mechanics of Rock". Edited by B.K. Atkinson, Academic Press, London, pp. 77-110.

Ingraffea, A.R. and Schmidt, R.A. (1978) Experimental verification of a fracture mechanics model for tensile strength prediction of Indiana limestone. Proceedings of the 19th U.S. Symposium on Rock Mechanics, Stateline, Nevada, pp. 247-253.

Ingraffea, A.R. (1979). The strength ratio effect in the fracture of rock structures. Proceedings of the 20th US Symposium on Rock Mechanics, Austin, Texas, pp. 153-169.

Ingraffea, A.R. (1977). Discrete Fracture Propagation in Rock: Laboratory tests and finite element analysis. Ph.D. Dissertation, University of Colorado, Boulder, Colorado, p. 347.

Irwin, G.R. (1957). Analysis of stresses and strains near the end of a crack traversing a plate. Journal of Applied Mechanics, Vol 24, Transactions of the American Society of Mechanical Engineers, Vol 79, pp. 361-364.

Ito, T. and Hayashi, K. (1991). Physical background to the breakdown pressure in hydraulic fracturing tectonic stress measurements. International Journal of Rock Mechanics and Mining Science & Geomechanics Abstracts, Vol 28, No 4, pp. 285-293.

Jaeger, J.C. and Cook, N.G.W. (1979). Fundamentals of Rock Mechanics. Chapman and Hall, London, 3rd ed.

Johnston, I.W. (1985*a*). Strength of intact geomechanical materials. Journal of Geotechnical Engineering, American Society of Civil Engineers, Vol 111, No 6, pp. 730-749.

Johnston, I.W. (1985*b*). Comparison of two strength criteria for intact rock. Journal of Geotechnical Engineering, American Society of Civil Engineers, Vol 111, No 12, pp. 1449-1454.

Kachanov, M.L. (1982). A microcrack model of rock inelasticity. Parts I & II. Mechanics of Materials, Vol 1, pp. 19-41.

Kaiser, P.K., Guenot, A. and Morgenstern, N.R. (1985). Deformation of small tunnels—IV. Behaviour during failure. International Journal of Rock Mechanics and Mining Science & Geomechanics Abstracts, Vol. 22, pp. 141-152.

Kaiser, P.K. and Maloney, S. (1987). Factors influencing the stability of deep boreholes. Proceedings of the 6th International Society of Rock Mechanics, Montreal, Canada, pp. 675-680.

Kaskiw, L. (1984). Static fatigue of Red River limestone. B.Sc. Thesis, Geological Engineering Department, University of Manitoba, Winnipeg, Canada.

Kemeny, J.M. and Cook, N.G.W. (1990). Micromechanics of deformation in rocks. NATO Advanced Workshop on Toughening Mechanisms in Quasi-Brittle Material.

Kemeny, J.M. and Cook, N.G.W. (1987). Crack models for the failure of rock in compression. Proceedings of the 2nd International Conference on Constitutive Laws for Engineering Materials, Tucson, Arizona, pp. 879-887.

Kilgour, J.D. (1984). Fracture toughness of Tyndall limestone. B.Sc. Thesis, Geological Engineering Department, University of Manitoba, Winnipeg, Canada.

Klause, G.K. (1988). Triaxial strength of Tyndall limestone. B.Sc. Thesis, Geological Engineering Department, University of Manitoba, Winnipeg, Canada.

Kowamoto, T. and Saito, T. (1976). Stress and stability analyses of underground openings taking post failure behavior of rock into consideration. Numerical Methods in Geomechanics, Vol 2, pp. 791-801.

Krajcinovic, D. and Fonseka, G.U. (1981). The continuous damage theory of brittle materials: Parts I & II. Journal of Applied Mechanics, Transactions of the American Society of Mechanical Engineers, Vol 48, pp. 809-824.

Kranz, R.L. (1979). Crack-crack and crack-pore interactions in stressed granite. International Journal of Rock Mechanics and Mining Science & Geomechanics Abstracts, Vol 16, pp. 37-47.

Kranz, R.L. (1983). Microcracks in rocks: A review. Tectonophysics, Vol 100, pp. 449-480.

Kroll, D.W. (1987). Basic geomechanical properties of the Dawson Bay Formation. M.Sc. Thesis, Civil Engineering Department, University of Manitoba, Winnipeg.

Labuz, J.F., Shah, S.P. and Dowding, C.H. (1985). Experimental analysis of crack propagation in granite. International Journal of Rock Mechanics and Mining Science & Geomechanics Abstracts, Vol 22, No 2, pp. 85-98.

Lajtai, E.Z. (1971). A theoretical and experimental evaluation of the Griffith theory of brittle fracture. Tectonophysics, Vol 11, pp. 129-156.

Lajtai, E.Z. (1972). Effect of tensile stress gradient on brittle fracture initiation. International Journal of Rock Mechanics Mining Science & Geomechanics Abstracts, Vol 9, pp. 569-578.

Lajtai, E.Z. (1974). Brittle fracture in compression. International Journal of Fracture, Vol 10, No 4, pp. 525-536.

Lajtai, E.Z. (1977). A mechanistic view of some aspects of jointing in rocks. Tectonophysics, Vol 38, pp. 327-338.

Lajtai, E.Z. (1982). The fracture of Lac du Bonnet granite. Report to Atomic Energy of Canada Ltd., Whiteshell Nuclear Research Establishment, p. 126.

Lajtai, E.Z., Carter, B.J. and Ayari, M.L. (1990). Criteria for brittle fracture in compression. Engineering Fracture Mechanics, Vol 37, pp.59-74.

Lajtai, E.Z., Carter, B.J. and Duncan, E.J.S. (1991*a*). Modeling rock fracture in compression. Engineering Geology, Vol 31, pp. 277-289.

Lajtai, E.Z., Duncan, E.J.S. and Carter, B.J. (1991*b*). The effect of strain rate on rock strength. Rock Mechanics and Rock Engineering, Vol 24, pp. 99-109.

Lajtai, E.Z. and Duncan, E.J.S. (1988). The mechanism of deformation and fracture in potash rock. Canadian Geotechnical Journal, Vol 25, pp. 262-278.

Lajtai, E.Z. and Lajtai, V.N. (1975). The collapse of cavities. International Journal of Rock Mechanics and Mining Science & Geomech. Abstracts, Vol 12, pp. 81-86.

Lane, D.M. (1959). Dawson Bay formation in the Quill Lades -- Qu'Appelle area, Saskatchewan. Department of Mineral Resources Report #28, 49 p.

Lawn, B.R. and Wilshaw, T.R. (1975). Fracture of Brittle Solids. Cambridge University Press, Cambridge, p. 204.

Leon, A. (1934). Uber the Rolle der Trennungsbruche ins Rahmen der Mohr'shen anstrengungshypothese. Bauingenieur, 15.

Lubliner, J., Oliver, J., Oller, S. and Onate, E. (1989). A plastic-damage model for concrete. International Journal of Solids and Structures. Vol 25, No 3, pp. 299-326.

Martin, C.D. and Christiansson, R. (1991). Overcoring in highly stressed granite - the influence of microcracking. International Journal of Rock Mechanics and Mining Science & Geomechanics Abstracts, Vol. 28, No. 1, pp. 53-70.

Martin, C.D. (1990). Characterizing in-situ stress domains at the AECL Underground Research Laboratory. Canadian Geotechnical Journal, Vol 27, pp. 631-646.

McClintock, F.A. and Walsh, J. (1962). Friction on Griffith cracks in rocks under pressure. Proceedings of the 4th National Congress on Applied Mechanics, Berkeley, Vol 2, pp. 1015-1021.

Morgenstern, N.R. and Sepehr, K. (1990). Time-dependent hydraulic fracturing of potash mines. International Journal of Rock Mechanics and Mining Science & Geomechanics Abstracts, Vol 28, pp. 187-197.

Mraz, D.Z. (1987). Proposed design for high pressure isolation structure in saltrock. Proceedings of the 6th Congress, International Society of Rock Mechanics, Montreal, pp. 195-198.

Murell, S.A.F and Digby, P.J. (1970). The theory of brittle fracture initiation under triaxial stress conditions - I. Geophysical Journal of the Royal Astronomical Society, 19, pp. 309-334.

Muskhelishvili, N.I. (1963). Some Basic Problems of the Mathematical Theory of Elasticity. 4th edition, P. Noordhoff Ltd, The Netherlands, p. 718.

Nemat-Nasser, S. (1985). Discussion of: Geometric probability approach to the characterization and analysis of microcracking in rocks. Mechanics of Materials, Vol 4, pp. 261-276.

Nemat-Nasser, S. and Horri, H. (1982). Compression induced nonplanar crack extension with application to splitting, exfoliation, and rockburst. Journal of Geophysical Research, Vol 87, No B8, pp. 6805-6821.

Nemat-Nasser, S. and Obata, M. (1988). A microcrack model of dilatancy in brittle materials. Journal of Applied Mechanics, Transactions of the American Society of Mechanical Engineers, Vol 55, pp. 24-35.

Nesetova, V. and Lajtai, E.Z. (1973). Fracture from compressive stress concentrations around elastic flaws. International Journal of Rock Mechanics and Mining Science & Geomechanics Abstracts, Vol 10, pp. 265-284.

Newman, D.A. and Bennett, D.G. (1990). The effect of specimen size and stress rate for the Brazilian test - a statistical analysis. Rock Mechanics and Rock Engineering, Vol 23, pp. 123-134.

Nowakowski, S.A. (1984) The size effect on the tensile strength of Lac du Bonnet granite using the Brazilian test. B.Sc. Thesis, Geological Engineering Department, University of Manitoba, Winnipeg, Canada.

Nuismer, R.J. and Lavor, J.D. (1978). Applications of the average stress failure criterion: Part I - tension. Journal of Composite Material, 12, pp 238-249.

Nuismer, R.J. and Whitney, J.M. (1975). Uniaxial failure of composite laminates containing stress concentrations. Fracture Mechanics of Composites, ASTM STP 593, American Society of Testing and Materials, pp. 117-142.

Nur, A. and Simmons, G. (1970) The origin of small cracks in igneous rocks. International Journal of Rock Mechanics and Mining Science, Vol 7, pp. 307-314.

Ortiz, M. (1988) Microcrack coalescence and macroscopic crack growth initiation in brittle solids. International Journal of Solids and Structures, Vol 24, pp. 231-250.

Ouchterlony, F. (1988) Suggested methods for determining the fracture toughness of rock. International Journal of Rock Mechanics and Mining Science & Geomechanics Abstracts, Vol 25, pp. 71-96.

Owen, D.R. and Hinton, E.A. (1980). Finite Elements in Plasticity: Theory and Practice. Pineridge Press, Swansea, UK.

Owen, D.R. and Fawkes, A.J. (1983). Engineering Fracture Mechanics Numerical Methods and Applications. Pineridge Press, Swansea, UK.

Paris, P.C. and Sih, G.C. (1965). Stress analysis of cracks. ASTM STP 381, Philadelphia, American Society of Testing and Materials, pp. 30-83.

Paul, B. (1961). Modification of the Coulomb-Mohr theory of fracture. Journal of Applied Mechanics, Vol 28, pp.259-268.

Peng, S. and Johnson, A.M. (1972). Crack growth and faulting in specimens of Chelmsford granite. International Journal of Rock Mechanics and Mining Science & Geomechanics Abstracts, Vol 9, pp 37-86.

Pollard, D.D. and Segall, P. (1987). Theoretical displacements and stresses near fractures in rock: with applications to faults, joints, veins, dikes, and solution surfaces, In: Fracture Mechanics of Rock. Ed. B.K. Atkinson, Academic Press, London, pp. 277-350.

Pollard, D.D., Segall, P. and Delaney, P.T. (1982). Formation and interpretation of dilatant echelon cracks. Geological Society of America Bulletin, Vol 93, pp. 1291-1303.

Price, N.J. (1968). Fault and Joint Development in Brittle and Semi-Brittle Rock. Pergamon Press, London, 2nd edition, p. 176.

Rummel, F. (1987). Fracture mechanics approach to hydraulic fracturing stress measurements. In: Fracture Mechanics of Rock, Edited by B.K. Atkinson, Academic Press, London, pp. 277-350.

Rummel, F. and Winter, R.B. (1983). Fracture mechanics as applied to hydraulic fracturing stress measurements. Earthquake Prediction Research, Vol 2, pp. 33-45.

Samchek, A.T. (1983). Analysis of rock creep under wet and dry conditions. Unpublished B.Sc. Thesis, Geological Engineering Department, University of Manitoba, Winnipeg, Canada.

Sammis, C.G. and Ashby, M.F. (1986). The failure of brittle porous solids under compressive stress states. Acta Metallurgica, Vol 34, No 3, pp. 511-526.

Santarelli, F.J. and Brown, E.T. (1987). Performance of deep well bores in rock with a confining pressure-dependent elastic modulus. Proceedings of the 6th Congress, International Society of Rock Mechanics, Montreal, Canada, pp. 1217-1222.

Santarelli, F.J., Brown, E.T. and Maury, V. (1986). Analyses of borehole stresses using pressure-dependent, linear elasticity. International Journal of Rock Mechanics and Mining Science & Geomechanics Abstracts, Vol 23, No 6, pp. 445-449.

Schmidt, R.A. and Lutz, T.J. (1979). K_{IC} and J_{IC} of Westerly Granite - Effects of thickness and in-plane dimensions, In: Fracture Mechanics Applied to Brittle Materials. ASTM STP 678, Ed. S.W. Frieman, American Society for Testing and Materials, pp. 166-182.

Scholz, C.H. (1968). Mechanisms of creep in brittle rock. Journal of Geophysical Research, Vol 73, pp. 3295-3302.

Secor, D.T. (1965). Role of fluid pressure in jointing. American Journal of Science, 263, pp. 633-646.

Senseny, P.E. (1984). Specimen size and stress history effects on creep of salt. Proceedings of the First Conference on The Mechanical Behavior of Salt, Pennsylvania State University, Trans Tech Publications, pp. 369-379.

Sepehr, K. (1988). Non-linear and time dependent finite element modeling of underground excavations with special reference to induced seismicity in potash mining. Ph.D. Dissertation, Civil Engineering Dept., University of Manitoba, Winnipeg, Canada.

Serata, S. (1983). Stress control method: quantitative approach to stabilizing mine openings in weak ground, In: Stability in Underground Mining, Edited by C. Brawner, pp. 52-93.

Sheory, P.R., Biswas, A.K. and Choubey, V.D. (1989) An empirical failure criterion for rocks and jointed rock masses. Engineering Geology, Vol 26, pp. 141-159.

Sih, G.C. (1973). Handbook of Stress Intensity Factors for Researchers and Engineers. Lehigh University, Bethlehem, Pa.

Simmons,G. and Richter, D. (1974) Microcracks in rocks. In: The Physics and Chemistry of Minerals and Rocks, Ed. R. Strens, Wiley, New York, pp. 105-137.

Singh, U.K. and Digby, P.J. (1989*a*). A continuum damage model for simulation of the progressive failure of brittle rocks. Internation Journal of Solids and Structures, Vol 25, No 6, pp. 647-663.

Singh, U.K. and Digby, P.J. (1989*b*). The application of a continuum damage model in the finite element simulation of the progressive failure and localization of deformation in brittle rock structures. Internation Journal of Solids and Structures, Vol 25, No 9, pp. 1023-1038.

Skrotzki, W. (1984). An estimate of the brittle to ductile transition in salt. Proceedings of the First Conference on The Mechanical Behavior of Salt, Pennsylvania State University, Pennsylvania, Trans Tech Publications, pp. 381-388.

Skrotzki, W. and Haasen, P. (1988*a*). The role of cross slip in the steady state creep of rock salt. Proceedings 2nd Conference, Mechanical Behavior of Salt, Hanover, Germany, Trans Tech Publications, pp. 69-81.

Skrotzki, W. and Haasen, P. (1988*b*). The influence of texture on the creep of salt. Proceedings 2nd Conference, Mechanical Behavior of Salt, Hanover, Germany, Trans Tech Publications, pp. 83-88.

Sneddon, I.N. (1946) The distribution of stress in the neighborhood of a crack in an elastic solid. Proceedings of Physical Society of London, Vol 187, pp. 229-260.

Sprunt, E.S. and Brace, W.F. (1974) Direct observation of microcavities in crystalline rocks. International Journal of Rock Mechanics and Mining Science, Vol 11, pp. 139-150.

Steed, C., Bawden, W.F., Coode, A.M. and Mottahed, P. (1985). Subsidence prediction for Saskatchewan potash mines. 26th US Symposium on Rock Mechanics, Rapid City, South Dakota, pp. 163-170.

Stevens, J.L. and Holcomb, D.J. (1980*a*). A theoretical investigation of the sliding crack model of dilatancy. Journal of Geophysical Research, Vol 85, No B12, pp. 7091-7100.

Stevens, J.L. and Holcomb, D.J. (1980*b*). The reversible Griffith crack: A viable model for dilatancy. Journal of Geophysical Research, Vol 85, No B12, pp.7101-7107.

Stimpson, B. and Chen, R. (1991). The measurement of rock moduli in compression and tension and its practical significance. Proceedings of the 44th Canadian Geotechnical Conference, Calgary, Alberta, Canada, paper # 34.

Suresh, S. and Brockenbrough, J.R. (1990). A theory for creep by interfacial flaw growth in ceramics and ceramic composites. Acta Metallurgica, Vol. 38, pp. 55-68.

Svab, M. and Lajtai, E.Z. (1981). Microstructural control of crack growth in Lac du Bonnet granite, In: Fracture Problem and Solutions in Industry. Proceedings of the Fifth Canadian Fracture Conference, Winnipeg, Pergamon Press, pp. 219-228.

Tapponier, P. and Brace, W.F. (1976) Development of stress induced microcracks in Westerly granite. International Journal of Rock Mechanics and Mining Science, Vol 13, pp. 103-112.

Timoshenko, S. and Goodier, J.N. (1951). Theory of Elasticity. 2nd edition, McGraw-Hill Book Company Inc., p. 506.

Van Hise, C.R. (1896). 16th Annual Report, US Geological Survey, US Government Printing Office, Washington, DC.

Vardoulakis, I. (1984). Rock bursting as a surface instability phenomenon. International Journal of Rock Mechanics and Mining Science & Geomechanics Abstracts, Vol 21, No 3, pp. 137-144.

von Mises, R. (1928). Mechanik der plastichen Formanderung von Kristallen. Z. fur Angew. Math. und Mech., 8, pp 161-185.

Wang, C., Liu, P., Hu, R. and Sun, X. (1990) Study of the fracture process zone in rock by laser speckle interferometry. International Journal of Rock Mechanics and Mining Science & Geomechanics Abstracts, Vol 27, No 1, pp. 65-69.

Wawersik, W.R. and Fairhurst, C. (1970). A study of brittle rock fracture in laboratory compression experiments. International Journal of Rock Mechanics and Mining Science & Geomechanics Abstracts, Vol 7, pp. 561-575.

Wawersik, W. and Hannum, D. (1980). Mechanical behavior of New Mexico rock salt in triaxial compression up to 200°C. Journal of Geophysical Research, Vol. 85, B2, pp. 891-900.

Wecharatana, M. and Shah, S.P. (1983). Predictions of nonlinear fracture process zone in concrete. Journal of Engineering Mechanics, American Society of Civil Engineers, Vol 109, No 5, pp. 1231-1246.

Weibull, W. (1939). A statistical theory of the strength of materials. Ingeniorsvetenskap Akademiens Handlingar, Nr 151, pp 5-44.

Weiss, R. (1984). Brazilian testing of Tyndall Limestone. B.Sc. Thesis, Geological Engineering Department, University of Manitoba, Winnipeg, Manitoba, Canada.

Westergaard, H.M. (1939). Bearing pressure and cracks. Journal of Applied Mechanics, Vol 61, pp. A49-A53.

Whittaker, B.N. and Frith, R.C. (1990). Tunnelling - Design, Stability and Construction. Institution of Mining and Metallurgy, p. 453.

Williams, M.L. (1956). On the stress distribution at the base of a stationary crack. Applied Mechanics, American Society of Mechanical Engineers, No 56, A - 16.

Worsely, N. and Fuzesy, A. (1979). The potash-bearing members of the Devonian Prairie Evaporite of southeastern Saskatchewan, south of the mining area. Economic Geology, Vol. 74, pp. 377-388.

Yamada, P.H. (1984). Analysis of slow crack growth in potash. B.Sc. Thesis, Geological Engineering Department, University of Manitoba, Winnipeg, Canada.

Yazdani, S. and Screyer, H.L. (1988). An anisotropic damage model with dilatation for concrete. Mechanics of Materials, Vol 7, pp. 231-244.

Yuan, Y., Ayari, M.L. and Lajtai, E.Z. Post-processing stresses from the finite element analysis using boundary integral equations. Submitted to: International Journal of Numerical Methods in Engineering.

Yukatake, H. (1989). Fracturing process of granite inferred from measurements of spatial and temporal variations in velocity during triaxial deformations. Journal of Geophysical Research, Vol 94, No B11, pp. 15639-15651.

Zienkiewicz, O.C. (1977). The Finite Element Method in Engineering Science. McGraw-Hill, London, 2nd edition.

Zheng, Z., Cook, N.G.W. and Myer, L.R. (1989*a*). Stress induced microcrack geometry at failure in unconfined and confined axial compressive tests. 30th US Rock Mechanics Symposium, West Virginia University, pp. 749-756.

Zheng, Z., Kemeny, J. and Cook, N.G.W. (1989*b*). Analysis of borehole breakouts. Journal of Geophysical Research, Vol 94, No B6, pp. 7171-7182.

Zoback, M.D., Moos, D. and Mastin, L. (1985). Well bore breakouts and in situ stress. Journal of Geophysical Research, 90, No B7, pp. 5523-5530.

APPENDIX A

Bazant's Size Effect Model (Bazant, 1984)

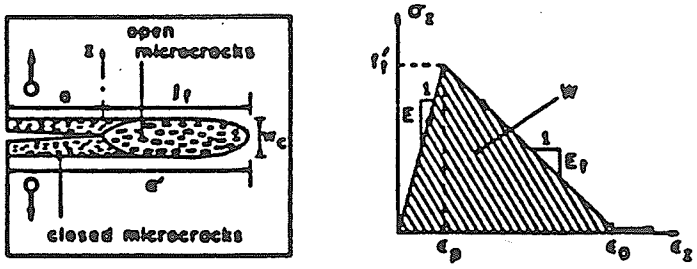

W_c - material property = (n) (d_a)
d_a - maximum aggregate size in concrete or grain size in rock
n - empirical constant, 3 for concrete and 5 for rock
f_t - peak tensile strength
E_c - elastic modulus
E_t - softening modulus (negative)

$$G_f = W_c \left(1 - \frac{E_c}{E_t}\right) \frac{f_t}{2\,E_c}$$

The energy release rate $\frac{\partial W}{\partial a}$ must be equal to the energy consumed per unit crack band extension

$$\frac{\partial W}{\partial a} = G_f \cdot b$$

substituting gives

$$\sigma_N = B \cdot f_t$$

where

$$\sigma_n = \sigma \qquad f_t = \frac{f_t}{\sqrt{1 + \frac{\lambda}{\lambda_o}}} \qquad B = \sqrt{1 + \frac{E_c}{E_t}} \qquad \lambda = \frac{d}{d_a}$$

B and λ_o are constants.

The f_t—equation may be transformed to a linear plot

$$\overline{Y} = \overline{a} + \overline{b} \cdot \lambda$$

where

$$Y = \left(\frac{f_t}{\sigma_N}\right)^2 \qquad \overline{a} = \frac{1}{B^2} \qquad \overline{b} = \frac{1}{B^2 \lambda_o}$$

slope (b) and y-intercept (a) may be determined by statistical regression and then

$$B = \frac{1}{\sqrt{\overline{a}}} \qquad \lambda_o = \frac{\overline{a}}{\overline{b}}$$

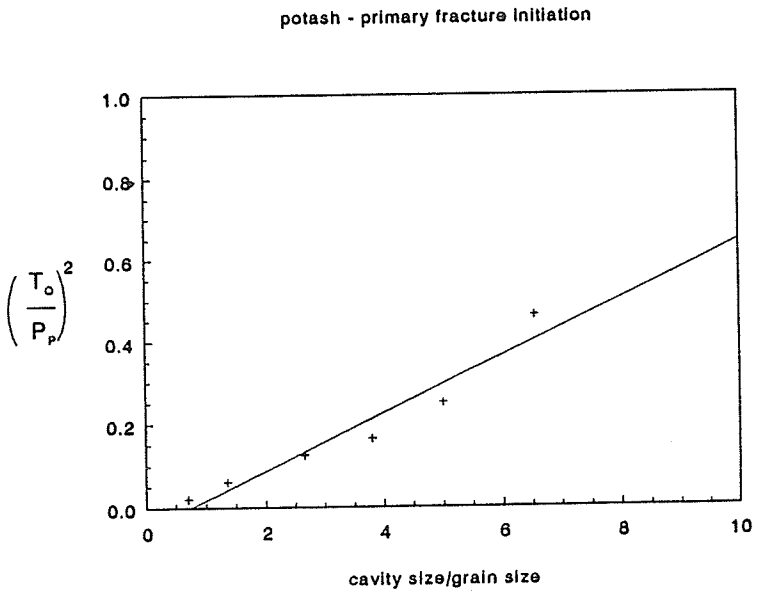

From the figure for potash, primary fracture initiation data—normalized with the material tensile strength and plotted against cavity radius—normalized with the average grain size

$a=-0.05136$ and $b=0.0694$.

To get B, one needs the square root of a, which in this case is undefined. Consequently, the parameters needed to fit Bazant's model (Bazant, 1984) cannot be obtained in this manner.